Coherence, tunability, spectral and spatial properties of femtosecond extreme-ultraviolet light sources

Benoît Mahieu

HAL Id: tel-00967018

https://theses.hal.science/tel-00967018

Submitted on 27 Mar 2014
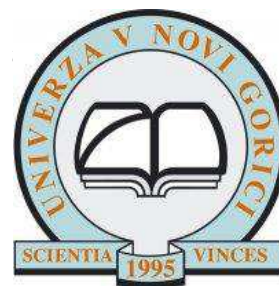
UNIVERSITE PARIS-SUD

ÉCOLE DOCTORALE : Ondes et Matière
Elettra – Sincrotrone Trieste & CEA Saclay, Service des Photons, Atomes et Molécules

DISCIPLINE *Physique*

Cohérence, accordabilité, propriétés spectrales et spatiales

de sources de lumière extrême-ultraviolette femtoseconde

THÈSE DE DOCTORAT

soutenue le 17/06/2013

par

Benoît Mahieu

Directeur de thèse :	Giovanni DE NINNO	Professeur (Université de Nova Gorica)
Co-directeur de thèse :	David GARZELLA	Docteur (Université Paris-Sud)

Composition du jury :

Président du jury :	Annie KLISNICK	Professeur (Université Paris-Sud)
Rapporteurs :	Serge BIELAWSKI	Professeur (Université Lille 1)
	Anne L'HUILLIER	Professeur (Université de Lund)
Examinateur :	Samo STANIC	Professeur (Université de Nova Gorica)

Abstract – English

Single-pass free-electron lasers (FELs) are currently the most promising facilities for providing light pulses with high energies (μJ to mJ) at femtosecond time scales ($1\ fs = 10^{-15}\ s$) and with ultrashort wavelengths (nanometer resolution i.e., down to extreme-ultraviolet and X-ray spectral regions). Extreme-ultraviolet FELs are still quite young so that many questions remain open. Those addressed within this manuscript concern the so-called seeded configuration, where an external coherent source (the "seed") initiates the process. In particular, we focus in this thesis on the transverse and longitudinal characteristics of the light, its coherence, the properties of the temporal phase and the direct correlations between the seed and the FEL emission.

With regard to FELs, high-order harmonics of femtosecond laser pulses generated in noble gases (HHG technique) exhibit both competitive and complementary features. Competitive, because the produced pulses have similar assets as the ones provided by an FEL. Complementary, because the generated harmonics can be used as a seed or, in combination with FEL light, to perform multi-beam experiments. Even though less powerful pulses are produced by a HHG source, its implementation requires a significantly smaller effort. The efficiency of harmonic conversion, the tunability and spatial quality of the generated beam, and how these parameters depend on the driving laser are the issues discussed within this manuscript.

The general will of the scientific community to perform novel experiments requires deep studies and optimization of FEL and HHG sources. In particular, on the seeded FEL facility FERMI@Elettra of Trieste, the induction of chirp in the radiation has led to remarkable results. Among others, a method of generation of split pulses with different wavelengths has been construed and developed. Such a possibility paves the way for the use of seeded FEL facilities as stand-alone sources for two-colour pump-probe setups. More generally, the study of phenomena involved in the FEL and HHG processes, together with the characterization of the light properties, are intrinsically exciting matters that have direct connections with fundamental aspects of physics.

Abstract – Slovenian

Laser na proste elektrone (LPE, ang. free-electron laser – FEL) z enojnim prehodom je trenutno najbolj obetaven vir femtosekundnih (1 $fs = 10^{-15}$ s) svetlobnih pulzov z visoko energijo (μJ do mJ) in ultra kratko valovno dolžino (nanometrska ločljivost, t.j., vse do spektralnega območja ekstremne ultravijolične in rentgenske svetlobe). LPE-ji, ki delujejo na področju ekstremne ultravijolične svetlobe, so razmeroma novi svetlobni viri, kar pomeni, da so glede njihovega delovanja odprta še mnoga vprašanja. V pričujočem doktorskem delu smo se ukvarjali predvsem z dvostopenjsko konfiguracijo, pri kateri LPE ojači zunanje (koherentno) elektromagnetno valovanje (seed). Osredotočili smo se na transverzalne in longitudinalne lastnosti proizvedene svetlobe, koherenco, lastnosti časovne faze ter na direktne korelacije med zunanjim virom (seed) in sevanjem LPE-ja.

Poleg LPE-jev so v vzponu tudi svetlobni viri, ki temeljijo na generaciji visokih harmonikov (GVH, ang. high-order harmonic generation – HHG) v žlahtnih plinih. Ti svetlobni viri so zaradi podobnih lastnosti pulzov konkurenčni LPE-jem, po drugi strani pa predstavljajo komplementarne izvore svetlobe, ker jih je mogoče uporabiti v dvostopenjski LPE konfiguraciji kot vir zunanjega elektromagnetnega valovanja (seed) ali v kombinaciji z LPE-jem v eksperimentih z dvema ali več žarki. Kljub temu, da so ti svetlobni viri šibkejši v primerjavi z LPE-ji, je njihova izvedba bistveno lažja. V dizertaciji obravnavamo izkoristek harmonične pretvorbe virov, ki temeljijo na principu GVH, nastavljivost in prostorsko kakovost žarkov, ter odvisnost omenjenih parametrov od gonilnega laserja.

Zaradi vse večje težnje po novih eksperimentih na vseh znanstvenih področjih sta ključna zelo natančno poznavanje delovanja in optimizacija LPE-jev in virov, ki temeljijo na GVH. Med bolj pomembne dosežke na LPE-ju FERMI@Elettra v Trstu spadajo možnost spreminjanja trenutne frekvence proizvedene svetlobe (ang. chirp) na podlagi katere je bila razvita metoda za generacijo razdeljenih pulzov z različnimi valovnimi dolžinami. S pomočjo te metode bo možno dvostopenjske LPE-je uporabljati kot samostojne vire svetlobe za poskuse v t.i. načinu "pump-probe". V dizertaciji so predstavljene študije pojavov, ki so prisotni pri generaciji svetlobe v LPE-jih ter virih, ki temeljijo na GVH. Ti pojavi so, skupaj z metodami karakterizacije proizvedene svetlobe, tesno povezani s temeljnimi principi v fiziki.

Abstract – French

Les lasers à électrons libres (LELs) à simple passage représentent actuellement la possibilité la plus prometteuse pour fournir des impulsions lumineuses de haute énergie (μJ à mJ) à des échelles de durée femtoseconde ($1\ fs = 10^{-15}\ s$) et des longueurs d'ondes ultra-courtes (résolution nanométrique c.-à-d. jusqu'aux domaines de l'extrême-ultraviolet et des rayons X). Les LELs émettant dans l'extrême-ultraviolet sont une technologie encore jeune, si bien que de nombreuses questions restent ouvertes. Celles posées au sein de ce manuscrit concernent la configuration dite injectée, dans laquelle le processus est initié par une source externe cohérente (le "seed"). Nous nous concentrons particulièrement dans cette thèse sur les caractéristiques transverses et longitudinales de la lumière, sa cohérence, les propriétés de la phase temporelle et les liens directs entre le seed et l'émission LEL.

La technique de génération dans un gaz noble d'harmoniques d'ordres élevés d'un laser femtoseconde (GHE) se montre à la fois complémentaire et en compétition avec les LELs. En compétition car les impulsions produites ont des qualités similaires à celles obtenues avec un LEL ; complémentaire car le rayonnement GHE peut être utilisé comme seed ou en combinaison avec la lumière LEL, par exemple pour effectuer des expériences mettant en jeu de multiples faisceaux. Bien que la GHE fournisse des impulsions moins puissantes, l'implémentation d'une telle source requiert un effort significativement moins important. Le taux de conversion harmonique, l'accordabilité et la qualité spatiale du faisceau généré, et la manière dont ces paramètres dépendent du laser générateur sont les problématiques traitées au sein de ce manuscrit.

La volonté de la communauté scientifique d'effectuer des expériences novatrices demande des études profondes et l'optimisation des sources de GHE et des LELs. En particulier, sur la source LEL injectée FERMI@Elettra de Trieste, l'induction d'une dérive de fréquence dans le rayonnement a conduite à des résultats marquants. Entre autres, une méthode de génération d'impulsions scindées avec différentes longueurs d'ondes a été analysée et développée. Une telle possibilité ouvre la voie à l'utilisation des LELs injectés en tant que source autonome pour des installations de type pompe-sonde à deux couleurs. Plus généralement, l'étude des phénomènes mis en jeu dans les processus de GHE et du LEL, ainsi que la caractérisation des propriétés de leur lumière, sont des sujets intrinsèquement excitants ayant des connexions directes avec de nombreux aspects fondamentaux de la physique.

Contents

Introduction

For the last two decades, marked by the Nobel Prize obtained in 1999 by Ahmed H. Zewail for his work on femtochemistry [1], the study of ultrafast processes has been in continuous development. The quest for short durations proceeded together with investigations on nanoscale samples. To probe ultrafast phenomena and/or fine structures, the best tool is a coherent and powerful photon beam, in other words, a laser.

For analysing the dynamics of a sample at an ultrafast time scale, pump-probe experiments have demonstrated to be of great interest: time-resolved absorption [2, 3, 4, 5], coherent anti-Stokes Raman scattering [6], probe-induced Raman scattering [7] and femtosecond transition-state spectroscopy [8] are examples of applications of such a setup. Beside this, the generation of multiple synchronized frequencies from femtosecond laser sources is a very important benefit, as in the case of degenerate four-wave mixing [9, 10]. Such asset can be combined to the pump-probe technique for the use in a two-colour pump-probe setup [11].

In order to reach sufficient resolution, needed for instance for coherent diffraction imaging [12], laser light must be ultrafast (picosecond to attosecond pulse duration) and have a short wavelength (down to X-ray). A large photon flux is also required, especially for the study of nonlinear processes, requiring high peak intensities. Tuning the photon beam wavelength and polarization, mastering its spectral and temporal structure, improving its stability and shaping it spatially are also important assets.

However, generating light with all these characteristics is not trivial, and all the pre-cited applications are therefore limited to photon energies of the order of some eV. The main reason stems from the lack of conventional lasers below $\approx 150\ nm$. Free-Electron Lasers (FEL's) [13, 14] and the technique of High-order Harmonic Generation (HHG) [15] in noble gases are the two main present-day solutions for overcoming this limit. Nevertheless, they still do not meet the expectations of the scientific community and many interesting issues concerning their underlying physics remain open. The work that I have carried out in the framework of my PhD has aimed at contributing to the investigations of such problems.

This manuscript hinges on five main chapters:

In Chapter I, I will present the main notions that will be essential all along the study. In particular, the two kind of sources of interest here, namely FEL's (especially the FERMI@Elettra facility) and HHG, will be described. The purpose will not be to deeply explain their mechanisms, rather their main characteristics and the physical processes of interest in the frame of my thesis. It will be forwarded by the definition of some "fundamental" concepts of femtosecond laser pulses.

Chapter II will focus on experiments characterizing the spatial quality of femtosecond light sources. As a first step, it will concern the transverse characterizations carried out on the

FERMI@Elettra source: spatial coherence, intensity spot and wavefront measurements. After this, a section will be dedicated to a series of experiments held a CEA Saclay on the LUCA source. The spatial quality of the latter, of the EUV photons and the optimization of the global HHG process will be studied.

Two next chapters will then be dedicated to the chirp in seeded FEL's. At the input of such a machine, they correspond to two different things: the frequency-vs-time dependence of the seed and the energy-vs-time dependence along the electron bunch. At the output, it corresponds to the frequency-vs-time dependence of the emitted pulse. These different chirps, their respective effects and their interplay will be studied in Chapter III.

As a consequence of these chirps, I will present in Chapter IV the effect of formation of two-colour pulses that we emphasized on FERMI@Elettra. After preliminary description and characterizations, a more comprehensive work will be presented. Thanks to this unique feature, chirped seeded FEL's can be utilized as stand-alone light sources for pump-probe experiments. It evidences the wide possibilities of temporal studies that can be done on seeded FEL's by playing with the different chirps. In particular, I will demonstrate that the temporal shape of the output pulses can be directly retrieved, without any additional setup or algorithm.

Finally, before concluding, Chapter V will continue on the topic of tunability introduced by spectral studies carried out on seeded FEL's. Different setups have been imagined for optimizing this asset on HHG sources. Here I will present a simple solution relying on the tunability of the driving field.

Before starting, I wish to stress that the activity on FERMI@Elettra has been quite intense within the last half of my PhD. It would have been possible to present a lot of results in this thesis, but I preferred to focus on the studies that I led, in order to provide an (hopefully) easy-to-read and personal manuscript.

General background

Contents

I.1 Some notions of (femtosecond) laser physics

I.1.a Ultrashort pulse and bandwidth

Temporally, a continuous wave can be described by a sinusoidal function. In an ultrashort wave (in this thesis, we will deal with durations of the order of the femtosecond, $1\ fs = 10^{-15}\ s$), there will be only a few cycles of this sinusoid. For instance, at a wavelength of $800\ nm$ corresponding to the limit visible/infrared, the duration of an optical cycle is $2.7\ fs$. If the duration

of the light pulse is $27\ fs$, there will be only 10 cycles within this burst. But in fact, intrinsically to this ultrashort duration, the pulse will not have only one single wavelength, but an addition of wavelengths forming the bandwidth. Indeed, let us look at the Fourier decomposition of our wave: $f(t) = \sum a_n \cos(n\omega - \varphi_n)$, where n is an integer, ω is the angular frequency, a_n and ϕ_n are the amplitudes and phase at the frequency components $n\omega$. In Fig. I.1, we considered a wave whose central frequency is an arbitrary value 8ω. In the case shown on the left panel, there is a single frequency and the sum of this single component is thus a continuous wave. In the middle panel, we considered that $f(t)$ is made of fifteen frequencies in phase, ranging from ω to 15ω (for simplicity, in the top graphs only three frequency components are represented): the wave, corresponding to the sum of these different frequency components, is not continuous any more but has a finite duration. We will thus call it a pulse. In the case where we take the same spectral components with same weights but dephased (right panel), $f(t)$ is lengthened. Moreover, if we have an accurate look to the shape of $f(t)$, we see that at the beginning the period of the oscillations is longer than at the end. In other words, the instantaneous frequency is not constant along the pulse: this phenomenon is called the chirp, and is a fundamental point in this thesis. It is due to the fact that the different spectral components are not in phase.
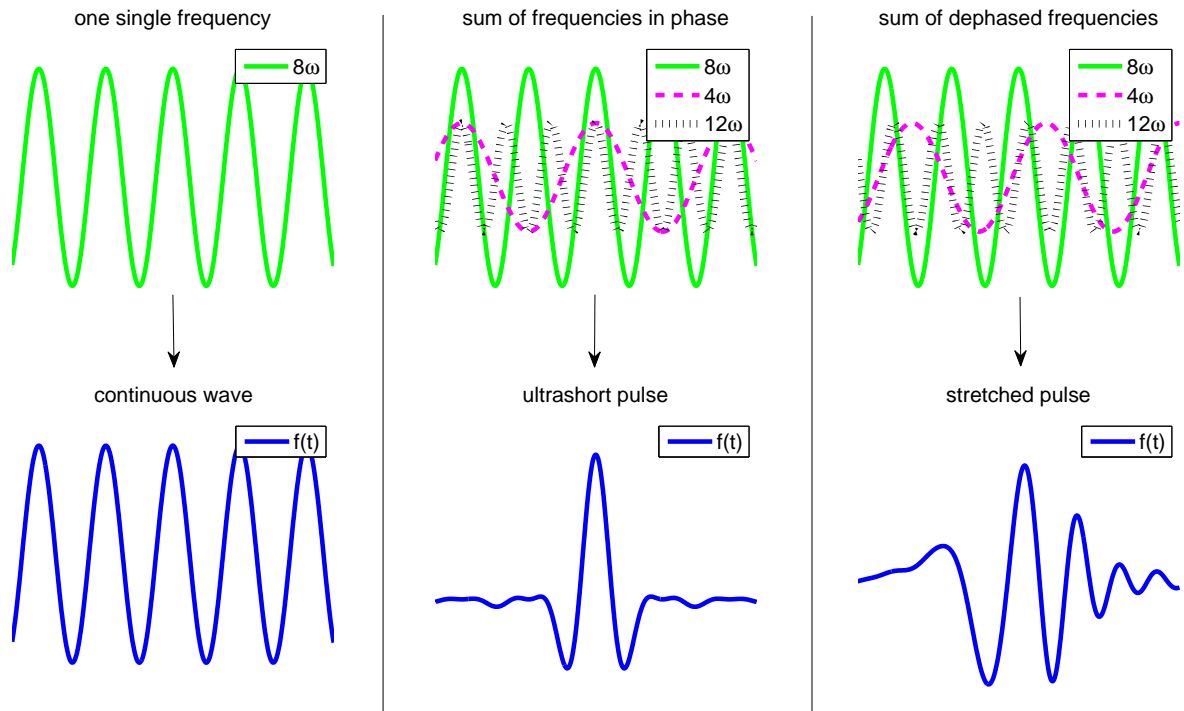

Figure I.1: *Wave f(t) (bottom pictures) resulting from the addition of different spectral components (top pictures). Left panel: one single spectral component; middle panel: sum of 15 spectral components, in phase; right panel: sum of the same 15 spectral components, but dephased.*

I.1.b Electric field

Like any wave, an ultrashort laser pulse can be described by its electric field depending on the spatio-temporal coordinates. As a first approach we will reduce to the temporal variations only. The temporal electric field corresponds to the function $f(t)$ that we considered above. One generally writes it as follows:

$$E(t) = A(t)e^{i[\omega_0 t + \varphi(t)]},$$
(I.1)

where $A(t)$ is the envelope of the pulse and $\varphi(t)$ is called the temporal phase of the pulse. In fact, the entity $\omega_0 t + \varphi(t)$ represents the whole phase of the oscillations of the field. To $E(t)$, which is an imaginary entity, we should actually sum its complex conjugate in order to obtain a real electric field, as $f(t)$. But this is usually not done for facilitating the calculations. The measured value is not the electric field but its intensity, which is given by $I(t) = E(t) \cdot E(t)^* = |A(t)|^2$. The Fourier transform of the electric field in the temporal domain leads to its expression in the spectral domain, that can be written:

$$\tilde{E}(\omega) = \tilde{A}(\omega)e^{i\phi(\omega)}.$$
(I.2)

Similarly, we have the spectral envelope $\tilde{A}(\omega)$ and the spectral phase $\phi(\omega)$. The spectral intensity, called the spectrum, is given by $\tilde{I}(\omega) = \tilde{E}(\omega) \cdot \tilde{E}(\omega)^* = |\tilde{A}(\omega)|^2$. One has to note that generally we will use the wavelength $\lambda = \frac{2\pi c}{\omega}$ (c being the speed of light) instead of the angular frequency ω. Since $\frac{d\omega}{d\lambda} = -\frac{2\pi c}{\lambda^2}$, there will not be a linear transformation between both scales. The consequence is that, for instance, a spectrum that has a Gaussian shape as a function of the frequency is not Gaussian as a function of the wavelength (see Fig. I.2). However, the approximation can be done, especially for sufficiently narrow spectra.
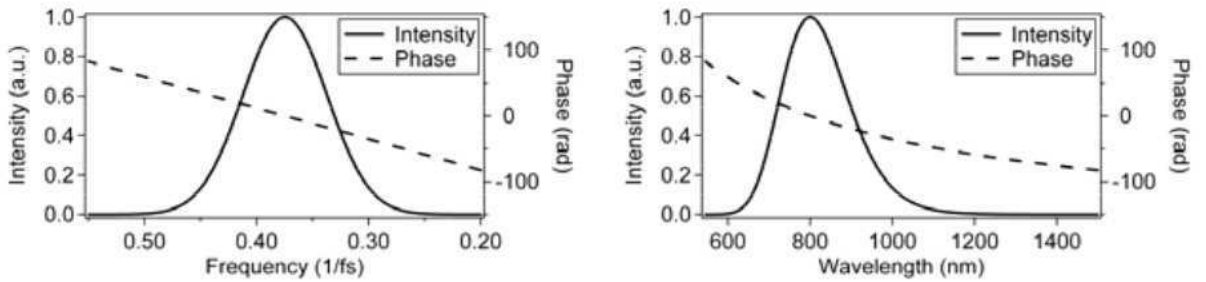
Figure I.2: Spectral intensity (full lines) and phase (dashed lines) as a function of the angular frequency (left) and the wavelength (right). (taken from [16])

It is important to understand the meaning of the phases. The temporal phase is an information of the frequency at a given time. The instantaneous central angular frequency of the pulse at a time t, noted $\omega_{inst}(t)$, is defined as the derivative of the whole temporal phase of the oscillations, i.e.:

$$\omega_{inst}(t) = \omega_0 + \frac{d\varphi(t)}{dt}.$$
(I.3)

Instead, the spectral phase is an information of the time corresponding to each spectral compo-
nent, which leads to the definition of the group delay i.e., the arrival time of a frequency:

$$t_{group}(\omega) = \frac{d\phi(\omega)}{d\omega}. \tag{I.4}$$

I.1.c   Phase effects

The spectral and temporal phases are generally expanded in Taylor series, so that we write
them as:

$$\varphi(t) = \varphi_0 + \varphi_1 t + \frac{1}{2}\varphi_2 t^2 + \frac{1}{6}\varphi_3 t^3 + ..., \tag{I.5}$$

and:

$$\phi(\omega) = \phi_0 + \phi_1(\omega - \omega_0) + \frac{1}{2}\phi_2(\omega - \omega_0)^2 + \frac{1}{6}\phi_3(\omega - \omega_0)^3 + ..., \tag{I.6}$$

ω_0 being the central angular frequency of the pulse.

The 0th order phases φ_0 and ϕ_0 are absolute phase terms that determine the position of
the electric field within the envelope. This is of interest when the pulse contains only few optical
cycles, as shown in Fig. I.3.
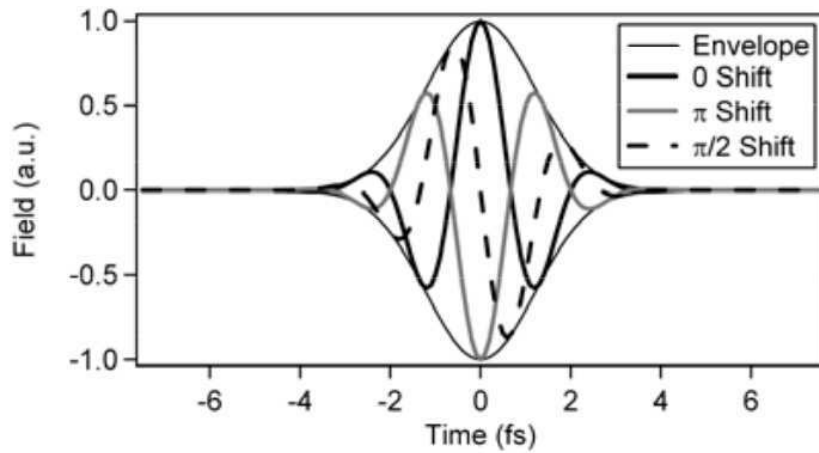
Figure I.3: *Temporal electric field for different values of φ_0. (taken from [16])*

A shift τ in time, giving $E(t - \tau)$, is transposed in the spectrum to an additional linear phase
term $e^{-i(\omega - \omega_0)\tau}$, via the Fourier transform. Similarly, a shift in frequency gives, via an inverse
Fourier transform, a linear phase term in the time domain. Hence, the consequences of the
linear phases φ_1 and ϕ_1 are a shift, respectively in frequency and in time (Fig. I.4).

A quadratic temporal phase φ_2 corresponds to a linear variation of $\omega_{inst}(t)$ i.e., a linear chirp.
It corresponds also to a quadratic spectral phase ϕ_2, but with opposite sign (see Appendix A).
When smaller frequencies i.e., longer wavelengths arrive first, the pulse has a positive chirp or is
said up-chirped. Instead, when larger frequencies i.e., smaller wavelengths arrive first, the pulse
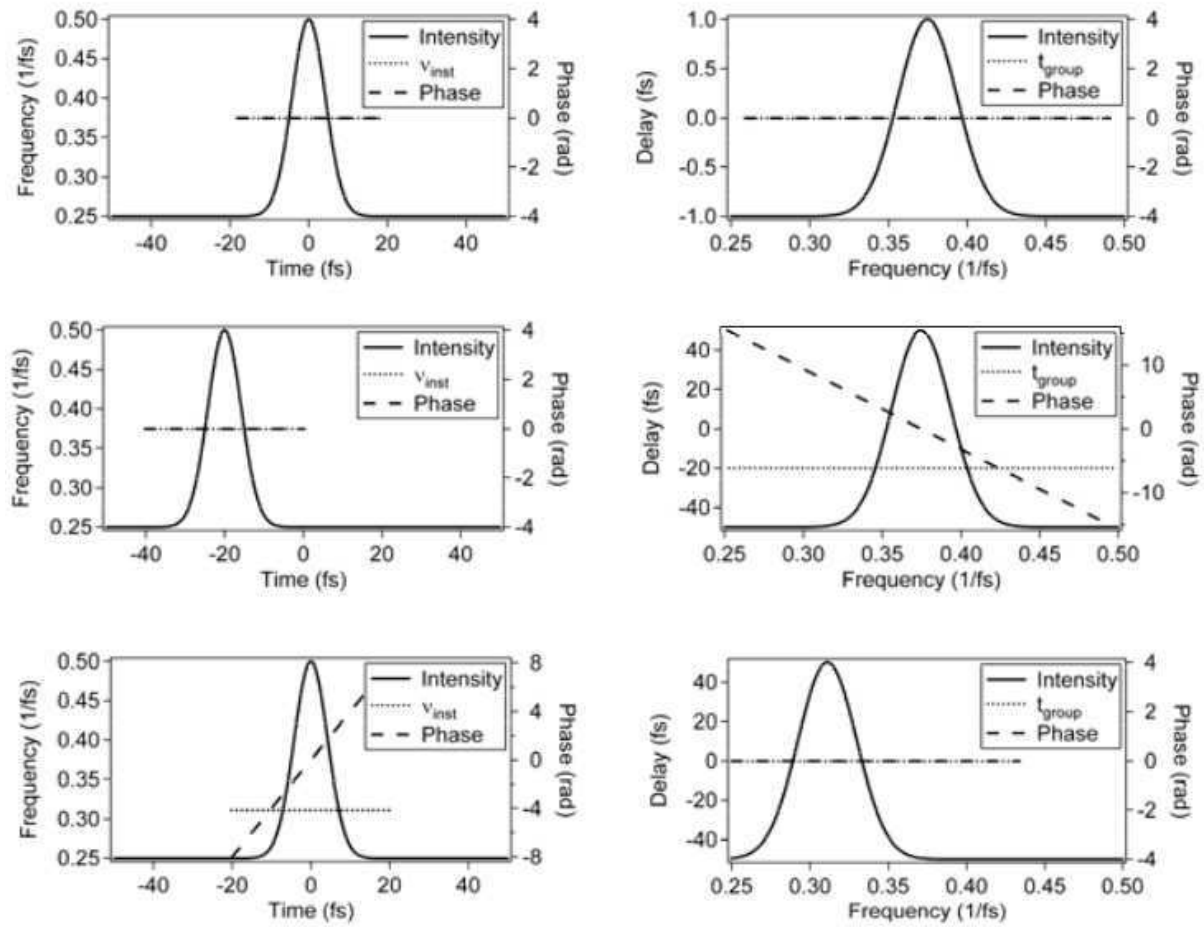
Figure I.4: *Left: temporal intensity (full line), temporal phase (dotted line) and instantaneous frequency $v_{inst} = \frac{\omega_{inst}}{2\pi}$ (dotted line); right: Corresponding spectrum (full line), spectral phase (dotted line) and group delay (dotted line). Top pictures: flat phases; middle pictures: $\varphi_1 = 0$ and $\phi_1 \neq 0$; bottom pictures: $\varphi_1 \neq 0$ and $\phi_1 = 0$. (taken from [16])*

has a negative chirp or is said down-chirped. The situation of an up-chirped pulse is shown in Fig. I.5.

Finally, for higher-order phase terms, the situation is more complicated, as shown in Fig. I.6 with a cubic spectral phase: the temporal profile exhibits distortions and the chirp becomes quadratic. Generally, we try to boil down to a situation where phase terms are limited to the second-order i.e., to a linear chirp. The ϕ_2 value, corresponding to $\frac{d^2\phi(\omega)}{d\omega^2} = \frac{dt_{group}}{d\omega}$, is called the group delay dispersion (GDD), which is an indication of the amount of linear chirp.

I.1.d   Fourier-transform and diffraction limits

We previously underlined a fundamental characteristic of ultrashort pulses: they must have a broadband spectrum. It is not possible to narrow indefinitely the spectrum and the temporal profile together. This property is due to the fact that the spectral and time components are linked by Fourier transform. We will thus define the time-bandwidth product, which can be retrieved
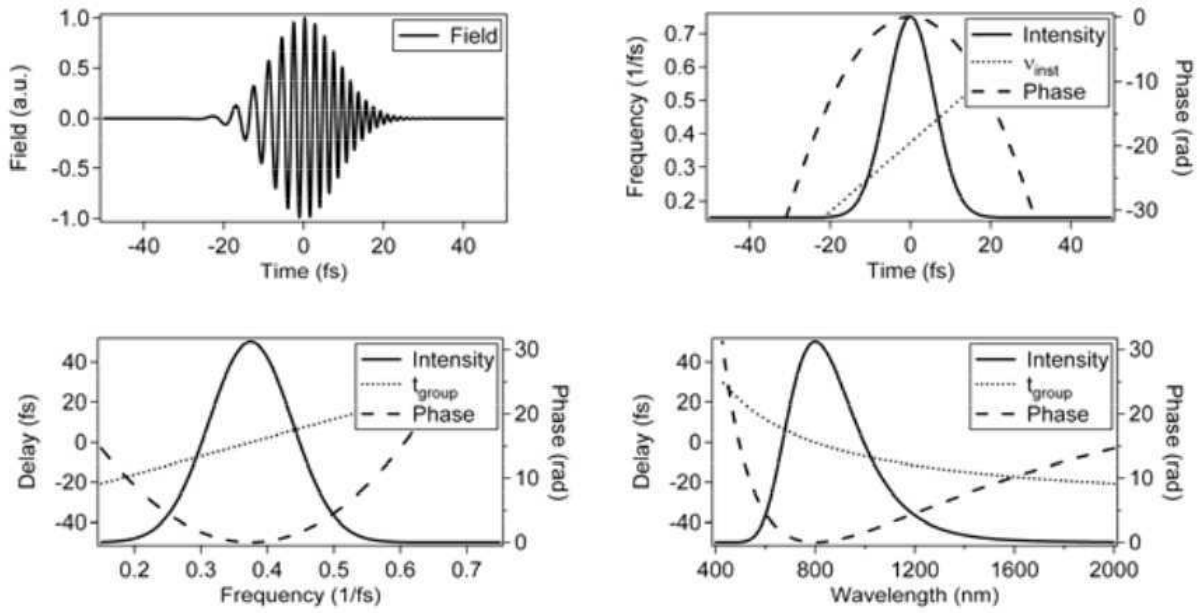
Figure I.5: Top left: temporal electric field. Top right: intensity, temporal phase, and instantaneous frequency vs. time. Bottom left: spectrum, spectral phase and group delay vs. frequency. Bottom right: spectrum, spectral phase and group delay vs. wavelength. (taken from [16])
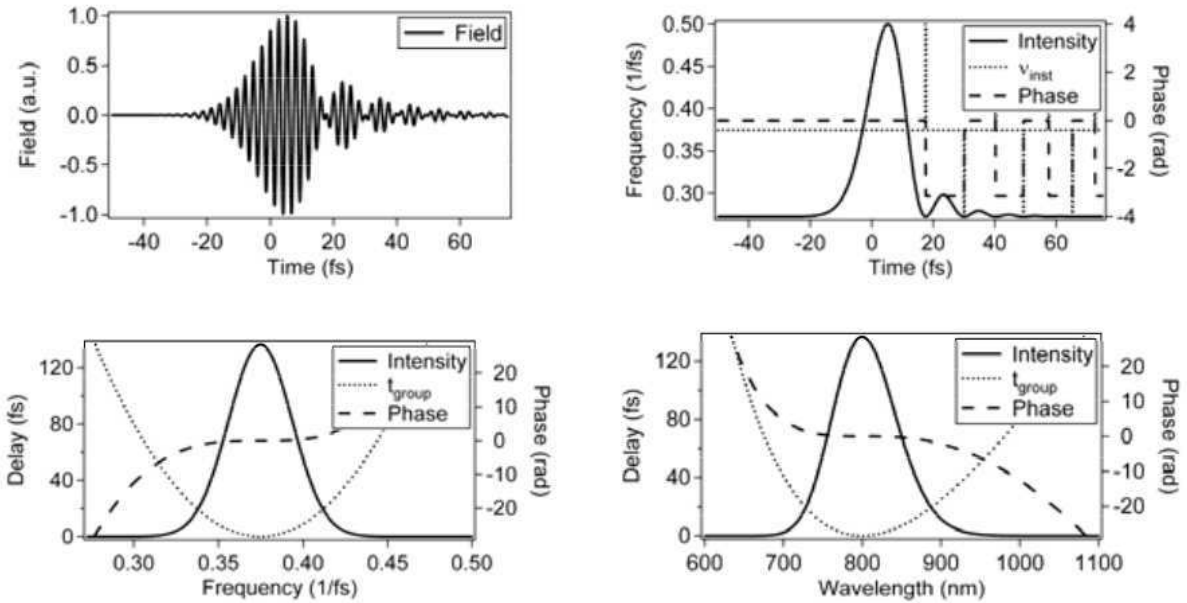
Figure I.6: Top left: temporal electric field. Top right: intensity, temporal phase, and instantaneous frequency vs. time. Bottom left: spec- trum, spectral phase and group delay vs. frequency. Bottom right: spec- trum, spectral phase and group delay vs. wavelength. (taken from [16])

mathematically (see, for instance, [17] for a general demonstration or Appendix A for a particular case), as:

$$\Delta\omega \cdot \Delta t \geqslant lim, \tag{I.7}$$

where $\Delta\omega$ and Δt are the widths of the spectral and temporal distributions of the pulse and lim is called the Fourier-transform limit whose value depends on how $\Delta\omega$ and Δt are defined. In a

general case, if $\Delta\omega$ and Δt are the standard deviations of the spectral and temporal electric field envelopes, $lim = 1$ and thus the minimum duration of the electric field envelope of the pulse is directly the inverse of the width of the electric field in the frequency domain. However, usually we deal with Gaussian pulses so that it is common to work with the full-width at half maximum (FWHM) values of the intensity distributions, that we will note H_t and H_ω. If we consider the frequency $\nu = \frac{\omega}{2\pi}$, the time-bandwidth product becomes, for Gaussian temporal and spectral profiles:

$$H_\nu \cdot H_t \geqslant 0.441, \tag{I.8}$$

which is the commonly used form.

Up to now we concentrated ourselves only on the basic time properties of laser pulses. However, similar properties are present in the spatial domain: like for the fact that the pulse duration is limited for a given bandwidth, the minimum transverse spot size of the beam is limited also. Let us write Heisenberg's uncertainty principle as :

$$\Delta\vec{x} \cdot \Delta\vec{p} \geqslant \frac{\hbar}{2}, \tag{I.9}$$

where $\Delta\vec{x}$ is the uncertainty on the position of a particle, $\Delta\vec{p}$ is the uncertainty on its momentum and $\hbar$ refers to the Planck constant. For the photons that compose our laser light, the momentum is $\hbar\vec{k}$, $\vec{k}$ being the wave vector with $|\vec{k}| = \frac{2\pi}{\lambda}$. For small angles θ, we can write $\Delta\vec{k} \simeq \vec{k}\Delta\theta$ so that $|\Delta\vec{p}| \simeq \hbar k\Delta\theta$. The uncertainty principle therefore reads:

$$\Delta x \Delta\theta \geqslant \frac{\lambda}{4\pi}. \tag{I.10}$$

Now, if we identify our laser beam source diameter as $d = 2\Delta x$ and the divergence half angle of the light as the uncertainty on the emission angle $\Delta\theta$, we obtain the size-divergence product bounded by the so-called diffraction limit:

$$d \cdot \theta \geqslant \frac{\lambda}{2\pi}. \tag{I.11}$$

This relation is the spatial analogy of the time-bandwidth product. It tells us that it is not possible to focus the laser beam without involving an increase of the divergence and, at a given spot size and wavelength, the transverse quality of a laser beam will be characterized by its divergence (lower divergence meaning better spatial quality).

I.1.e   Coherence

The temporal and spatial quality of the light is often characterized by its coherence. Figure I.7 represents the propagation of the wavefront of a beam, in the transverse x dimension. The wavefronts are defined as the surfaces over which the temporal electric field of the wave reaches

its maximum; hence, successive wavefronts are theoretically separated by the wavelength λ. Over the width Δx, the wavefront keeps the same characteristics along a distance of propagation delimited by the dashed lines. We say that the wave is spatially (or transversally) coherent over Δx (or for two positions taken within Δx). Similarly, along Δt the wavefront is unchanged within the transverse boundaries of the dotted lines. Hence we say that the wave is temporally (or longitudinally) coherent during Δt.
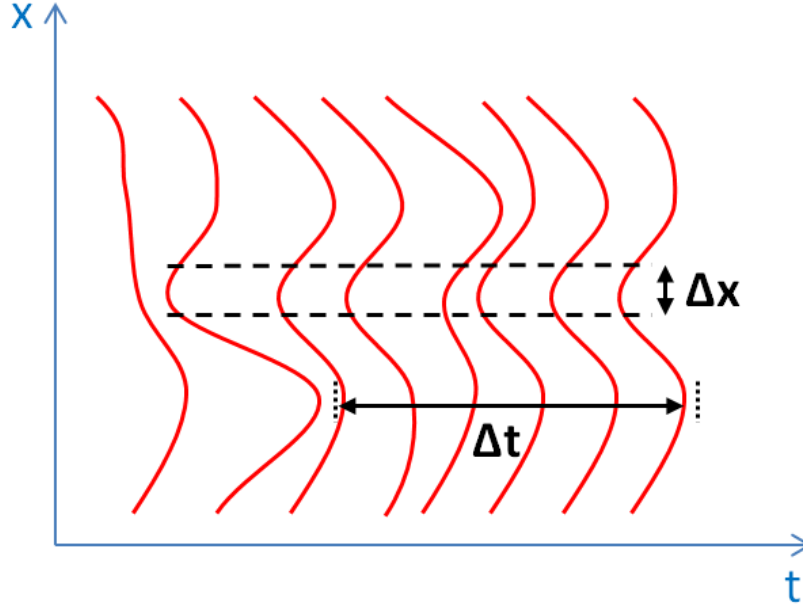
Figure I.7: *Wavefront propagations with areas of spatial coherence (Δx) and temporal coherence (Δt).*

If an ultrashort pulse is chirped, the distance between each wavefront will vary along the pulse, since the instantaneous frequency is not constant. A pulse that is far from the Fourier-transform limit will thus present a lack of temporal coherence. Similarly, the spatial qualities of the beam and its propensity to reach the diffraction limit are linked to the transverse quality of its wavefront.

The overall coherence between two points in the space, located at the transverse positions x_1 and x_2 measured at times separated by τ, is characterized by the mutual coherence function representing the correlation of two points in space and time:

$$\Gamma(x_1, x_2, \tau) = <E(x_1, t)E^*(x_2, t + \tau)> . \tag{I.12}$$

The "$<>$" means the averaging over a given time, for instance the duration of the pulse whose coherence is characterized. The Fourier transform of this function gives the so-called cross-spectral density:

$$W(x_1, x_2, \omega) = \int_{-\infty}^{+\infty} \Gamma(x_1, x_2, \tau)e^{-i\omega\tau} \, d\tau, \tag{I.13}$$

which characterizes the coherence of the light at a given frequency ω. We note that, for $x_1 =$

x_2, Γ represents the autocorrelation of first order of the field (that can be used, for instance, for measuring the duration of a pulse with known shape) and W is the power spectrum. The normalization of these two functions leads, respectively, to the complex degree of coherence:

$$\gamma(x_1, x_2, \tau) = \frac{\Gamma(x_1, x_2, \tau)}{\sqrt{\Gamma(x_1, x_1, \tau)\Gamma(x_2, x_2, \tau)}},$$
(I.14)

and the complex coherence factor:

$$\mu(x_1, x_2, \omega) = \frac{W(x_1, x_2, \omega)}{\sqrt{W(x_1, x_1, \omega)W(x_2, x_2, \omega)}}.$$
(I.15)

γ represents (as Γ) the overall coherence and when $|\gamma| = 1$, there is full coherence between the points x_1 and x_2 and no coherence when $|\gamma| = 0$; only partial coherence for intermediate values. When $\tau = 0$ (i.e., when the two points are taken at the same time), the complex degree of coherence is equal to the complex coherence factor and the modulus of the latter characterizes the spatial coherence.

For a further description of the coherence, see [18].

Now, the very basic notions that will be useful in this thesis have been presented. In the next two sections, I will present the kind of facilities on which I relied for carrying out my work, namely Free-Electron Lasers (FEL's) and High-order Harmonic Generation (HHG) sources providing both femtosecond pulses in the ultraviolet to X-ray spectral range i.e., from less than 400 nm down to wavelengths of few nanometers.

I.2 Single-pass Free-Electron Lasers

In its most straightforward configuration, an FEL relies on the following scheme: a relativistic electron beam wiggles through the periodic and static magnetic field provided by a magnetic device called *undulator* (Fig. I.8). Due to this motion, the electrons lose kinetic energy. The latter is transferred to emitted photons, whose wavelength depends on electrons and undulator characteristics. Since this wavelength corresponds also to the resonant condition of an energy transfer between electrons and photons, the emission becomes stimulated and is thus amplified along the undulator. If no external wave originates the photons emission, this configuration is thus called the self-amplification of spontaneous emission, or SASE. When the bunch enters the undulator, each electron emits independently, so that the overall emission is incoherent. The energy transfer between the photons and the wiggling electrons leads to a spatial density modulation of the latter, called *bunching*. The micro-bunches thus emit in phase, providing a coherent radiation.

However, due to the initial random distribution of the electrons, the first photons correspond
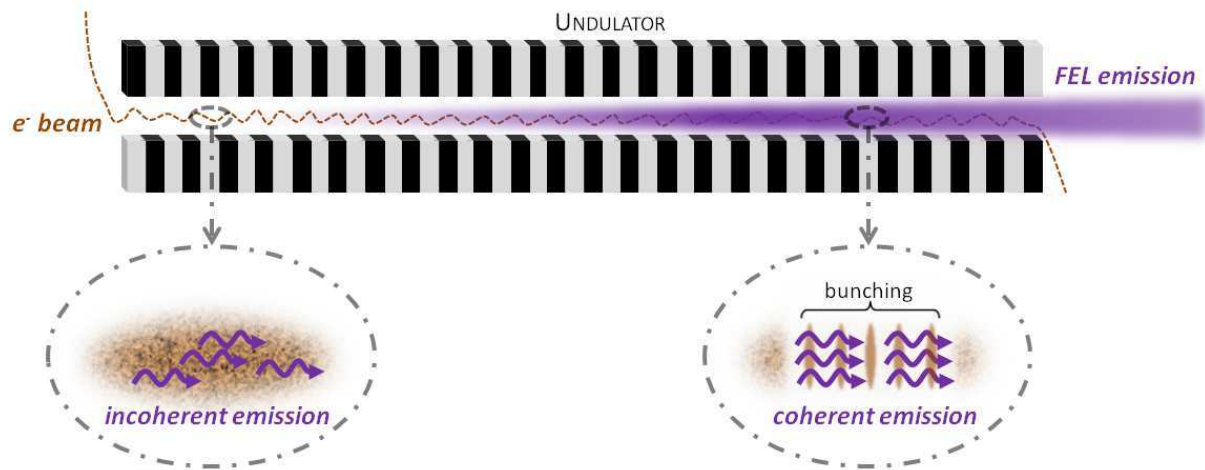
Figure I.8: Basic layout of a SASE FEL.

to a noisy signal, whose amplification thus results in spikes in time and spectrum. Figure I.9 illustrates this situation in the spectral domain: when they enter the undulator, the electrons start emitting around the wavelength λ of emission of the undulator. However, this signal is very noisy and the SASE process corresponds to the amplification of this noise. Since, initially, electrons emit photons at random positions along the bunch, such a spiky structure is also found in the time domain. From one shot to the other, this random start intrinsically differs so that the properties of the final radiation will not be identical, and strong fluctuations of the spectral and temporal shapes are present. A correlated issue is the presence of shot-to-shot variations of intensity if the signal is monochromatized.
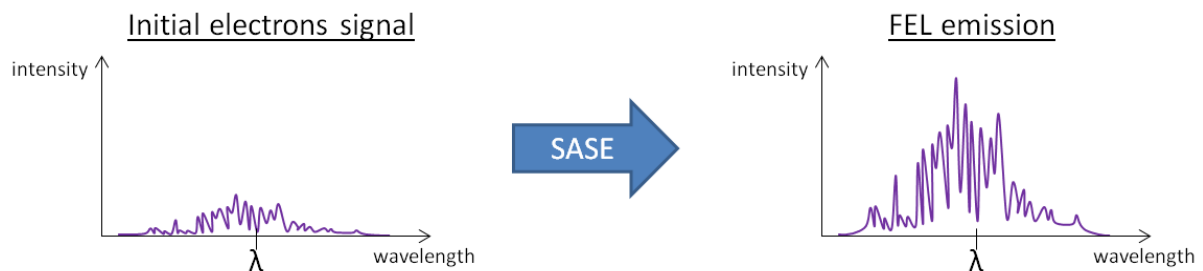
Figure I.9: Typical SASE spectrum.

To overcome these drawbacks, it has been proposed [19] to initiate the FEL process by an external coherent source (called the *seed*), instead of the shot-noise emission of the electrons. Consequently, the temporal (longitudinal) phase relation is preserved along the electron beam, the temporal and spectral shapes being dictated by the seed. Moreover, the bunching of the electrons presents significant components at the harmonics of the seed's fundamental wavelength. This is why a second undulator can be set so as to put the electrons in resonance at a harmonic wavelength of the seed, and thus amplify this harmonic. This is the principle of the coherent-harmonic generation scheme (CHG), whose typical layout is shown in Fig. I.10. In a

first undulator, called *modulator*, the seed and the electrons overlap and electron energy modulation is created. In a second undulator, called *radiator*, an harmonic wavelength of the seed is amplified. Between the modulator and the radiator, a strong magnetic chicane called *dispersive section*, where electrons do experience an energy-dependent path (like light in a pair of gratings), allows transferring this energy modulation into spatial bunching at the desired harmonic (as we will see below, the harmonic number is however limited). Practically, the peak power of the seed should be higher than electrons shot noise at modulator's entrance so as to drive an efficient energy modulation.
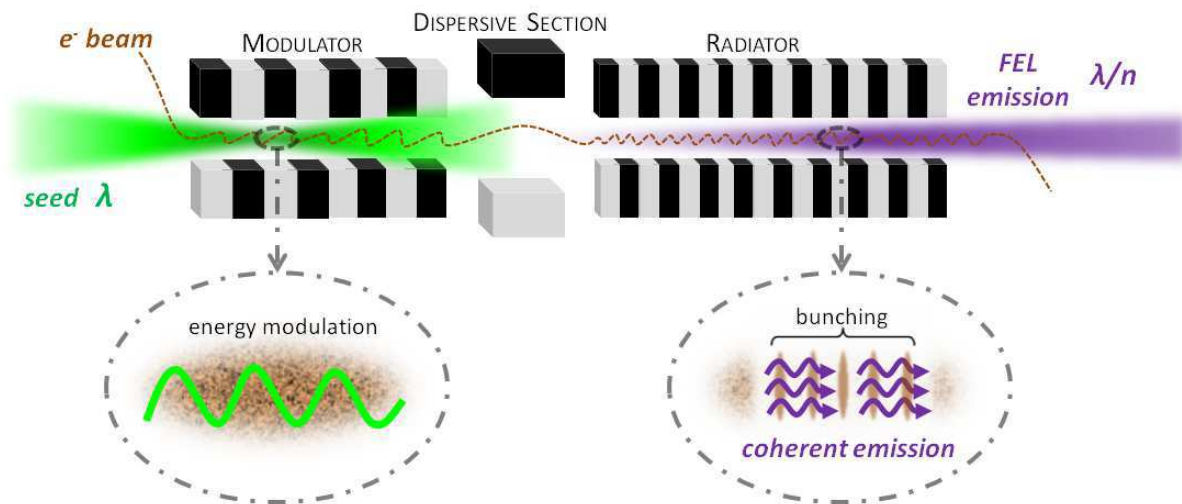
Figure I.10: Basic layout of a CHG FEL.

As it can be seen in Fig. I.11, in ideal conditions (peculiar conditions will be studied in Chapter IV) the spectrum of the CHG emission is a copy of the one of the seed. This is also true in the temporal domain. Normally, a Gaussian pulse is injected so that the FEL emission is Gaussian. In this configuration, seeded FEL's are thus very attractive facilities for generating extreme-ultraviolet radiation (noted EUV, defined here as wavelengths between 10 and 100 *nm*) with nice spectro-temporal properties.
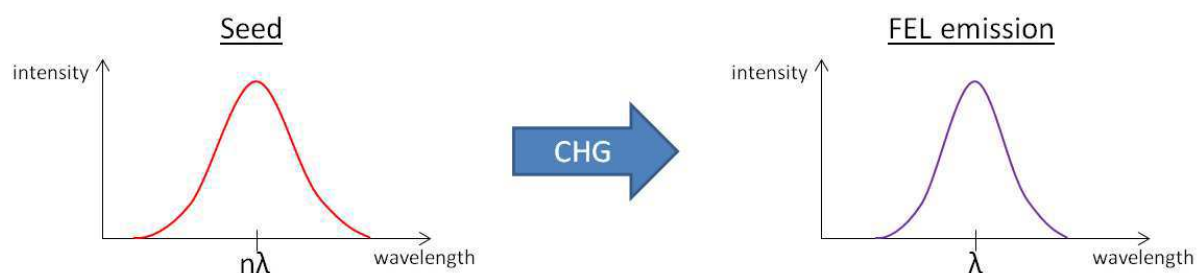
Figure I.11: Typical CHG spectrum.

After this short overview, we will know have a more detailed look to the FEL process.

I.2.a Electron motion into an undulator

The first step to understand how is emitted the FEL radiation is to study the motion of the electrons into an undulator. Here we will only consider the case of a planar undulator i.e., with magnet blocks in phase. In this configuration, the magnetic field $\vec{B}$ provided by the undulator is characterized by only a vertical component:

$$|\vec{B}| = B_y = -B_0 \sin(k_U z). \tag{I.16}$$

The magnetic field is static (no time dependence), periodic (length of one magnetic period L_U, $k_U = \frac{2\pi}{L_U}$) and of magnitude B_0 expressed in Tesla (T). The Lorentz force undergone by the electrons travelling at a velocity $\vec{v}$ into the undulator is:

$$m\gamma \frac{d\vec{v}}{dt} = -e\vec{v} \times \vec{B}, \tag{I.17}$$

where e and m are respectively the elementary charge and the mass of the electrons; $\gamma = \frac{1}{\sqrt{1-\beta^2}}$ with $\beta = \frac{v}{c}$ is the relativistic Lorentz factor, c being the speed of light. Here we do not take into accounts terms such as the magnetic field of the earth (small with respect to undulator's one) and the radiated electric field of the electrons which, at the beginning of the undulator, has a negligible effect on electrons' motion. We wish to calculate the components of the velocity along each coordinate. The expression of the Lorentz force leads to $v_y(t) = 0$ if $v_y(0) = 0$ (i.e., if the electrons are injected into the undulator along the forward direction). For the horizontal component, we have:

$$\frac{dv_x(t)}{dt} = \frac{e}{m\gamma} B_y v_z(t) \tag{I.18}$$

As a first step, we assume that the longitudinal component of the velocity is much larger than the transverse i.e., $v_x \ll v_z$, which is reasonable (the electrons go ahead faster than they wiggle). Therefore, $v_z \simeq v = \beta c = constant$. We can thus integrate easily the previous equation (replacing z by βct), which gives :

$$v_x(t) = \frac{Kc}{\gamma} \cos(k_U \beta ct), \tag{I.19}$$

where K is the so-called *undulator parameter* defined by:

$$K = \frac{eB_0}{mck_U} \approx 0.934 \cdot B_0[T] \cdot L_U[cm]. \tag{I.20}$$

We can rewrite the expression of the Lorentz factor as $\frac{1}{\gamma^2} = 1 - \left(\frac{v}{c}\right)^2 = 1 - \frac{1}{c^2}(v_x^2 + v_z^2)$,

which leads to a more accurate expression for the longitudinal velocity:

$$
\begin{aligned}
v_z(t) &= \sqrt{c^2\left(1-\tfrac{1}{\gamma^2}\right)+v_x(t)^2} \\
&= \sqrt{c^2\left(1-\tfrac{1}{\gamma^2}\right)+\tfrac{K^2 c^2}{\gamma^2}\cos^2(k_U\beta ct)} \\
&= c\sqrt{1-\tfrac{1}{\gamma^2}\left(1+K^2\cos^2(k_U\beta ct)\right)}.
\end{aligned}
\tag{I.21}
$$

According to this, for a relativistic electron beam, we must have $\frac{1}{\gamma^2}\left(1+K^2\cos^2(k_U\beta ct)\right)\ll 1$ if we want v_z to be close to c. In this case, we can develop Eq. I.21 as a Taylor series at the first order, which gives:

$$
v_z(t)\simeq c\left[1-\frac{1}{2\gamma^2}\left(1+K^2\cos^2(k_U\beta ct)\right)\right].
\tag{I.22}
$$

Over one undulator period, the average longitudinal speed is thus:

$$
\bar{v}_z = c\left[1-\frac{1}{2\gamma^2}\left(1+\frac{K^2}{2}\right)\right].
\tag{I.23}
$$

As it can be seen, the electrons motion is quite easy to describe into the undulators, and one will retrieve the coordinates $x(t)$ and $z(t)$ by simple integration of $v_x(t)$ and $v_z(t)$. Similar simple calculations can be done for elliptical or helical undulators (i.e., where the magnet blocks are dephased so that the horizontal component of the magnetic field is not null any more and the motion of the electrons is not confined in a plane).

I.2.b Energy exchange

Now we inject into the undulator an external wave polarized horizontally:

$$
|\vec{E}(z,t)| = E_x(z,t) = E_0 cos(kz-\omega t)
\tag{I.24}
$$

This wave represents the seed in the CHG configuration. For simplicity, we consider a continuous wave and do not take into account the absolute phase term. Its wavelength will be noted λ and $k=\frac{2\pi}{\lambda}=\frac{\omega}{c}$. The infinitesimal energy exchange between the wave and an electron of velocity $\vec{v}$ during a time dt will be:

$$
d(\gamma mc^2) = \vec{v}\cdot\vec{F}\cdot dt,
\tag{I.25}
$$

where $\vec{F}$ is the Coulomb force. From this equation, we see that other polarization components of the seed do not exchange any energy with the electrons. We thus obtain, using Eqs. I.25,

I.24 and I.19:

$$
\begin{aligned}
\frac{d\gamma}{dt} &= -\frac{e}{mc^2}v_x(t)E(t) \\
&= -\frac{eK}{m\gamma c}\cos(k_U z)E_0\cos(kz-\omega t) \\
&= -\frac{eKE_0}{2m\gamma c}[\cos(kz+k_U z-\omega t)+\cos(kz-k_U z-\omega t)] \\
&= -\frac{eKE_0}{2m\gamma c}[\cos(\theta)+\cos(\theta-2k_U z)],
\end{aligned}
\tag{I.26}
$$

with $\theta = (k+k_U)z-\omega t \simeq (k+k_U)\bar{v}_z t-\omega t$. The energy conservation tells us that the light wave gains energy if $\frac{d\gamma}{dt} < 0$. Ideally, a continuous energy transfer should be maintained. Concerning the first cosine term in the last term of Eq. I.26, such a condition is fulfilled when:

$$
\begin{aligned}
\frac{d\theta}{dt} &= 0 \\
\Rightarrow \quad (k+k_U)\bar{v}_z - kc &= 0 \\
\Rightarrow \quad k-k_U &= \frac{k_U 2\gamma^2}{1+\frac{K^2}{2}}.
\end{aligned}
\tag{I.27}
$$

Since the undulator period is much larger than the radiation wavelength i.e., $\frac{1}{\lambda} \ll \frac{1}{L_U}$, we get:

$$
\lambda = \frac{L_U}{2\gamma^2}\left(1+\frac{K^2}{2}\right).
\tag{I.28}
$$

This is the resonance equation for a sustained energy transfer allowing amplification of the light of wavelength λ. Remarkably, this wavelength corresponds to the wavelength of spontaneous emission of the electrons in the undulator in the z direction (this result can be easily derived, see for instance [20]). Concerning the second cosine term in Eq. I.26, we remark that if Eq. I.28 is fulfilled, this term will do two oscillations per undulator period, and thus cancels out in the energy transfer.

Numerous codes [22, 23, 24, 25] simulate the behaviour of the FEL process starting from the coupled equations of motion and energy exchange of electrons along the undulators. A numerical result of the evolution of electron-beam distribution along an undulator, obtained with [23], is shown in Fig. I.12. The electrons energy is characterized by its Lorentz γ factor and shown as a function of its position characterized by its phase θ, within one "slice" of length λ (equivalent to 2π) of the electron bunch. Such a representation of electrons' dynamics refers to the phase space of the electrons. After entering the undulator (Fig. I.12a), there will be a modulation of energy of the electrons (Fig. I.12b): this is the direct effect of Eq. I.26. The new γ values of the electrons lead to new velocities (see Eq. I.23) and thus new phases θ: the electrons that have gained energy go faster and the electrons that have lost energy are slowered. The process goes on so that the electrons "meet" at $\theta = 0$: the energy modulation is transformed into bunching (Fig. I.12c). The electron beam is thus formed of micro-structures spaced by a wavelength λ (in Fig. I.12 only one slice of length λ is shown, but the density modulation is
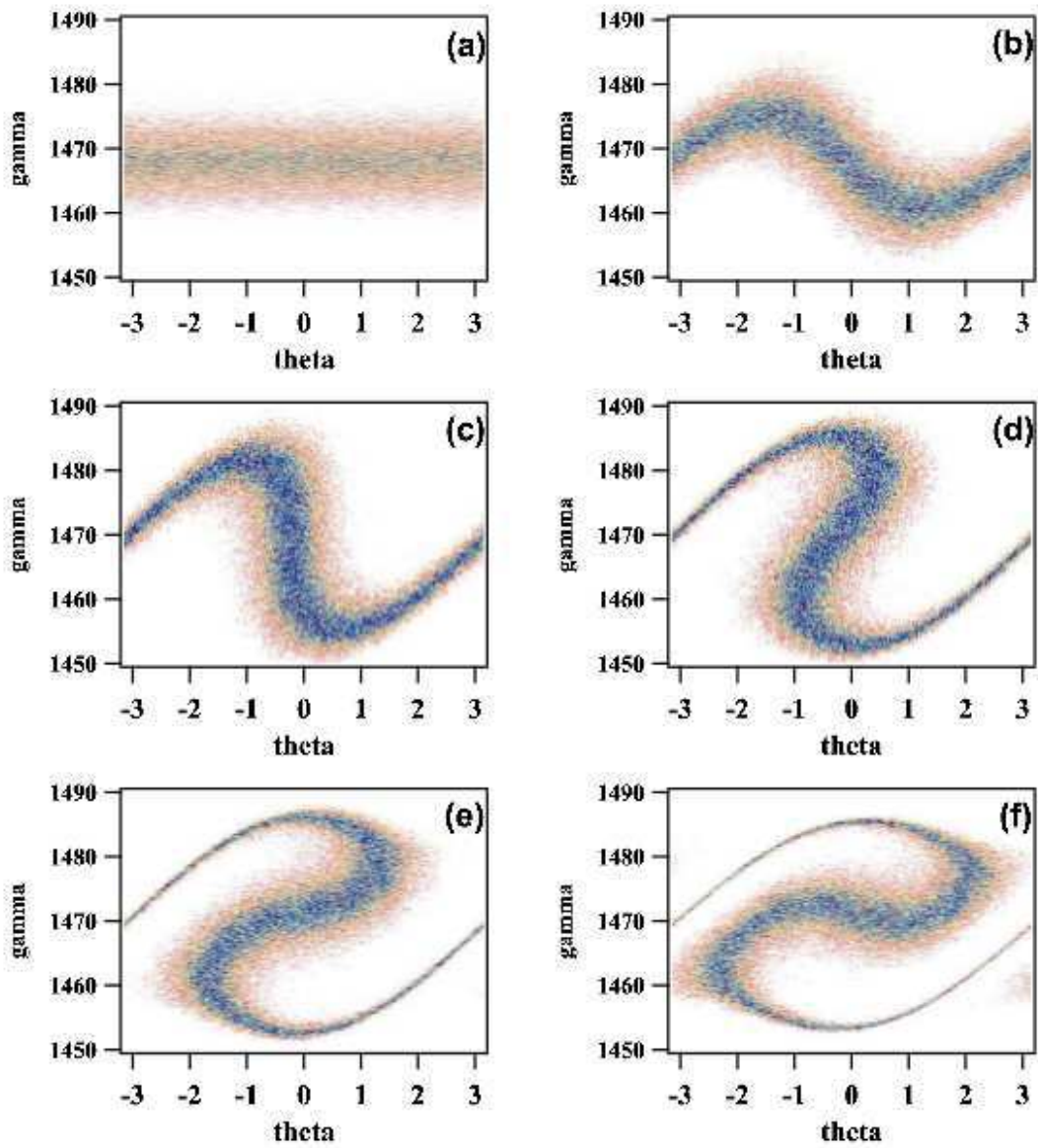
Figure I.12: Evolution of the electron-beam distribution in the phase space γ as a function of θ, along the amplification process. Initial distribution (a); energy modulation (b); spatial modulation (bunching (c); slight overbunching (d); overbunching (e)(f). (taken from [21])

repeated all along the bunch) that emit in phase. Along the undulator, the electrons will provide energy to the wave until the moment when they will have lost so much energy that they will come out the resonance condition (see Eq. I.28). At this point, the amplification stops and the saturation is reached. The energy exchange is then reversed: $\frac{d\gamma}{dt}$ changes sign so that the wave transfers energy to the electrons, which start to get overbunched (Fig. I.12d). Electrons will then continue to rotate into the phase space until they go into a strong overbunching (Fig. I.12e-f). The latter state is not a stationary one and the particles motion is pursued, so that the energy exchange becomes again reversed after a while. However, ideally the undulator ends at the saturation point. In the CHG configuration, the passage from energy modulation to spatial

separation (i.e., from situation reported in Fig. I.12b to Fig. I.12c) is enhanced by the effect of the dispersive section, which is discussed hereafter.

I.2.c Harmonic generation

The modulation process described above occurs in fact not only at the fundamental wavelength λ, but also at its harmonics, as shown in [26]. This can be easily understood. Indeed, the resonance condition corresponds to the fact that, all along the undulator, the electrons and the wave remain in phase so that, after each undulator period, the wave must be shifted by a length equal to the wavelength λ with respect to the electron bunch: this effect is called the slippage of the electromagnetic wave with respect to the electron bunch. However, slippages of $n\lambda$ are also possible values leading to a resonance condition:

$$\lambda_n = \frac{L_U}{2n\gamma^2}\left(1+\frac{K^2}{2}\right). \tag{I.29}$$

We now study the evolution of the electrons position in the CHG configuration (see Fig. I.10), following the reasoning described in [27]. At the end of the modulator ($z = z_M$), the phase of an electron is described by:

$$\theta_M = (k + k_M)z_M - \omega t_M, \tag{I.30}$$

where k_M has the same meaning as k_U, but specific to the modulator, and t_M is the arrival time at the end of the modulator. After the dispersive section i.e., at the entrance of the radiator ($z = z_R$), the phase of the same electron is given by:

$$\theta_R = (k_n + k_R)z_R - \omega_n t_R, \tag{I.31}$$

where k_R has the same meaning as k_U, but specific to the radiator, t_R is the arrival time at the entrance of the radiator and $k_n = nk$. The energy modulation in the modulator led to an overall variaton of $\Delta\gamma$ for the considered electron. The dispersive section transforms this energy separation into time separation:

$$\Delta t = t_R - t_M = \frac{dt}{d\gamma}\Delta\gamma. \tag{I.32}$$

From the previous relations, we can rewrite the phase of the electrons at the entrance of the radiator:

$$\theta_R = n\left(\theta_M + \frac{d\theta}{d\gamma}\Delta\gamma + \theta_0\right), \tag{I.33}$$

where θ_0 is an absolute phase term that it is not useful to develop. The term $\frac{d\theta}{d\gamma}$ represents the strength of the dispersive section. It can be written as:

$$\frac{d\theta}{d\gamma} = \frac{kR_{56}}{\gamma_0}, \tag{I.34}$$

with γ_0 corresponding to the mean energy of the electron beam. The parameter R_{56} (usually given in μm) is the one that we will use for characterizing the strength of the dispersive section.

Knowing the initial energy distribution of the electron beam, it is thus possible to retrieve the phase distribution at the entrance of the radiator. A Fourier analysis of this phase distribution, considering an initial Gaussian distribution of the energy with standard deviation σ_γ at the entrance of the modulator, leads to the following entity [27]:

$$b_n(\theta, \gamma, n) = |\langle e^{-in\theta} \rangle| = 2 \left| J_n \left(n\Delta\gamma \frac{d\theta}{d\gamma} \right) \right| \cdot e^{-\frac{1}{2} \left(n\sigma_\gamma \frac{d\theta}{d\gamma} \right)^2}. \tag{I.35}$$

This is called the bunching function and characterizes the quality of the bunching of an electron according to its position along the bunch. One can thus expect the longitudinal profile of the FEL emission to have a similar shape as the bunching function. The dependence on the J_n Bessel functions tells us that the bunching can theoretically be maximized for a given harmonic number n with an appropriate strength of the dispersive section R_{56} (see Eq. I.34). The exponential dependence tells us that the harmonic number is limited for an efficient CHG FEL emission: indeed, according to Eq. I.35, the higher the harmonic number, the lower the bunching quality. This can also be seen from a Fourier decomposition of the bunching function. Going to higher orders, amplitudes of Fourier components decrease so that very high harmonics cannot be efficiently generated in a CHG configuration. Qualitatively, the harmonic limitation in standard CHG configuration and the bunching maximization via optimization of R_{56} are true; quantitatively, what we get from Eq. I.35 is valid for an initial Gaussian energy distribution of the energy and under the assumption that, in the modulator, there is only energy modulation but no bunching, the latter occurring only during its passage through the dispersive section. In the real world, the bunching formation is not as well separated as this, and can start being formed prior to the dispersive section, or still not well done when the bunch enters the radiator.

I.2.d FERMI@Elettra

The FEL facility on which the experiments reported in this manuscript have been carried out is the FERMI@Elettra source [124]. The configuration that we used relies on the CHG principle (see Fig. I.10). A sketch of the machine is represented in Fig. I.13. A linear accelerator (linac) accelerates the electron beam up to an energy of $1-1.5\ GeV$ (see [111] for more details about the linac). The seed, of central wavelength $\approx 261\ nm$ and Gaussian spectrum with an energy of some tens of μJ per pulse in standard conditions, is produced by third harmonic generation (THG) of a classical chirped-pulse amplified Ti:Sapphire femtosecond laser source. More accurate descriptions of the seed and electron beam properties will be done in Chapter III. The seed pulse and the electron bunch overlap in time and space in the modulator (32 periods $L_M = 10\ cm$) tuned at the central wavelength λ of the seed. The electron bunch then passes
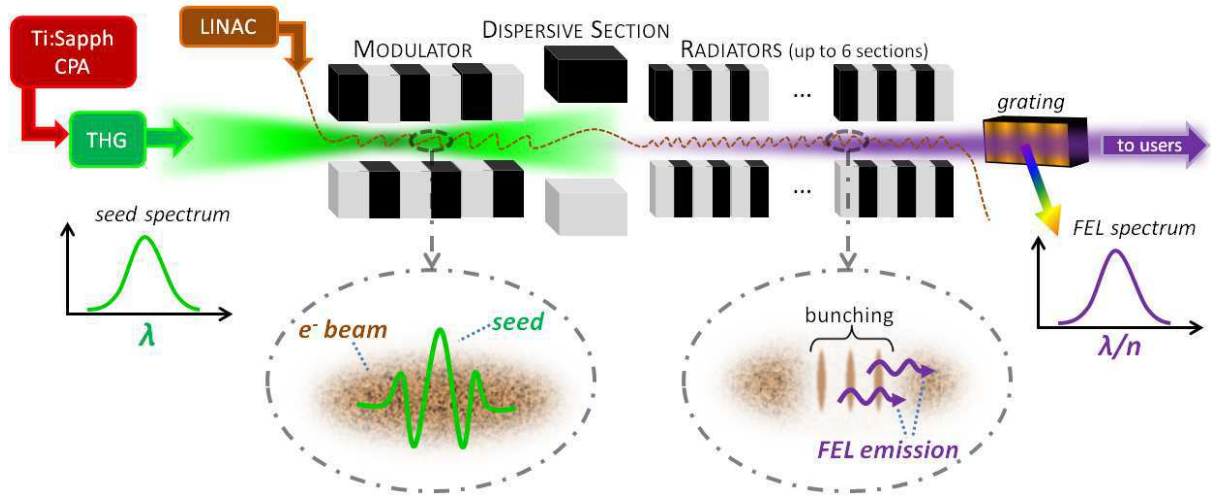
Figure I.13: *Basic layout of FERMI@Elettra.*

through a dispersive section before entering the radiator area. The radiator is divided into six successive sections (each of them being made of 44 periods $L_R = 5.5\ cm$), between which the transverse properties of the electron beam are adjusted (no description of the transverse electron beam dynamics is done here; the reader can refer, for instance, to [28]). The radiators are tuned at a harmonic n, typically of the order of 10, so that EUV wavelengths are generated. The phase of the magnet blocks of the radiators can be changed so as to modify the polarization of the output light (from linear to circular). After the radiators, the electrons are dumped and not used again, so that FERMI@Elettra is a single-pass FEL. The seed pulse is shorter than the bunch (respective full-width at half maximum durations are $\approx 200\ fs$ vs. $\approx 2\ ps$). The amplified emission is thus shorter than the bunch. Therefore, on areas where the seed does not overlap with the bunch, there is no amplification and only spontaneous emission is generated, which remains at the level of noise and is negligible. The femtosecond duration of the seed ensures a femtosecond duration of the FEL emission. The latter is analysed, after the undulator area, by an on-line spectrometer relying on a grating placed at grazing incidence. The zero-th order of diffraction (that we will call also the direct beam) is almost not deviated and is directly sent to the experimental beamlines, while the first order of diffraction is used for measuring the spectrum on a CCD [29, 30]. Several other optics or diagnostics are present and can be inserted, such as CCD's or photodiodes, on which we usually measure energies per pulse of some tens of μJ for the FEL emission. The seed signal can eventually be filtered, but its intensity (power per unit surface) is quite low at the end of the chain of radiators since its focus is located far upstream (in the modulator) and the FEL beam, due to its lower wavelength, diverges less than the seed. Currently, the machine works at a repetition rate of $10\ Hz$, which, in the future, will be raised to $50\ Hz$. The total length of the facility is of the order of $250\ m$: half of this distance represents the linac, the other half is shared between the undulator area and the experimental hall (including diagnostics of the FEL emission).

As shown in Fig. I.14, the transverse shape of the FEL light in far-field is very satisfactory. Furthermore, Fig. I.15 gives the evidence of very nice spectral stability and shape of the FEL
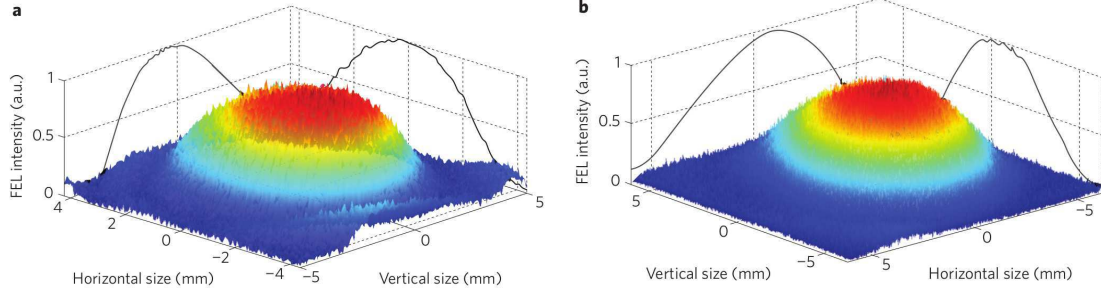

Figure I.14: FEL spot measured 52.4 m (a) and 72.5 m (b) downstream from the last radiator exit.

spectra. In Fig. I.15a, we see that the Gaussian shape of the seed spectrum is well reproduced by the FEL emission, as expected, and Fig. I.15b shows that the variations of the FEL in terms of intensity and spectral shape are quite low (500 successive single-shot measurements are shown).
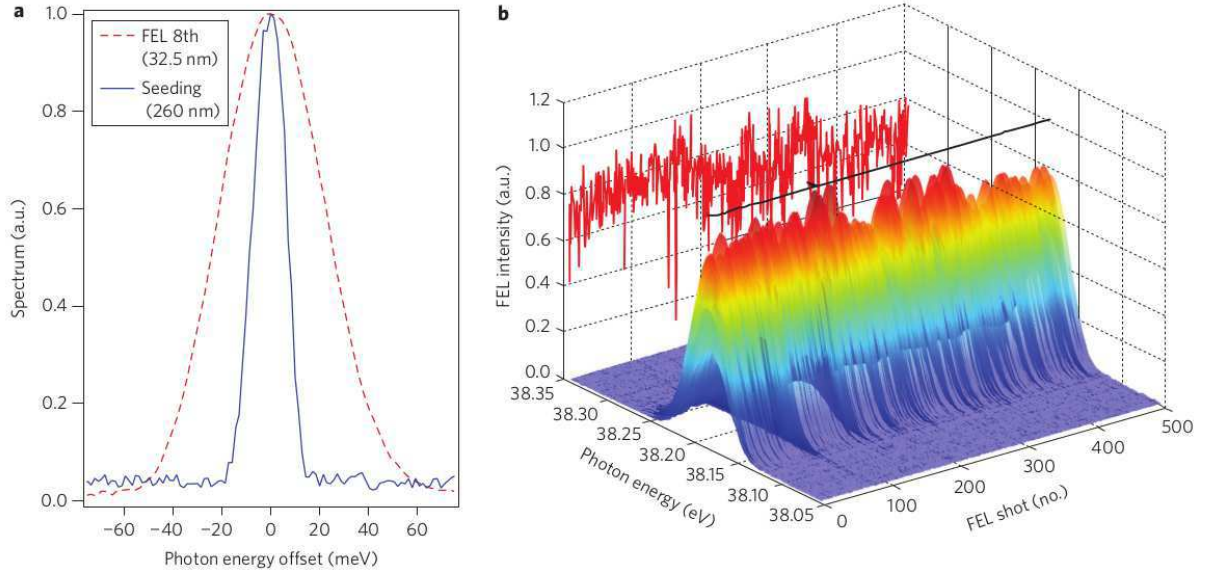
Figure I.15: (a) Measured FEL (dashed line) and seed laser (full line) spectrum. (b) Acquisition of 500 consecutive FEL spectra.

In this thesis, I will remain in the framework of the so-called "low-gain" regime of the FEL. The gain regime is characterized by the following factor [31, 32]:

$$g_0 = \frac{\mu_0 e}{mc^2} \cdot \frac{I}{\sigma_x \sigma_y \sigma_z} \cdot L_U^2 N_U^3 \cdot \frac{K^2 F_{JJ}^2}{\gamma^3}. \tag{I.36}$$

$\mu_0 = 4\pi \cdot 10^{-7} \frac{V \cdot s}{A \cdot m}$ is the permeability of the vacuum; I is the electron beam current; σ_x, σ_y and σ_z the standard deviations of its distribution respectively in the horizontal, vertical and longitudi-

nal directions; N_U is the number of undulator periods. F_{JJ} stands for the weighting of K due to the oscillating term in $v_z(t)$ (see Eq. I.21). For a planar undulator, $F_{JJ} = J_0\left(\frac{K^2}{4+2K^2}\right) - J_1\left(\frac{K^2}{4+2K^2}\right)$, where J_0 and J_1 are respectively the Bessel functions of 0th and 1st order. For an helical undulator, there is no oscillating term in the longitudinal motion of the electrons i.e., $v_z(t) = \bar{v}_z$ so $F_{JJ} = 1$. It is interesting to note that, for designing an X-ray FEL, one has to lower L_u and K while increasing γ (see Eq. I.28)... which make g_0 drop down. In order to built an high-gain X-ray FEL, very long undulators and small electron bunches with high current are thus required.

Roughly, the conditions of the experiments that are reported in this thesis are: $I < 300\ A$, $\sigma_x \approx \sigma_y > 150\ \mu m$, $\sigma_z > 300\ \mu m$, $L_U = L_R = 5.5\ cm$, $K < 10$, $N_U = N_R < 6 \times 44 = 264$ and $\gamma > 2000$. It gives $g_0 < 1$, which characterizes a low-gain regime, in which the FEL power is almost not amplified. For $g_0 \gg 1$, the FEL operates in high-gain regime (and CHG is better called HGHG, for high-gain harmonic generation): the amplification of the signal is exponential until saturation is reached.

Moreover, even if this will not be treated here partly because results are still quite recent and not optimized, FERMI@Elettra is also able to work in SASE mode when sufficient peak currents are reached in the electron beam. This would make possible, in the future, to confront phenomena related to SASE and seeding schemes on the single FERMI@Elettra facility.

Finally, one has to note that the configuration of FERMI@Elettra described here is only the first step of the facility. Indeed, in order to overcome the aforementioned limitations of harmonic number amplification due to energy spread growth, a second FEL line has been built: it relies on a first CHG stage, whose emission at harmonic n_1 of the seed is injected into a second stage, tuned at the harmonic n_2 of the emission of the first stage, so that the final emission is done at the harmonic number $n_1 \times n_2$. This is made possible by the fact that the amplification in the second stage occurs on a new portion of the bunch i.e., where electrons have not been modulated in energy (neither in space) within the first stage. This is called the "fresh-bunch" technique [33]. We already obtained first successful results that allow providing powerful femtosecond pulses in the soft X-ray spectral region [34].

I.3   High-order Harmonic Generation in rare gases

FEL's are probably the kind of facilities that allow providing most powerful femtosecond EUV/X-ray pulses, at the price of a huge installation requiring lots of controls and diagnostics. Sources of high-order harmonic generation (HHG) in rare gases are the most common and "affordable" alternatives. This section describes the main properties of HHG. The purpose is not to provide here a comprehensive description; for that, the reader can for instance refer to [35, 36] as a good overview giving also further literature.

I.3.a   Description

Thanks to the technique of chirped-pulse amplification, laser sources (especially Ti:Sapphire ones) have been able to reach very high peak intensities (energy of more than some mJ into femtosecond pulse durations, focused on spot diameters smaller than $100 \ \mu m$). In 1988, teams at Saclay and Chicago discovered in parallel the HHG effect. When focusing a laser at an intensity of the order of $10^{14} \ W/cm^2$ into a rare gas medium, ultraviolet light is emitted by interaction of the laser with the rare gas and a spectrum such as the one represented in Fig. I.16 can be collected. It is made of a comb of odd harmonics of the input laser beam. The
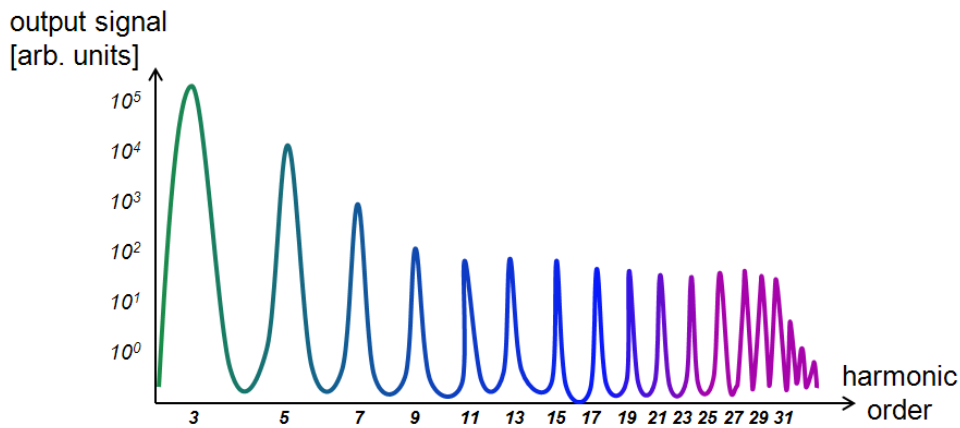

Figure I.16: *Typical spectrum obtained when focusing an intense laser beam in a rare gase medium.*

spectrum can be divided in three parts: for harmonic orders ranging from 3 to 9, the harmonic signal constantly decreases. Then, from the 9th order, there is a plateau of harmonics whose signal is of the same order of magnitude, until a cut-off (located at the order 31 in our case, but that can be different) after which the harmonic signal dramatically falls. Generally, the laser has a central wavelength of the order of about $800 \ nm$, so that its high-order harmonics are within the EUV spectral region.

I.3.b   Low-order harmonics

For the first orders, the explanation stems from the multi-photon absorption of the gas atoms: n photons of energy $h\nu$ (h being the Planck constant) of the laser (of frequency ν) kick an electron of a gas atom to an upper energy level; when getting back to its stable state, the electron loses energy emitting one single harmonic photon of energy $nh\nu$. The probability for the photons of the input laser to combine and then for the kicked electron to get down to its former energy level decreases as n increases, which explains why the signal drops down for first harmonic numbers. More accurately, the polarization in the gas medium can be expanded as $P = \varepsilon_0 \sum \chi^{(n)} E_{laser}^n$, where ε_0 is the permittivity of the vacuum, $\chi^{(n)}$ are the susceptibilities of nth order of the gas medium and E_{laser} is the input laser field. The central symmetry of

the gas medium makes that the even components of the polarization vanish, and only odd components i.e., odd harmonics, can be present. Generation of low-order harmonics has been initiated by Franken et al. in 1961 in a crystal [37], and in gas by New and Ward in 1967 [38], making possible the generation of a coherent light down to vacuum-ultraviolet wavelengths (below $200\,nm$), where no conventional lasers exist. For these first orders, laser intensities of the order of $10^{12}\,W/cm^2$ are already sufficient, which explains that low-order harmonic generation in gases could already be observed before more powerful femtosecond laser were available. The expression of the polarization P tells us that the overall properties of the low-order harmonic emission are strongly linked to the ones of the driving laser. In particular, the temporal shape and spectrum of the harmonics are very similar to those of the laser. The condition of phase-matching between the generating and emitted waves, of respective wave vectors $\vec{k}$ and $\vec{k}_n$, is simply $\vec{k}_n = n\vec{k}$.

For higher orders however (from the 9th harmonic), this explanation of classical non-linear optics is not valid any more. How to explain the presence of the plateau, which would mean that the probability of multi-photon absorption is the same whatever n? And how to explain the sudden cut-off of the harmonic signal?

I.3.c   Three-step model, cut-off law and electrons trajectory

A semi-classic model has been developed [39] giving a practical explanation of the HHG process. It is represented in Fig. I.17. At its fundamental state, the electron of a gas atom is in a well of potential. The atom experiences the action of the laser field, which can be written as $|\vec{E}_{laser}| = E\cos(\omega t)$ if its pulse duration is much longer than one optical cycle. The potential barrier is thus distorted so that the electron can pass through this barrier by tunnel ionization. Whereas the energy levels of the electron were quantized before this first step, the electron is now melt into a continuum of energy. Under the action of the Coulomb force due to the laser field, the electron gains kinetic energy: this is the second step. Then, as a final step, it can recombine radiatively to the fundamental state: for that, it has to free, in the form of a photon, an energy equal to the kinetic energy it gained plus the ionization potential of the atom. The polarization of the input laser must be linear, otherwise there is no recombination of the electron and thus no harmonic emission. The process is repeated every half-period of the laser field (for $\omega t \simeq 0$ and $\omega t \simeq \pi$). This gives rise to spectral interference which leads to an emission of harmonic lines separated by 2ω. Moreover, the sign change in the emission from one half period to the other involves that the generated harmonics are the odd ones. Since the recombination of the electron has very low probability, the process has poor efficiency.

This description was in fact preceded by a study of the motion of the ejected electron that allows finding the wavelength at cut-off [40]. According to the second Newton's law, we get the
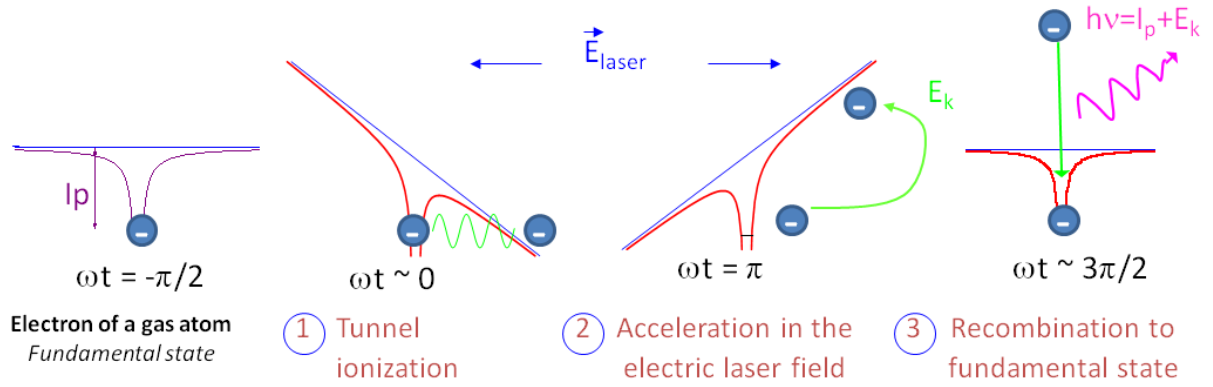
Figure I.17: Steps of the semi-classical model for the HHG.

acceleration of the electron due to the Coulomb force $F = -eE_{laser}$:

$$a(t) = -\frac{eE}{m}\cos(\omega t), \tag{I.37}$$

e being the elementary charge and m the mass of an electron. By integration, its velocity is found to be:

$$v(t) = -\frac{eE}{\omega m}[\sin(\omega t) - \sin(\omega t_i)], \tag{I.38}$$

where t_i is the ionization time. The kinetic energy of the electron is thus:

$$E_k(t) = \frac{e^2 E^2}{2\omega^2 m^2}[\sin(\omega t) - \sin(\omega t_i)]^2. \tag{I.39}$$

At the recombination time t_r, the energy of the emitted photon will therefore be $\hbar\omega_n = E_k(t_r) + I_p$. This value finds a maximum, corresponding to the harmonic frequency at cut-off, for $\omega t_r = 17°$ and $\omega t_i = 255°$. This maximum harmonic frequency is also proportional to the intensity of the laser field and the square of the wavelength of the driving field. It is thus possible to extend the harmonic plateau by increasing the driving wavelength; however, since the electrons thus spend more time in the continuum, it is more probable that they will be "lost" and will not recombine, leading to a decrease of the harmonic conversion efficiency, as will be confirmed in Chapter V. The effect of increasing too much the intensity of the laser beam would be to suppress completely the potential barrier and the electrons would gain too much energy to recollide, which would also lead to a degradation of the HHG process.

By integration of Eq. I.38, one obtains the trajectory of an ejected electron as a function of time. We will not detail it here as it is not of specific interest in the remainder of this manuscript, but it shows that each harmonic can be generated through either a long or a short trajectory of the electron [41]. An electron follows a long trajectory when the laser field is close to its maximum: the electron is thus kicked out very far from the atom, which lessens the recollision probability. The harmonic conversion efficiency is thus lower for long trajectories with respect to

short ones. At the cut-off, short and long trajectories merge.

This semi-classical view of the microscopic response was then corroborated by quantum calculations [46, 47, 48, 49]. In these models, the atomic dipole ion-electron is viewed as a sum of amplitudes of probability corresponding to different quantum paths of the electron wave packet, which are identified to trajectories described in the semi-classical model including the ionization, the acceleration in the laser field and the recombination. Due to this proximity with quantum calculations, the semi-classical view is a good model for understanding and giving most qualitative properties of the harmonic emission.

Beyond the microscopic response of a single atom, the macroscopic construction of the harmonics in the whole volume of interaction between the laser and the gas has to be studied. Numerically, it is done by three-dimensional propagation codes; analytically, optimum phase-matching conditions can be found: this is detailed in the next section.

I.3.d Phase-matching and characteristic lengths

The total EUV field is the result of the coherent superposition of the fields emitted at the frequency $\omega_n = n\omega$ by the atomic dipoles contained in the whole volume of interaction. In order to obtain an optimum harmonic generation, these fields have to interfere constructively. This is the matter of phase-matching between the laser and harmonic fields, which have to propagate at the same velocity in the gas. The simplified phase-matching condition for the wave vectors $\vec{k}$ and $\vec{k}_n$ of respectively the laser and harmonic field can be written as:

$$\vec{k}_n = n\vec{k} + \vec{K}, \tag{I.40}$$

where $\vec{K}$ is proportional to the gradient of laser intensity and represents the phase of the atomic dipole formed by the electron and its parent ion. Since the refractive index of the gas medium is different for the fundamental laser wavelength and its harmonics, $\vec{k}_n$ and $\vec{k}$ have a component emanating from the dispersion, depending on the kind of gas that is used, its pressure, how much it is ionized, etc. Moreover, both wave vectors depend also on their focusing or guiding in the medium. To this extent, the more concerned by geometrical dependence is $\vec{k}$, since it is more diverging. The distributions of the two vectors $\vec{k}$ and $\vec{K}$ will determine the regions of space where the phase-matching is made possible. They are represented in Fig. I.18 around the focal point in the gas medium.

We can concentrate on four different cases, sketched in Fig. I.19:

- in (a), $\vec{K}$ is zero so that phase-matching is not achieved.

- in (b), $\vec{K}$ is present but points in the wrong direction so that there is again no phase-matching.
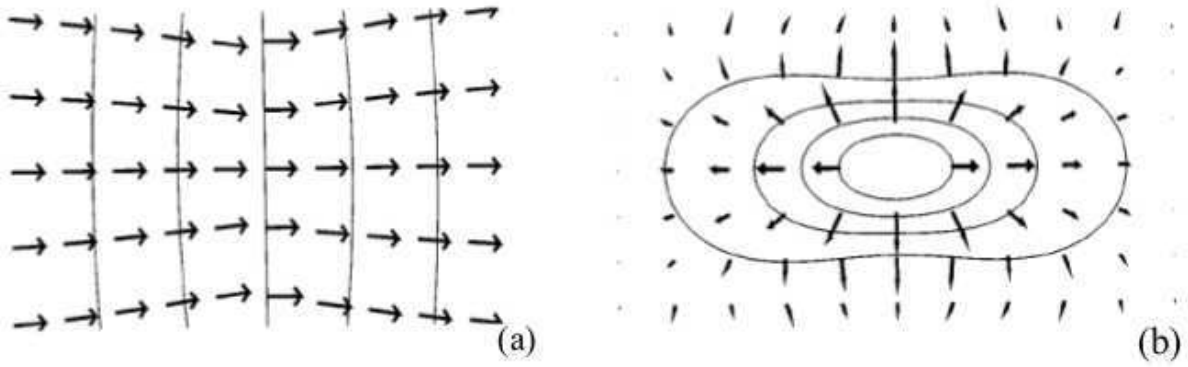
Figure I.18: *Distribution of the vectors $\vec{k}$ (a) and $\vec{K}$ (b) around focus. (taken from [42])*

- in (c), $\vec{K}$ compensates, thanks to the variation of laser intensity, for the geometrical de-phasing induced by the focusing of the laser beam. It thus allow a macroscopic construction of the harmonic field on-axis.

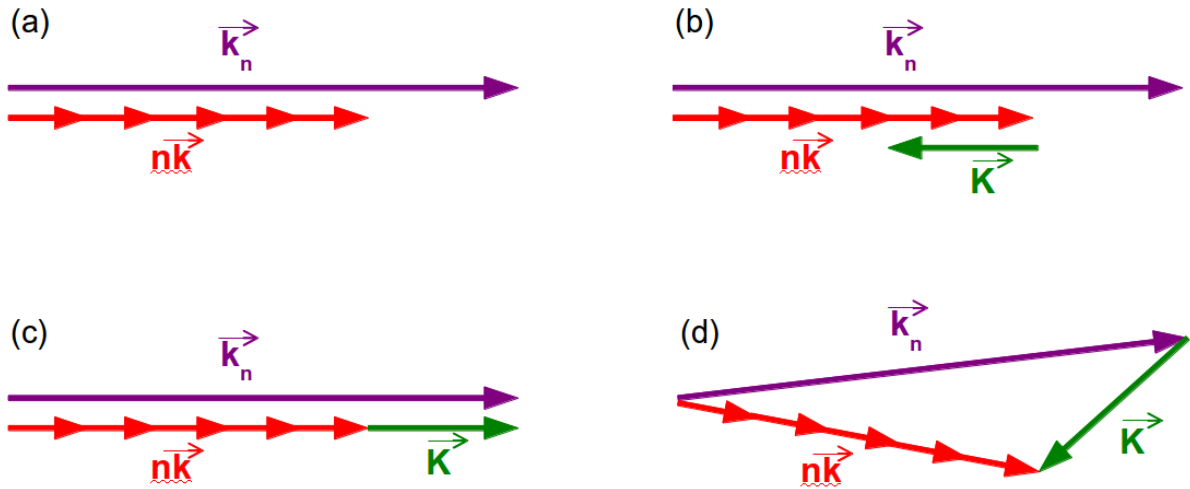- in (d), phase-matching is achieved in some off-axis regions so that an annular harmonic field is emitted.

Figure I.19: *Geometrical representation of the phase-matching on-axis at focus (a), on-axis after focus (b), on-axis before focus (c), off-axis after focus (d).*

The conditions in Fig. I.19c and Fig. I.19d have been illustrated in [43], confirming that an efficient, on-axis, EUV emission is usually obtained for a laser beam focused before the gas medium. However, usually a perfect phase-matching cannot be achieved so that one will define a coherence length corresponding to the distance before which the interference between the microscopic emissions becomes destructive. It corresponds to the length on which the harmonic field and the non-linear polarization of the laser field are dephased by π. This length, defined by $L_{coh} = \frac{\pi}{\Delta k_n}$, limits the efficient macroscopic construction of the harmonic emission.

The interaction length i.e., the length of the gas medium noted L_{med}, should therefore be smaller than the coherence length. Moreover, another limiting factor of the harmonic generation is the absorption of the harmonic emission by the gas itself. It is defined as the distance over which the harmonic field is attenuated by a factor $\frac{1}{e}$ i.e., $L_{abs} = \frac{1}{\sigma_n d_{at}}$, where σ_n is the cross-section of photo-absorption of the gas at the frequency $n\omega$ and d_{at} the atomic density. These lengths allow giving an approximation of the number of generated photons N_n at the harmonic number n [44]:

$$N_n \propto \frac{4L_{abs}^2}{1 + \left(\frac{2\pi L_{abs}}{L_{coh}}\right)^2} \left[1 + e^{-\frac{L_{med}}{L_{abs}}} - 2\cos\left(\pi \frac{L_{med}}{L_{coh}}\right) e^{-\frac{L_{med}}{2L_{abs}}} \right]. \qquad (I.41)$$

Figure I.20 plots the relative number of generated photons as a function of the length of the gas medium, for different coherence lengths. We see that the number of emitted photons grows until the radiation becomes absorbed by the gas, and that the harmonic efficiency is optimized for a coherence length much larger than the absorption length. The optimization of harmonic generation will therefore rely on the fine tuning of the length of the medium, the coherence length (which depends mainly on the geometry chosen for phase-matching) and the absorption length (which can be changed mainly via the gas pressure). From Fig. I.20, we conclude that, for obtaining a number of photons at least equal to half the maximum accessible one, we must have $L_{med} > 3L_{abs}$ and $L_{coh} > 5L_{abs}$. When increasing the medium length does not provide more harmonic photons, the generation becomes limited by absorption.
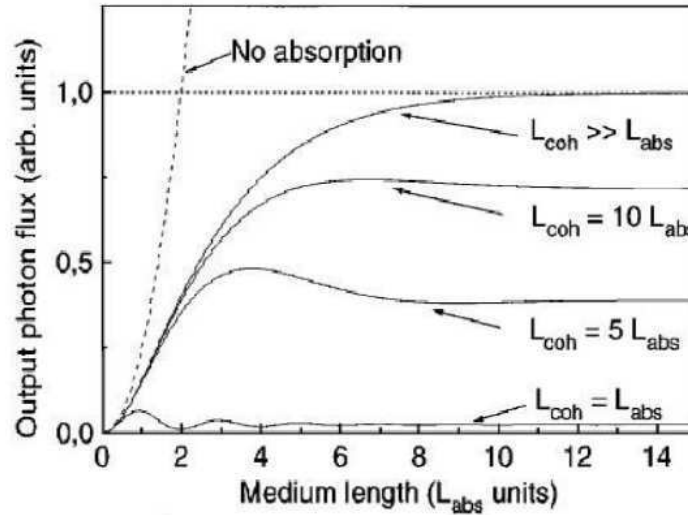
Figure I.20: Relative number of generated harmonic photons as a function of the length of the gas medium, for different coherence lengths. (taken from [44])

Different configurations can be used for the harmonic generation. We can separate them into three: short medium (< 1 cm), via a gas jet (eventually pulsed at the repetition rate of the driving laser) or short cell; loose-focusing into a long gas cell; in a capillary (few centimeters) filled with the rare gas. In the latter configuration, the waveguiding facilitates the phase-matching

[45]. The loose-focusing configuration is achieved via a focusing lens of some meters of focal length that provides a laser beam (almost) collimated over some centimeters. An important volume can then be used for harmonic generation since the intensity and the phase of the laser beam are only slowly varying transversally and longitudinally. The advantage is that it allows producing μJ-level EUV photons, using an important energy of the driving laser (tens of mJ). We remind that the laser beam intensity should not be too high, in particular in order to avoid a consequent ionization of the gas atoms that would change the recombination process and induce a stronger dispersion due to the free electrons. The drawback of such a configuration is that a lot of space, to be put under vacuum, is required: some meters for focusing into the gas cell, but also some meters after the gas cell for getting rid of the infrared beam. Indeed, the latter has to be filtered for diagnostics and experiments. In tight-focusing, it rapidly diverges, making things easier, whereas in loose-focusing, its intensity remains high over a long distance.

I.4 Summary

We introduced the fundamental notions that are needed for the work I report within this manuscript. We saw the fundamental notion of Fourier-transform limit, which limits the duration of a pulse for a given bandwidth. Similarly, the diffraction limit has been presented, such as the notions of spatial and temporal coherence.

The experiments on which my study has relied have been performed on two kind of sources: the FEL FERMI@Elettra and HHG sources. FERMI@Elettra works as follows: modulation of the energy of the electron bunch in a first undulator, bunching in the dispersive section and coherent emission at a chosen harmonic in the radiators. The energy modulation is induced by the seed laser, the bunching controlled by the value of R_{56} and the efficiency of the emission depends, among other parameters, on the peak current of the bunch (see Eq. I.36).

HHG is, in fact, comparable to seeded FEL's: it is driven by an external laser and relies on electrons motion and manipulation. The HHG is well-described by a semi-classical model which gives a very good insight of the main properties of the EUV radiation and of the underlying mechanisms of its emission. We also saw the importance of the macroscopic construction of the harmonics.

In the next chapter, we will start with a study of the spatial properties of FERMI@Elettra and of a drive source used for HHG. Spectro-temporal studies, which have many analogies with spatial ones, will follow.

Coherence and spatial quality

Contents

II.1   Spatial properties of FERMI@Elettra

In a seeded FEL, the main mission of the seed is to imprint its spectro-temporal properties on the electron bunch and thus, on the FEL emission. However, the impact of the seed is still unclear on the spatial properties of the EUV light. Studying them therefore represents a novel work, and observed effects can be traced back to the causes, which potentially allows to better understand the FEL process in seeded mode. In the recent years, the spatial coherence of FEL facilities has been extensively characterized. In most of the cases, the FEL was operated in the so-called SASE mode [51, 52]. Spatial coherence measurements have thus been performed at FERMI@Elettra for three purposes: characterizing the coherence properties as a function of the different FEL regimes, confronting the results with SASE-based facilities and providing information for experiments requiring a high degree of coherence, like diffraction imaging [53]. The experimental characterizations have also been compared to theoretical predictions that can be done. In addition to the spatial coherence, the overall FEL spot quality and stability have been measured. Preliminary wavefront measurements will also be presented in this section.

II.1.a   Spatial coherence setup and principle

As a first step, it has been decided to carry out a campaign of measurements with the setup of a Young's experiment [77]. The experiment was performed on the direct beam i.e., without any focusing optics on the beam path, so that the "real" coherence of the source is characterized. A basic drawing of the setup is shown on Fig. II.1.
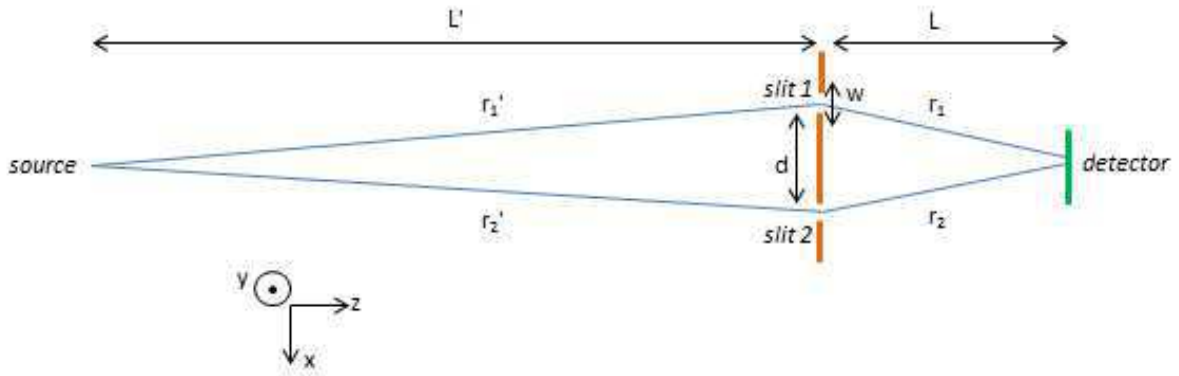
Figure II.1: *Simplified layout of the Young slits experiment. The position of the source (FEL light), considered as a point, is estimated to be at the center of the last radiator. The mask of the slits, where the FEL light is assumed to be a plane wave, is thus at $L' = 65.2\ m$ far from the source. The detector (a CCD made of 1004x1004 pixels of $18.8\ \mu m$ side, looking at a fluorescent screen) is placed at $L = 8.5\ m$ downstream the slits. For a given couple of slits, the slits have equal widths w and are separated by d.*

Table II.1.a gives the characteristics of the different couples of slits that were used: for each couple, the two slits have the same width w and are separated by a distance d in the x direction (see Fig. II.1). The height (y directon) of each slit is approximatively $1\ cm$, which is almost the

slits separation $d\,[mm]$	slits width $w\,[\mu m]$
0.8	20
1	40
1.5	40
2	40
4	40

Table II.1: *Characteristics of the different couples of slits.*

full beam transverse size. All the slits are disposed on the same copper plate. The latter was moved via a mechanical actuator, so as to change the couple of slits through which the light goes.

The FEL light follows two different paths passing through each slit. For the path through slit 1 (see Fig. II.1), without considering the contribution of the other path, a single diffraction pattern is produced with intensity $I_1(M)$ at a point $M(x,y)$ on the detector. Similarly, the beam on the second path produces another single diffraction pattern of intensity $I_2(M)$. The joint contribution of the two paths provides the interference between the two waves, at positions where the diffraction patterns overlap. The vertical slits allow performing a one-dimension analysis in the x (transverse horizontal) direction. Fig II.2 is a basic drawing of the obtained profile on the detector, at a given vertical coordinate y: a typical interference profile (fringes) modulated by the intensity of the diffraction patterns. For a slit, the profile of the diffraction pattern is a function
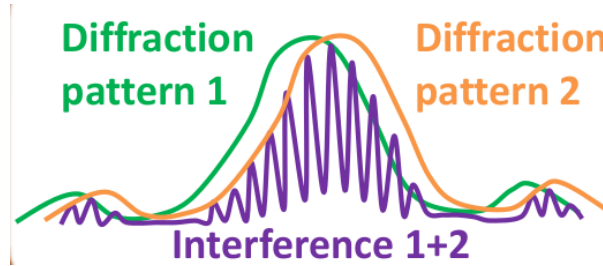
Figure II.2: *Example of a profile obtained on the detection system. The waves coming from each slit interfere "under" the envelope of the diffraction patterns of each slit.*

$sinc(x) = \frac{\sin(x)}{x}$, under the hypothesis of Fraunhofer (far-field) diffraction i.e., $\frac{w^2}{L\lambda} \ll 1$, λ being the wavelength of the FEL emission. $\lambda = 32.5\,nm$ in our experiment (8th harmonic of the seed). Therefore $\frac{w^2}{L\lambda} = 1.4 \cdot 10^{-3}$ for the first couple of slits and $\frac{w^2}{L\lambda} = 5.8 \cdot 10^{-3}$ for the other ones. The width of a diffraction pattern (defined as the distance between the zeros from each side of the peak) is $\frac{2L\lambda}{w}$. The distance between the peaks of the two diffraction patterns is equal to $\frac{L+L'}{L}d$. The width of the fringes of the interference profile is $\frac{L\lambda}{d}$.

Figure II.3 shows what is observed on the detection system without (a) and with (b) slits. For the matter of data analysis, a profile $I(x)$ is done (c) on a narrow slice. In the case shown here, the diffraction patterns overlap very well, so that we can distinguish only one single envelope

Figure II.3: *Typical pattern observed on the CCD without slits inserted (a); pattern with slits separated by $d = 1\ mm$, with a region of interest (b); integrated profile of the region of interest (c).*
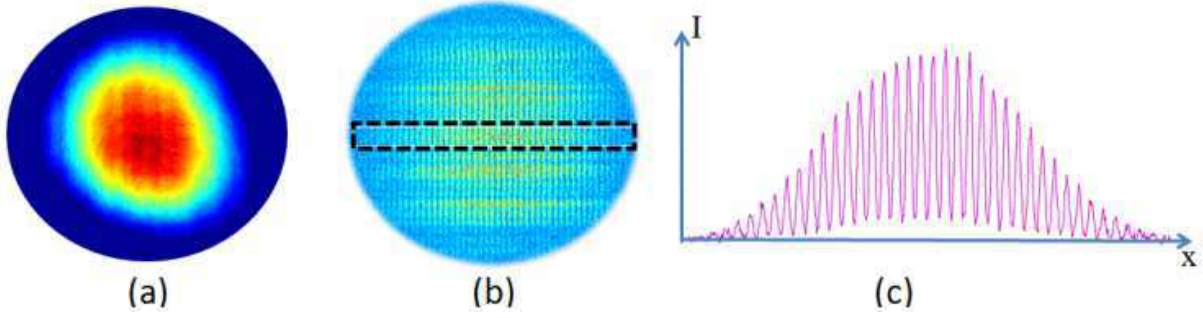
surrounding the interference profile. Along the latter, we can define the visibility of the fringes:

$$V(x) = \frac{I_{max}(x) - I_{min}(x)}{I_{max}(x) + I_{min}(x)}, \tag{II.1}$$

where I_{min} and I_{max} are respectively the local minimum and maximum around a position x. For instance, in Fig. II.3c, we find an almost constant visibility $V(x) \approx 0.84$.

If the spectrum is narrow enough ($H_\nu \ll \nu$, where ν is the central frequency of FEL emission and H_ν its FWHM bandwidth) and the delay τ between the two beams is much shorter than the coherence time τ_c, then V is constant over the interference profile and the coherence factor μ (see Chapter 1) is equal to [18]:

$$|\mu(M)| = \frac{I_1(M) + I_2(M)}{2\sqrt{I_1(M)I_2(M)}} V. \tag{II.2}$$

In our case, $\nu = 9.2 \cdot 10^{15}\ Hz$, $H_\nu = 2.9 \cdot 10^{12}\ Hz$, $\tau_c = \frac{0.664}{H_\nu}$ (for a Gaussian spectrum) i.e., $\tau_c = 230\ fs$ and $\tau = \frac{|(r_1 + r_1') - (r_2 + r_2')|}{c}$. In the conditions of the experiment, Fig. II.4 shows that, whatever the point M considered on the CCD (left panel) or the misalignment of the setup, τ remains below $20\ fs$ i.e., significantly smaller than τ_c. Therefore, the conditions stated above are fulfilled. In these conditions, we can thus also conclude that we won't be able to see any effect of temporal coherence over the interference pattern: this is the reason why V is (almost) constant over the interference profile in our case. By changing the couple of slits, we will probe different areas of the wavefront that arrives on the slits. The spatial coherence between two vertical slices of the spot separated by a distance d is thus characterized, and the degree of coherence is then analysed as a function of this separation.

A typical interference profile and its spatial Fourier transform are displayed in Fig. II.5. Graphically, the Fourier transform gives one central peak plus two identical side ones and can be written as a convolution of the Fourier transform of the diffraction envelope with the following expression:

$$2\delta(f_x) + S(f_x)V(f_x) * [\delta(f_x - f_0)\delta(f_x + f_0)]. \tag{II.3}$$
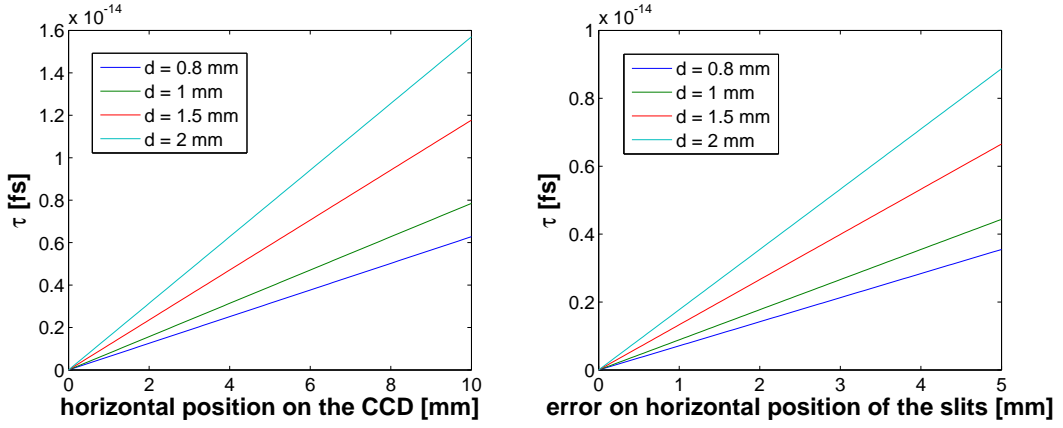
Figure II.4: Delay τ between the two paths of the beam for the four couples of slits used in the experiment. In the ideal case, the source, the slits and the center pixel of the CCD are centered and τ = 0 s. Left panel: τ as a function of the pixel that is read on the CCD if the source, the slits and the central pixel of the CCD are centered; right panel: τ measured on the central pixel of the CCD as a function of the misalignment of the slits. In both cases, it remains significantly smaller than τ_c.
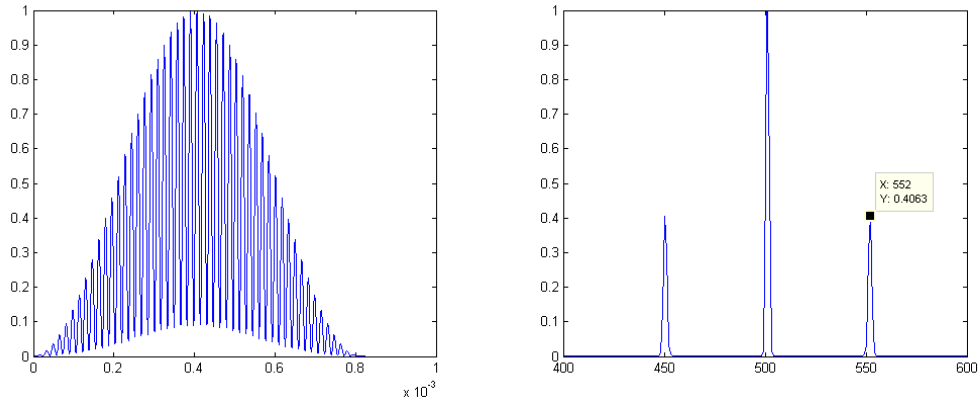
Figure II.5: Typical interference profile $I(x)$ (left panel) and its normalized Fourier transform $TF[I_0(x)] = F(f_x)$ (right part), giving one central peak and two identical side ones. The visibility is given by twice the height of a side peak, normalized by the height of the central one.

Here δ is the Dirac delta function and S is the spectral intensity at the spatial frequency f_x of the Fourier transform, corresponding to a wavelength $\lambda = \frac{d}{f_x L}$ (f_0 isthe spatial frequency corresponding to the central wavelength). V is then given by the sum of integrals of the side peaks over the integral of the central one. The fact that the spectral intensity appears in Eq. II.3 theoretically allows measuring the spectrum with a Young's experiment [54]. This is however true for an enough wide spectrum ($H_\nu \sim \nu$), whereas in our case the narrowness of the spectrum does not provide enough resolution for such a retrieval. Besides, V is thus simply given by twice the relative height of a side peak since the spectrum is almost a delta function as well.

This method has been chosen for performing the data analysis for two main reasons: it allows exploiting easily a large sample of data and it directly averages the value of V over the whole interference profile. However the direct measurement of visibility on the interference profile has also often been used as a cross-check. For obtaining μ, one also needs to know $I_1(M)$

and $I_2(M)$, the intensities of each single diffraction pattern on a given position of the detector. The latter measurement has not been done in our experiment. Thus, since $\frac{I_1(M)+I_2(M)}{2\sqrt{I_1(M)I_2(M)}} < 1$, we assume that $I_1 = I_2$ and thereby we slightly underestimate the coherence factor. However, we estimate the error to be of the order of $1-2\%$ only (it is worth noting that this factor is also usually neglected in most of coherence measurements). So we consider that $\mu = V$. Moreover, for improving the signal-to-noise ratio, we usually integrated the results over some successive shots. This averaging is an additional reason of undervaluation of the degree of coherence.

II.1.b   Spot characterization

The degree of coherence is usually given as a function of the slits' separation. We wish to normalize the slits separation to the transverse size of the beam, in order to be able to compare results obtained for different spot sizes. That is why, for the experiments reported here, a series of FEL spots has been measured on the detection system without the slits inserted. A typical result is shown in Fig. II.6. As it can be seen, the pointing is very stable, such as the shape, which
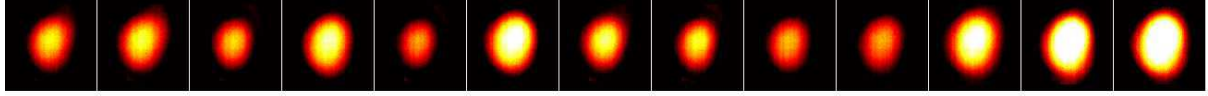

Figure II.6: Series of 13 successive FEL spots observed on the CCD.

presents a small astigmatism. Only the intensity is slightly varying shot-to-shot, but there are no "dead-shots". An analysis of these images has been done in order to characterize the transverse size of the beam before carrying out the Young's experiment. In the horizontal direction, we found, over 13 successive shots, a radius $\sigma_x(\text{after slits}) \approx 2.50 \pm 0.06 \ mm$. In the vertical one, on which we do not focus our attention in this work, we found $\sigma_y(\text{after slits}) \approx 3.01 \pm 0.06 \ mm$. In both directions, the profiles are Gaussian-like.

The horizontal profiles traced on Fig. II.8, corresponding to the same series of measurements (see Fig. II.6), emphasize the stability of the transverse shape. Each profile has been normalized to its maximum value, in order to get rid of shot-to-shot intensity fluctuations on the graphical display. From this figure, we can say that the horizontal profile of the beam seems sufficiently stable for the slits to probe the same portions of the FEL spot at every coherence measurement.

In order to calculate the divergence of the beam, a similar characterization has been carried out on a detection system placed $11.6 \ m$ before the slits. The transverse sizes of the beam measured in the horizontal and vertical directions were, respectively, $\sigma_x(\text{before slits}) \approx 1.8 \pm 0.04 \ mm$ and $\sigma_y(\text{before slits}) \approx 1.9 \pm 0.04 \ mm$. The shapes are still Gaussian-like and the spot
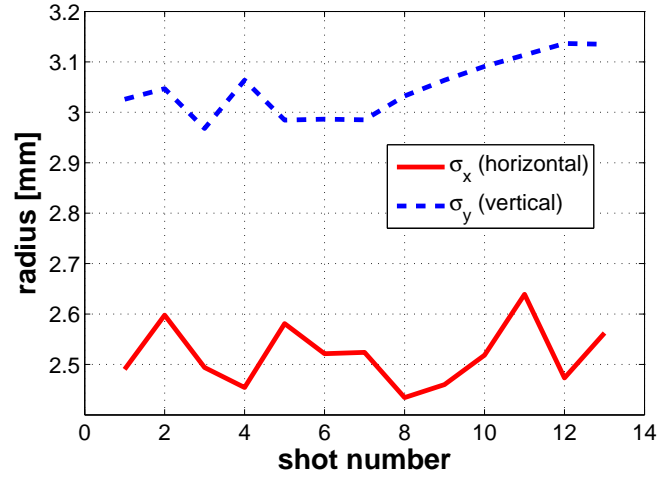
Figure II.7: Evolution, in the vertical (dashed line) and horizontal (full line) directions, of the radius of the FEL spot (standard deviations of the transverse intensity profiles).
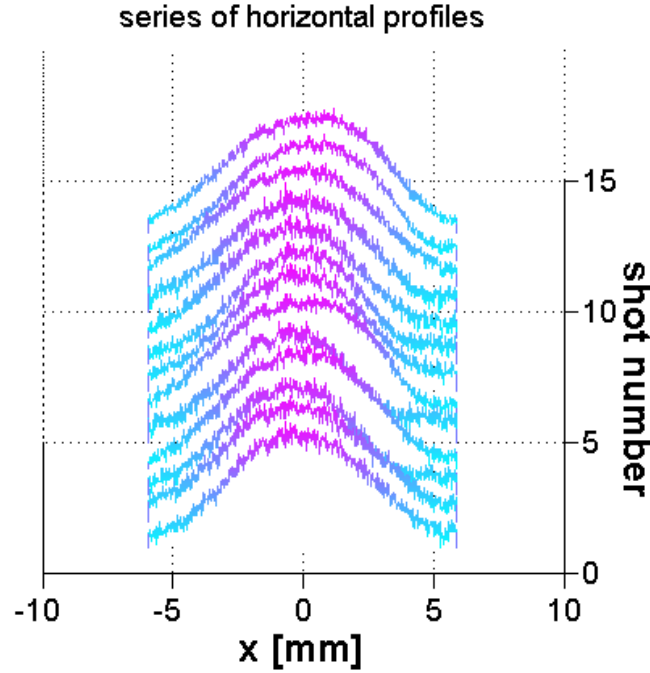
Figure II.8: Horizontal profiles of the series of FEL spots measured on the detection system without the slits. Each profile has been normalized to its maximum value.

still very stable, in terms of pointing and size. The divergence is given by:

$$\theta_{x,y} = 2\arctan\left(\frac{\sigma_{x,y}(\text{after slits}) - \sigma_{x,y}(\text{before slits})}{2l}\right) \sim \frac{\sigma_{x,y}(\text{after slits}) - \sigma_{x,y}(\text{before slits})}{l},$$

(II.4)

where l is the distance between the two detection systems (before and after the slits) i.e., $l = 11.6 + L = 11.6 + 8.5 = 20.1 \ m$. We thus obtain $\theta_x = 35 \ \mu rad$ in the horizontal direction and $\theta_y = 55 \ \mu rad$ in the horizontal one (the beam is thus astigmatic). This enables es-

timating the size of the spot at slits' positions: from the previous formula, we get $\sigma_{x,y}(\text{slits}) = \sigma_{x,y}(\text{after slits}) - L\theta_{x,y}$, that will be simply noted $\sigma_{x,y}$. I chose $\sigma_{x,y}(\text{after slits})$ as the "reference" spot size for calculating $\sigma_{x,y}$ because it is larger than $\sigma_{x,y}(\text{before slits})$ and the uncertainty on the measurement is therefore lower. We thus obtain: $\sigma_x = 2.2\ mm$ and $\sigma_y = 2.5\ mm$.

II.1.c   Spatial coherence results

In our measurements, we centered "by eye" the slits on the FEL spot, considering also that a maximum value of V is obtained if the slits are centered and the FEL spot is symmetric with respect to the vertical axis. Typical results are summarized by Fig. II.9, which gives the visibility of the fringes (equivalent to the degree of coherence) as a function of the relative slits' separation. We find that the visibility is above 0.8 for $\frac{d}{\sigma_x} < 0.5$. It is important to note that, for the couple of slits separated by $d = 0.8\ mm$ (corresponding to $\frac{d}{\sigma_x} = 0.36$), the visibility of the fringes is probably undervalued due to a low signal-to-noise ratio, which is caused by a smaller slits' width of $20\ \mu m$ (whereas $w = 40\ \mu m$ for other couples of slits, through which more signal is thus transmitted and collected on the CCD). Hence the spatial coherence at the center of the FEL spot is possibly even higher. Indeed, in the limit of $\frac{d}{\sigma_x} = 0$, the same parts of the wavefront interfere so that the coherence factor should tend to 1 towards the central position of the FEL spot.
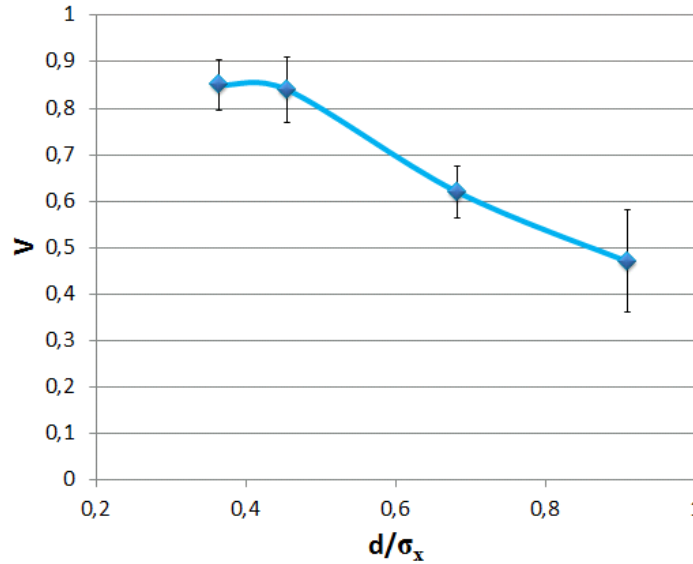
Figure II.9: Results (visibility as a function of relative slits' separation) obtained in standard conditions. Each point corresponds to the average of 10 successive measurements with their standard deviation, one single measurement being integrated over 10 shots. For the first point, V may be underestimated due to a low signal-to-noise ratio.

As a comparison, the results of V as a function of $\frac{d}{\sigma_x}$ found here for FERMI@Elettra are approximately twice better than the ones obtained on the SASE-based facility FLASH and reported in [51] (dashed line in Fig. II.10). It is worth noting that in the latter experiment, the wavelength was not the same (13.7 nm for experiments held at FLASH and 32.5 nm at FERMI@Elettra),

even if still in the EUV spectral region. Also, the beam was smaller ($\sigma_x \approx 750 \ \mu m$), but what is important is that there were also no focusing optics on the beam path, and in any case the relative separation $\frac{d}{\sigma_x}$ is taken into account. The comparison seems therefore justified, and is at the advantadge of the seeded facility FERMI@Elettra. On the other hand, other femtosecond extreme-ultraviolet sources such as high-order harmonics generated in a hollow fiber filled with gas can exhibit much higher transverse coherence degrees, close to 1 over the whole spot (dotted line in Fig. II.10) due to a nearly single-mode structure [55] (a modal filtering – see Section II.2 – is done on the EUV signal propagating through the fiber). It is worth noting that a
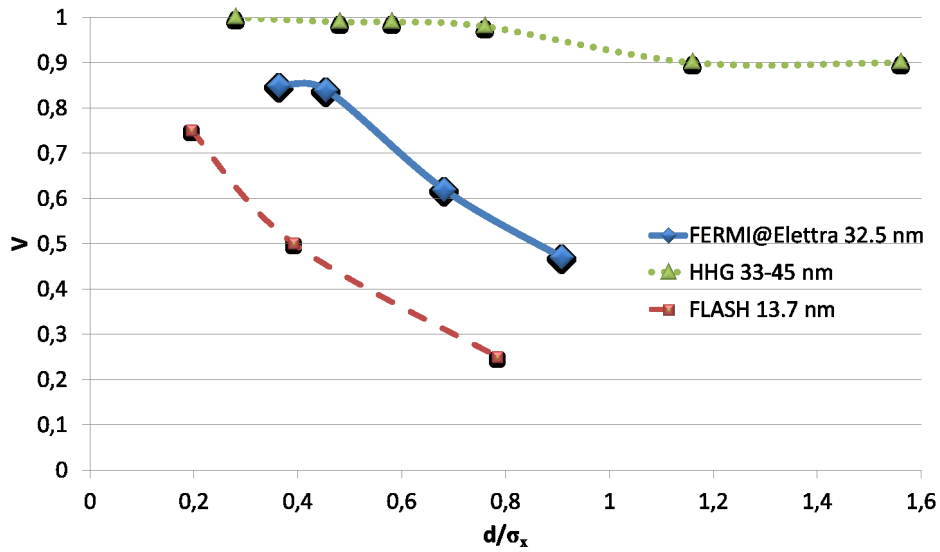
Figure II.10: *Results (visibility as a function of relative slits' separation) obtained on FERMI@Elettra (losange markers, full line), at FLASH [51] (square markers, dashed line) and on a HHG source [55] (triangle markers, dotted line).*

multi-mode field does not inevitably involve a lower coherence than the single-mode one: both can theoretically exhibit stable intensity shape and wavefront, and in this case they are both coherent. Nevertheless, this situation, which is already difficult to imagine for a single mode, seems even more challenging for an electric field made of an addition of modes.

We then performed new series of coherence measurements for which we obtained slightly lower visibility. We do not have definitive reason for that, even if a degraded quality of the transverse electron beam properties is suspected. In any case, here the aim was not to obtain the best spatial coherence as possible here, but to study the effect of saturation and over-bunching on the spatial coherence. Figure II.11 shows that, when going into over-bunching, the spatial coherence is degraded. As a first example, when the seed power is higher (dashed line), the coherence at the center of the FEL spot gets lower. Indeed, in this situation, the saturation is reached earlier in the radiators chain leading to over-bunching at the end of the radiators chain, at least in the central portion of the spot – where the seed intensity is the highest. A second example is, when keeping the seed at the same usual value but removing (detuning, in fact) two

radiators (the first two, in order not to change the source point of the FEL light) of the chain, the spatial coherence at the center of the spot does not decrease very much with respect to the "normal case" (full line), but it does on the outer parts of the spot. As a matter of fact, the outer parts of the bunch (the ones that received less seed intensity) are, in the presence of only four radiators, far from saturation. This may explain why the light they emit is relatively less spatially coherent. Indeed, obtaining saturation corresponds longitudinally to the emission of wavefronts in phase and thus to a good temporal coherence. Transversally, there is thus the same effect. However, the fall of V for $\frac{d}{\sigma_x} \approx 0.35$ with a strong seed can be surprising: V should tend to unity when close portions of the wavefront interfere.
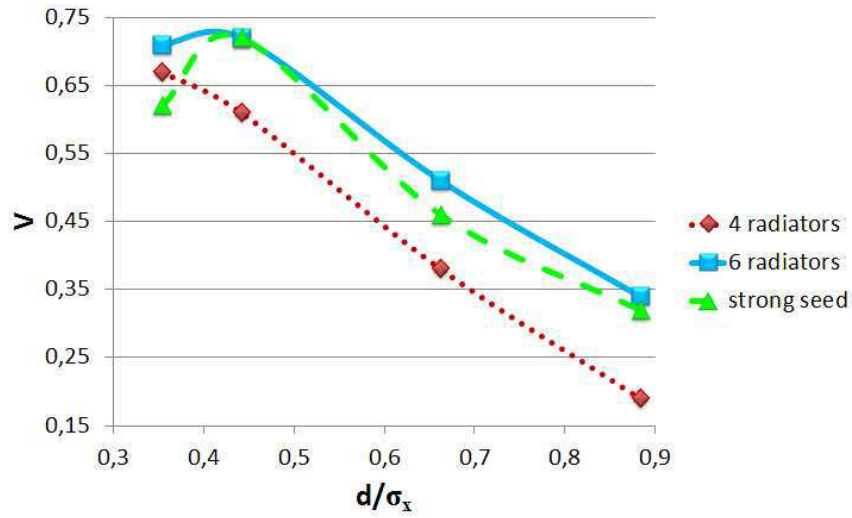
Figure II.11: Results obtained for three different configurations: 4 radiators only (losange markers, dotted line), 6 radiators (square markers, full line), 6 radiators with strong seed (triangle markers, dashed line).

It has not been possible to analyse the measurements of visibility for slits separated by $d = 4\,mm$. Indeed, as shown in Fig. II.12, two problems occur:

1. The diffraction patterns (for $d = 4\,mm$) do not overlap well. This makes the analysis more difficult and the assumption $I_1 = I_2$ (probably) not valid anymore.

2. Moreover, the resolution of the CCD is too small in the current layout of our setup. To probe a larger part of the FEL spot, L should be increased and/or w lowered, which would have the drawback to decrease the signal collected on the detection system. This can be solved by using a CCD placed directly on the beam path instead of using the current detection system, where the CCD looks at a fluorescent crystal, which is significantly less efficient in terms of signal collected by the CCD. Such a solution would also enable a single-shot characterization.
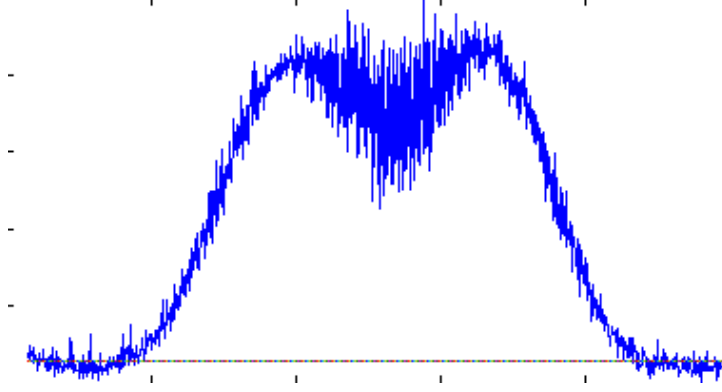
Figure II.12: Typical profile obtained for a slits separation $d = 4$ mm.

II.1.d Comparison with a Gauss-Schell Model beam

The aim of this section is to predict the spatial coherence of the FEL light at any longitudinal position, on the basis of similar works that have been already carried out e.g., at FLASH [56]. Let us recall the mutual coherence function, from which one can derive other coherence functions (see Chapter I):

$$\Gamma(x_1, x_2, z_0, \tau) = < E(x_1, z_0, t) E^*(x_2, z_0, t + \tau) >, \tag{II.5}$$

where z_0 is the position at which the electric field is measured. The knowledge of the electric field at one position gives the coherence not only at this position, but at any position along the propagation axis. Indeed, by means of the paraxial propagation of the electric field, one can obtain $E(x, z, t)$ from $E(x, z_0, t)$, which leads to:

$$\Gamma(x_1, x_2, z, \tau) = < E(x_1, z, t) E^*(x_2, z, t + \tau) > . \tag{II.6}$$

The similar reasoning can be transposed to the Fourier transform of this function, that is the cross-spectral density $W(x_1, x_2, \omega, z)$, whose normalized version is the coherence factor $\mu(x_1, x_2, \omega, z) = \frac{W(x_1, x_2, \omega, z)}{\sqrt{W(x_1, x_1, \omega, z) W(x_2, x_2, \omega, z)}}$ (see Chapter I). It is thus theoretically possible to know the degree of coherence of the light at any position z.

For this purpose, we will first do a strong hypothesis on the nature of the FEL source. Indeed, let us assume that our FEL source is a Gauss-Schell Model (GSM) one [57]. A GSM beam is characterized by a Gaussian transverse profile all along the propagation. At the source position, the intensity can be written as:

$$I(x, z = 0) = I_0 e^{-\frac{2x^2}{w_0^2}}, \tag{II.7}$$

where $w_0 = 2\sigma_x(z = 0)$ is the waist size. A GSM beam is also characterized all along the propagation by a Gaussian profile of the coherence factor, that depends only on the distance between the considered points x_1 and x_2 (whose spatial coherence is probed). At source, it can

thus be written as follows:

$$\mu(x_1, x_2, \omega, z = 0) = e^{-\frac{(x_1 - x_2)^2}{2\sigma_{\mu o}^2}}, \tag{II.8}$$

$\sigma_{\mu o}$ being the standard deviation of the distribution of the degree of coherence of the beam at $z = 0$.

In the beginning of the 1980s, many studies have been done concerning the propagation of the cross-spectral density [58]. For a GSM beam, it has been shown [59] that it can be written as a sum of independent Hermite-Gauss modes Ψ_j, weighted by a factor β_j:

$$W(x_1, x_2, \omega, z) = \sum_{j \geqslant 0} \beta_j \Psi_j(x_1, \omega, z) \Psi_j^*(x_2, \omega, z). \tag{II.9}$$

Ψ_j are the same functions describing the TEM modes, and their expression is given, in one dimension, by:

$$\Psi_j(x, \lambda, z) = \left(\frac{2}{\pi}\right)^{1/4} \left(\frac{q_0}{2^j w_0 q(z) j!}\right)^{1/2} \left(\frac{q_0 q^*(z)}{q_0^* q(z)}\right)^{j/2} H_j\left(\frac{x\sqrt{2}}{w(z)}\right) e^{-i\frac{\pi x^2}{2\lambda q(z)}}, \tag{II.10}$$

where $H_j(x)$ are the Hermite polynomials of order j (see Appendix B), $w(z) = w_0\sqrt{1 + \left(\frac{z}{Z_r}\right)^2}$ is the beam size with $Z_r = \frac{\pi w_0}{\lambda}\left(\frac{1}{w_0^2} + \frac{1}{\sigma_{\mu o}^2}\right)^{-1/2}$ the effective Rayleigh length [60] (by analogy with a Gaussian beam) and $q(z) = z + iZ_r$ ($q_0 = q(0)$). It is interesting to note that in the case of a fully spatially coherent source ($\sigma_{\mu o} \to \infty$), Z_r becomes $\frac{\pi w_0^2}{\lambda}$ as in the case of a classical, diffraction-limited, Gaussian beam, whereas it tends to 0 for an incoherent source ($\sigma_{\mu o} \to 0$), which corresponds to a completely diverging beam. The Rayleigh range (i.e., half the distance over which the beam size $w(z)$ remains smaller than $\sqrt{2}w_0$ and considered as collimated) of a GSM beam is thus bounded by:

$$0 \leqslant Z_r \leqslant \frac{\pi w_0^2}{\lambda}. \tag{II.11}$$

The ratio $\frac{\beta_j}{\beta_0}$ giving the proportion of the function Ψ_j with respect to the function Ψ_0 is given by [61]:

$$\frac{\beta_j}{\beta_0} = \left(1 + \frac{K^2}{2} + K\sqrt{1 + \frac{K^2}{4}}\right)^{-j}, \tag{II.12}$$

where $K = \frac{\sigma_{\mu o}}{\sigma_x}$. The absolute proportion of each function is thus $\frac{1}{\sum_j \beta_j}\left(\frac{\beta_j}{\beta_0}\right)$.

Now we have almost everything for retrieving the cross-spectral density W (see Eq. II.9) at any position z. According to the previous equations, we need the waist size w_0. Since, the transverse size of the source point should approximately correspond to the transverse size of the electron bunch, we can assume $w_0 \approx 600 \ \mu m$ (in the machine configuration of the day of the experiment).

First of all, knowing w_0 we get $w(z)$ (see previously) and thus can calculate the intensity profile at any position, that is given by $I(x,z) = I_0 e^{-\frac{2x^2}{w(z)^2}}$. The dashed curve in Fig. II.13 shows this theoretical profile after $L' + L = 73.7\ m$ of propagation i.e., on the detection system used for the Young's experiment. In full line a typical measured profile without the slits inserted is drawn. The agreement is very satisfactory.
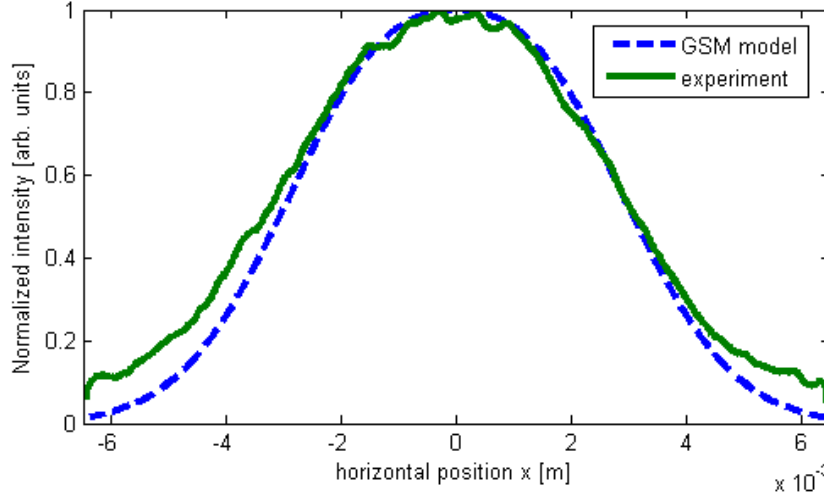
Figure II.13: Comparison of the measured intensity profile on the detection system without slits (full line) and of the one of a GSM beam at the same position (dashed line).

Then, for retrieving the theoretical degree of coherence, we need the standard deviation of the distribution of the degree of coherence at source i.e., $\sigma_{\mu o}$. According to [56], the latter parameter is given by:

$$\sigma_{\mu o} = \frac{w_0}{\sqrt{\left(\frac{2\pi w_0 \theta_x}{\lambda}\right)^2 - 1}}, \tag{II.13}$$

where θ_x is the divergence of the FEL light, measured in the previous section. In our case, we get $\sigma_{\mu o} = 152\ \mu m$.

It is now possible to compare the GSM model with the real FEL emission. At slits' position, the theoretical values of the coherence factor of a GSM beam fit very well with the results we obtained experimentally (Fig. II.14). The agreement remains quite good when considering a source size w_0 down to $400\ \mu m$, so that the uncertainty on the value of w_0 is not a big problem in this case. The GSM model does not fit with the results obtained in Fig. II.10, but in the latter the electron beam and FEL light properties (size, divergence) were also probably different. It would be interesting to do a systematic study of the agreement between experimental results and predictions for a GSM beam for different machine configurations.

Table II.2 gives the proportion of each Ψ_j function participating to the cross-spectral density function. We considered a total number of 10 functions: on this basis, the first five Hermite-Gauss functions (j from 0 to 4) include 93% of the total contribution.
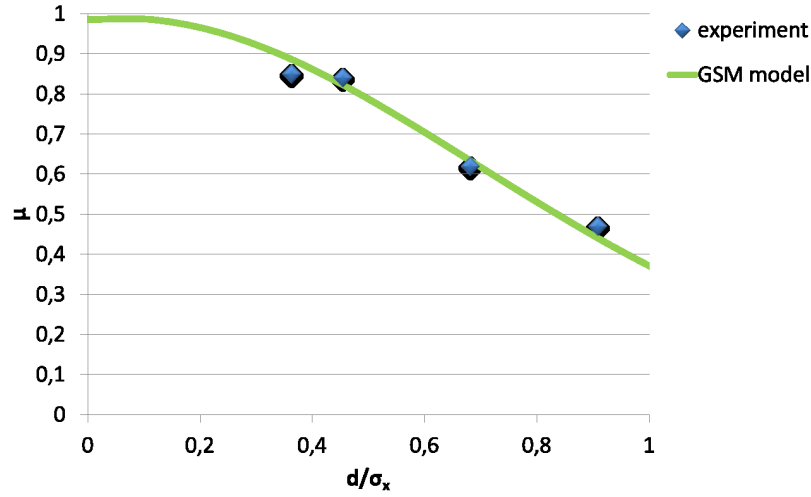
Figure II.14: *Comparison between the degree of coherence characterized experimentally (losange markers, see Fig. II.9) and theoretical prediction assuming that the FEL emission is a GSM beam.*

function number j	contribution $\frac{1}{\sum_j \beta_j}\left(\frac{\beta_j}{\beta_0}\right)$
0	40%
1	24%
2	15%
3	9%
4	5%

Table II.2: *Contribution of the first five Hermite-Gauss functions to the cross-spectral density of the FEL light considered as a GSM beam.*

Since the Ψ_j functions contribute independently to the cross-spectral density (see Eq. II.9), a high number of functions leads to a decrease of the spatial coherence, whereas the presence of a single function corresponds to a fully spatially coherent emission. This is shown in Fig. II.15, where the coherence factor decreases towards the edges of the spot when the number of Ψ_j functions in the decomposition of W is not unity.

As a final remark, we can notice that the transverse intensity profile can also be retrieved (instead of directly calculated by $I(x,z) = I_0 e^{-\frac{2x^2}{w(z)^2}}$) through the properties of the coherence functions: since $W(x_1,x_2,\omega,z) = FT^{-1}[\Gamma(x_1,x_2,\tau,z)]$ and the average intensity is $< I(x,z) >= \Gamma(x,x,0,z)$, we get that:

$$< I(x,z) >= \sum_j \beta_j FT^{-1}\left[|\Psi_j(x,\lambda,z)|^2\right]. \tag{II.14}$$

In the case where W is described by a single function Ψ_0, the intensity is thus a TEM_0 mode i.e., a Gaussian beam, that is fully coherent: we retrieve what we said previously.

The conclusion of this section is very simple: in the conditions of the measurements that we

Figure II.15: *Degree of coherence as a function of the relative slits' separation for a GSM beam whose cross-spectral density is described with only $\Psi_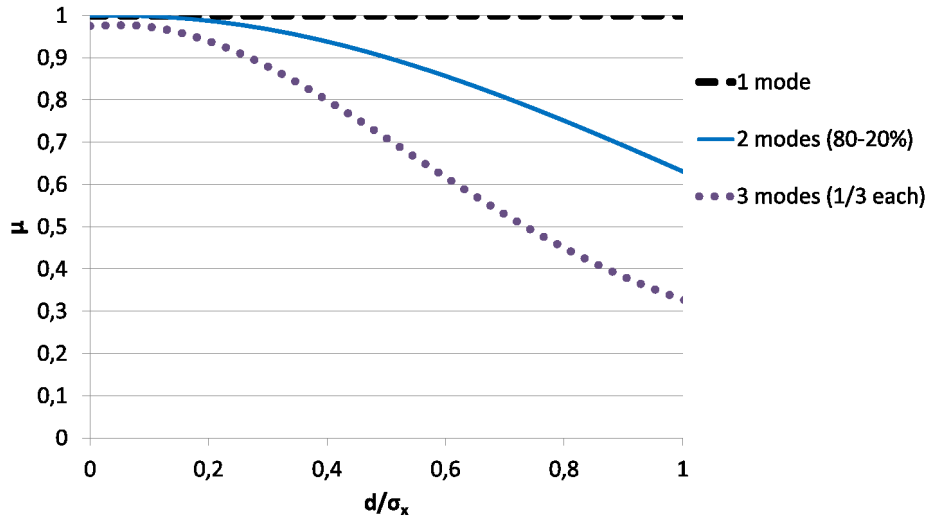0$ (dashed line), with 80% of Ψ_0 and 20% of Ψ_1 (full line) and the sum of one third of Ψ_0, one third of Ψ_1 and one third of Ψ_2.*

carried out for the Young's experiment, we find that the GSM is a very good model of the FEL emission in terms of the degree of spatial coherence μ (see Fig. II.14) and of the transverse intensity profile (see Fig. II.13) in the horizontal direction. The knowledge of the FEL spot size at the source point is the only parameter to know in order to retrieve the transverse properties of the FEL along the propagation axis, assuming Eq. II.13 is reliable.

II.1.e   Wavefront measurements

II.1.e.1   Description of the sensor

In order to complete the study of spatial characterization of our FEL light, we have performed measurements using a Shack-Hartmann wavefront sensor placed approximately $80\ m$ after the last radiator exit. Such a device provides information about the spatial phase of the FEL emission, allowing to better evaluate its aberrations than with only the intensity profiles, as we already measured in Section II.1.b. We used a *Haso* 4386 from *Imagine Optic*[TM] composed of a grid and an EUV camera located $21.1\ cm$ behind the grid (Fig. II.16a). The harmonic beam goes through the Hartmann grid, which is an array of holes of width $130\ \mu m$ and step $381\ \mu m$, producing an array of diffraction patterns on the EUV camera whose pixel size is $13\ \mu m$. The positions of the individual spot centroids are measured (Fig. II.16c) and compared with reference positions (calibrated with perfect wavefront, Fig. II.16b). Local wavefront deviations at grid position are thus inferred and allow reconstructing the whole wavefront. The intensity of the measured diffraction peaks directly provide the transverse intensity distribution of the measured beam at the grid position, at the sampling rate of the grid.

One has to take care that very strong aberrations cannot be detected if they induce more
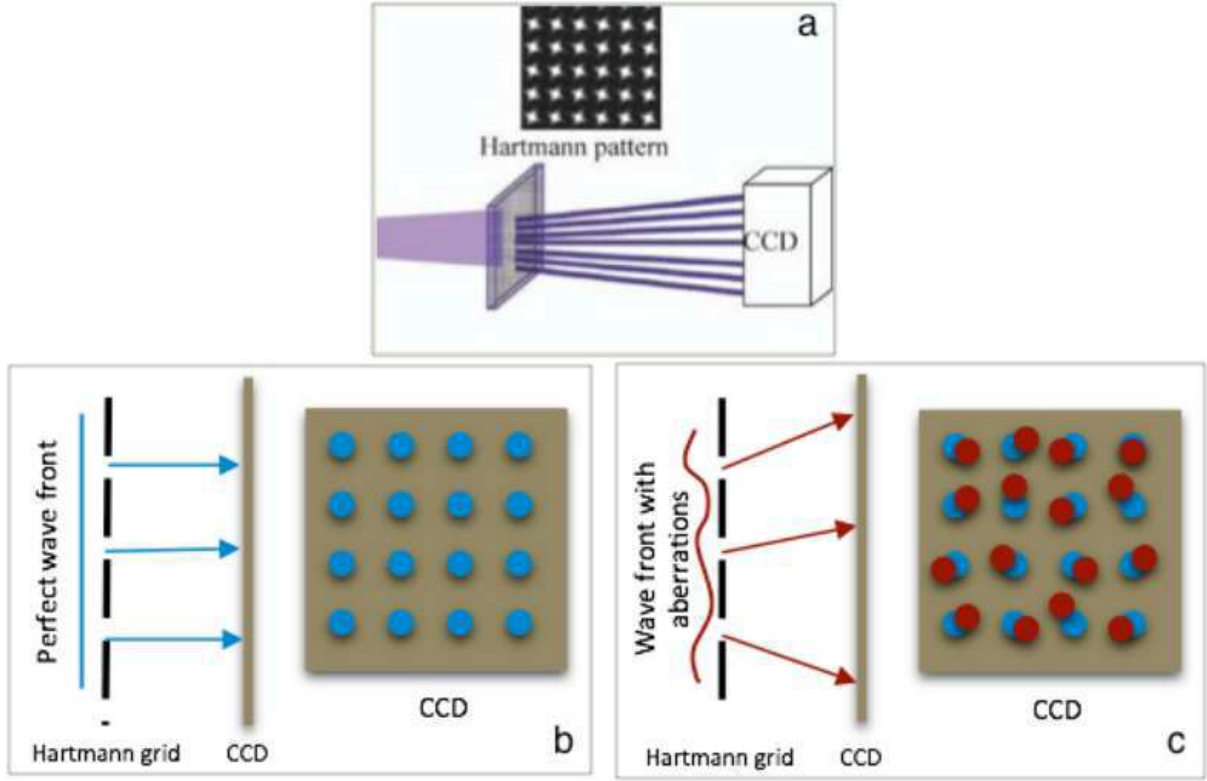
Figure II.16: Description of the Hartmann type wave front sensor. (a) The target beam goes through the Hartmann pattern grid, which is an array of holes, and projects onto the XUV camera behind. The XUV camera detects the sampled intensity of the beam. (b) The wavefront sensor should be calibrated with a perfect beam before first use. The positions of the beamlets on the camera will be registered as reference positions (blue points). (c) The wave front is reconstructed from the measured local shift (red points) of each beamlet compared to the reference positions. (courtesy of X. Ge)

than 2π-jumps in the wavefront profile. Moreover, completely incoherent light cannot be analysed since it corresponds to fluctuations of the wavefront. We should not face this problem since we just evidenced that, at least spatially, the light from FERMI@Elettra exhibits good coherence properties and the intrinsic effect of seeding should provide good temporal coherence to the FEL emission.

II.1.e.2   Experimental results

Here we present results that have been taken for an FEL emission centered at 20 nm i.e., the 13th harmonic of the seed. In Fig. II.17, we can see the image of the array of diffracted patterns collected on the CCD. The positions of the diffraction peaks is compared with the ones of a plane wave in order to evaluate the local wavefront tilts at the different positions on the grid and to reconstruct the whole wavefront. In the right image of Fig. II.17, we simulated the expected diffraction pattern of a plane wave at 20 nm, which seems in good agreement with the measured ones.

Figure II.18 shows the retrieval of the Haso software for the intensity spot (left image) and the wavefront (right image). On the intensity spot, we can see a ring surrounding the central
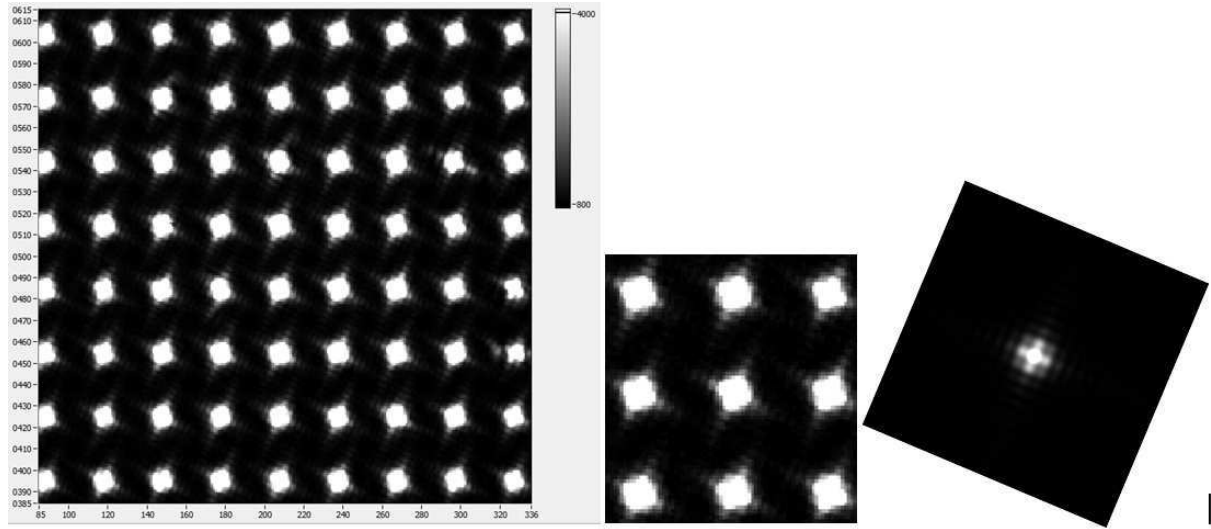
Figure II.17: Image collected on the camera of the wavefront sensor (left), zoom on a selection of pixels (center) and simulation of the expected pattern (right).

lobe. At first sight, we could say that the FEL emission is composed of mainly two modes, a nearly-Gaussian one and an annular one. In the wavefront (right image), we see that there are very small distortions. They in fact appear, mainly as a phase jump, in the area corresponding to the ring of intensity. The standard deviation of the overall wavefront surface is approximately equal to $\frac{\lambda}{6}$. When optimizing the FEL emission in order to get rid of the ring, we were able to reach wavefront amplitudes of less than $\frac{\lambda}{7}$. These are very good results, of the order of magnitude of what was found in [62] on a HHG beamline at CEA Saclay (see Section II.2). Our measurements, which are only preliminary, characterize a beam only twice far from the diffraction limit (see Chapter I) according to the Marechal's criterion [63] stating that a beam is diffraction limited if its wavefront amplitude presents a standard deviation of $\frac{\lambda}{14}$.
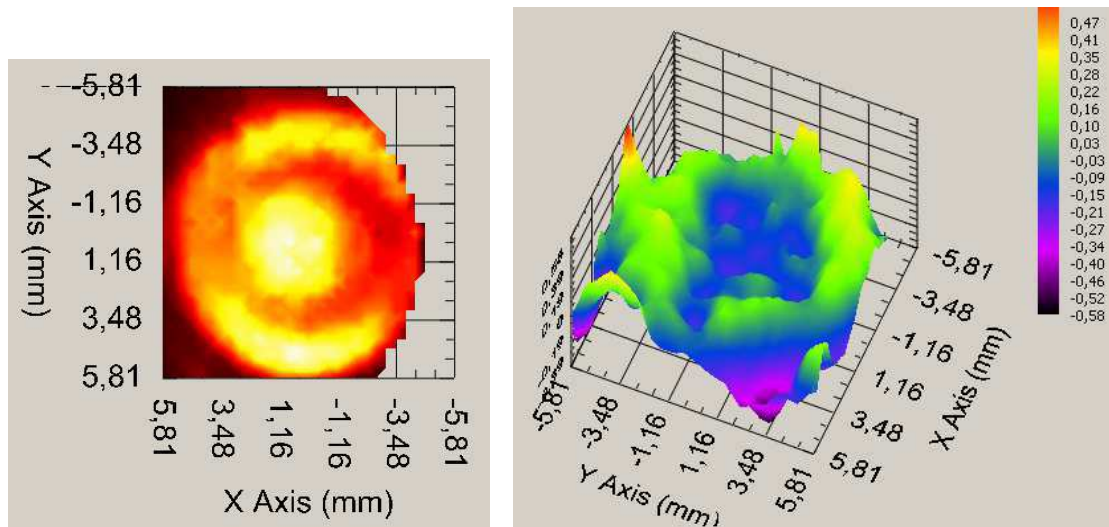
Figure II.18: Output of the Haso software: FEL spot normalized to the maximum intensity (left) and wavefront given in units of the wavelength of FEL emission (right) i.e., $\lambda = 20\ nm$.

The presence of the surrounding ring in the FEL emission is well understood. It is related to a mismatch of the undulator tuning. Indeed, the full resonant condition of the undulator is in fact [20]:

$$\lambda = \frac{L_U}{2\gamma^2}\left(1 + \frac{K^2}{2} + \gamma^2\theta^2\right),$$

(II.15)

where θ is the emission angle. According to that, if K is not well tuned, the emission will be done off-axis to respect the resonance condition. Hence, we have been able to generate completely annular FEL radiation only by changing the undulator's tuning.

After this study of the transverse properties of the FEL emission at FERMI@Elettra, I will now present a work carried out at CEA Saclay where the effect of spatial quality of the driving laser on the HHG properties is analysed.

II.2   HHG optimization through spatial improvement of driving laser

II.2.a   Motivation and state of the art

The motivation of the present work was the general optimization of the generation of high-order harmonics in loose-focusing geometry [65, 66] on the beamline of the chirped-pulse amplified (CPA, [64]) LUCA facility dedicated to experiments of coherent diffraction imaging [67, 68]. In HHG, homogeneous intensity distribution and low wavefront distortion of the driving laser are crucial for the efficient and coherent macroscopic construction of the harmonic beam. This is especially true in the loose-focusing geometry where the interaction occurs on a long distance (some centimeters) compared to the wavelength of the fundamental beam ($795\ nm$). This is why, for optimizing the HHG, it has been decided to perform an optimization of the spatial quality of the driving laser provided by the LUCA source. Indeed, the importance and the effects of the spatial quality of the driving beem, managed by different techniques, have already been stressed in [69, 70, 71].

As it is often the case for a high-energy Ti:Sapphire laser facilities, the IR beam suffers from bad spatial quality. Aberrations resulting from anisotropic thermal dissipation in the amplification media [72], self-phase modulation during propagation of such intense pulses in the air or in materials [73], intracavity beam distortions [74] and imperfections in optical components involve a deterioration of both wavefront and transverse intensity profile. Hence, the laser beam is not usually very close to a TEM_{00} mode. A common technique to recover a good spatial beam quality is to focus the laser through a pinhole. This operates a spatial Fourier transform [76] of the field in the plane of the pinhole where there is a one-to-one mapping between transverse position and spatial frequencies, and allows for filtering the high spatial frequencies, blocked

by the pinhole [77]. However, the beam keeps its low spatial frequencies distortions and a significant amount of energy may be lost. Moreover, unless a specific conic pinhole is used [78], any misalignment of the high-power laser beam can permanently damage the pinhole. Other or complementary techniques include the use of a saturable absorber [79] or a deformable mirror [80] and diffraction from Bragg gratings [81]. Moreover, active filtering can be achieved through nonlinear processes like second harmonic generation via a nonlinear crystal [82] or a plasma mirror [83] and cross-polarized wave generation (XPW) [84]. It should be noticed, however, that these active filters are not useable with chirped pulses in CPA laser systems.

A scheme based on the propagation of an electromagnetic wave in a cylindrical dielectric waveguide has been considered. In the community of ultrafast lasers, studies of propagation into such kind of waveguides have been initiated by the post compression technique used to generate sub-10 fs laser pulses, where a mJ-level femtosecond laser beam propagates over a short distance in a capillary filled with gas [85]. The electromagnetic field of the laser beam can be expressed as a linear superposition of the modes specific to this waveguide. By choosing appropriate parameters, the beam couples preferentially into the LP_{01} (EH_{11}) mode, whose specifications will be detailed later on. The properties of this mode are very similar to the TEM_{00} ones in free space. Other guided modes suffer from higher attenuation. Therefore, if the capillary is sufficiently long and has a sufficiently small core diameter, a modal filtering is made on the laser beam. Thus, a setup aimed at spatial quality improvement of a laser beam can be designed by propagation in a carefully chosen waveguide. Modal filtering techniques have already been used in domains other than ultrafast lasers such as, for instance, stellar interferometry [86].

The efficiency of such a setup for HHG optimization has already been demonstrated in [87]. Here we test this technique in a slightly different configuration; in particular, the filtering stage will be placed before compression of the IR pulse and harmonics will be generated in a long interaction medium, instead of a short gas jet. Moreover, the originality of our work relies on comprehensive theoretical, experimental and numerical studies of the quality of the IR beam over its propagation along the system, which allows a better understanding of the HHG enhancement.

II.2.a.1 Description of the LUCA facility

Figure II.19 summarizes the principle of the LUCA laser chain on which has been carried out the experiment. The Ti-Sapphire oscillator delivers nJ-level pulses with temporal Gaussian profile of duration $30\ fs$ FWHM, at a repetition rate of $76\ MHz$. Pulses are selected at a repetition rate of $20\ Hz$ and sent to an Offner stretcher [88], so that the pulses are lengthened to a duration of about $200\ ps$. A regenerative amplifier allows the pulses to reach a mJ level. To provide higher energies, two successive multipass amplifiers [89] are used and the pulse are finally compressed, so that their final characteristics are a repetition rate of $20\ Hz$, an FWHM

duration of $50\,fs$, a maximum energy of $50\,mJ$ at a central wavelength of $795\,nm$.   A sketch
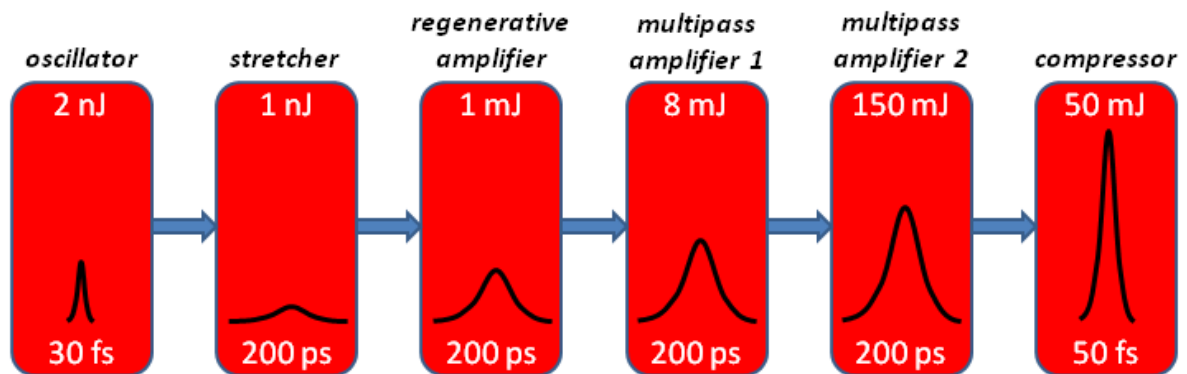
Figure II.19: Description of the LUCA source. Only a fraction of the energy ($8\,mJ$ over $20\,mJ$ effectively available) is used after the first multipass amplifier, the other fraction being sent to another beamline. The stretcher and the compressor have transmissions of the order of $30-50\,\%$.
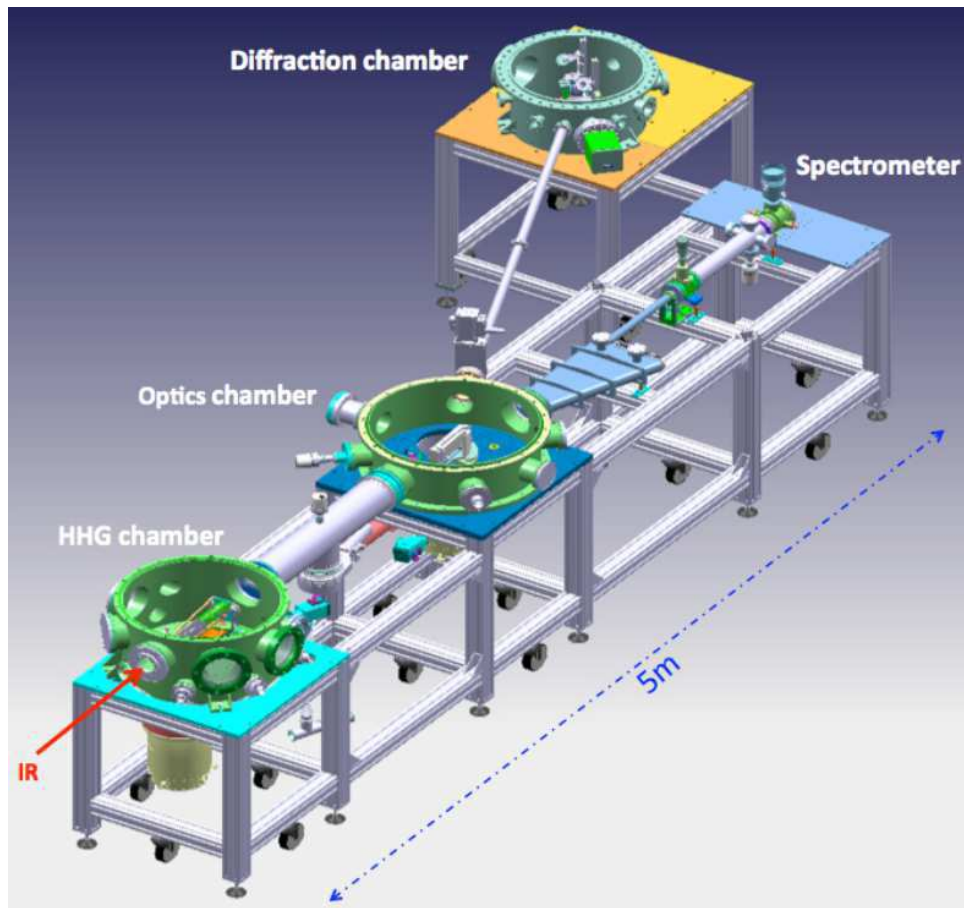
Figure II.20: Drawing of the harmonic beamline. The arrow at the left bottom indicates the beam propagation direction.

of the beamline is showed in Fig. II.20. The IR beam is focused by means of a lens of focal

length $5.65\,m$ into a gas cell of length variable from 0 to $15\,cm$, usually set at a value of $8\,cm$

corresponding to the optimum condition of generation. In the optics chamber, a mirror reflects the EUV light and send it either to the users chamber, called the diffraction chamber, or to a spectrometer (or other diagnostics) while most of the IR beam is transmitted and can be used for control (principally, IR beam alignment in the gas cell). The entire setup is about 5 meters long.

II.2.a.2 Description of the setup

The chosen cylindrical waveguide for the modal filtering setup built on the LUCA facility is a straight hollow-core fiber in silica with a core radius $a = 125 \ \mu m$ and a length $L = 30 \ cm$. The

Figure II.21: Beamline layout and modal filtering setup. The picosecond laser beam, of radius $3.5 \ mm$, is focused into the fiber, of core radius $a = 125 \ \mu m$ and length $L = 30 \ cm$, by means of lens 1 ($f_1 = 750 \ mm$, for which a maximum fiber transmission has been found). In order to adjust the coupling conditions, the fiber is mounted on $x - y$ translation stages an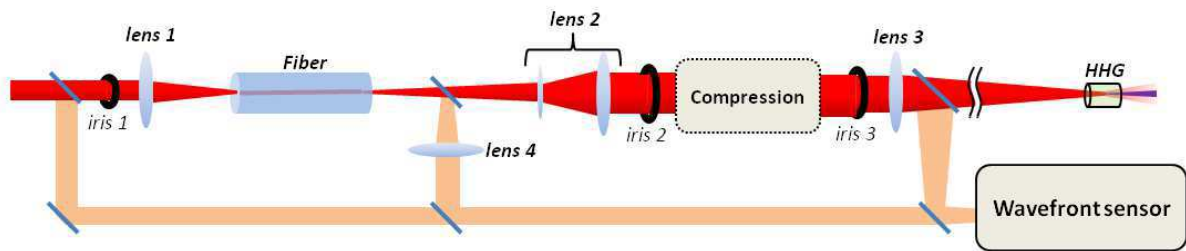d the lens on a z translation stage. A control loop has been implemented for correcting the beam pointing at the fiber entrance. By means of a set of two lenses forming lens 2, the output beam is collimated to a radius of $16 \ mm$ and sent to the compression stage, where pulses reach the femtosecond level. The beam is then used for a HHG experiment, being loosely focused by lens 3 ($f_3 = 5650 \ mm$) into a gas cell filled with argon. Mirrors and lens 4 ($f_4 = 1250 \ mm$, positioned at $1150 \ mm$ of the fiber output) enable to send the beam to the wavefront sensor with a size adapted to its entrance pupil. Three irises are placed at the front focal plane of lens 1, lens 2 and the back focal plane of lens 3.

overall setup implemented on the LUCA source is shown in Fig. II.21. The fiber has been put under vacuum (at a pressure of the order of $10^{-3} \ mbar$) and the whole modal filtering setup placed before the compressor (see Fig. II.19) in order to reduce nonlinear effects due to the propagation of such an intense beam in the air (indeed, even before compression, intensities of the order of $10^{16} \ W/cm^2$ are reached when the beam is focused at the entrance of the fiber). The latter choice is also motivated by the easier degradation of optical elements when the laser is operated in a femtosecond (high-power) regime. Similarly, this will to avoid non-linear effects into the core of the waveguide and its degradation leads us to choose a hollow-core fiber.

The central point of the study relies on the measurement of the spatial phase and transverse intensity distribution of the laser by means of a Shack-Hartmann wavefront sensor (see principle in Section II.1.e.1 – the main difference with the EUV sensor is that the grid of holes is replaced by a grid of microlenses, that could not be used with EUV wavelengths). We used a *Haso* 64 from *Imagine Optic*^{TM}with a pupil of $1.5 \ cm$ and a discretization step of $186 \ \mu m$. The complete determination of the electric field in one plane provided by such an analyser allows calculating

the electric field in any other plane by means of the theory of wave propagation in free space in the paraxial approximation [90]. The propagation has been done by two (cross-checked) methods: with "home-made" calculations and with the professional software *FRESNEL*®. We measured the wavefront and intensity distributions with the sensor at three different positions: at the front focal planes of lenses 1, 3 and at the back focal plane of lens 4 (see Fig. II.21). In every case, the tilt and curvature (quadratic phase term due to beam focusing) of the wavefront were taken into account during data analysis. One has to note that the sensor has a threshold at $\frac{1}{e^2}$ of the maximum fluence: below this value, no information is collected. This has an impact on the accuracy of the simulation of the experimental results since information of the input beam is lacking.

In addition, direct measurements of intensity patterns have been performed around the waist of the focused beam, before and after the fiber. The collected data enabled the calculation of the M^2 factor [91]. The measurements were done using a beam analyser and the M^2 calculated following the standard technique that considers the measurements of the second moment widths of the beam [92, 93]. The second moment width, corresponding to four times the standard deviation σ_r of the transverse intensity distribution at a given position z along the propagation axis, is the beam diameter definition used in the following. For a Gaussian beam, it matches the parameter w ($2w = 4\sigma_r$, including 86.5% of the beam energy).

II.2.b Theory

II.2.b.1 Mode structure in the fiber

A clear description of the modes of a cylindrical dielectric waveguide is difficult to find in the literature. This is why it is useful to present it before coming to experimental results. This theoretical part will also allow to model the coupling and the propagation of the laser field into the fiber and to give a first insight of the expected improvements of modal filtering on the laser beam.

The general theory of the propagation of electromagnetic waves in a cylindrical waveguide was developed a long time ago and general solutions can be found in Stratton [94]. In 1961, Snitzer [95] studied the characteristics of cylindrical metallic waveguides and cylindrical dielectric waveguides. In 1964, Marcatili [96] was the first to give the expressions of the modes of a hollow dielectric cylinder when the core radius is much larger than the wavelength. In [97], Degnan gave a more accurate definition of the hybrid modes and proposed to call LP_{nm} modes the set of linearly polarized eigenmodes. These modes are of interest for us since the LUCA source is also linearly polarized.

Within the fiber core ($r \leqslant a$), the transverse characteristics of the LP modes can be written as:

$$LP_{nm}(r,\theta) = A_{nm}J_n\left(\frac{u_{nm}r}{a}\right)\left\{\begin{array}{c}\cos(n\theta)\\\sin(n\theta)\end{array}\right\}, \tag{II.16}$$

with $n \geqslant 0$ and $m \geqslant 1$. J_n is the Bessel function of the first kind and u_{nm} is the mth solution of the equation $J_n(r) = 0$. For $n \geqslant 1$, the modes can be separated in two groups, according to the dependence either on the sine or on the cosine, giving the direction of the nodal planes. They will be respectively noted LP_{nm}^{sin} and LP_{nm}^{cos}. A_{nm} are the energy normalization constants so that $\int_0^a \int_0^{2\pi} |LP_{nm}|^2 r\,dr\,d\theta = 1$ (the integration is done over the transverse fiber core area i.e., πa^2). It gives:

$$A_{nm} = \frac{1}{aJ_{n+1}(u_{nm})} \sqrt{\frac{\kappa_n}{\pi}}, \tag{II.17}$$

with $\kappa_n = \begin{cases} 1 \ (n=0) \\ 2 \ (n \neq 0) \end{cases}$.

The family of LP modes is very similar to the Laguerre-Gauss modes in free space, as shown on Fig. II.22. The LP_{01} mode is quite close to that of a Gaussian beam; this is the reason one
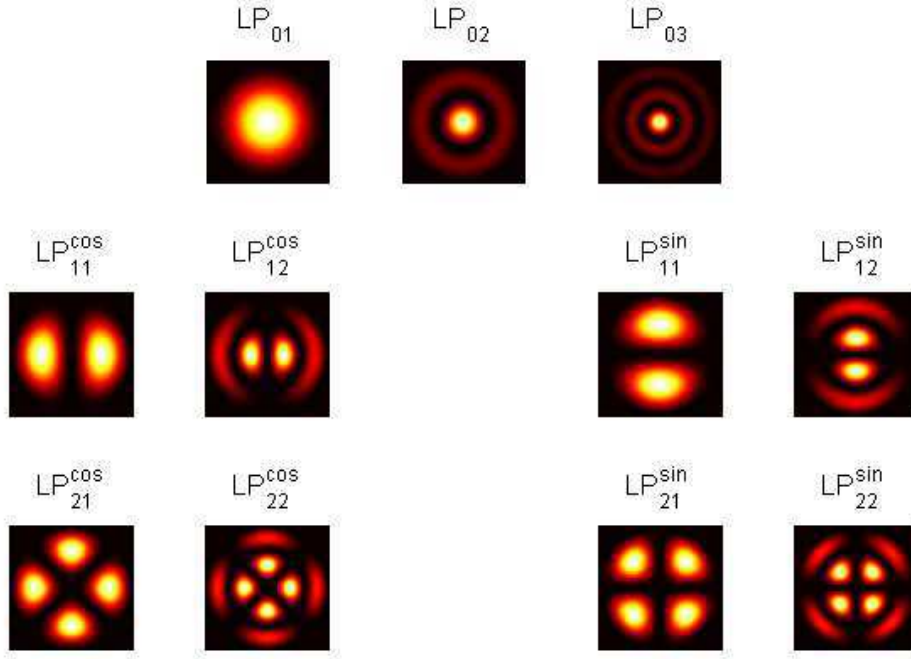
Figure II.22: Patterns of the first LP_{nm} modes. The upperscript cos (respectively sin) stands for the cosine (respectively sine) dependence in Eq. II.16.

normally tries to couple a maximum of the energy in this mode. Its behaviour in the near field and the far field (free space) will be more accurately detailed later. The fraction of the electric field injected at the fiber entrance, described by the transverse function $E_{laser}(r,\theta)$, that will couple into a given mode is given by [98]

$$P_{nm} = \frac{|\eta_{nm}|^2}{\int_{-\infty}^{+\infty} \int_0^{2\pi} E_{laser} E_{laser}^* r\,dr\,d\theta}. \tag{II.18}$$

The η_{nm} coefficients are equal to:

$$\eta_{nm} = \int_0^a \int_0^{2\pi} E_{laser} LP_{nm} r \, dr \, d\theta. \tag{II.19}$$

Inside the fiber, every linearly polarized electromagnetic wave propagates as a linear combination of the LP_{nm} modes [99]. That is to say, for $0 \leqslant r \leqslant a$ and $0 \leqslant z \leqslant L$, the total electric field can thus be written as:

$$E_{fiber}(r, \theta, z, t) = \sum_n \sum_m \eta_{nm} LP_{nm}(r, \theta) \cdot e^{-\alpha_{nm}z} \cdot e^{i(\beta_{nm}z - \omega t)}, \tag{II.20}$$

where α_{nm} are the attenuation coefficients of each mode and $\beta_{nm}z$ the phase that they acquire along the propagation. These parameters are defined by:

$$\alpha_{nm} = \left(\frac{2\pi u_{nm}}{\lambda} \right)^2 \frac{1}{a^3} \frac{\varepsilon + 1}{2\sqrt{\varepsilon - 1}}, \tag{II.21}$$

and:

$$\beta_{nm} = \frac{2\pi}{\lambda} - \frac{\lambda}{4\pi} \left(\frac{u_{nm}}{a} \right)^2. \tag{II.22}$$

λ is the wavelength of the field propagating through the fiber and ε the dielectric permittivity (we consider here real valued ε and $\frac{\varepsilon + 1}{2\sqrt{\varepsilon - 1}}$, conditions which are always fulfilled for dielectric waveguides). The mode with smaller attenuation (smaller α_{nm}) is called the fundamental mode of the waveguide.

In this section, we omitted the vector sign for a matter of simplicity: the LUCA source is vertically polarized and we consider the LP modes matching this polarization. Moreover, outside the fiber core, we assume that the energy of the modes is zero due to the absorption of the cladding.

II.2.b.2 Mode coupling and propagation

We wish to favour the LP_{01} mode into our modal filtering setup. The first step is to couple as much energy as possible into it at the fiber entrance. The fraction of energy of the input laser field E_{laser} that is coupled into LP_{01} is given by P_{01} (see Eq. II.18). As a first approximation, we will consider a Gaussian shape $E_{laser} = e^{-\frac{r^2}{w_0^2}}$ of the input laser field in order to have a first insight of the beam size that is required for maximizing P_{01}. Figure II.23 gives P_{01} as a function of the w_0 parameter of the input Gaussian profile. This curve tells us that a maximum coupling into LP_{01} is found for a Gaussian beam size of $w_0 = 0.645a \approx 81\ \mu m$, for which 98 % of the input energy is coupled into LP_{01}.

Table II.2.b.2 gives the attenuations of each mode calculated with Eq. II.21. It tells us that LP_{01} is the fundamental mode of the chosen waveguide i.e., it is the less attenuated into the
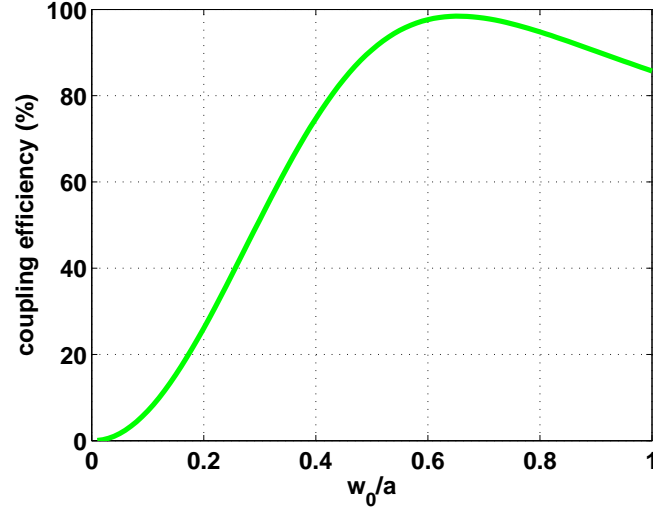
Figure II.23: Proportion of the energy of a Gaussian beam, focused at the fiber entrance, coupled into the LP_{01} mode as a function of its size w_0, relative to the core radius a.

n \ m	1	2	3
0	2.1	10.9	26.8
1	5.2	17.6	37.0
2	9.4	25.3	48.3
3	14.5	34.1	60.5
4	20.6	43.8	73.8
5	27.5	54.4	88.1

Table II.3: Attenuation in % of the LP_{nm} modes after the $30\ cm$ of propagation into the fiber.

fiber so that the proportion of LP_{01} is increased at the fiber output. From this data it is clear that the good coupling into the mode of interest is very important: the proportion of LP_{01} that is attenuated is very low (2.1 %); nevertheless, some other modes like LP_{02} or LP_{11} have also a quite low attenuation. A possibility to favour even more LP_{01} would be to lengthen the fiber or reduce its core radius (see Eq. II.21).

At the output of the fiber, the electric field propagates in free space and lens 2 (see Fig. II.21) is used to collimate the beam. It is then important to know the behaviour of the beam, and especially of LP_{01}, both in the near and the far field. As was already discussed by Degnan [97], a small modulation appears in the central part of the LP_{01} mode in the near field for planes where $\frac{r^2}{\lambda}$ is close to an integer value. This phenomenon is also encountered with a Gaussian beam truncated by a circular aperture. The expression of the field in the back focal plane of a lens 2 can be obtained analytically [100]:

$$LP_{01}^{farfield}(r) = 2u_{01}a\sqrt{\pi}\frac{J_0\left(\frac{2\pi a}{\lambda f_2}r\right)}{u_{01}^2 - \left(\frac{2\pi a}{\lambda f_2}r\right)^2}, \tag{II.23}$$

modes	LP_{01}	LP_{02}	LP_{03}	LP_{04}	LP_{05}	LP_{06}	LP_{07}
M^2	1.12	3.08	4.93	6.76	8.58	9.08	38.6
Transmission through iris 2	99.2 %	59.1 %	6.49 %	2.96 %	1.73 %	1.15 %	0.82 %

Table II.4: First line: modes; second line: corresponding M^2 factor; third line: according to the M^2, proportion of energy transmitted through iris 2 closed at a diameter $\frac{u_{01}\lambda f_2}{\pi a}$.

f_2 being the focal length of lens 2 and the mode shape being still circularly symmetric (so that there is no azimuthal dependence in the equation). Figure II.24 underlines the similarity between the TEM_{00} and LP_{01} modes both in near (Fig. II.24a) and far field (Fig. II.24b). Calculations have been done using Eq. II.16 and Eq. II.23. The truncature of the LP_{01} mode in the fiber (Fig.
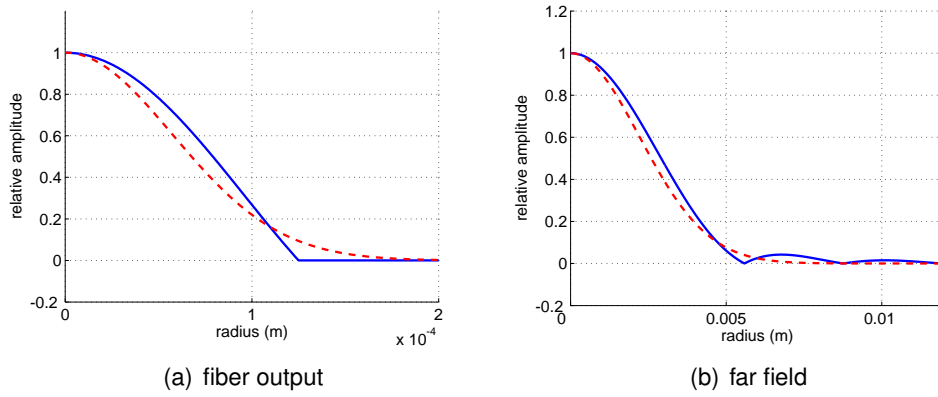

(a) fiber output

(b) far field

Figure II.24: Comparison of amplitude profiles of a Gaussian beam of parameter $w_0 = 0.645a$ (dashed curves) and the LP_{01} mode (full line) in the fiber (a) and after 1 m of propagation in free space (b).

II.24a (full line)) is, in far field, responsible for rings surrounding the main lobe of the energy distribution. These rings can be seen on the profile of LP_{01} in Fig. II.24b (full line). To suppress this energy in the pedestal, an iris (iris 2 in Fig. II.21) of aperture diameter $\frac{u_{01}\lambda f_2}{\pi a}$, corresponding to the first zero of the energy distribution of the LP_{01} mode in the back focal plane of lens 2 (see Eq. II.23), is used. A very important point here is related to the fact that higher order modes exhibit a higher divergence in the far field. This can be seen from the calculated values of the M^2 factor for the LP_{0m} given in Table II.2.b.2. To calculate the M^2 of each mode, we propagated it numerically and measured its divergence, whose ratio with the divergence of a Gaussian beam with same size at focus gives the M^2. In the last line of the table, we show that the use of iris 2 modifies the transmissions of the different modes. These results demonstrate that part of the efficiency of the modal filtering is linked to the spatial filtering in the far field. It can be noted also that, apart from the filtering of the other modes, the aperture size of the iris also improves the

quality of the beam in the back focal plane of lens 3 (see Fig. II.21).

II.2.c Experimental results

II.2.c.1 Laser beam analyser measurements

Figure II.25 shows the beam analyser measurements at the waist of the beam. Before the fiber, the beam is elliptic and "twisted" along the longitudinal axis (typical of a general astigmatic beam), while after the fiber astigmatism and high spatial frequencies are mainly suppressed (see the profiles in Fig. II.25b), so that the transverse beam profile is quasi-Gaussian. As pointed out in the theoretical part, an optimization of the beam quality is obtained, additionally to the propagation through the fiber, by using iris 2 with a diameter corresponding to the first zero of the LP_{01} mode. These direct characterizations evidence an improvement of the spatial quality of the beam in near-field (which is, in this case, the focus of a lens of short focal length). At the entrance of the fiber, the beam is estimated to be 1.5 times larger than the one measured in Fig. II.25a i.e., having a radius of $142.5\ \mu m$. This value, corresponding to a maximum transmission into the fiber, and thus probably to a maximum coupling into LP_{01}, is larger than the core radius. On the other hand, we calculated (see Fig. II.23) for a Gaussian beam that the optimum radius for a maximum coupling into LP_{01} is much smaller i.e., $81\ \mu m$. This shows that the beam cannot be considered as Gaussian at the entrance of the fiber: even if in Fig. II.25a the intensity distribution does not exhibit strong modulations, the phase is probably distorted, which has a direct impact on the coupling.
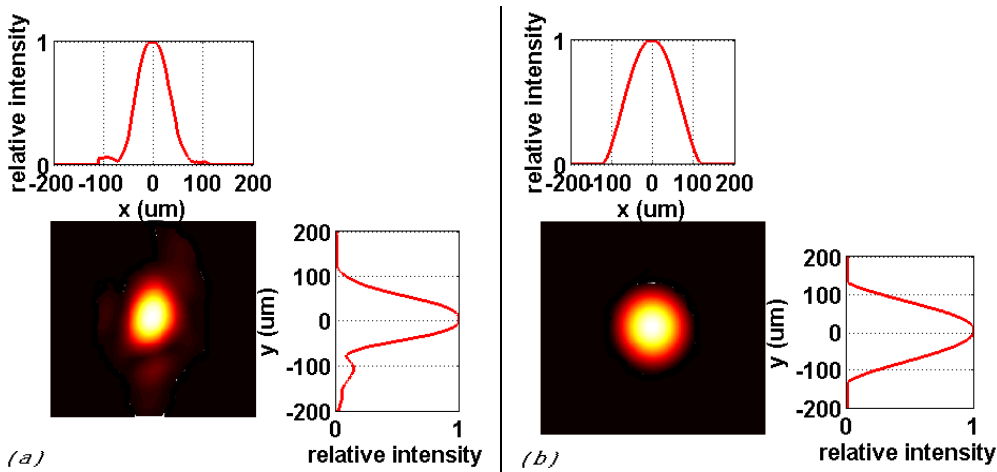
Figure II.25: Spot of the IR beam at focus, measured by the beam analyser before (a) and after (b) modal filtering. For (a), the measurement has been done at the focus of a lens of focal length $500\ mm$ placed before lens 1. For (b), the measurement has been done by imaging the output of the fiber by means of a 4f-system. The images have been cropped at a background level for the M^2 calculation, which can be seen on (a) with the non-negligible amount of high spatial frequencies.

Figure II.26 shows the evolution of the diameter of the measured beam spots around the waist and the one of a Gaussian beam with same width at focus. The ratio of their divergences

wavefront amplitude	before the fiber	after the fiber
peak-to-valley [nm]	414.75 ± 17.94	82.84 ± 13.33
RMS [nm]	66.13 ± 2.30	13.80 ± 1.87

Table II.5: *Measurements of the wavefront amplitude of the laser beam before and after modal filtering. Peak-to-valley and RMS amplitudes of the wavefront are indicated with the standard deviation of the series of measurements.*

corresponds to the M^2 of the beam. It is equal to 2.1 before the fiber and 1.4 after it. As a comparison, the M^2 of LP_{01} that has been previously calculated is 1.12. This difference underlines the presence of residual high-order modes in the output beam. The calculated radius of the laser beam at the output of the fiber, by means of the propagation laws of Gaussian beams corrected by the M^2 factor [90], is estimated to be 105 μm.
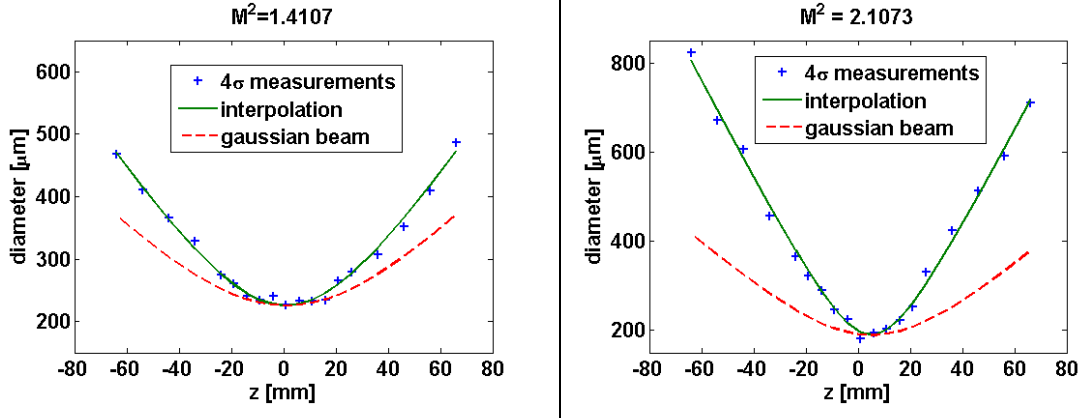

Figure II.26: *Evolution of the beam diameter (geometrical mean of diameters measured in x and y directions) along the propagation axis, in front of (left) and behind (right) the fiber. Crosses are experimental values and full-line curves their interpolations. The dashed curve represents the diameters of a Gaussian beam of same size at focus.*

II.2.c.2 Laser characterization at fiber stage

I now present characterizations of both intensity and wavefront (equivalent to amplitude of the electric field and spatial phase) of the beam, first through Shack-Hartmann sensor's measurements. In the front focal plane of lens 1, the beam intensity distribution has no cylindrical symmetry and the wavefront is distorted (left side of Fig. II.27). The transverse intensity is roughly super-Gaussian with three hot regions, corresponding also to peaks in the wavefront profile. After filtering (right side of Fig. II.27), the wavefront exhibits a nearly flat profile. The intensity distribution has a quasi-perfect cylindrical symmetry and a nearly Gaussian profile.

From Table II.5, it can be seen that the peak-to-valley and RMS (root-mean square) values are divided by a factor of ≈ 5 after the propagation in the fiber, giving values of nearly $\frac{\lambda}{10}$ peak-to-valley and $\frac{\lambda}{58}$ RMS.

From these measurements, we made a simulation of the modal filtering using the theory discussed previously: the wavefront and intensity measurements are used to calculate the electric
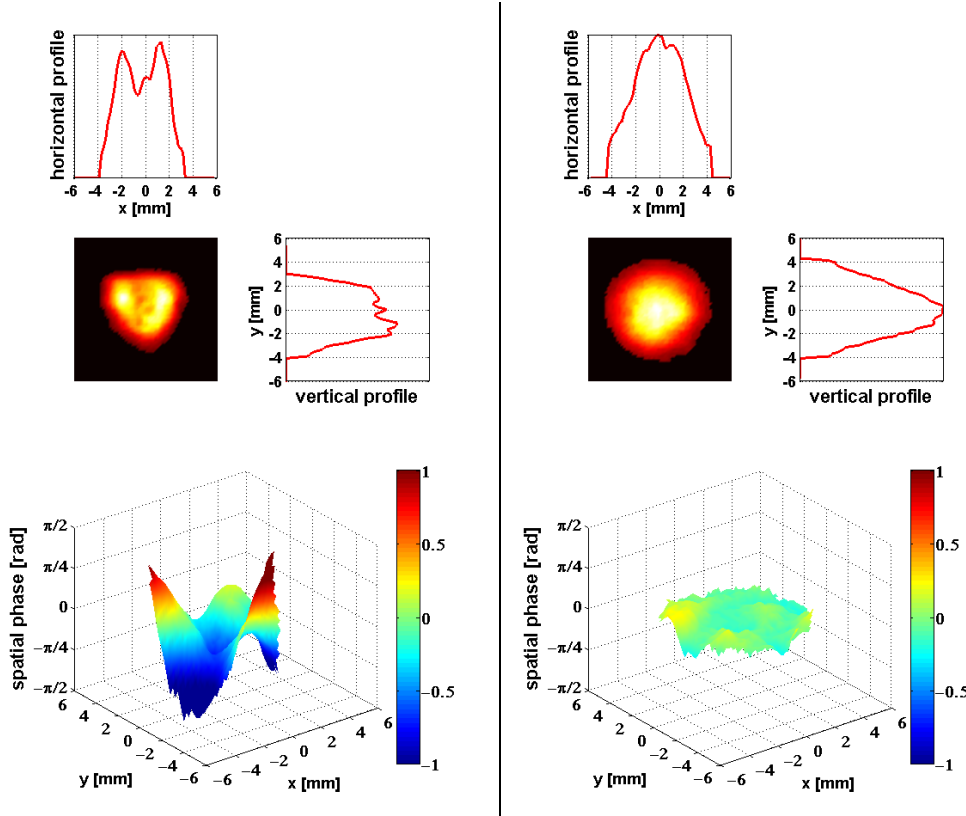
Figure II.27: Shack-Hartmann measurements: intensity and wavefront at the front focal plane of lens 1 (left) and the back focal plane of lens 2 (right).

field at the input of the fiber (Fig. II.28, left panel), by operating a spatial Fourier transform of the measured field; the propagated field at the output of the fiber is then decomposed on the fiber modes by means of Eq. II.18; each mode is then propagated through the fiber taking into account its attenuation coefficient (see Eq. II.21) so that the field at its output (see Eq. II.20, $z = L$) can be computed (Fig. II.28, center panel); finally, by operating a spatial Fourier transform, we calculate the intensity and wavefront of the beam at the back focal plane of lens 2 (Fig. II.28, right panel). The result is in quite good agreement with the measurements (Fig. II.27, right panel). The cut of the Shack-Hartmann measurements taken as input for the simulations (Fig. II.27, left panel) has non-negligible effects. In these high-spatial frequencies that are not taken into account, information about the aberrations (e.g., astigmatism) and high-order modes (which are more divergent, and thus more present in the high-spatial frequencies) is lost. Moreover, according to the diffraction theory, this sharp cut is the source of rings in the intensity pattern of the field propagated at the fiber entrance – which is not in agreement with what is experimentally obtained. In order to avoid this issue, we have to smooth the Shack-Hartmann measurements. The consequence is thus that, in comparison with what was observed with the direct measurement of the beam analyser (see Fig. II.25a), the intensity shape at the fiber entrance given by our simulations is "cleaner", even if the astigmatism is evident in the wavefront shape (Fig. II.28, left panel). This involves an error on the calculation of the P_{nm} coefficients. In the propagation
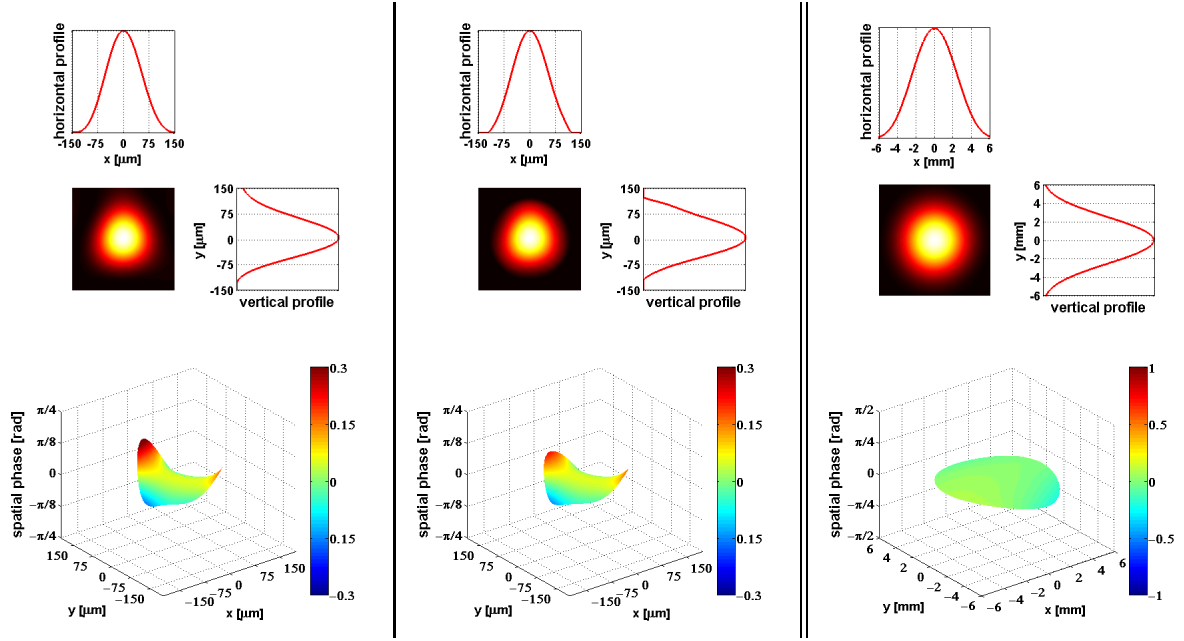
Figure II.28: Simulations of beam propagation. Left: fiber input (back focal plane of lens 1); center: fiber output; right: back focal plane of lens 2. The wavefront is displayed only where the intensity is higher than $\frac{1}{e^2}$ of the maximum intensity.

at the output of the fiber (Fig. II.28, center panel), the wavefront distortion is reduced with respect to the one at the entrance (Fig. II.28, left panel) and, overall, is quasi-inexistant for the propagation far-field (Fig. II.28, right panel).

Through those simulations of beam propagation, a M^2 of 2 is calculated before the fiber, to be compared with the 2.1 value deduced from measurement with the beam analyser. At the output, the M^2 value obtained is 1.3 which is again in good agreement with the 1.4 value found in Fig. II.26. The slight differences of M^2 values deduced from direct measurements and simulations of beam propagation can again be explained by the cut of the outer part of the beam done by the Shack-Hartmann sensor that leads to the undervaluation of the fraction of high-order, more diverging, modes.

Results of the fraction of energy coupled in each mode at the fiber input i.e., the P_{nm} coefficients (Eq. II.18, E_{laser} being the field propagated at the fiber entrance and LP_{nm} given in Eq. II.16), and the fraction of each mode at the fiber output calculated according to each mode attenuation along the fiber (Eq. II.21) are collected in Table II.6. The good coupling proportion into LP_{01} and its low attenuation with respect to higher-order modes (see Table II.2.b.2) result in an output beam mostly composed of this mode: a proportion of more than 90 % is found. From these results, the theoretical transmission through the fiber is ≈ 83 %, while a maximum of 78 % has been measured experimentally. The slight difference stems probably from the over-valuation of P_{nm} for lowest-order modes due to the Shack-Hartmann cut, the uncertainty on the transverse beam position, losses during beam propagation and thermal effects at the edges of the core of the fiber. Indeed, as stated before, the injected beam is larger than the core of the fiber. This

mode	LP_{01}	LP_{02}	LP_{31}^{sin}	LP_{21}^{cos}	LP_{11}^{sin}
P_{nm} [%]	88.64	3.96	2.03	1.46	0.97
output fraction [%]	91.40	3.72	1.83	1.39	0.95

Table II.6: Mode matching at the fiber input and fiber output. First line: five modes most efficiently coupled; second line: coupling efficiency calculated from the electric field of the beam propagated at the fiber entrance with simulations; third line: output proportion of each mode according to their coupling efficiencies and attenuation in the fiber.

leads to an observable deterioration of the edges at fiber entrance without, however, any change in the efficiency of the process (which evidences the robustness of the setup). Increasing the input power emphasizes these thermal effects and the transverse beam instability, resulting in a decrease of the energy transmission in the fiber. It is interesting to note that the five main modes (those reported in Table II.2.b.2) on which the laser field is decomposed in the fiber have their electric field symmetric with respect to the vertical axis, which is also the direction of polarization of the laser and the – apparent – symmetry of the intensity and wavefront shapes of the laser field before the fiber (Figs. II.27 and II.28, left panels). On the other hand, antisymmetric modes couple very low (even negligible, according to the accuracy of the calculation) fractions of energy. It could thus be interesting to study if the base of modes could be reduced according to specific symmetry properties (this has not been done).

As a cross-check, instead of propagating the field from the position before the fiber, we performed a numerical back-propagation of the field measured by the Shack-Hartmann sensor after the fiber directly towards the fiber output. The results should be the same as the third line of Table II.6. In fact, through this method we found a slightly higher proportion of LP_{01} (≈ 95 %) and thus a slightly lower proportions of other modes, but the most present modes are still the same five ones, in the same order.

Up to this point, the laser beam is still in the picosecond regime. After the fiber stage, it is the injected into the compressor (see Fig. II.21) so as to reach femtosecond durations and then be used for HHG. Let us study the properties of the IR beam after pulse compression.

II.2.c.3 Laser characterization after pulse compression

First of all, one has to note that SPIDER [101] characterizations, not reported here, have been performed after the stage of pulse compression and showed that the spectro-temporal characteristics of the filtered beam are not altered: the spectral shape is preserved and the FWHM pulse duration remains smaller than $50\ fs$ at moderate intensities. This is, of course, a very important point for users' applications.

But let us continue with spatial characterizations: the results of measurements carried out with the Shack-Hartmann sensor after the stage of pulse compression are presented in Fig. II.29. Imperfections of the optics (lenses, gratings of the compressor, mirrors which send the

wavefront amplitude	without the fiber	with the fiber
peak-to-valley [nm]	681.00 ± 45.19	288.00 ± 49.68
RMS [nm]	146.75 ± 9.71	54.40 ± 11.08

Table II.7: Measurements of the wavefront amplitude of the laser beam without and with the fiber, after pulse compression. Peak-to-valley and RMS mean amplitudes of the wavefront are indicated with the standard deviation of the series of measurements.

beam to the sensor) cause intensity and phase modulation on the beam. Nevertheless, the beam quality is far better with the modal filtering setup inserted before the pulse compression stage than without it. Wavefront amplitudes are given in Table II.7: the RMS value is improved from $\frac{\lambda}{5.5}$ to $\frac{\lambda}{14.5}$ with modal filtering.
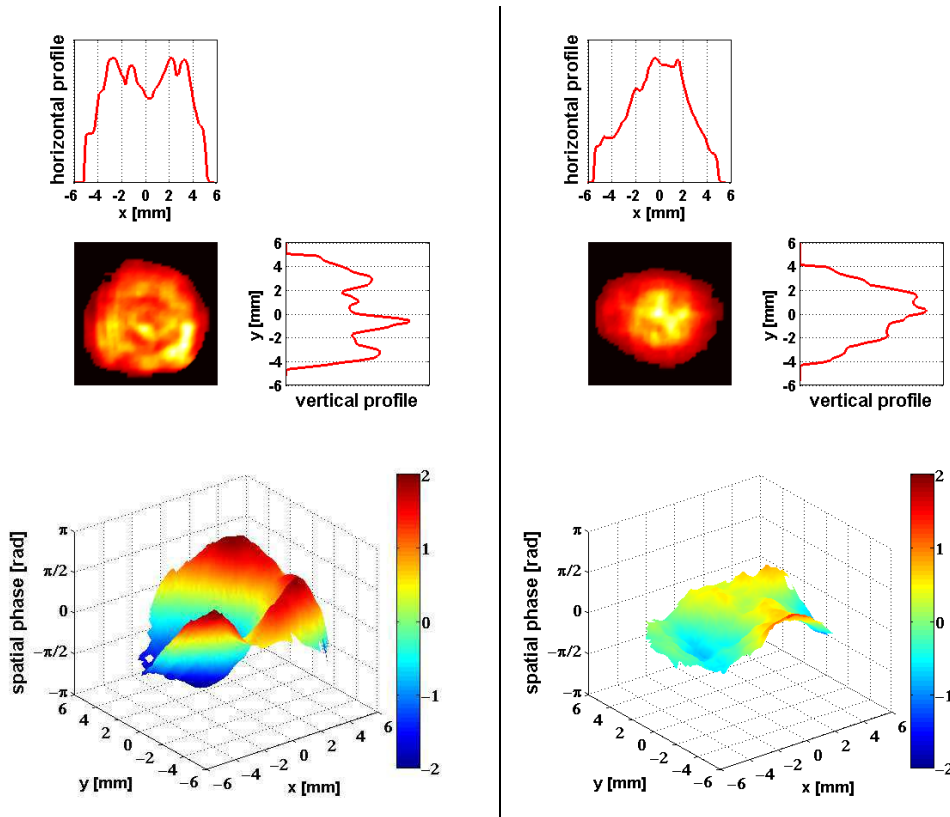

Figure II.29: Shack-Hartmann measurements: intensity and wavefront without (left) and with (right) the fiber. In both cases, the beam mean intensity is similar ($\approx 15\,TW/cm^2$).

The beam is then focused by lens 3. A spatial Fourier transform of the measurements of the laser field reported in II.7 provides the field at the back focal plane, where a clear improvement is found for the filtered beam (Fig. II.30). In the standard setup, the wavefront exhibits an important deformation and the intensity profiles include a non-negligible amount of high spatial frequencies. On the other hand, the filtered beam is Gaussian-like at its focus. Considering only the part of the beam above $\frac{1}{e^2}$ of the maximum intensity, the RMS amplitude of the wavefront is decreased by a factor ≈ 5 (from $\frac{\lambda}{9}$ to $\frac{\lambda}{48}$). The significant improvement at this point of the beamline is very important: indeed, the beam focused by lens 3 will be the one used for experiments
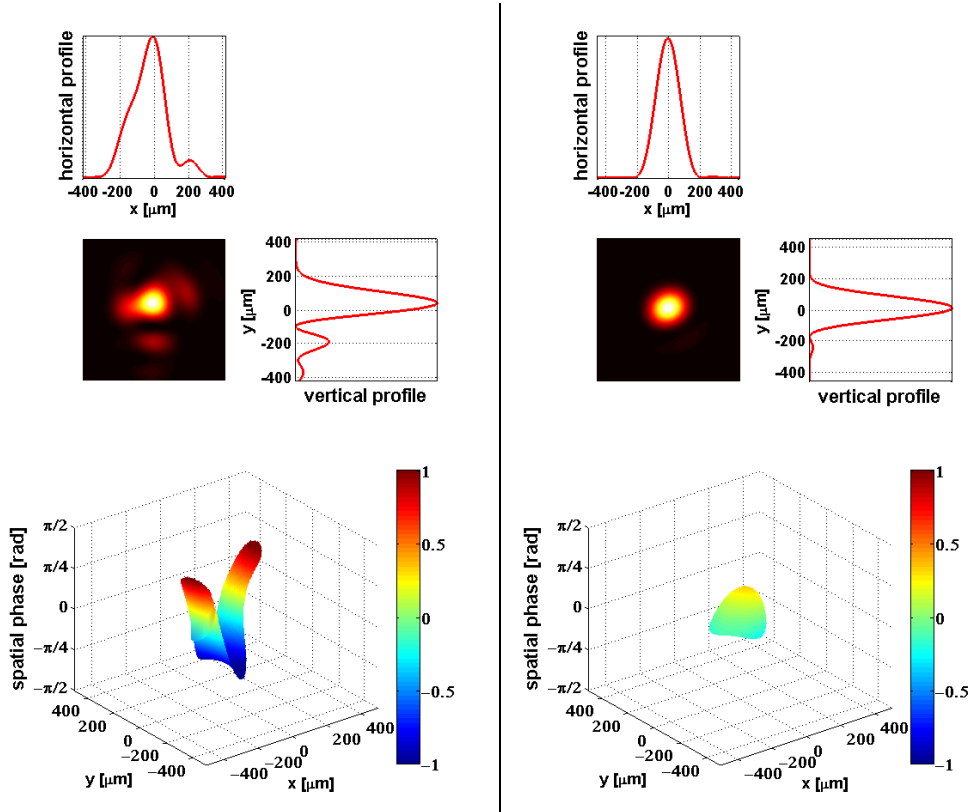
– HHG, in our case.

Figure II.30: Propagated electric field: intensity and wavefront at the back focal plane of lens 3, without (left) and with (right) modal filtering. The wavefront is displayed only where the intensity is higher than $\frac{1}{e^2}$ of the maximum intensity.

II.2.c.4   Effect of modal filtering on harmonic generation

The HHG, as an highly-nonlinear phenomenon, is a very interesting application for illustrating the efficiency of the filtering setup. Homogeneous intensity distribution and low wavefront distortions of the driving laser are crucial for the efficient and coherent macroscopic construction of the harmonic beam. This is especially true in the so-called loose-focusing geometry, where the interaction occurs on a long distance (some centimeters), compared to the wavelength of the fundamental beam ($795\ nm$).

This is why it is interesting to look at the simulation results of IR beam propagation also before and after the focus. Transverse IR spots are shown in Fig. II.31 before, at and after the focus of lens 3, the coordinate $z = 0\ mm$ referring to the position of the focus. As a reminder, iris 3 is placed just before lens 3 that focuses the beam into the gas cell for harmonic generation. It is clear that, especially before the focal point, the transverse intensity shape of the IR beam without modal filtering is quite dirty. However, in both cases (filtered and non-filtered beam), closing iris 3 allows improving the beam spatial quality. In our setup, the beginning of the gas cell is located approximately at $z = -100mm$. Figure II.32 shows the intensity and wavefront
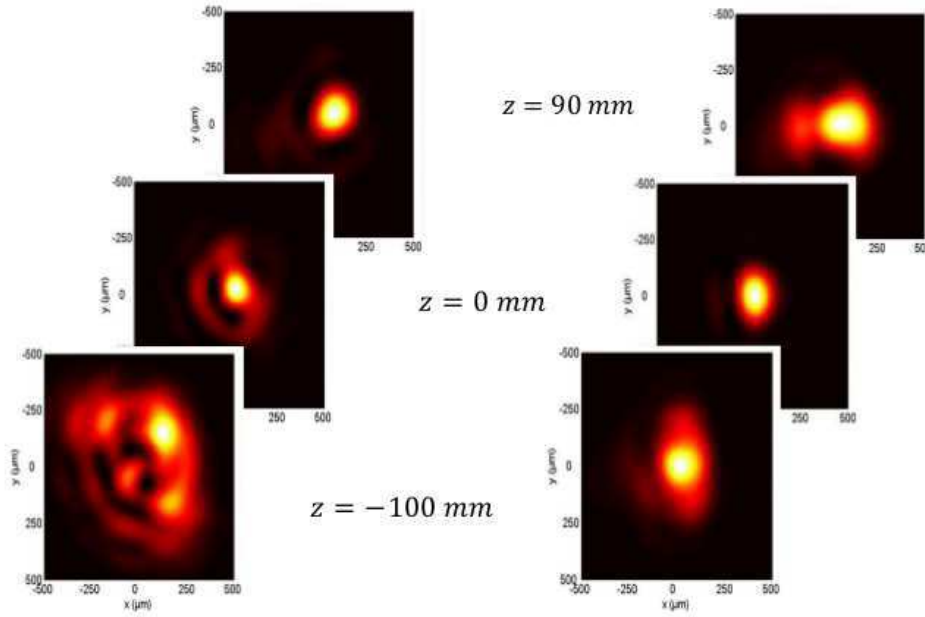
Figure II.31: *Intensity of the IR beam before ($z = -100$ mm), at ($z = 0$ mm) and after ($z = 90$ mm) the focus of lens 3, for the non-filtered (a) and filtered (b) beam, according to numerical propagation of the laser field in free space in the paraxial approximation. [Courtesy of D. Gauthier]*

shapes at $z = -100$ mm and $z = 0$ mm when iris 3 is closed at a diameter of 22 mm. One should note that the quadratic term of the phase (generated by focusing) has not been removed for $z = -100$ mm, so that the wavefronts have a parabolic shape. The intensity distributions of the beam are improved in both cases (filtered and unfiltered beam) with respect to Fig. II.31, even if a higher proportion of high spatial frequencies is still present when there is no modal filtering (Fig. II.32a). In this case also, the situation is greatly improved at focus but the intensity distributions and the wavefront shapes evidence an astigmatism less present in Fig. II.32b.

Similarly to what was observed in [87], we noted a significant improvement of the spatial quality of the generated EUV radiation (Fig. II.33). Indeed, even reducing the aperture size of iris 3 on the unfiltered beam for improving the generation [102] is clearly not sufficient. In addition, the stability and furthermore the harmonic conversion efficiency are enhanced: without modal filtering, the use of 30 mJ of IR (measured after iris 3) allows obtaining $3.3 \cdot 10^7$ harmonic photons per shot (measured on the CCD at 32 nm i.e., the 25th harmonic of the driving laser) while $5.7 \cdot 10^7$ photons per shot are collected with only 8.5 mJ of the driving laser when using the modal filtering stage. In other words, the harmonic conversion efficiency is ≈ 6 times better with the filtered beam, making negligible the drawback of the loss of ≈ 30 % of IR energy within the fiber stage. This is partly explained, in the non-filtered infrared beam (Fig. II.32a), by the presence of a larger number of high spatial frequencies that do not have sufficient energy for driving HHG, and thus that are not involved in the HHG process and represent a waste of IR energy. Moreover, the stability of the intensity and overall of the wavefront of the filtered beam is a great advantage for the macroscopic effects occurring all along the generating medium.
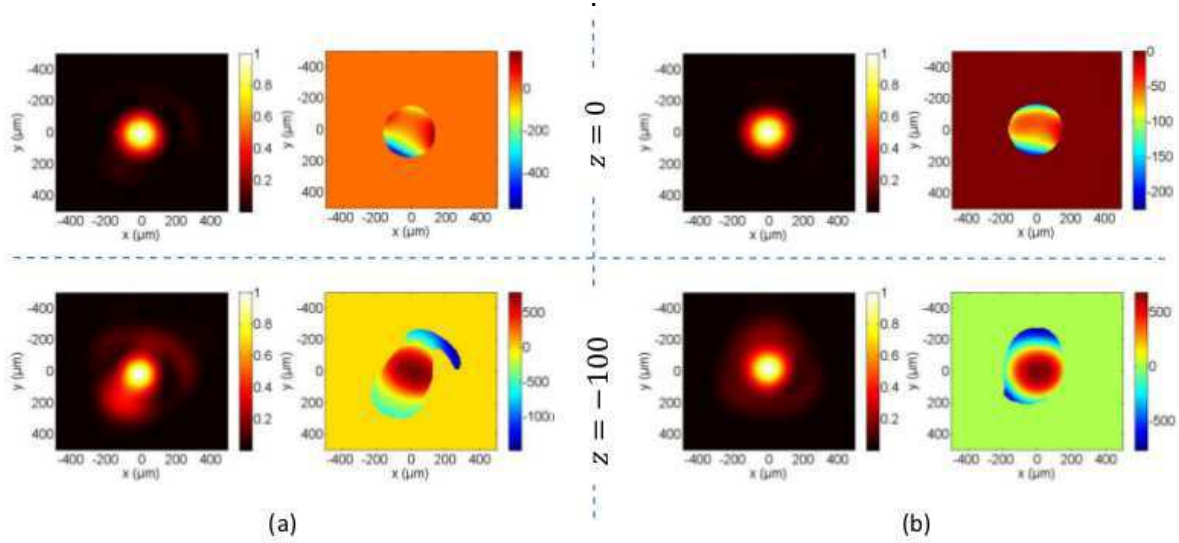
Figure II.32: Simulations of intensity and wavefront of the IR beam at $z = -100$ mm and $z = 0$ mm for the non-filtered (a) and filtered (b) beam with iris 3 closed at a diameter of 22 mm. In each quadrant, the left picture corresponds to the intensity pattern and the right one to the wavefront. The wavefront is displayed only where the intensity is higher than $\frac{1}{e^2}$ of the maximum intensity. [Courtesy of D. Gauthier]
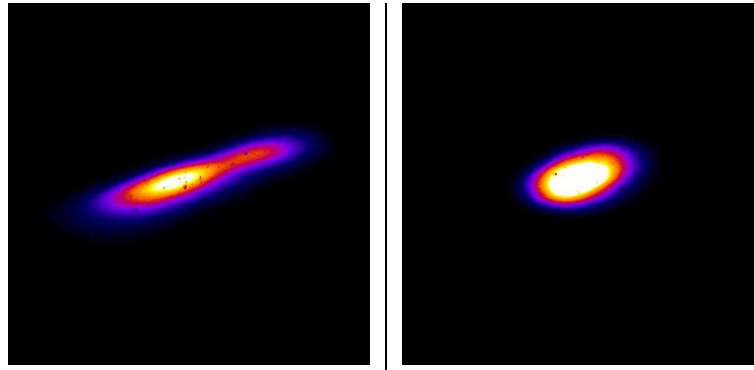

Figure II.33: Far-field footprints of the twenty-fifth harmonic (32 nm) of the fundamental wavelength of LUCA, measured without (left) and with modal filtering (right). In both cases, iris 3 is closed (respectively to a diameter of 25 mm and 19.5 mm) so as to filter the outer part of the IR beam. Harmonics were generated in a gas cell filled with argon at a backing pressure of ≈ 10 mbars. Patterns are measured on a CCD camera placed after a monochromator.

The results presented correspond to optimal conditions of generation (aperture size of iris 3, gas pressure, focus position with respect to the cell, IR energy) where a trade-off was found between spatial quality and intensity of the harmonic signal.

Finally, qualitative HHG simulations have been confronted to experimental results. The code developed by Thierry Auguste models the three-dimensional propagation in combination with the strong field approximation [48, 49] of the microscopic response. In both filtered and non-filtered IR beam cases, similar parameters as the ones of the experiments whose results are presented in Fig. II.33 have been taken as input (gas pressure, IR energy, iris aperture size through which we numerically propagated the laser field towards the gas cell, etc.). The simulations have not

been performed over the all length of gas medium for a lack of computing time, but far-field harmonic patterns shown in Fig. II.34 are in good agreement with those measured (Fig. II.33) and the spatial quality of the harmonic beam seems correlated to the one of the driving IR (whose patterns, taken as simulation inputs, are shown at the top of the figure): the direction of "deformation" of the latter is the same for the harmonic beam. This HHG enhancement therefore corroborates the efficiency of modal filtering.
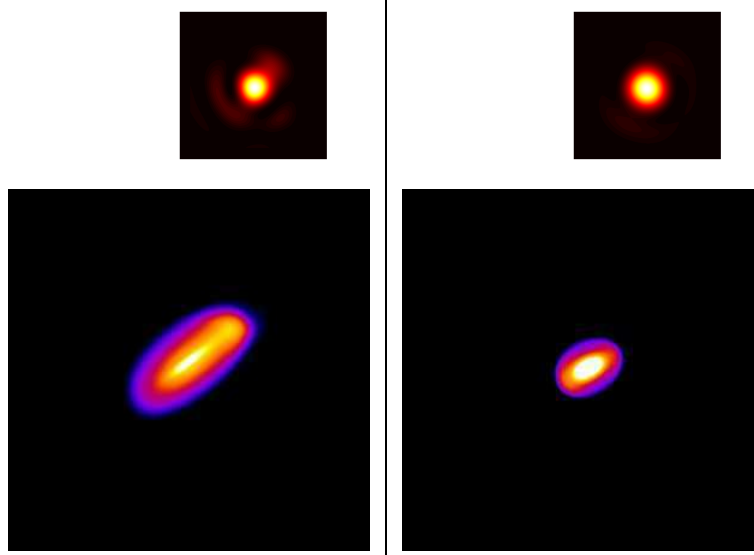

Figure II.34: *HHG simulations: far-field footprints of the twenty-fifth harmonic (32 nm) without (left) and with modal filtering (right). The simulations have been done for a propagation length of* $500 \ \mu m$*, starting* $750 \ \mu m$ *in front of the IR focus. The footprints of the IR beam that have been used at the input of each simulation are shown on the top-right of the EUV footprints, and correspond to the conditions described in the caption of Fig. II.33.*

II.2.c.5   Spatial coherence of the EUV light

Finally, spatial coherence measurements of the harmonic signal have been carried out. Pinholes (instead of slits, but the principle remains the same as the one described in Section II.1) were placed at the focal plane in the diffraction chamber (were the diffracting objects are placed for the users experiments, see Fig. II.20) i.e., the coherence is measured on the image of the EUV source. The focusing optics is a multilayer parabolic mirror that has a maximum reflection around $32 \ nm$ in order to select the 25th harmonic of the IR source. The detection system is the same used for the diffraction experiments i.e., a CCD of pixel size $13.5 \ \mu m$. The pinholes have a diameter of $610 \ nm$ and are separated by a distance of $5 \ \mu m$, which is approximately the whole transverse size of the EUV beam at this position. The pinholes thus probe two outer positions of the EUV spot. I present here measurements performed with the modal filtering stage installed on the IR source. A typical profile obtained on the CCD is shown in Fig. II.35a. Unlike on the FERMI@Elettra source, the harmonic bandwidth is quite large so that the visibility is not constant over the interference profile. Another correlated consequence is that, in the Fourier
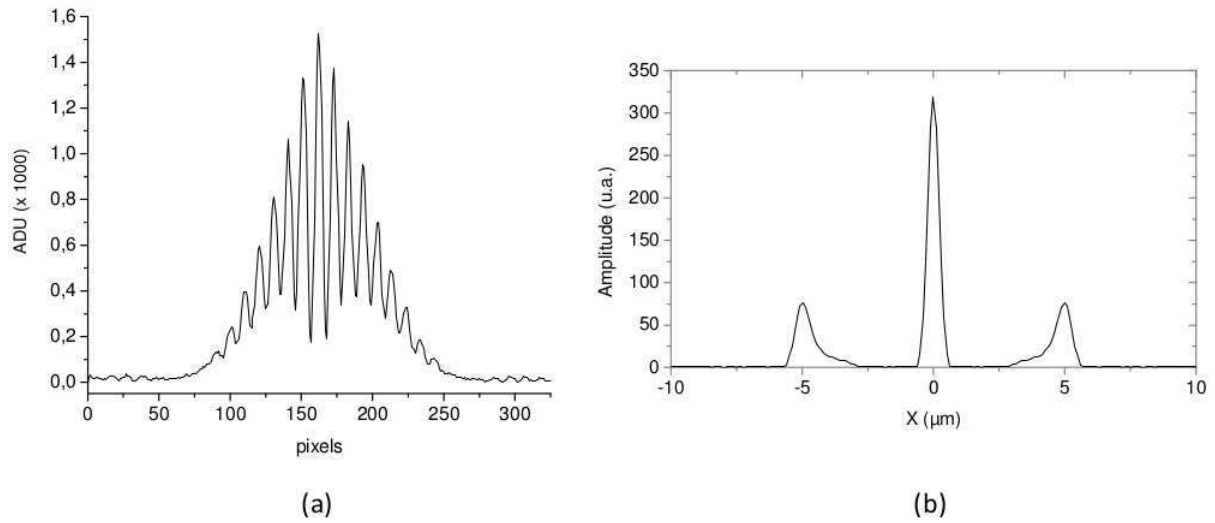
Figure II.35: Interference profile obtained by the Young's experiment carried out on the EUV beam generated with filtered IR source (a) and Fourier transform of the profile. [Courtesy of D. Gauthier]

transform of the profile (Fig. II.35b), the side peaks do not have a negligible width. This allows obtaining information on the spectral shape of the harmonic signal (see II.1): the width of a side peak is equal to the sum of pinholes' diameter and of the spectral width of the 25th harmonic, which is thus found to be $0.64\ nm$ FWHM i.e., similar to what is obtained when measured with the spectrometer. The peaks have a pedestal which correspond to the presence in the spectrum of a remaining part of lower-order harmonics (not well filtered by the multilayer parabolic mirror), especially the 23rd one since it is spectrally very close to the 25th one. The obtained degree of coherence (measured via the visibility of the interference profile or the ratio between the side peaks' area and the central peak's area) is $\approx 0.8 - 0.85$, for measurements taken with one to ten shot accumulations on the CCD.

Previous spatial coherence measurements performed without modal filtering on the IR beam gave quite similar results, of the order of $\approx 0.75 - 0.8$. This very small difference is probably explained by the fact that the modal filtering stage improves the stability of the IR beam (pointing stability due to the fixed point that represents the output of the fiber, and general stability of the transverse intensity and wavefront shapes), and such a stability is transmitted to the generated harmonics. Since the transverse instability degrades the spatial coherence measurements due to the averaging on different transverse positions, that can be the reason for slight better spatial coherence results with the filtered IR beam. Hence, with such a small difference, we cannot conclude on any advantage of the modal filtering from the point of view of harmonics' spatial coherence.

II.3   Summary

In this chapter, I studied the spatial properties of the two femtosecond sources that are the seeded FEL FERMI@Elettra and the LUCA facility.

In the latter case, an optimization of the EUV radiation (conversion efficiency, stability, transverse shape) has been obtained by means of an improvement of the spatial quality and the stability of the IR driving beam via the technique of modal filtering that we developed. Since the HHG acts as a highly nonlinear filter, its enhancement evidences the qualities of modal filtering. The astigmatism of the input beam is still partially present at the output of the fiber. In order to cancel it more efficiently, the use of a longer fiber and/or with smaller core radius is envisaged, which would make even more clear the superiority of modal filtering with respect to classical spatial filtering [103]. However, an important proportion of the remaining high-order modes is already filtered in far-field by means of an iris closed around the first lobe of the LP_{01} mode.

On FERMI@Elettra, the transverse properties of the EUV radiation have been directly characterized. Mainly, the spatial coherence has been measured, providing satisfying results, and the GSM beam has been found to be a good model for describing the transverse properties of FERMI@Elettra's light. Nevertheless, the work has to be continued, for instance with novel complementary and/or more comprehensive methods [104, 105], or parallel ones, like wavefront measurements. As a prospect, the consequences of the spatial quality of the seed laser and of the electron beam on the FEL radiation have to be studied.

Chirp studies at FERMI@Elettra

Contents

With this chapter, I start presenting the spectro-temporal studies that I carried out on seeded FEL's, correlated to the presence of chirps (see Chapter I) at different levels of such a facility. Hereafter, I will provide the description, origins and interplay of these chirps, with the particular case of FERMI@Elettra on which I worked. The next chapter will focus on peculiar effects of the presence of chirps in a seeded FEL, and analogies will be drawn with the spatial studies previously discussed.

III.1   Chirp on the seed pulse

III.1.a Seed laser setup at FERMI@Elettra

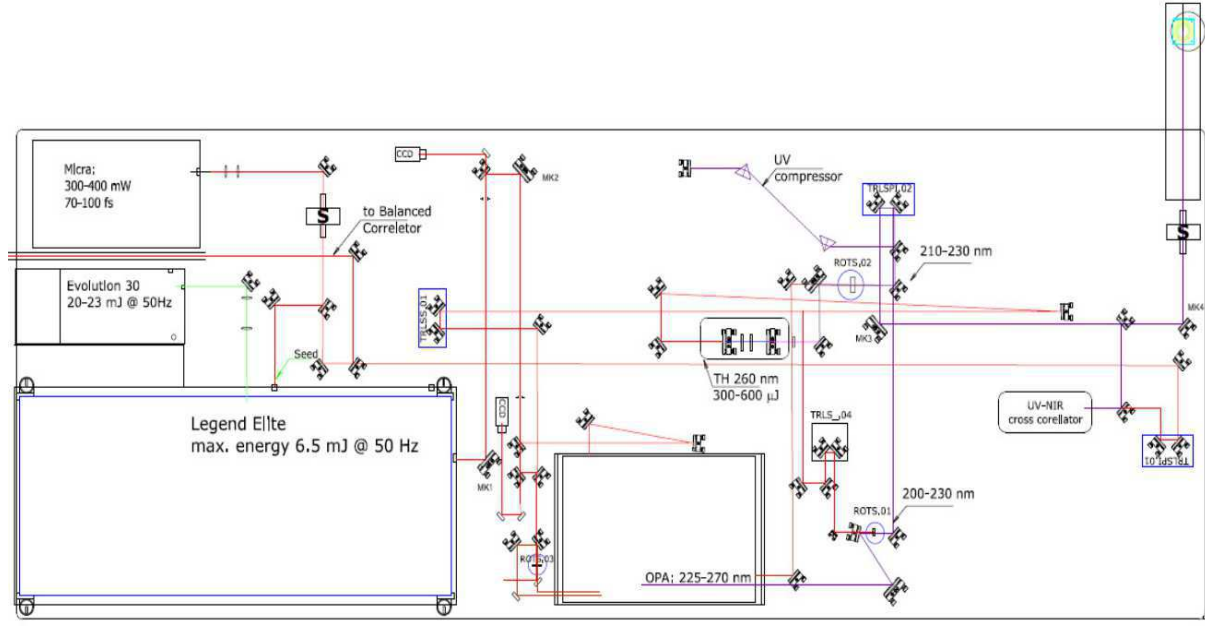The layout of the current laser setup for seeding the FERMI@Elettra FEL [106] is shown in Fig. III.1.

Figure III.1: Layout of the seed laser setup. The Micra® Ti:Sapphire oscillator (top-left box) delivers pulses centered at ∼ 780 nm of Fourier-transform limited duration 70 fs. It is sent to a Legend Elite® regenerative amplifier (bottom-left box), pumped by an Evolution 30® frequency-doubled Nd:YLF laser (middle-left box) centered at 527 nm. The beam can then follow two paths: either the optical parametric amplifier (center-down part) way, providing a wide tunability in the deep-ultraviolet (DUV, 200 − 300 nm), or the frequency tripling scheme (middle of the breadboard). The chosen path is sent down to the undulator hall, by means of a periscope (top-right of the drawing) before which the pulses can travel through a UV compressor, relying on two transmission gratings, or be sent to the UV-IR cross-correlator. The focusing optics that adapt the beam size in the modulator is placed just prior to the periscope.

The setup relies on a commercial Ti:Sapphire chirped-pulse amplified system by *Coherent*®, delivering pulses at a repetition rate of $10\ Hz$ of maximum energy $6.5\ mJ$. We used the third harmonic of the fundamental laser emission ($\approx \frac{780}{3}$). For the experiments reported here, the latter is generated in two steps. First, a non-linear crystal performs a frequency doubling so that, after the crystal, the fundamental wavelength and its second harmonic are present. Both components are mixed in a second crystal in order to create the third harmonic of the fundamental wavelength. This beam is sent by means of a periscope down to the undulators hall, where steering optics is present on an "insertion breadboard" (Fig. III.2), for aligning the beam in the modulator. The center of the modulator is located quite far from the last mirror ($\sim 11\ m$), which makes the alignment difficult. The focal point of the seed is approximately located at the entrance of the modulator so that the overlap with the electron bunch is optimized at the beginning of the interaction. The standard deviation of the transverse intensity profile at focus is $\sigma_r \approx 300\ \mu m$, the standard deviation of the transverse charge distribution of the electron bunch in the undulator area being usually in the range $150 − 300\ \mu m$ (depending on the conditions of the machine). On each side of the focal point, the seed can be considered as collimated (i.e.,
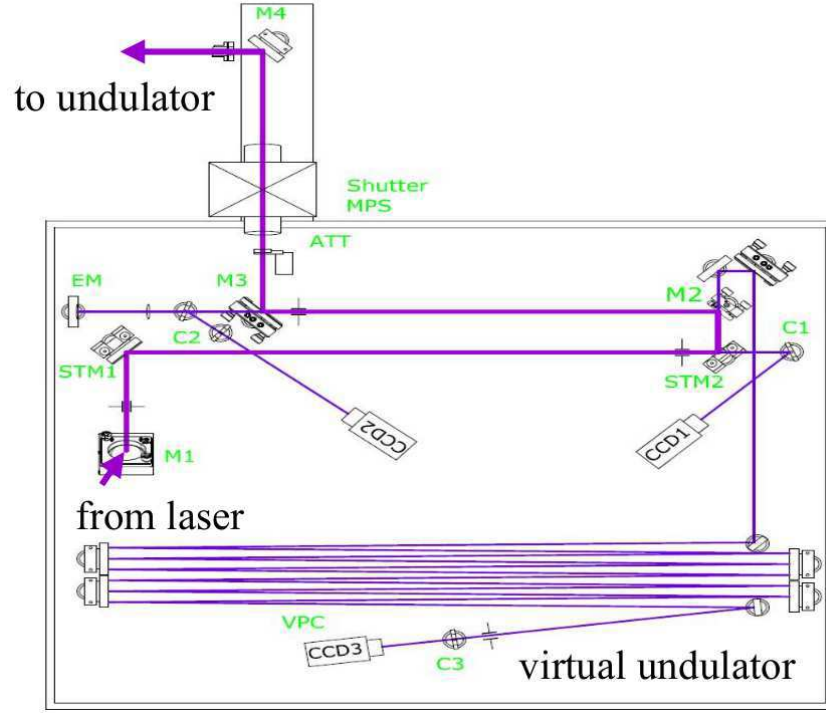
Figure III.2: Insertion breadboard. On the left part, the beam arrives from the upper room through the periscope (see Fig. III.1). The beam is then aligned by means of mirrors and sent directly to the undulators. The small fraction of energy of the beam that is transmitted through mirrors STM2, M2 and M3 is collected by CCDs for getting the beam footprints at different positions. In particular, CCD3 is placed after a long path (bottom part of the drawing) that equates the distance to the beam waist in the modulator. The collected image thus mimics the laser beam cross-section at the entrance of the undulator chain.

Parameter	Value
center wavelength λ	$261\ nm$
bandwidth FWHM H_λ	$0.8 - 0.9\ nm$
duration FWHM H_t	$> 140\ fs$
energy per pulse	$10 - 50\ \mu J$

Table III.1: Main seed parameters for a standard FEL operation.

having a constant transverse size with parallel beams) on the Rayleigh range that is:

$$Z_r = \frac{4\pi\sigma_r^2}{M^2\lambda} \approx 3\ m, \qquad \text{(III.1)}$$

$M^2 \approx 1.5$ being a factor characterizing the beam quality with respect to the one of a Gaussian beam (for which $M^2 = 1$); $\lambda = 261\ nm$ is the usual seeding wavelength. Z_r is very close to the modulator length that is $3.2\ m$, which should ensure a good overlap of the seed and the electrons all along the modulator.

Both temporal and spectral intensity profiles of the seed can be considered as Gaussian. The main seed characteristics in the standard regime of operation are summarized in Table III.1.a. The energy per pulse of the seed does not usually exceed $50\ \mu J$. It is however possible

to go beyond this limit, but usually not above $\approx 150\ \mu J$ in order not to degrade the UV optics that are on the beam path. Also, as we will see later on, increasing the energy per pulse affects the spectro-temporal properties of the pulse. The attenuation is achieved by means of a system composed of a half-wave plate followed by a polarizer, placed just after the generation of the third harmonic.

Finally, the whole laser setup (seed laser, photo-injector laser) is synchronized by an all-optical locking at a repetition rate of $10\ Hz$ [107], for ensuring smallest jitter as possible between the seed pulses and the electron bunch. This signal is linked to the more global clock system of the machine, described in [108, 109, 110].

III.1.b   Sources of chirp on the seed laser

Three main sources of chirp are present in the seed laser: one due the natural dispersion, one to self-phase modulation and one generated in the compressor stage.

Natural dispersion   The first unavoidable effect is the dispersion (see Introduction) that becomes non-negligible for a sufficiently broad spectrum, such as for the seed pulse used at FERMI@Elettra. The beam travels in vacuum only after the insertion breadboard (Fig. III.2). Before that, it travels through normally-dispersive media that are the air and transmission optics (such as windows). A slight positive dispersion is thus induced leading to an up-chirping of the pulse. We call it "natural dispersion" because it is not created intentionally: this is the state of the seed pulse that we get "out of the box", after the generation of the third harmonic ($\approx 261\ nm$). As we will see, in some case it may be desirable to increase this dispersion before the seed reaches the modulator. For this purpose, one can place additional materials on the beam path. However, This generally induces an effect of self-phase modulation.

Self-phase modulation   The optical Kerr effect [90] relies on the fact that the overall refractive index of a medium is proportional to the intensity I of the laser beam:

$$n(I) = n + n_2 I, \tag{III.2}$$

where $n_2 = \frac{3}{\varepsilon_0 n^3} \chi^{(3)}$, with ε_0 the permittivity of the vacuum and $\chi^{(3)}$ the third-order susceptibility of the material, is the non-linear refractive index (said non-linear because it represents a third-order non-linearity, even if it is a linear coefficient of $n(I)$). For moderate laser intensities, n_2 has a negligible effect and only the usual refractive index n is considered. However, if the order of magnitude of I is sufficient to counterbalance the small value of n_2, the overall refractive index has to be taken into account and involves non-linear effects such as self-focusing [17] and self-phase modulation. In the latter, the temporal phase of the pulse is shifted. Indeed, in the

temporal domain, the electric field can be written as:

$$E(t) = A(t)e^{i\Phi(t)} = A(t)e^{-i(\omega_0 t - k_0 z)} = A(t)e^{-i[\omega_0 t - \frac{2\pi}{\lambda_0}n(I)L]}, \tag{III.3}$$

where $A(t)$ is the electric field envelope and L is the distance of propagation in the considered medium. The instantaneous frequency is:

$$\omega(t) = \frac{d\Phi(t)}{dt} = \omega_0 - \frac{2\pi}{\lambda_0}n_2 L \frac{dI}{dt}. \tag{III.4}$$

A frequency shift is thus induced along the pulse i.e., a chirp is created. For a gaussian pulse of intensity profile $I(t) = I_0 e^{-\frac{t^2}{2\sigma_t^2}}$ and standard deviation σ_t, the frequency shift becomes:

$$\delta\omega(t) = \frac{2\pi L n_2 I_0 t}{\lambda_0 \sigma_t^2}e^{-\frac{t^2}{2\sigma_t^2}}. \tag{III.5}$$

For convenience, we shall express it in terms of wavelength. Since $\omega = \frac{2\pi c}{\lambda}$, we have $\frac{d\omega}{d\lambda} = -\frac{2\pi c}{\lambda^2}$ and therefore:

$$\delta\lambda(t) = -\frac{\lambda_0 L n_2 I_0 t}{c\sigma_t^2}e^{-\frac{t^2}{2\sigma_t^2}}. \tag{III.6}$$

Around its center, the Gaussian profile can be considered as a parabola (see Fig. III.3 top): $e^{-\frac{t^2}{2\sigma_t^2}} \approx 1 - \frac{t^2}{2\sigma_t^2}$. Hence the shift of the central wavelength along the pulse becomes simply:

$$\delta\lambda(t) = -\frac{\lambda_0 L n_2 I_0}{c\sigma_t^2}t, \tag{III.7}$$

which is a linear function of t (providin the position along the pulse). As shown in Fig. III.3, this is a good approximation only at the center of the pulse, for a duration of the order of σ_t. At the edges of the pulse, the chirp cannot be considered any more as linear. In the calculations presented in Fig. III.3, we used a set of parameters matching a typical configuration of FERMI@Elettra i.e., a seed with intensity of $I \approx 1 \cdot 10^{14} \frac{W}{cm^2}$ propagating in $10\ cm$ of fused silica, for which $n_2 \sim 10^{-16} \frac{cm^2}{W}$ and $n \approx 1.5$. As shown in Fig. III.3 (bottom graph), an overall variation of the central wavelength of more than $1\ nm$ can be expected. For stressing the effect, I took a strong seed energy of $100\ \mu J$. The chirp created by the self-phase modulation leads to a spectral broadening since the pulse duration is not changed. If we do the mistake to consider that the chirp is linear (taking, all along the pulse, the linear approximation described here above), we obtain a gaussian spectrum (dotted curve in the right panel of Fig. III.4), but whose shape is far from the truth. Indeed, since the phase shift is not quadratic (i.e., the chirp is not linear), the spectral shape will theoretically be distorted, not gaussian (full line in the right panel of Fig. III.4).
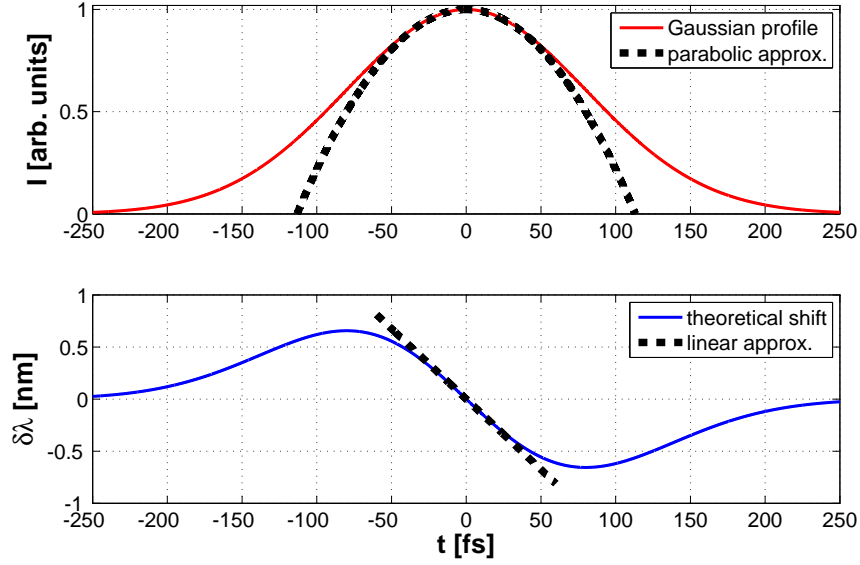
Figure III.3: Chirp along a seed pulse subject to self-phase modulation. Top figure: Gaussian temporal intensity profile (full line) and parabolic approximation (dashed line). Bottom: calculated central wavelength shift for the Gaussian intensity profile (full line) and for the parabolic intensity profile (dashed line). The parameters are: $L = 10\ cm$; $n_2 = 1 \cdot 10^{-16}\ \frac{cm^2}{W}$; $\lambda_0 = 261\ nm$; $\sigma_t = 80\ fs$; $I_0 = \frac{E_0}{\sigma_t(4\pi\sigma_r^2)}$ with $E_0 = 100\ \mu J$ and $\sigma_r = 1\ mm$.
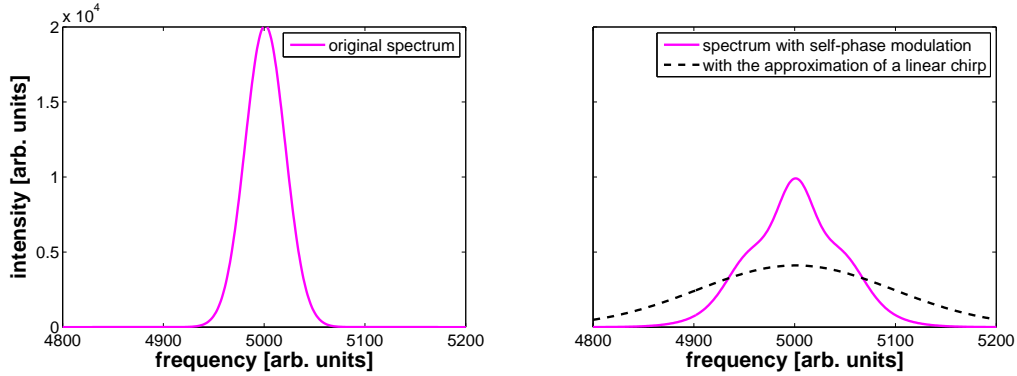
Figure III.4: Comparison of the spectral shape of the seed at FERMI@Elettra in its standard condition (left) and with the effect of self-phase modulation (right), with the set of parameters considered in Fig. III.3. In dotted line: calculated spectrum considering a linear chirp on the whole temporal distribution; the full line in right panel takes into account the chirp as described by Eq. III.6.

Compressor stage   The compressor stage is similar to what can be found on a classical chirped-pulse amplified laser chain [64]. A basic drawing is provided in Fig. III.5. The system relies on two transmission gratings dispersing the light. The different wavelengths arrive at normal incidence on a mirror which sends back the light through the system so that the wavelengths are spatially recombined. The angles and distances of the three optical components are set so that a negative dispersion is induced: longer wavelengths do a longer path than shorter ones. As a result, the initial positive dispersion is eventually compensated and the beam is compressed to its minimal duration. Alternatively (in case of over-compensating negative dispersion), a down-chirped pulse may be generated.

Figure III.5: Scheme of the compressor stage of the seed pulses. When it enters, the pulse is up-chirped: longer wavelengths (to the red) arrive first. Two transmission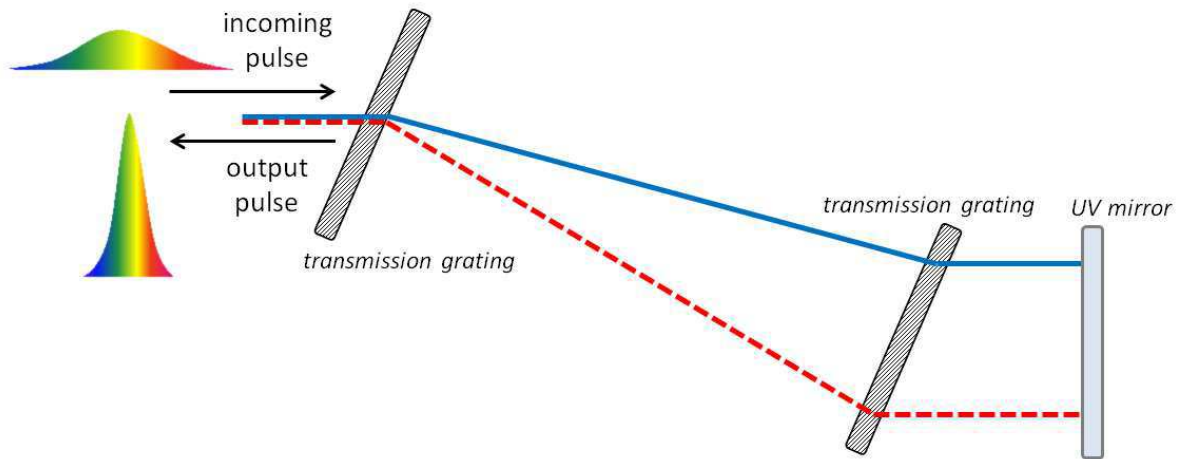 gratings are responsible for the dispersion of the light. Due to their distance and angle, longer wavelengths (dotted line) travel a longer path than shorter ones (full line). A UV-reflective mirror sends back the light and the output pulse is either compressed with respect to the incoming one, or down-chirped if enough negative dispersion has been brought by the system.

Given the bandwidth value specified in Table III.1.a, the Fourier-transform limited duration of the FERMI@Elettra seed laser is $H_t = \frac{4\lambda_0^2 \ln 2}{2\pi c H_\lambda} \approx 120 \; fs$. However, in its standard operation it is lengthened to $\sim 200 \; fs$ due to the aforementioned first two effects. The compressor stage enables shortening the pulse down to $\sim 140 \; fs$ i.e., ~ 1.2 times the Fourier-transform limit. The fact that the compressor cannot totally counterbalance the pulse lengthening emphasizes the presence of higher-order chirps, that partly come from self-phase modulation. Therefore, in order to boil down to a situation where linear chirp is dominant, we will most of the time not compensate the natural dispersion of the seed, or we will eventually induce a strong negative dispersion via the compressor to get a dominant negative linear chirp. Moreover, in order to avoid a too strong self-phase modulation, we will take care to maintain the seed energies below the value at which a spectral distortion may take place i.e., as said previously, below $\approx 150 \; \mu J$.

In the approximation of a linear chirp and Gaussian spectral and temporal profiles, a simple description of the electric field of the seed laser can thus be done, and is developed in the following lines.

III.1.c   Analytical description of linearly-chirped Gaussian laser pulse

In the temporal domain, the electric field of a linearly chirped laser pulse can be written as:

$$E(t) \propto e^{-\Gamma_r t^2} e^{-i[\omega_0 t + \Gamma_i t^2]}. \tag{III.8}$$

The first exponential stands for the temporal envelope (Gaussian, here) and the second one for the phase of the oscillations, including the rapidly-oscillating term at the center pulse frequency

ω_0 and a quadratic term $\varphi(t) = \Gamma_i t^2$. The instantaneous frequency of the pulse is:

$$\omega(t) = \frac{d[\omega_0 t + \Gamma_i t^2]}{dt} = \omega_0 + 2\Gamma_i t. \tag{III.9}$$

We get indeed a linear dependence of the frequency on time of – constant – slope $2\Gamma_i$: the quadratic phase $\varphi(t)$ induces a temporal linear dispersion of the pulse spectral component. A positive Γ_i corresponds to an up-chirped pulse: shorter frequencies i.e., longer wavelengths, arrive first while negative values of Γ_i stand for down-chirped pulses.

The Fourier transform of the temporal electric field gives its expression in the spectral domain:

$$\tilde{E}(\omega) \propto e^{-\frac{\Gamma_r}{4(\Gamma_r^2 + \Gamma_i^2)}(\omega - \omega_0)^2} e^{i\frac{\Gamma_i}{4(\Gamma_r^2 + \Gamma_i^2)}(\omega - \omega_0)^2}. \tag{III.10}$$

As for the case of the temporal electric field, we get a Gaussian envelope with a quadratic phase, but with opposite sign, $\phi(\omega) = -\frac{\Gamma_i}{4(\Gamma_r^2 + \Gamma_i^2)}(\omega - \omega_0)^2$. Here we define the parameter β that characterizes the curvature of the spectral phase, and thus the amount of chirp:

$$\beta = \frac{\Gamma_i}{\Gamma_r^2 + \Gamma_i^2}. \tag{III.11}$$

β is equal to two times $\frac{d^2\phi(\omega)}{d\omega^2}$, which is the group delay dispersion (GDD, see Chapter I).

From Eqs. III.8 and III.10, we get that the temporal and spectral intensities are, respectively:

$$I(t) \propto e^{-2\Gamma_r t^2} \quad \text{and} \quad \tilde{I}(\omega) \propto e^{-\frac{\Gamma_r}{2(\Gamma_r^2 + \Gamma_i^2)}(\omega - \omega_0)^2}. \tag{III.12}$$

These intensity profiles have Gaussian shapes, of standard deviations σ_t and σ_ω respectively. Hence, by identification into $I(t)$ and $\tilde{(I)}(\omega)$, we get (see Appendix A):

$$\Gamma_r = \frac{1}{4\sigma_t^2} \quad \text{and} \quad \Gamma_i = \pm\frac{1}{4\sigma_t^2}\sqrt{4\sigma_t^2\sigma_\omega^2 - 1}. \tag{III.13}$$

From the latter relation, we find back the Fourier-transform limit: $\sigma_t \sigma_\omega = \sqrt{\frac{1}{4} + 4\Gamma_i^2\sigma_t^4} \geqslant \frac{1}{2}$. For a non-chirped pulse ($\Gamma_i = 0$), $\sigma_t = \frac{1}{2\sigma_\omega}$: the duration is inversely proportional to the bandwidth. For Gaussian pulses, we will often speak in terms of the FWHM values (noted H_t and H_ω) instead of the standard deviations ones. Γ_r, Γ_i and the relation of Fourier-transform limit can then be easily rewritten in terms of the FWHM values.

A more comprehensive description of the above part can be found in Appendix A.

According to Eq. III.9, the difference between two frequencies, ω' and ω'', located (respectively) at the times t' and t'' within the pulse, will be:

$$\omega'' - \omega' = \Delta\omega = 2\Gamma_i(t'' - t') = 2\Gamma_i\Delta t. \tag{III.14}$$

In terms of wavelength, it gives:

$$\Delta\lambda = \frac{\lambda_0^2 \Gamma_i \Delta t}{\pi c},$$
(III.15)

where λ_0 is the mean frequency of the spectrum and c the speed of light. It is interesting to calculate this value for $\Delta t = 6\sigma_t$; indeed, within $6\sigma_t$, almost 100% of the pulse energy is present. Therefore, $|\Delta\lambda(6\sigma_t)|$ gives the overall difference of central wavelength within the linearly-chirped seed pulse.
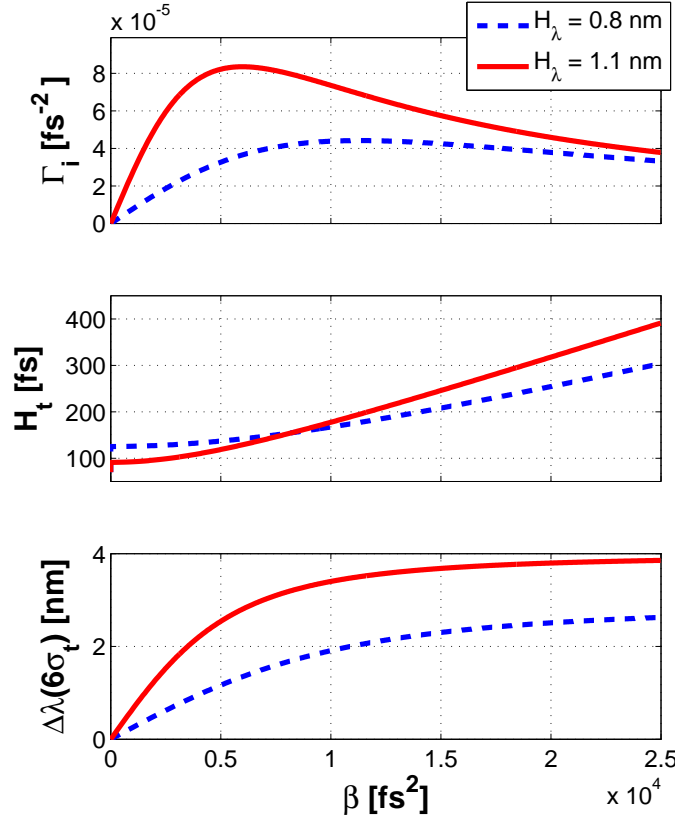

Figure III.6: *Parameters of the FERMI@Elettra seed laser as a function of β, for two different bandwidths, with an up-chirped pulse. Top panel: Γ_i; middle panel: FWHM duration; bottom panel: overall difference of central wavelength within the seed pulse. The latter entity has an opposite sign for a down-chirped pulse, Γ_i also.*

Figure III.6 shows, in the case of an up-chirped pulse, the behavior of three important quantities as a function of β. As the pulse length grows, the slope of the chirp Γ_i rapidly grows but then decreases while the increase of the pulse duration becomes linear. Hence, the increase of $\Delta\lambda(6\sigma_t)$ is more and more slow so that the overall difference of central wavelength within the seed pulse is practically limited. In these graphs, we considered two different values of the bandwidth of the seed that are the fact our two limiting cases: in its standard configuration, the seed has an FWHM bandwidth of $0.8 - 0.9\ nm$ (see Table III.1.a). But as said previously, this number can grow, due to self-phase modulation, if the energy of the seed is sufficiently high. Until an FWHM bandwidth of $1.1\ nm$, the shape of the spectrum remains clean and Gaussian so

that we have always kept it under this limit. It becomes distorted above $1.2 - 1.3 \, nm$ (for seed energies $> 150 \, \mu J$). Therefore, in our conditions, $\Delta\lambda \left(6\sigma_t\right) < 4 \, nm$.

III.1.d   Characterizaton of seed laser pulses

The fundamental quantities characterizing the FERMI@Elettra seed laser pulse are its spectral width and duration. While measuring the spectrum is generally not an issue, the determination of pulse duration is not a trivial task. At FERMI@Elettra, such a measurement is carried out by performing a cross-correlation between the fundamental IR pulse, of Gaussian temporal shape and intensity $I_{IR}(t)$, extracted from the oscillator of the Ti:Sapphire laser chain, and the seed pulse i.e., the third harmonic of the IR signal, of intensity $I_{seed}(t)$. The two pulses overlap in a non-linear crystal where occurs a sum frequency generation: the fourth harmonic is thus created. The delay τ between the two pulses is controlled by a delay-line and the intensity of the generated signal is:

$$I_{XCorr}(\tau) = \int_{-\infty}^{+\infty} I_{IR}(t) I_{seed}(t - \tau) \, \mathrm{d}\tau \tag{III.16}$$

A typical cross-correlation trace that we collected is shown in Fig. III.7. The location of the
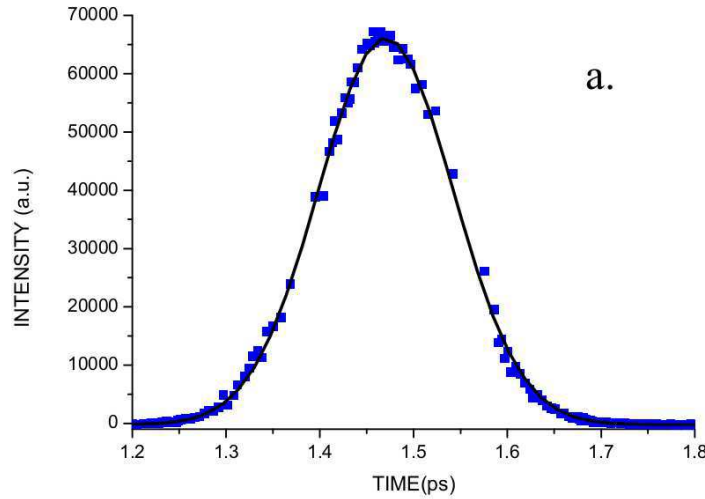
Figure III.7: Typical cross-correlation trace allowing to measure the seed pulse duration. Squares are experimental data and the line is a Gaussian fit. The FWHM duration is $170 \, fs$, corresponding to a pulse FWHM duration of about $150 \, fs$. On the vertical axis is reported the intensity of the correlation signal, $I_{XCorr}(\tau)$, while the horizontal one shows the delay τ.

cross-correlation setup is shown in the right part of Fig. III.1. One has to note that a thickness of $15 \, mm$ of fused silica has been inserted to take into account the material through which the seed pulse propagates on the path to reach the undulator. From this measurement, we obtain the FWHM duration of the seed pulse:

$$H_{tseed} = \sqrt{H_{tXCorr}^2 - H_{tIR}^2} \tag{III.17}$$

In Table III.1.d are reported different characterizations of the seed pulse, obtained for different induced temporal chirps. In the standard configuration, the FWHM duration is about $200 \, fs$ for energies per pulse larger than $50 \, \mu J$. Below this energy, the pulse duration may be undervalued due to a lower signal. The bandwidth grows as a function of the energy per pulse, due to self-phase modulation; as a consequence, the time-bandwidth product increases as well. In this standard configuration, the pulses are up-chirped i.e., $\Gamma_i > 0$. This holds also for the two configurations where additional pieces of a normally-dispersive material, calcium fluoride CaF_2, are placed on the beam path. In these two configurations, one observes an augmentation of both the bandwidth and the duration: the first effect is again due to self-phase modulation, the second one to the dispersion. Here the measurements corresponding to to a distorted spectrum are not reported. We also tested four different configurations of the compressor, corresponding to a different spacing between the gratings. We limited the energy per pulse in order not do degrade the gratings. The measurements clearly show the grating efficiency: for every configuration, the time-bandwidth product is maintained at an almost constant value, whatever the energy per pulse. For the first position, we achieved pulses with a minimum duration of $140 - 150 \, fs$ i.e., ~ 1.2 times far from the Fourier-transform limit. This does not mean that the compressor sets the quadratic phase to zero, but that the quadratic phase is set to a value that compensates the higher-order phase terms. Here, the pulses are so close to the Fourier-transform limit that they are at the borderline of the model of a linearly-chirped Gaussian pulse (high-order phase terms can not be neglected any more in Eqs. III.8 and III.10). Hence, it is difficult to define e.g., Γ_i, and furthermore to say what is the sign of the slight residual chirp. For the three other gratings configurations, the sufficient anomalous dispersion that is provided by the compressor allows defining again a dominant linear chirp, with $\Gamma_i < 0$.

One has to note that we measured the FWHM bandwidth implying a Gaussian spectrum in terms of wavelength, which strictly speaking means that it is not Gaussian in terms of frequency (whereas our analysis relies on a Gaussian spectrum in terms of frequency). However, the spectrum is not enough wide to see a difference: $\frac{d\omega}{d\lambda}$ is almost constant on the whole spectrum, hence the error is very small.

The measurements are done before the seed is focused and sent to the undulators hall i.e., at a position where its transverse size, and thus its power density, is lower than what is really experienced by the electrons. It means that the pulses may suffer from a self-phase modulation that is not taken into account in our characterizations. Therefore, as a safety margin, in the simulations presented later on, we considered a bandwidth $\approx 10\%$ higher than measured.

The frequency chirp on the seed pulse is the one usually defined in the femtosecond laser community. However, a second chirp is present in a seeded FEL: the energy chirp of the electrons, which is defined as the dependence of their energy as a function of the longitudinal position. Its description is provided in the next section.

	Energy [μJ]	H_λ [nm]	H_t [fs]	TBP vs. FT limit
standard configuration	8	0.75	162	1.2
	36	0.83	177	1.5
slight up-chirp	72	0.9	200	1.8
	205	1.07	217	2.3
	269	1.21	211	2.6
dispersive material	7	0.76	265	2.0
5 *cm* of CaF_2	17	0.8	288	2.3
	33	0.83	302	2.5
moderate up-chirp	66	0.99	345	3.4
	92	0.99	380	3.8
	132	1.14	409	4.7
	159	1.21	451	5.4
dispersive material	7	0.8	396	3.2
10 *cm* of CaF_2	16	0.83	423	3.5
	30	0.96	453	4.3
strong up-chirp	62	0.99	525	5.2
	87	1.14	602	6.8
	127	1.21	646	7.8
compressor	5	0.76	141	1.1
position 1	12	0.8	148	1.2
	23	0.83	149	1.2
set for	46	0.83	150	1.2
minimum duration	63	0.83	153	1.3
	89	0.91	149	1.4
compressor	5	0.71	241	1.7
position 2	12	0.71	235	1.7
	23	0.74	233	1.7
slight down-chirp	45	0.76	228	1.7
	63	0.76	224	1.7
	89	0.83	222	1.8
compressor	5	0.8	341	2.7
position 3	12	0.8	333	2.7
	24	0.81	328	2.7
moderate down-chirp	48	0.84	320	2.7
	67	0.85	327	2.8
	96	0.86	326	2.8
compressor	5	0.8	436	3.5
position 4	12	0.83	438	3.6
	24	0.88	437	3.8
strong down-chirp	48	0.88	427	3.7
	67	0.87	429	3.7
	96	0.88	436	3.8

Table III.2: Results of seed pulses characterizations. First column: different configurations; second column: energy per pulse; third column: FWHM bandwidth; fourth column: FWHM duration; fifth column: ratio between time-bandwidth product (TBP) and Fourier-transform (FT) limit. The central wavelength was always around 261.2 nm.

III.2   Energy chirp of the electron beam

III.2.a   Electron acceleration

Before describing the energy chirp that may affect the longitudinal electron beam distribution, and discussing its provenance, it is necessary to give a simple remind of the process of electron acceleration. The electron source [111] generates a bunch of charge $\sim 500\ pC$ and duration $\sim 8\ ps$. In order to reach a sufficient energy that is required for the FEL to reach low wavelengths (see Chapter 1, resonance equation of the FEL), the electron bunch is accelerated through a linear accelerator (linac). It passes through successive sections within which is present a sinusoidal electric field. Such sections are called radio-frequency (RF) cavities, characterized by V_{RF}, λ_{RF} and φ_{RF} that are respectively the amplitude of the field, its wavelength and its phase with respect to the center of the bunch. The gain of energy of an electron located at the position z ($z = 0$ being the center of the bunch) is thus given by [112]:

$$\delta E(z) = eV_{RF}\cos(\varphi_{RF} + \frac{2\pi}{\lambda_{RF}}z) \tag{III.18}$$

where $e \approx 1.6 \cdot 10^{-19}$ is the elementary charge. The total gain of energy of an electron along the linac is thus equal to the sum of the δE acquired within each RF cavity. The particular value $\varphi_{RF} = 0°$ corresponds to the crest of the field. In a RF cavity, the electrons gain / lose different energies according to their position with respect to the field i.e., they are dispersed in energy. Thus, similarly to the notion of chirp in the community of ultrafast lasers, we define the chirp of the electrons as the dependence of the mean energy of the particles from their position z along the bunch (or, equivalently, the time t).

III.2.b   Description of the electron-beam energy chirp

At FERMI@Elettra, the energy profile of the electron bunch is well described by a parabolic function:

$$E(t) = E_0 + \chi_1 t + \chi_2 t^2. \tag{III.19}$$

Here, E_0 is the energy at the center of the parabola, χ_1 the coefficient of the linear component and χ_2 the coefficient of the quadratic one.

The parabolic nature of the energy chirp at FERMI@Elettra is due to the sources which it stems from (see [113]):

- The first is the direct consequence of the process of RF acceleration. When the electron bunch is "on-crest" (centered on the peak of the sinusoid i.e., $\varphi_{RF} = 0°$), the electrons acquire a negative quadratic chirp due to the curvature of the accelerating field.

- In order to reach higher peak currents (i.e., to increase the density of particles that emit FEL radiation and thus enhance the power of the latter), the electron bunch is longitudinally compressed. For this purpose, the electrons are set "off-crest" in some RF sections i.e., de-phased with respect to the peak of the sinusoid by $-45° < \varphi_{RF} < 0°$, so that they acquire a linear chirp component $\frac{\Delta E}{E_0}$. Chirped electrons are then sent through a magnetic chicane where they follow energy-dependent trajectories (like in the dispersive section of the undulator line) so as to shorten the bunch. The particles, of initial position z, are thus moved to the position $z + R_{56}\frac{\Delta E}{E_0} + T_{566}\left(\frac{\Delta E}{E_0}\right)^2$, where R_{56} and T_{566} are the dispersion coefficients. The presence of T_{566} is responsible for an additional negative curvature of the electrons energy profile.

- A specific RF section, called X-band cavity, has been installed at FERMI@Elettra before the dispersive section of the bunch compression stage. Its sinusoidal field, of higher frequency and thus higher on-crest curvature than other classical RF sections, is de-phased by $\varphi_{RF} = 180°$ with respect to the other sections, so that the electron energy acquires a strong positive quadratic component aiming at compensating the negative energy curvature (see first two points).

For a simple view of the mind accounting for our study of the energy chirp, the FERMI@Elettra linac can thus be reduced to a simplified structure (Fig. III.8): a first linac segment L0, a second L1 in which is created the linear chirp component $\frac{\Delta E}{E_0}$ prior to bunch compression, the magnetic chicane BC (for "bunch compression") of parameters R_{56} and T_{566} and the X-band cavity. The final electron beam mean energy is given by:

$$E_0 = E_i + e[V_0 \cos(\varphi_0 + \frac{2\pi}{\lambda_s}z) + V_1 \cos(\varphi_1 + \frac{2\pi}{\lambda_s}z) + V_x \cos(\varphi_x + \frac{2\pi}{\lambda_x}z)], \qquad \text{(III.20)}$$

where the different variables are defined in the caption of Fig. III.8. The accurate structure of the linac can be found in [111].

Finally, one has to note that the accelerated particles also generate fields, called wakefields. The effect of the latter becomes important when the bunch is shortened. Longitudinal wakefields [114] cause a negative linear energy chirp (possibly compensated by a slight dephasing of last RF cavities) and a positive quadratic one (that competes with the other sources of quadratic chirp described previously).

In the following lines, I describe the method and the results of measurements of the energy chirp of the electrons.

III.2.c   Characterization of the energy chirp

At FERMI@Elettra, the energy profile at the end of the linac is characterized by a so-called high-energy radio-frequency deflector (HERFD) [115]. An RF section tilts the bunch in the ver-
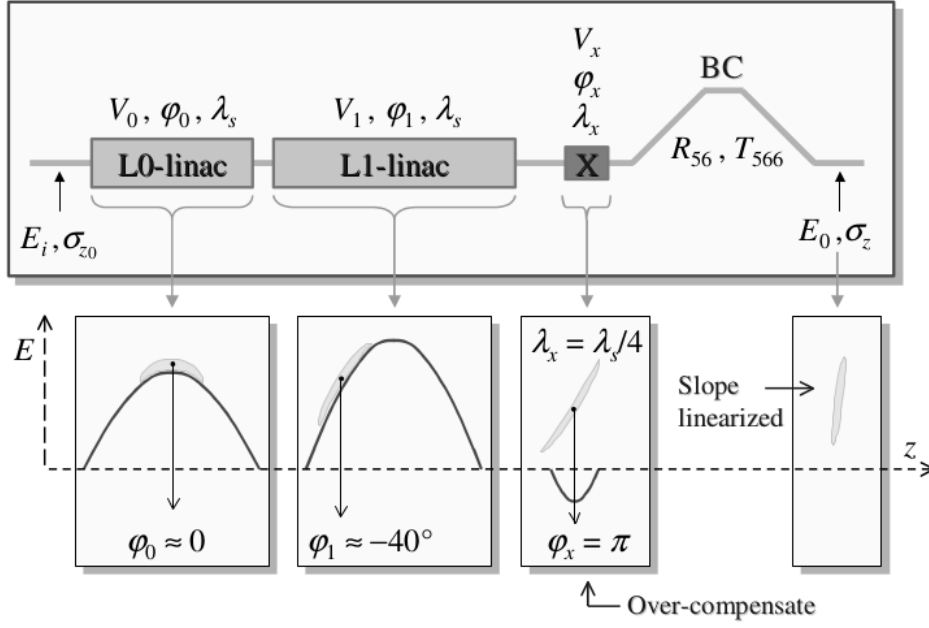
Figure III.8: Simple view of the linac structure at FERMI@Elettra, picture taken from [113]. The electron beam, of initial energy E_i and duration σ_{z0}, is accelerated in a first RF cavity (L0) with field amplitude V_0, phase φ_0 and wavelength λ_s. A second cavity (L1), with field amplitude V_1, phase φ_1 and wavelength λ_s is used to induce a linear energy dispersion needed for bunch compression. The X-band cavity (X), with field amplitude V_x, phase φ_x and wavelength λ_x is used to pre-compensate the quadratic chirp component that will be induced by in the bunch compression (BC) stage, after which the electron beam reaches its final characteristics, with mean energy E_0 and compressed duration σ_z.

tical direction, making the information about the beam time structure available along that axis. Then, a bending magnet disperses the electrons in the horizontal plane, making the information about the beam energy profile available along that direction. The beam longitudinal phase space can thus be visualized on a fluorescent YAG crystal placed downstream the magnet. Typical results are reported respectively in the top and bottom pictures of Fig. III.9. For the first configuration (top pictures), the interpolation with previous Eq. III.19 results in following parameters: $E_0 \approx 1275\ MeV$, $\chi_1 \approx 8\ MeV/ps$ and $\chi_2 \approx 0.3\ MeV/ps^2$. Hence, the chirp is almost linear only. For the second configuration (bottom pictures), following parameters are obtained: $E_0 \approx 1006\ MeV$, $\chi_1 \approx 1\ MeV/ps$ and $\chi_2 \approx 7\ MeV/ps^2$. This time, the chirp can be considered as almost quadratic only. In this second configuration, we see clearly, due to a stronger compression than in the first configuration, the more important effect of longitudinal wakefields, that generate a positive value of χ_2. The right panels of Fig. III.9 display the current profiles, whose shapes (roughly a ramp with negative slope) are explained by the longitudinal compression process of the bunch [116]. The current affects the homogeneity of the FEL process along the bunch.

We have now characterized the frequency chirp of the seed and the energy chirp of the electrons. Both have consequences on the properties of the FEL emission [117]. Before showing in
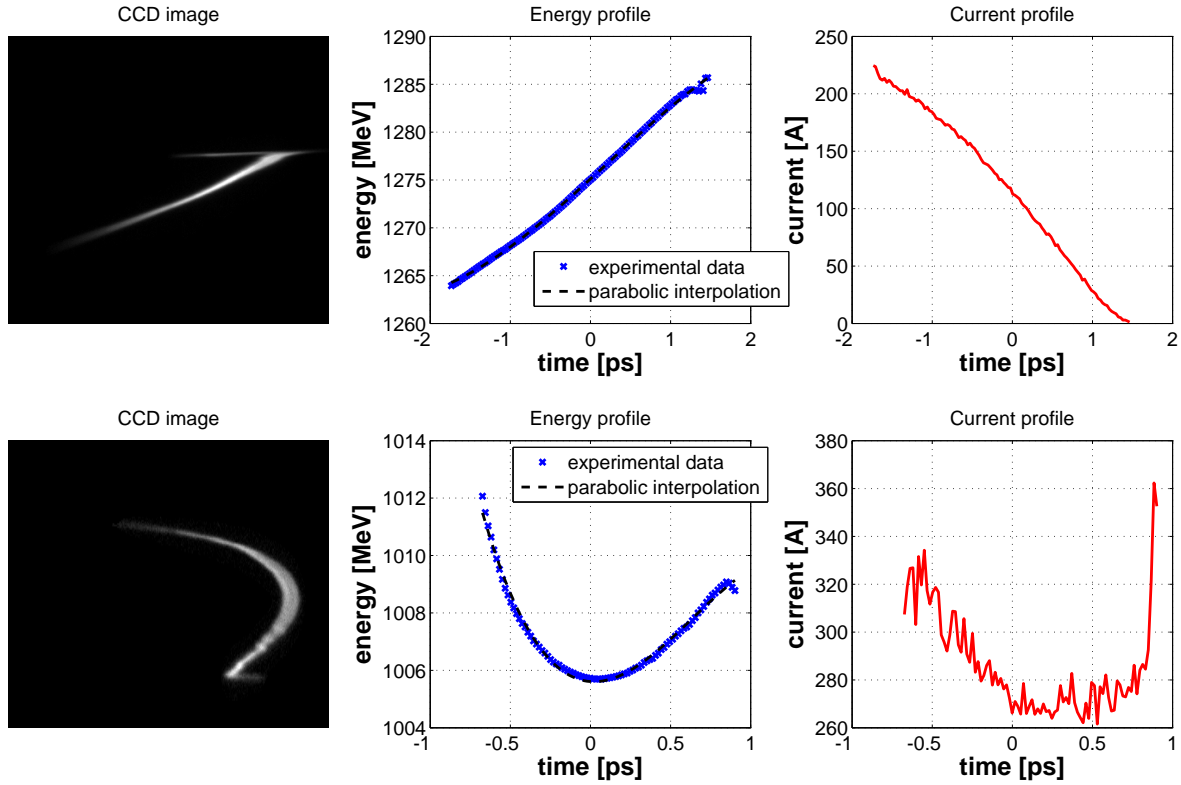
Figure III.9: Longitudinal phase space measured at the end of the FERMI@Elettra linac for two different configurations of the machine. Left: image observed by a CCD on the YAG crystal; center: analysis of the left picture, showing the energy profile; right: analysis of the left picture, showing the current profile. Larger values of time correspond to a displacement from the tail to the head of the bunch.

the next chapter an experimental application, it is interesting to start with simulation results to give a first insight of the chirp interplay in a seeded FEL.

III.3   Numerical study on the effects of seed and electron chirps on the FEL emission

III.3.a   Simulation parameters

In order to understand and characterize the effect of the different chirps on the FEL emission, we have carried out an extensive campaign of simulations using the code Perseo [22]. Such a code simulates the FEL process in the temporal (longitudinal) domain. The spectral properties of the FEL emission are instead retrieved by a Fourier transform of the temporal electric field. Transverse effects that might affect the FEL evolution are taken into account via correction factors [118]. The obtained results have been validated by the three-dimensional code GENESIS [23], which is the "standard" of the FEL community.

The effect of chirps has been studied independently: linear frequency chirp on the seed (by introducing a quadratic phase term in the temporal electric field of the pulse), linear and

quadratic energy chirps of the electron. In [117], Lutman et al. provide an expression of the temporal electric field of the FEL emission in the presence of these three chirps. Unfortunately, this analytic work concern only the amplification of the fundamental of the seed pulse, whereas here we focus on the usual state of FERMI@Elettra, that is devoted to amplify harmonics of the seed pulse in order to generate short-wavelength radiation.

We will therefore rely only on simulations for giving a first idea of the effect of each chirp on the output radiation. The simulation parameters that have been used are reported in Table III.3. Note that the used seed intensity ($25\ GW/cm^2$) is the value above which the spectro-temporal properties of the FEL emission become distorted.

Electron beam	Energy	$1.3\ GeV$
	Relative energy spread	0.01%
	Peak current	$200\ A$
	Emittance	$2\ mm.mrad$
Seed	Central wavelength	$260.8\ nm$
	FWHM bandwidth	$0.81\ nm$
	Peak intensity	$25\ GW/cm^2$
Undulators	Harmonic number n	8
	Dispersive section R_{56}	$20\ \mu m$

Table III.3: Parameters of simulations presented in this section.

In the simulation results presented hereafter, the spectral phase is quite difficult to unwrap (suppress 2π phase jumps), partly due to the narrow spectrum and a too small resolution in the frequency domain. Hence, the spectral phase won't be displayed on the graphs of the FEL emission. The spectral and temporal profiles have been fitted to a Gaussian and the temporal phase to a parabola, separated into a quadratic and a linear phase term.

III.3.b Individual effects

Intrinsic chirp Here we consider the simplest (ideal) case i.e., when neither the seed pulse nor the electron beam are chirped. This enables emphasizing the presence of a positive intrinsic chirp that grows during the FEL process. The presence of this chirp has been pointed out by Wu et al. [119]. It comes from the fact that the wiggling relativistic electron beam, representing the FEL gain medium, is a dispersive medium, of group velocity [120]:

$$v_g \simeq \frac{\omega_n}{k_n + \frac{k_w}{2}} = \frac{c}{1 + \frac{\lambda_n}{2L}}.$$

(III.21)

λ_n is the center wavelength of the FEL emission (n^{th} harmonic of the seed), $k_n = \frac{2\pi}{\lambda_n}$ and L is the undulator period, $k_w = \frac{2\pi}{L}$. If we assume that there is no bunching and thus no coherent emission in the modulator, v_g accounts only for the emission in the radiators and L is the radiators

period i.e., $5.5\ cm$. From the group velocity, we get the group velocity dispersion:

$$GVD_n = \frac{k_w}{2\omega_n^2} = \frac{\lambda_n^2}{4\pi L c^2}, \tag{III.22}$$

which is the group delay dispersion i.e., the second-order term of the spectral phase of the FEL emission, per unit length of propagation. The non-zero value of the group-velocity dispersion implies the presence of a frequency chirp in the FEL emission, even without chirps on the seed and on the electrons.

Due to the intrinsic chirp, the FEL emission is not Fourier-transform limited. However, this chirp is typically very small: for instance, in the simulation presented in Fig. III.10, the parabolic interpolation of the temporal phase of the FEL pulse gives $\varphi_{FEL}(t) \approx 5.3 \cdot 10^{-5} t^2 - 0.025t$ and the FEL pulse remains <1.2 times far from the Fourier-transform limit.
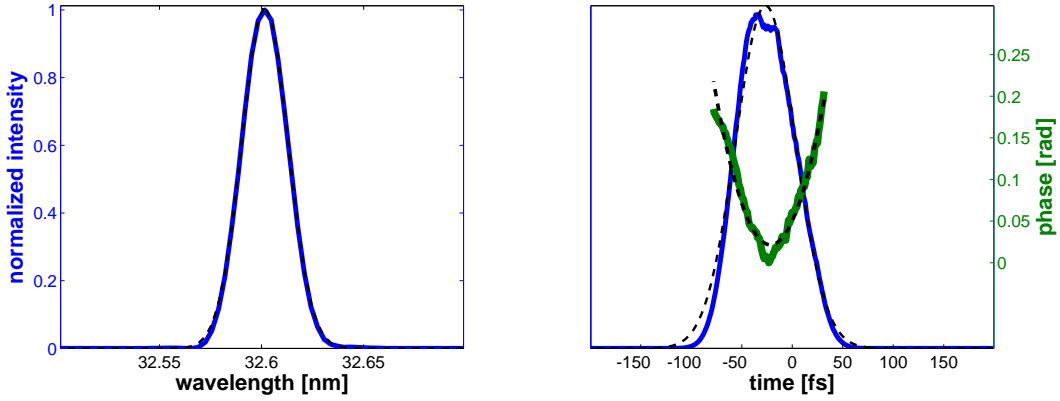

Figure III.10: *Perseo output in the ideal case of no chirps, neither on seed nor on electron beam. Full lines are simulation results and dotted lines their interpolations (Gaussian for the intensity profiles and parabolic for the phase).*

Linear frequency chirp (quadratic phase on the seed pulse)   For typical values of the chirp on the seed pulse, the intrinsic chirp becomes negligible and is dominated by the quadratic term imprinted by the seed: the phase of the FEL pulse is also parabolic. For the situation reported in Fig. III.11 accounting for a seed chirp parameter $\beta = 10000\ fs^2$, the parabolic interpolation of the FEL phase gives $\varphi_{FEL}(t) \approx 3.2 \cdot 10^{-4} t^2 - 0.15t$: the quadratic and linear phase terms are one order of magnitude larger than those obtained in the presence of the intrinsic chirp only. The latter may therefore be neglected. The Γ_i parameter of the seed is equal to $4.5 \cdot 10^{-5}\ fs^{-2}$. If we multiply it by the harmonic order ($n = 8$), we find a value of $3.6 \cdot 10^{-4}\ fs^{-2}$, which is very close to the quadratic component $3.2 \cdot 10^{-4}$ of the FEL phase. We thus have that, neglecting the linear phase term which only corresponds to a wavelength shift, $\varphi_{FEL}(t) \approx n\Gamma_i t^2$ This property, generally verified in every simulation, is very important and will be discussed in the next Chapter. The presence of a stronger quadratic phase term affects the time-bandwidth product of the

FEL pulse: it is >2.2 times far from the Fourier-transform limit (for the reported simulation). In other words, the fact that the seed pulse is usually up-chirped at FERMI@Elettra directly affects the longitudinal quality of the FEL pulse. Moreover, as reported in [128], this effect is directly proportional to the harmonic order i.e., the lower the amplified wavelength, the poorer is the longitudinal quality of the FEL emission.
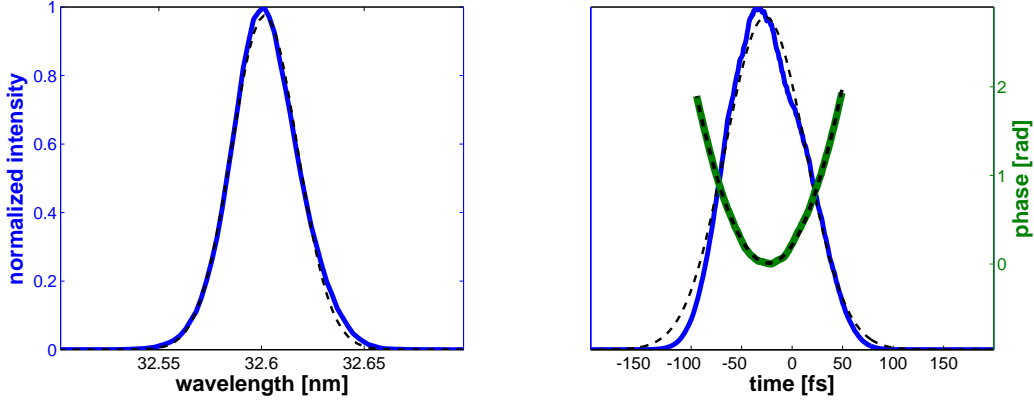

Figure III.11: Perseo output with linear frequency chirp $\beta = 10000\ fs^2$. Full lines are simulation results and dotted lines their interpolations (Gaussian for the intensity profiles and parabolic for the phase).

As shown in Fig. III.12, the duration of the FEL pulse increases as a function of the amount of chirp, and follows the duration of the seed (their ratio is always approximately 2.5 i.e., close to $n^{1/3} \approx 2.8$ as predicted in [127]). At the same time, the bandwidth grows due to the resonance along the electron bunch with the different central wavelengths of the seed (whereas, without chirp on the seed, the resonance is always centered on λ_n whatever the longitudinal position). But the latter effect is limited by the fact that, at some point, the seed becomes longer than the electron bunch. Another limit, that is not reached in this case, is the one of the gain bandwidth that is, in the low-gain regime in which we remain, $\Delta\lambda = \frac{\lambda}{N_r}$ where N_r is the number of radiator periods. Here $\Delta\lambda = \frac{32.6\cdot10^{-9}}{6\times44} \approx 0.12\ nm$.

Figure III.13 shows the evolution of the quadratic and linear terms of the phase of the FEL emission, as a function of the quadratic component of the phase of the seed pulse i.e., Γ_i. We see that phase curvature of the seed pulse is proportional to the quadratic phase of the FEL pulse. The linear phase term of the FEL pulse is also function of the quadratic seed phase.

Linear energy chirp on the electron beam   In general, the phase of the FEL pulse reproduces the energy chirp of the electron beam. A linear energy chirp generates a linear component of the phase in the emission, see Fig. III.14. Spectrally, this linear term in the temporal phase results in a shift of the central wavelength of the FEL radiation. The temporal coherence is not affected: for instance, in the presented simulation, the output pulse is only 1.14 times far from the Fourier-transform limit.
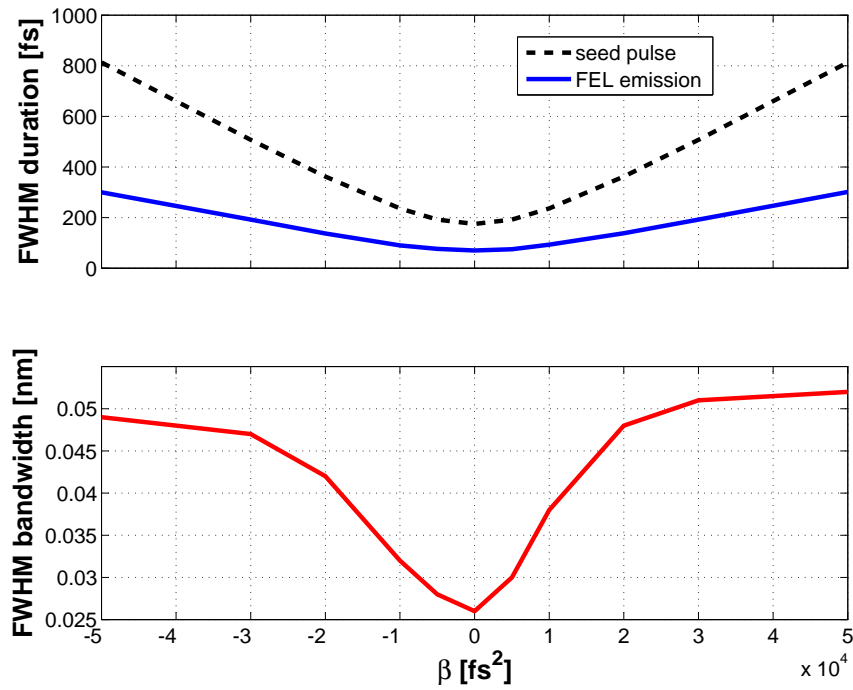
Figure III.12: In solid lines, FWHM duration (top panel) and bandwidth (bottom panel) of the FEL emission as a function of the β parameter, without chirp on the electron beam. In the top panel, the dashed line corresponds to the FWHM duration of the seed pulse.
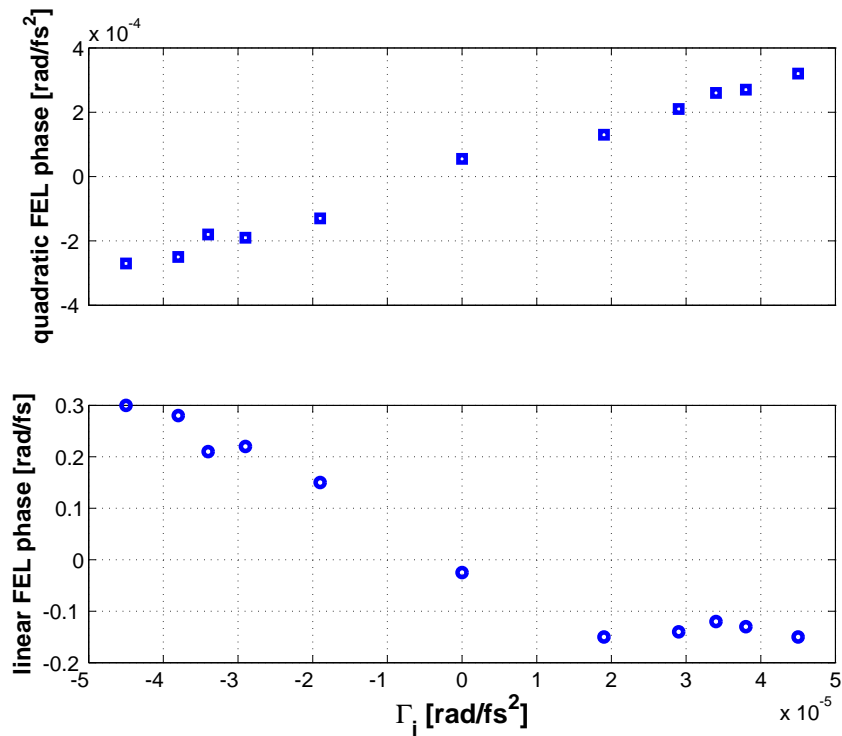

Figure III.13: Quadratic and linear terms of the parabolic interpolation of the temporal phase of the FEL emission as a function of the Γ_i parameter of the linearly-chirped seed. No chirp on the the electron beam.
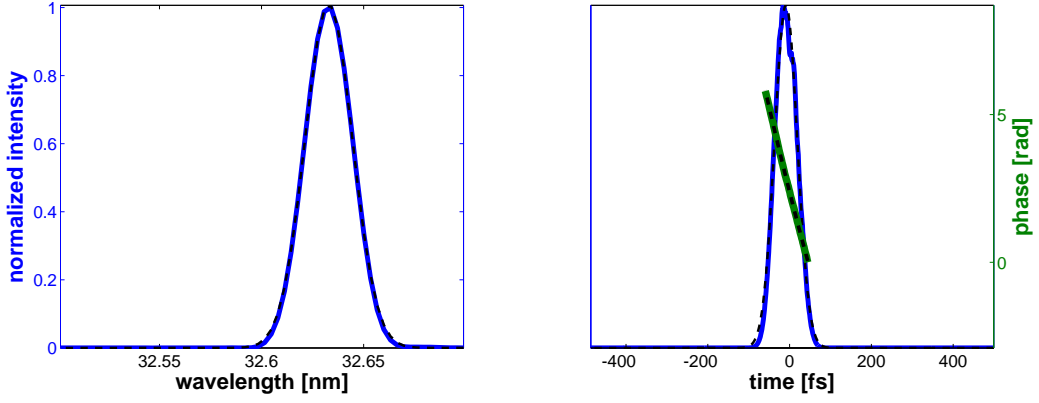
Figure III.14: Perseo output with $\chi_1 = 10 \ MeV/ps$, $\chi_2 = 0 \ MeV/ps^2$ and seed non-chirped. Full lines are simulation results and dotted lines their interpolations (Gaussian for the intensity profiles and parabolic for the phase).
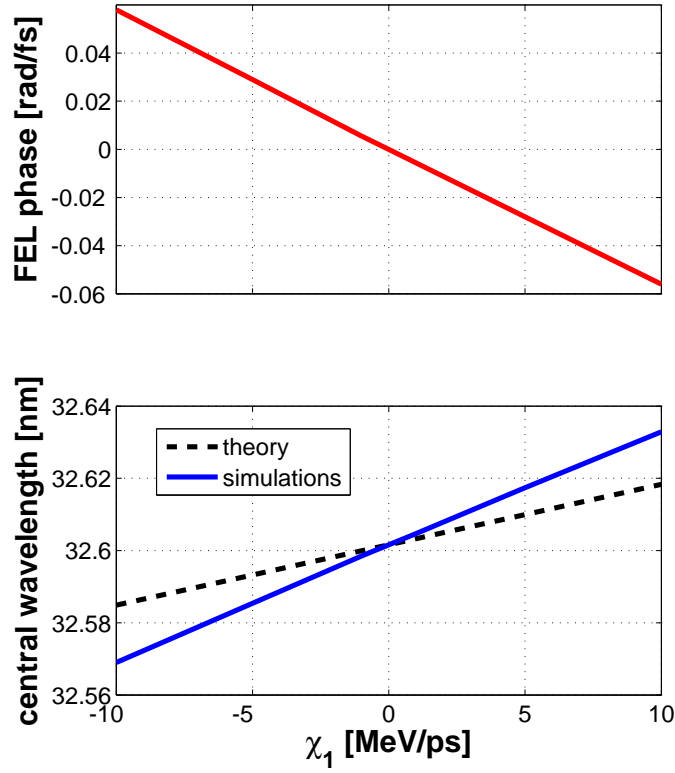

Figure III.15: Slope of the temporal phase of the FEL emission (top panel) and central wavelength of the FEL emission (bottom panel; solid line: simulations, dashed line: theory), as a function of χ_1, with $\chi_2 = 0 \ MeV/ps^2$ and seed non-chirped.

This effect is well-known and has been reported e.g., in [121], where the theoretical wavelength shift that is predicted is $\frac{\Delta\lambda}{\lambda} = R_{56} \cdot \frac{1}{E} \cdot \frac{dE}{dz}$. Figure III.15 reports the evolution of the slope of the FEL phase, as a function of the linear energy chirp. We see that, here again, it is directly proportional. On the bottom graph, we can see the central wavelength that is observed in sim-

ulations and the one predicted through the previous formula: the effective shift is higher than expected.

Quadratic energy chirp on the electron beam   Figure III.16 shows the result of a simulation where the seed is non-chirped but the electron beam presents a strong quadratic energy chirp. In agreement with what what was observed previously, the FEL phase mimics the electrons energy profile so that it is well fitted by a parabola. Since the pulse is not affected temporally, it results in a spectral broadening (left panel).
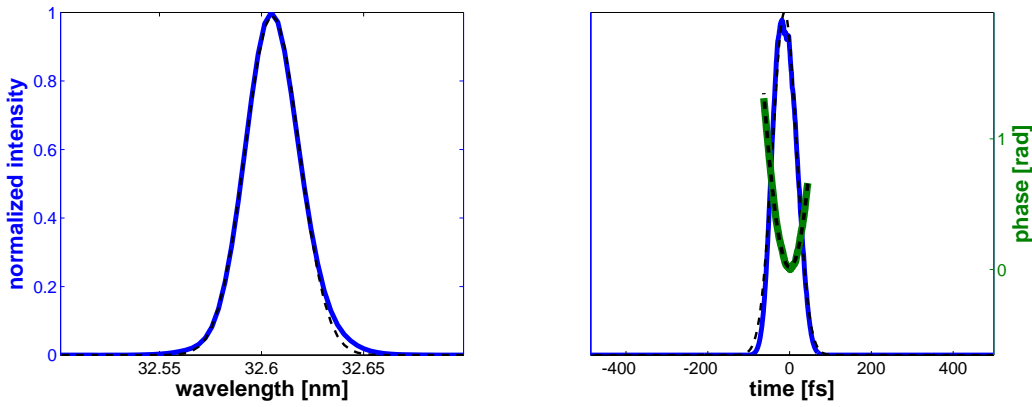

Figure III.16: Perseo output with $\chi_2 = 50\ MeV/ps^2$, $\chi_1 = 0\ MeV/ps$ and seed non-chirped. Full lines are simulation results and dotted lines their interpolations (Gaussian for the intensity profiles and parabolic for the phase).

Indeed, as shown in Fig. III.17, the duration is almost constant, whatever χ_2 is. The chirp brought by the electrons is added to the intrinsic chirp. The latter being positive, this explains the asymmetry of the curve in the bottom panel.

If we look at the evolution of the temporal phase of the FEL pulse (Fig. III.18), we observe the same behaviour as with the linear chirp on the seed. However, the effect of the latter is much stronger, especially because experimentally it is difficult to reach $\chi_2 > 10\ MeV/ps^2$. Here again, we see that the linear term of the FEL phase is proportional to the amount of quadratic chirp on the electrons. This does not imply that the central wavelength of the emission will be shifted: the phase is parabolic, not fully linear, as in the case where the energy chirp is linear. Hence, the slope of the phase depends on the position along the FEL pulse: this is why there is a spectral broadening instead of a wavelength shift (as it occurs for a linearly-chirped seed). For $\chi_2 = -5\ MeV/ps^2$ and $\chi_2 = -10\ MeV/ps^2$, the quadratic energy chirp compensates the presence of other phase terms in the FEL emission so that the latter comes close to 1.1 times far from the Fourier-transform limit and it is not possible any more to interpolate the phase by a parabola: higher-order terms become dominant at this boundary.
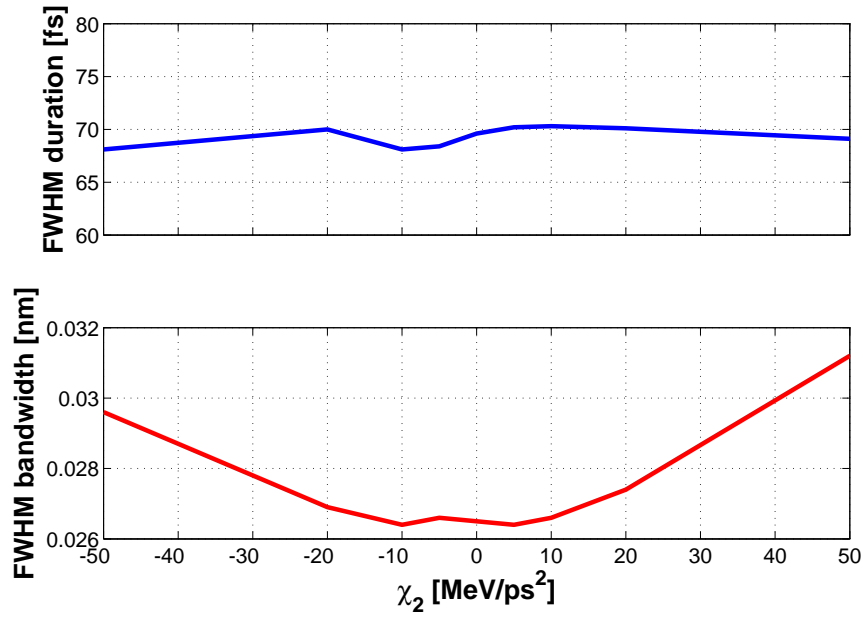
Figure III.17: *FWHM duration (top panel) and bandwidth (bottom panel) of the FEL emission as a function of the χ_2 parameter of the electrons energy, with $\chi_1 = 0 \, MeV/ps$ and seed non-chirped.*

Figure III.18: *Quadratic and linear terms of the parabolic interpolation of the temporal phase of the FEL emission as a function of the χ_2 parameter of the electrons energy, with $\chi_1 = 0 \, MeV/ps$ and seed non-chirped.*
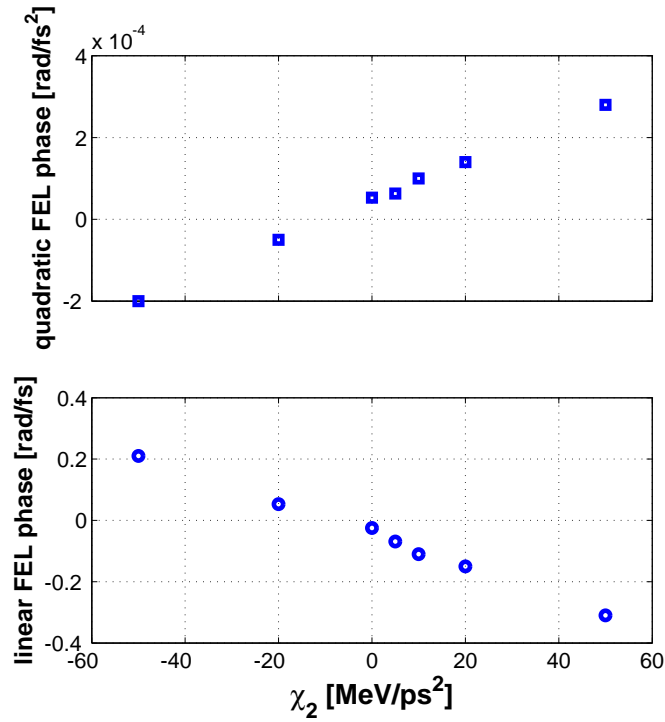
III.3.c Interplay

The quadratic energy chirp of the electrons, the linear frequency chirp of the seed, and the intrinsic chirp of the FEL process have similar effects. The "advantadge" of the first one is that

it is not correlated to a pulse lengthening. Its drawback is that it is less easy to control than the chirp of the seed. We will not focus on the linear chirp of the electrons, since its main and well-known effect is a shift of the central wavelength of the FEL emission.
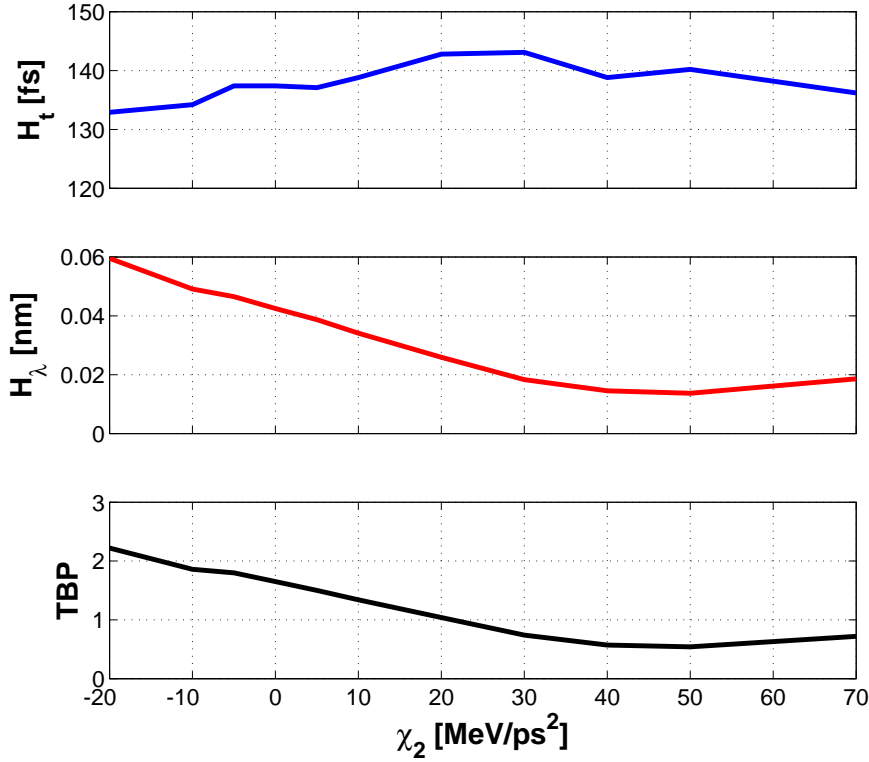

Figure III.19: Evolution of the FWHM duration (top panel), the FWHM bandwidth (middle panel) and the time-bandwidth product (bottom panel) of the FEL pulse, as a function of the quadratic energy chirp, for a down-chirped seed pulse ($\beta = -20000\ fs^2$).

Let us consider a situation where the seed is down-chirped (e.g., $\beta = -20000\ fs^2$) and let us try to compensate this chirp plus the intrinsic chirp by a proper quadratic energy chirp of the electrons in order to lower the time-bandwidth product of the FEL emission. Figure III.19 shows that, as expected, the duration (top panel) is almost constant but that a proper value of $\chi_2 \approx 50\ MeV/ps^2$ is able to minimize the spectral width (middle panel). Therefore, starting from a pulse that is 3.7 times far from the Fourier-transform limit for $\chi_2 = 0\ MeV/ps^2$, one reaches a time-bandwidth product $H_t \cdot H_v = 0.54$ for $\chi_2 = 50\ MeV/ps^2$ i.e., a pulse 1.2 times far from the Fourier-transform limit (for which $H_t \cdot H_v = 0.441$, assuming Gaussian temporal and spectral pulses), see bottom panel of Fig. III.19.

I have tried to evaluate how the different chirps compensate each other i.e., how the quadratic temporal phases that each of them induces in the FEL emission could be added. In fact, I found a very simple law. If we neglect the linear terms in the parabolic interpolations of the phase so

that the temporal phase is considered as quadratic only, it can be written as:

$$\varphi_{FEL}(\chi_2, \beta) = \varphi_{FEL}(\chi_2, \beta = 0) + \varphi_{FEL}(\chi_2 = 0, \beta) - \varphi_{FEL}(\chi_2 = 0, \beta = 0). \qquad \text{(III.23)}$$

In other words, the temporal phase of the FEL emission can be decomposed in a sum of the phases that are induced separately by each of the chirps. The first term of the sum is the phase of the FEL emission in the presence of a quadratic energy chirp only and the second term stands for the phase in the presence of the linear frequency chirp of the seed only. To them is substracted the intrinsic chirp of the FEL process, when no other chirp is present.

Simulations have been carried out for retrieving each single term of the previous equation. The values of the FEL phase obtained through the equation are compared to the "real" values predicted by simulations in Fig. III.20, as a function of the electrons chirp χ_2 and for two values of the seed chirp β. The agreement is very satisfactory.
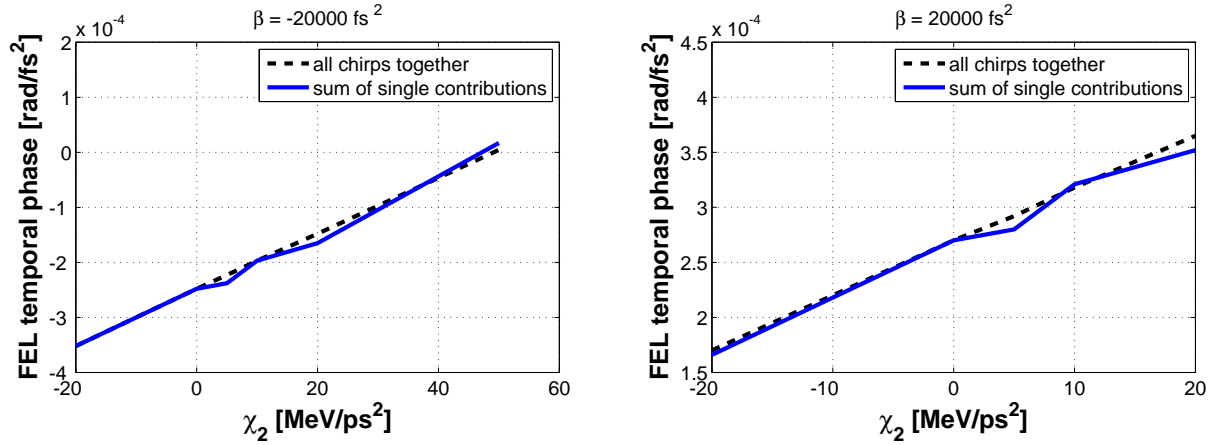

Figure III.20: Evolution of the quadratic term of the temporal phase of the FEL emission (dashed line) compared with the result of Eq. III.23 (solid line), as a function of χ_2, for a down-chirped (left panel, $\beta = -20000\ fs^2$) and an up-chirped (left panel, $\beta = 20000\ fs^2$) seed pulse. The results are taken from the outputs of Perseo simulations.

III.4   Summary

The emission of a seeded FEL can be frequency chirped. The sources of this chirp are the following: the frequency chirp of the seed pulse, the energy chirp of the electrons and the intrinsic phase that is induced within the FEL process. The final FEL phase can be equated to the sum of these three individual contributions. Simple numerical results have been presented in order to understand the effects of the different chirps on the FEL emission. The intrinsic FEL chirp can be usually neglected. The quadratic electrons energy chirp and the linear frequency chirp of the seed compete, and both induce a linear frequency chirp on the seed. However, whereas both induce a spectral broadening, only the frequency chirp of the seed is responsible for a FEL pulse lengthening. In the usual conditions encountered at FERMI@Elettra, the

contribution of the quadratic energy chirp of the electrons is relatively small with respect to the consequences of the seed frequency chirp. In this case, the electrons energy chirp can also be neglected, and the curvature of the FEL phase is thus directly proportional to the one of the seed and to the harmonic order: $\varphi_{FEL}(t) \approx n\varphi_{seed}(t) = n\Gamma_i t^2$. As I presented in the first part of this chapter, the spectro-temporal characteristics of the seed and the energy profile of the electron bunch are well known and can be easily measured and managed, allowing to develop the spectro-temporal studies discussed in the next chapter.

Effects of chirp in the seeded-FEL emission

Contents

IV.1 Spectral double peak

IV.1.a First observation and understanding

During the period of commissioning of summer 2011, E. Allaria and S. Spampinati observed for the first time the intringuing phenomenon displayed in Fig. IV.1 [122]. As the power of the seed gets higher, the total bandwidth increases and the spectrum splits in two, leaving a hole in the middle.

Ideally, the CHG emission can be seen, in the longitudinal (spectro-temporal) dimension, as a copy of the seed [123, 124], see Fig. IV.2a. However, this statement (which, in the temporal domain, is mainly an assumption or teh prediction of simulations due to the lack of temporal
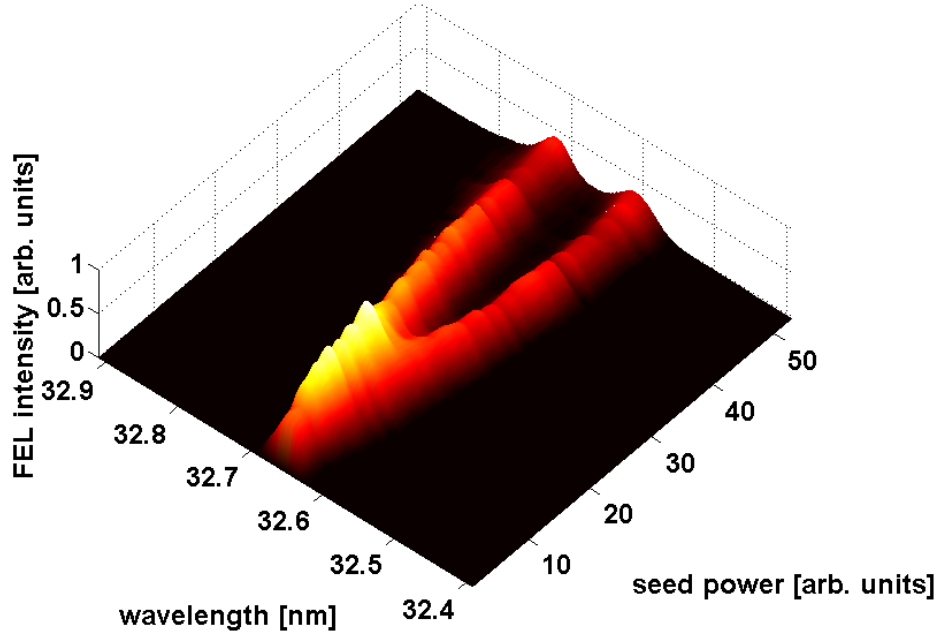
Figure IV.1: *First experimental evidence of the spectral separation between FEL peaks, as a function of seed energy per pulse.*

diagnostics in the vacuum-ultraviolet spectral range), is true only under certain limits. The explanation of the above phenomenon is the following: when increasing the seed power, the electron-beam modulation at the peak of the seed (the central position for a Gaussian) becomes too strong. The bunching is deteriorated and thus the FEL emission falls. On the contrary, the edge electrons experience a lower power level that well matches the bunching condition and, accordingly, the FEL signal starts growing in these regions. This scenario is represented in Fig. IV.2b. For a sufficiently high seed intensity, the FEL power at the central position almost vanishes and two consecutive pulses appear. This process is described in [125]. This phenomenon becomes particularly interesting if the seed is chirped i.e., if its frequency depends on the longitudinal position. As shown in Fig. IV.2c, in this situation the split pulses have also different frequencies. In other words, two independent pulses with two different frequencies are created. That is what we observe in Fig. IV.1.

The basic explanation of spectral splitting is simple. Let us recall Eq. III.15.:

$$\Delta\lambda = \frac{\lambda^2 \Gamma_i \Delta t}{\pi c},$$
(IV.1)

where λ is the central seed wavelength, Γ_i its chirp parameter (quadratic coefficient of the temporal phase, see Chapter III), c the speed of light, Δt the temporal distance between the sub-pulses and $\Delta\lambda$ their spectral separation. According to this equation, two portions of the electron bunch separated by a duration Δt see two different seed wavelengths separated by
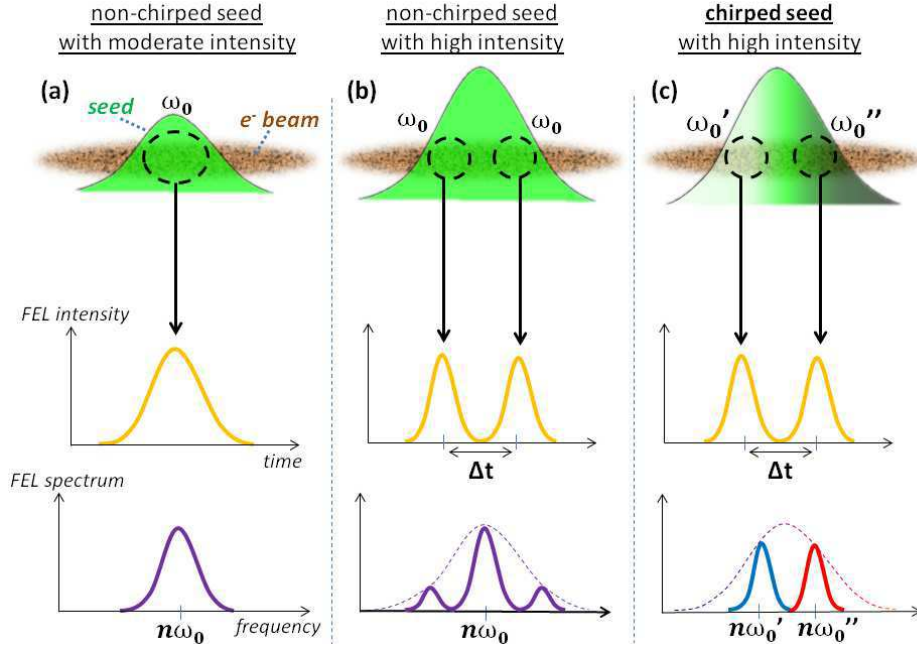
Figure IV.2: Sketch of the seed-electrons interaction and resulting FEL (temporal and spectral) outputs for different seed configurations: no chirp and moderate seed intensity (a), no chirp and high seed intensity (b), chirped seed with high intensity (c). In (a), the optimum seed-electrons interaction occurs around the center of the seed pulse so that the FEL output mimics the shape of the seed. In (b), the FEL pulse temporally splits in two because the seed power is too high in the middle of the pulse: a beating between the two sub-pulses involves a frequency modulation but the spectrum remains centered on a single peak at the harmonic n of the constant seed frequency ω_0. In (c), the chirp of the seed combined with the temporal pulse splitting leads to the creation of two separated spectral peaks corresponding to the harmonics of the frequencies ω_0' and ω_0'' at the respective position of each sub-pulse.

$\Delta\lambda$, λ being the center seed wavelength. At each of these two positions will grow a sub-pulse during the FEL process. If the radiators are tuned at the nth harmonic of the seed, and if the effect of both intrinsic and electrons' chirps are neglected (see Section III.3), the wavelengths of the peaks are separated by:

$$\Delta\lambda_n = \frac{\Delta\lambda}{n}. \tag{IV.2}$$

The knowledge of this separation and of the chirp parameters of the seed theoretically allows retrieving the temporal distance between the two corresponding sub-pulses. Indeed, according to Eqs. III.15 and IV.2:

$$\Delta t = \frac{n\pi c}{\Gamma_i \lambda^2}\Delta\lambda_n. \tag{IV.3}$$

For a given harmonic number n and seed wavelength λ, the temporal distance between the two sub-pulses is inversely proportional to the spectral separation $\Delta\lambda_n$ of their associated spectral peaks. As discussed in [126], this formula is reliable if the seed frequency chirp is dominant with respect to electrons energy chirp.

IV.1.b   Experiment

The main parameters of FERMI@Elettra relevant in the present work are listed in Table IV.1. The seed pulse and electron beam parameters are similar to the one presented respectively in Table III.1.d (standard configuration) and in Fig. III.9 (bottom panels).

Electron beam	Mean energy	$1005 - 1010 \ MeV$
	Peak current	$\approx 300 \ A$
	Duration FWHM	$1.5 \ ps$
	Linear chirp component χ_1	$1 \ MeV/ps$
	Quadratic chirp component χ_2	$7 \ MeV/ps^2$
Seed	Central wavelength	$261 \ nm$
	Temporal and spectral profiles	Gaussian
	Bandwidth FWHM	$0.8 - 1.1 \ nm$
	Duration FWHM	$\approx 200 \ fs$
	Energy	$10 - 150 \ \mu J$
Modulator	Period L	$10 \ cm$
	Number of periods	32
Dispersive section	R_{56}	$20 - 50 \ \mu m$
Radiators	Number	2
	Harmonic order n	6
	Period L	$5.5 \ cm$
	Number of periods	44

Table IV.1: Parameters of FERMI@Elettra relevant for most of the experiments reported in this paper. FWHM stands for the full-width at half maximum of the distribution. The R_{56} parameter is the momentum compaction factor characterizing the strength of the dispersive section [27]. The undulators were set so as to generate circularly polarized radiation, whose energy reached about $20 \ \mu J$ per shot.

Figure IV.3 shows a typical measurement of the FEL spectrum as a function of the seed power. By increasing the seed power, the portion of electrons getting over-modulated is lengthened and therefore the distance between the two sub-pulses grows, which leads to a higher separation of the spectral peaks. As shown by the insets, the spectra are very stable, allowing shot-to-shot repeatability of the two-colour emission.

Pictures of a "fork" have also been obtained by increasing the value of R_{56} in the dispersive section while keeping the seed intensity constant: indeed, it directly enhances the bunching. Figure IV.4 shows this phenomenon for a moderate value of the energy per pulse of the seed i.e., $72 \ \mu J$. At $R_{56} \approx 18 \ \mu m$, the single peak emission arrives a its maximum. The spectrum then begins splitting in two and at $R_{56} \approx 27 \ \mu m$, a clear separation can be seen. When increasing even more the strength of the dispersive section, a modulation appears between the two peaks (for $R_{56} \approx 32 \ \mu m$). For a stronger dispersive section, the intensity of this modulation becomes negligible with respect to the side peaks. This new peak then undergoes the same splitting process: two very small peaks can be seen in the central hole of the spectrum for $R_{56} \approx 38 \ \mu m$, between the two main peaks.
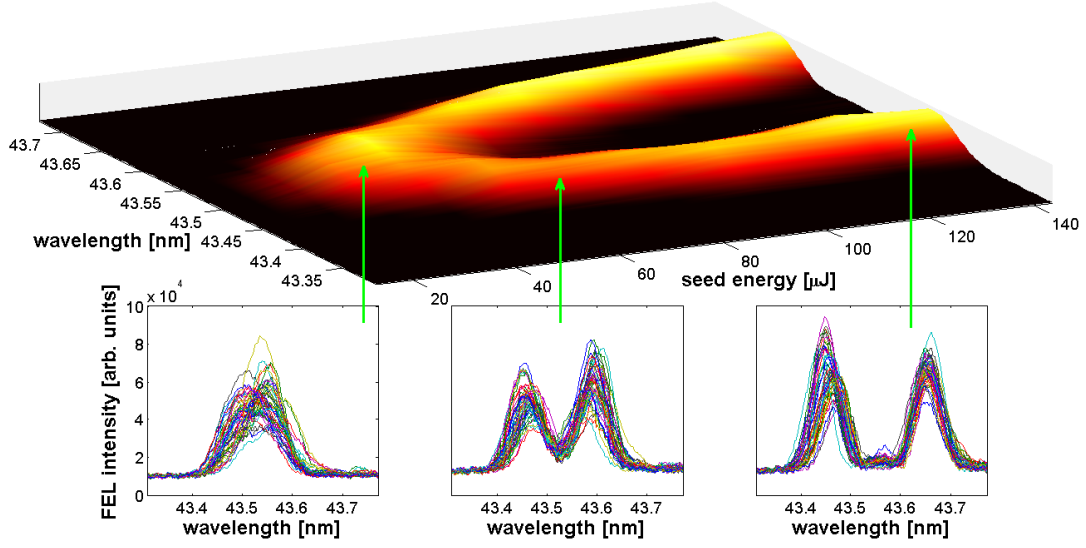
Figure IV.3: Experimental characterization of the spectral separation between FEL peaks, as a function of the seed energy per pulse. The insets show the spectrum of fifty consecutive shots, integrated at positions selected by the arrows on the projected figure (higher part).
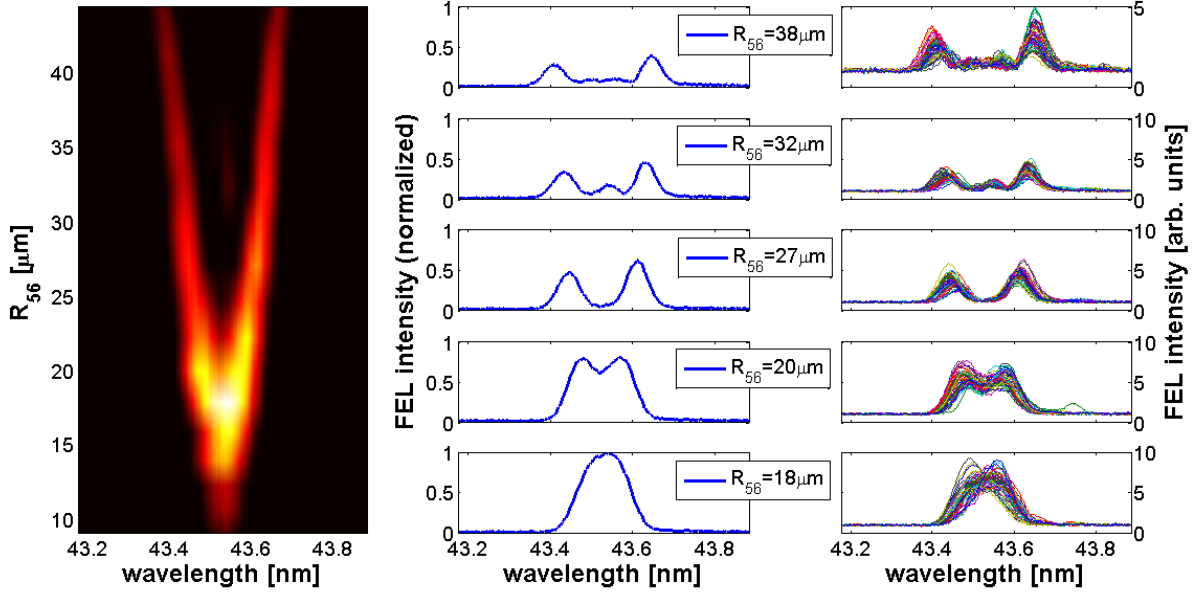
Figure IV.4: Experimental characterization of the spectral separation between FEL peaks, as a function of the R_{56} parameter of the dispersive section, for a seed pulse energy of $72\ \mu J$. Left: projected image of the spectra integrated over 50 successive shots; middle: integrated spectral profiles for selected values of R_{56}; right: corresponding series of 50 single spectra.

If we compare the splitting as a function of R_{56} for a moderate seed intensity (Fig. IV.5(a)) and for a stronger one (Fig. IV.5(b)), we see, without surprise, that similar splitting requires a lower value of R_{56} in the case of the stronger seed. On Fig. IV.5(b), one can distinguish the modulation that appears between the two peaks, at $R_{56} \approx 30\ \mu m$, and then splits also in two, behaving like the two main peaks. At the maximum strength of the dispersive section

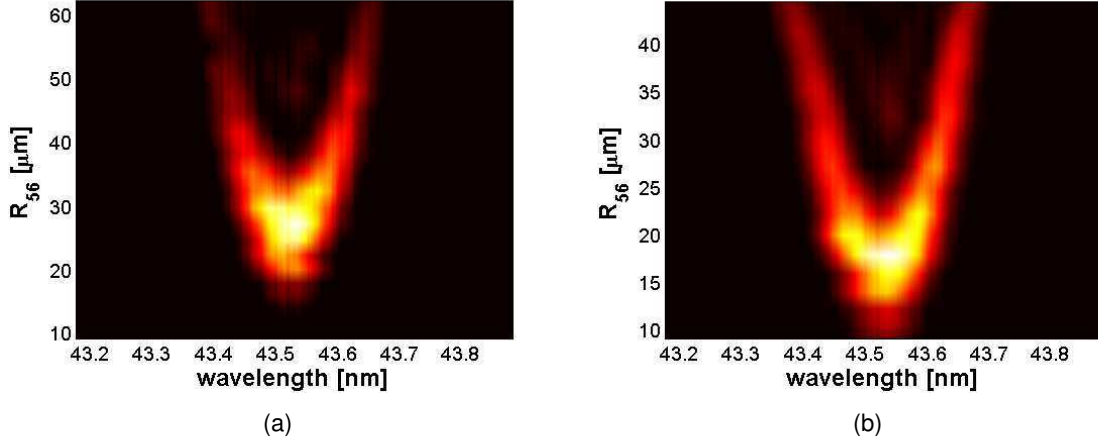($R_{56} \approx 45 \ \mu m$), a new central modulation starts rising again.

(a)   (b)

Figure IV.5: Spectral splitting as a function of R_{56} for an energy per pulse of the seed of $36 \ \mu J$ (a) and $72 \ \mu J$ (b).

Similarly to Fig. IV.5, Fig. IV.6 shows the spectral splitting, but as a function of the seed energy, and for different fixed values of the R_{56}. For $R_{56} = 17.9 \ \mu m$ (Fig. IV.6(a)), no clear splitting occurs, the FEL radiation is simply amplified to its maximal bandwidth, for seed energies $> 100 \ \mu J$. For higher values of R_{56} (Figs. IV.6(b), IV.6(c) and IV.6(d)), the splitting is made possible thanks to a sufficiently strong dispersive section. Increasing the strength of the latter makes the double peak appear for lower seed energies and widens the spectral separation between the two peaks. In Fig. IV.6(c), the central modulation can be seen and in Fig. IV.6(d) the latter splits also in two due to the high value of R_{56}. In the latter case, the spectrum is thus composed of two main peaks and, in between, two secondary peaks whose height is about 10% of the height of the main peaks. Although these secondary peaks seem negligible, one should take care of the following: if their intensity (which is the experimentally measured parameter) is, for instance, $I_{secondary} \approx 0.1 I_{main}$ (I_{main} being the intensity of the main peaks), it means than the amplitude of their electric field is $E_{secondary} = \sqrt{I_{secondary}} = \sqrt{0.1 I_{main}} \approx 0.32 E_{main}$ i.e., about one third of the electric field amplitude of the main peaks... which is much less negligible.

There are clearly two main differences between the patterns of Figs. IV.5 and IV.6:

1. In the second case, the spectral broadening is not symmetric so that the forks are also asymmetric.

2. In the first case, just after the splitting begins, the signal of the two peaks decreases, which does not seem to be true in the second case.

Concerning 1), a possible explanation may be due to the position of the seed pulse with respect to the electron bunch. For these measurements, the seed pulse may not have been placed at the center of the parabola of the energy profile of the electrons (see Fig. III.9, lower panels), but slightly towards the head. In this case, the first sub-pulse (corresponding to longer
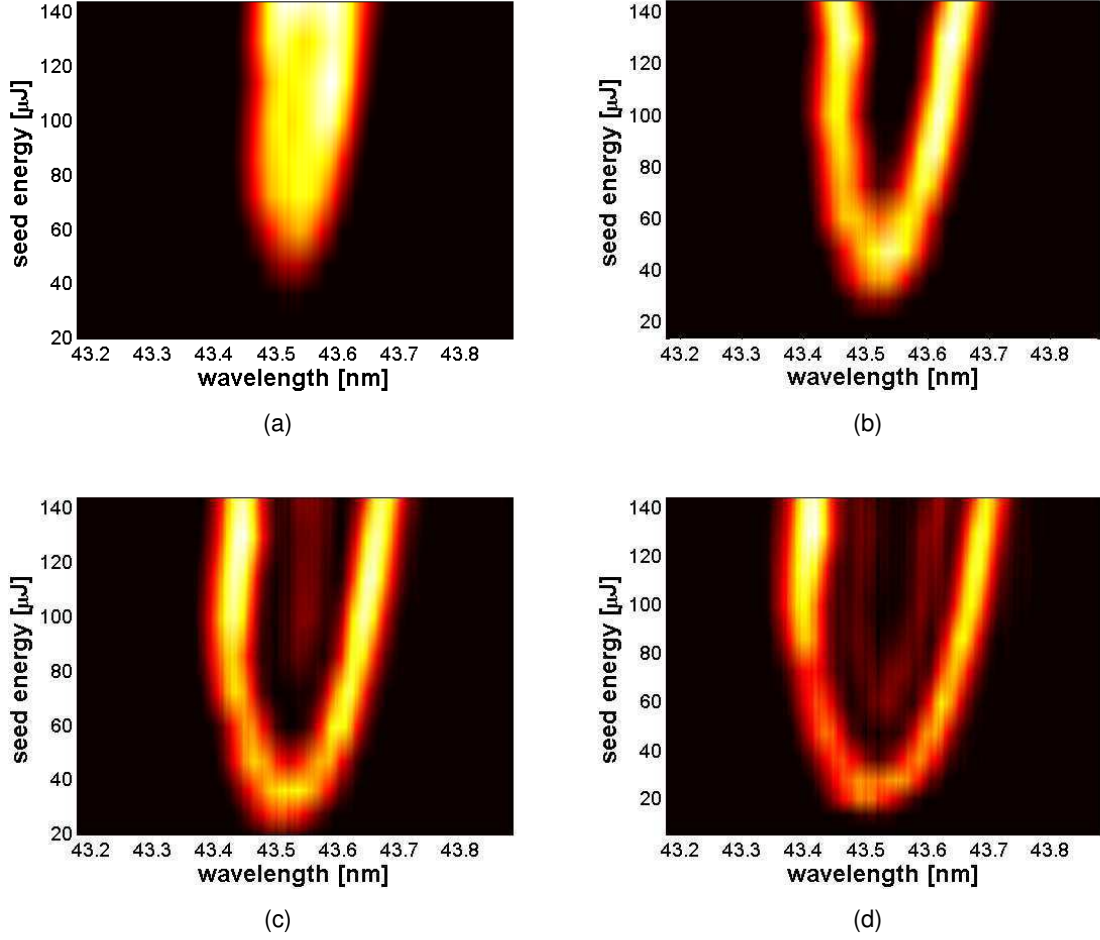
Figure IV.6: Spectral splitting as a function of seed energy for $R_{56} = 17.9 \ \mu m$ (a), $R_{56} = 23.4 \ \mu m$ (b), $R_{56} = 29.6 \ \mu m$ (c) and $R_{56} = 36.6 \ \mu m$ (d).

wavelengths) undergoes a strong local linear energy chirp of the electrons, which results in a shift towards longer wavelengths, while the second sub-pulse is closer to the center of the parabola and less affected by electrons' chirp. This might be the reason why, in Fig. IV.6, the left part of the spectral patterns (or left branch of the forks, shorter wavelengths) do not behave as the right parts (longer wavelengths).

For studying 2), let us look at the overall variation of energy emitted by the FEL as a function of the parameter that drives the temporal splitting i.e., the strength of the dispersive section (Fig. IV.7, for two different values of the seed energy) or the energy of the seed pulse (Fig. IV.8, for three different values of R_{56}). In both cases, there is a similar increase of the FEL power until a turning point is reached corresponding to the value above which the FEL spectrum starts splitting in two. After that, the behaviour is different: in the first case (Fig. IV.7 i.e., variation of R_{56}), the overall intensity of the FEL radiation slowly decreases, whereas it keeps on growing slowly in the second case (Fig. IV.8 i.e., variation of seed energy). Thus, even if the dispersive section and the intensity of the seed pulse have similar effects on the bunching, the strength

of the first one is more likely to degrade the output signal. It could be the sign that the spatial modulation (provided by the dispersive section) is more "sensitive" than the energy modulation (initiated by the seed): R_{56} requires a finer tuning than the seed intensity.
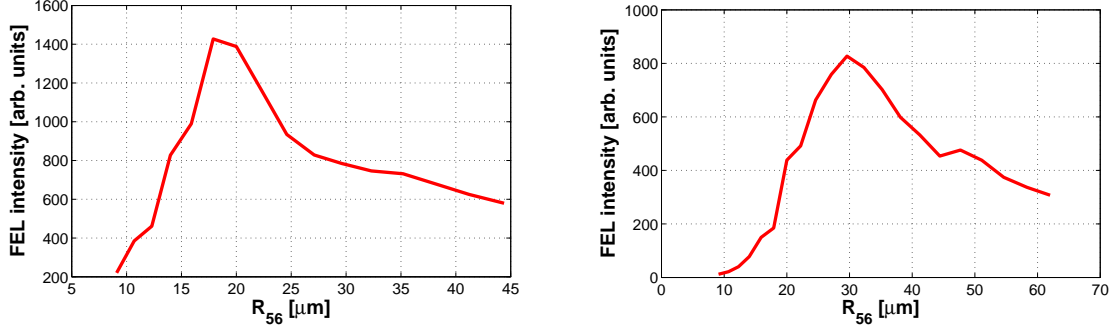

Figure IV.7: *Overall intensity of the FEL radiation as a function of R_{56} for an energy per pulse of the seed of* $72\ \mu J$ *(left) and* $36\ \mu J$ *(right).*
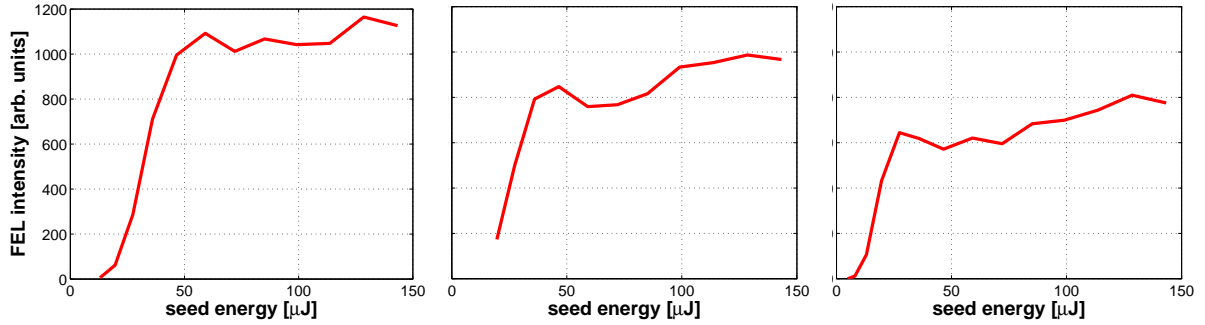

Figure IV.8: *Overall intensity of the FEL radiation as a function of the seed energy for different values of R_{56}:* $23.4\ \mu m$ *(left),* $29.6\ \mu m$ *(middle) and* $36.6\ \mu m$ *(right).*

The relative height of the peaks can be adjusted by changing the resonance condition of the FEL (see Chapter I), which can be done easily by changing the undulators' gaps. It is shown in Fig. IV.9. The spectrum represented by the dotted line in Fig. IV.9 corresponds to a central tuning of the undulators. Instead, the data represented by the full line have been taken for a slight negative detuning and, even if both peaks can be seen, the one at shorter wavelength is significantly stronger. The dashed curve shows a situation where the detuning is positive, which implies a stronger amplification of the peak at longer wavelengths, the other one being almost suppressed.

Now that the spectral properties of the splitting have been well characterized, it is interesting to use Eq. IV.3 in order to retrieve the temporal distance between the two temporal sub-pulses corresponding to each of the two peaks. For instance, Fig. IV.10 shows this estimation for the data reported in Fig. IV.5.

For the same value of R_{56} e.g., $40\ \mu m$, one obtains two different possible working points: if the seed energy is $36\ \mu J$ (left panel of Fig. IV.10), we have $\Delta\lambda_6 = 0.15\ nm$ and $\Delta t = 225\ fs$ while
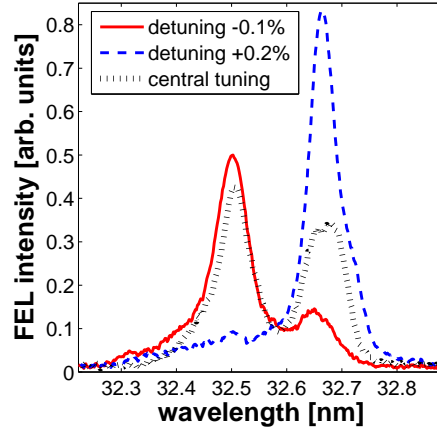
Figure IV.9: *Double peak for different tuning conditions of the radiators. The radiators are tuned at the 8th harmonic of the seed (32.6 nm). Here the seed energy per pulse is about 70 µJ and $R_{56} = 60$ µm. The configuration of the rest of the machine was different than the one described in Table IV.1: the radiators were tuned at the 8th harmonic of the seed (32.6 nm), $R_{56} = 60$ µm and the electron beam had following parameters: mean energy 1175 MeV, $\chi_1 \approx 0$ MeV/ps, $\chi_2 \approx 10$ MeV/ps^2, FWHM duration 0.8 ps, peak current ≈ 600 A.*
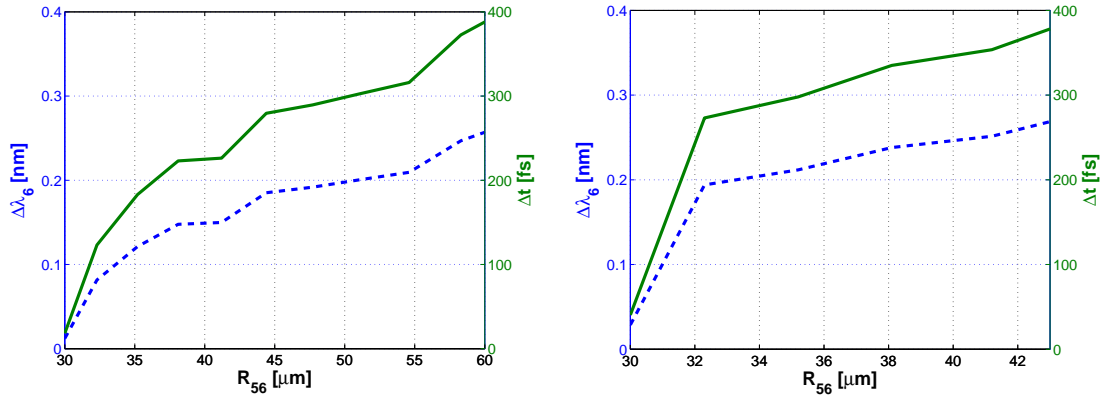

Figure IV.10: *Spectral separation of the two peaks (dashed line) and retrieval of the temporal distance between the sub-pulses (full line) as a function of R_{56} for an energy per pulse of the seed of 36 µJ (left) for which $\Gamma_i \approx 5.5 \cdot 10^{-5}$ fs^{-2} and 72 µJ (right) for which $\Gamma_i \approx 5.9 \cdot 10^{-5}$ fs^{-2}.*

$\Delta\lambda_6 = 0.25$ nm and $\Delta t = 350$ fs for a seed energy of 72 µJ (right panel of Fig. IV.10). Changing Γ_i (while keeping the same all other parameters), one can control the spectral separation between the peaks, maintaining Δt invariant. This is shown in Fig. IV.11. In the case in which a piece of CaF_2 is added in the seed's path (spectrum in full line), the Γ_i is decreased by about 30% but, at the same time, the peaks separation is increased by about 30% (from 0.9 nm to 1.2 nm), with respect to the situation where the seed is in its "standard" configuration (spectrum in dashed line) (see Table III.1.d). Hence, according to Eq. IV.3, the temporal distance between the sub-pulses is the same is both cases (approximately 200 fs). It is worth noting that, for a given configuration of the seed (standard, addition of dispersive material, compressor stage – see Table III.1.d), Γ_i varies a function of the power delivered by the seed. However, unless the difference of seed intensity is large, the values of Γ_i remain quite close and, experimentally, the
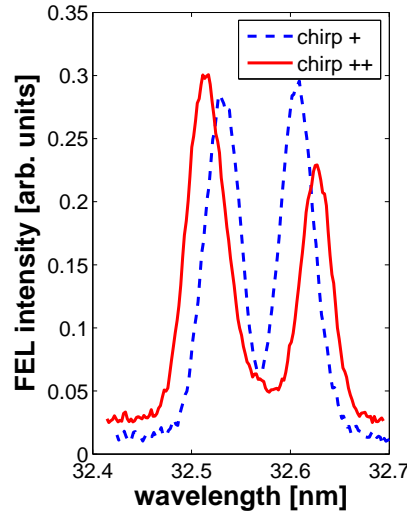
Figure IV.11: Double peak for two different chirp values of the seed (b), corresponding to the standard positive chirp ("chirp +", $\sigma_\lambda \approx 0.45\ nm$ and $\sigma_t \approx 90\ fs$, with a seed energy of $\approx 70\ \mu J$) and a stronger chirp ("chirp ++", $\sigma_\lambda \approx 0.5\ nm$ and $\sigma_t \approx 160\ fs$, with a seed energy of $\approx 75\ \mu J$) induced by adding a piece of CaF_2 of 5-cm thickness. The radiators were tuned at the 8th harmonic of the seed (32.6 nm), $R_{56} = 80\ \mu m$ and the electron beam is similar the one shown in the top half of Fig. III.9.

difference is small and thus at the level of the uncertainty. It it thus better to change configuration, as was done for obtaining the results shown in Fig. IV.11, in order to get a significantly different Γ_i.

A last interesting result is shown in Fig. IV.12, in which the FEL spectrum is studied as a function of the position of the seed pulse with respect to the electron bunch, whose longitudinal properties are shown in Fig. IV.13. At delay $\approx -0.8\ ps$, the seed arrives on the tail of the
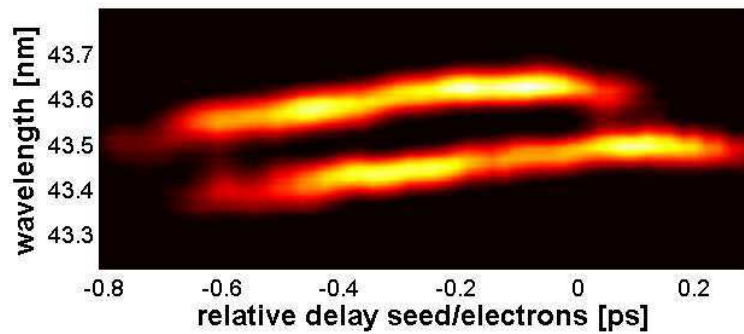
Figure IV.12: FEL spectrum at the 6th harmonic of the seed (43.5 nm), as a function of the relative delay between the seed pulse and the electron beam. At the zero value of the delay, the seed pulse is approximately centered on the bunch of electrons. The dispersive section and seed energy were set, respectively, to 23 μm and 80 μJ.

bunch, so that the first peak appears (at larger wavelength, since the frequency chirp of the seed, that is transmitted to the FEL emission, is positive). Then, as the value of the delay grows, the whole seed is coupled to the bunch, and, for a delay $\approx -0.6\ ps$, also the second peak (at shorter wavelength) appears. As we remarked in Section III.3, a linear energy chirp of the

electron energy induces a spectral shift of the FEL emission. Hence, when they appear, both peaks are detuned towards shorter wavelengths, because the seed experiences a strong local negative slope of the electron beam chirp. By further increasing the delay (i.e., moving from the tail to the head of the bunch), the peaks central wavelengths drift, due to the increase of the local linear chirp of the electron energy distribution. However, the relative heights and respective widths of the spectral peaks remain practically constant, so as their separation $\Delta\lambda_6 \approx 0.17 \ nm$. The wavelength drift goes on until the center of the parabola of the electrons energy profile is reached, for a delay $\approx 0 \ ps$. Soon after that, the lasing becomes less efficient and each peak disappears one after the other, in the same order as they appeared. The reason why the lasing does not remain efficient on the whole bunch is still an open question: possible reasons are the lower charge on the second half of the electron bunch (see Fig. IV.13, right picture) and/or a degradation of the transverse electron-beam properties. As will be detailed in the simulations presented later on, in our conditions the curvature of the electrons energy profile is too small to have a significant effect on the FEL bandwidth and thus, on the peaks' separation. But in any case, for a parabolic electrons' energy profile, the quadratic component is constant all along the bunch, which explains why $\Delta\lambda_6$ is also constant all along the bunch.
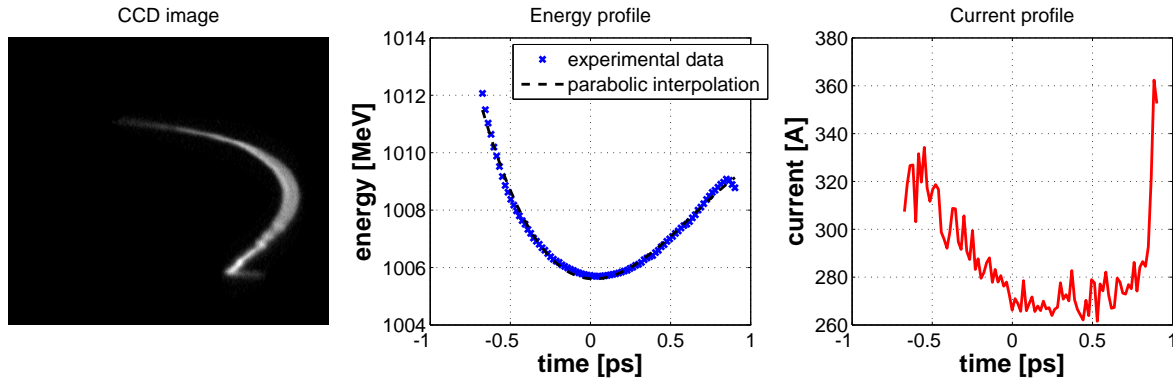
Figure IV.13: Longitudinal phase space measured at the end of the FERMI@Elettra linac for the results shown in Fig. IV.12. Left: image observed by a CCD on the YAG crystal; center: analysis of the left picture, showing the energy profile; right: analysis of the left picture, showing the current profile. Larger values of time correspond to a displacement from the tail to the head of the bunch.

IV.1.c Simulations

Fig. IV.14 compares a typical measurement of spectral splitting with what has been obtained with Perseo simulations, using similar experimental parameters. As it can be seen, the experimental pattern of spectra (Fig. IV.14(a)) is well reproduced by the simulations (Fig. IV.14(b)). In the latter, the arm of the fork at larger wavelengths is favoured. Since the chirp of the seed, and thus of the FEL emission, is positive, this corresponds to the first sub-pulse: the arm at lower time values (Fig. IV.14(c))) has a higher signal. Obviously, according to simulations, the spectral and temporal patterns are very similar: this will be discussed in the Section IV.2.

(a) experiment   (b) simulations   (c) simulations

Figure IV.14: *Comparison of the experimental observation of the spectral splitting (a) with the spectral splitting retrieved by simulations (b). The corresponding (simulated) temporal pattern is shown in (c).*
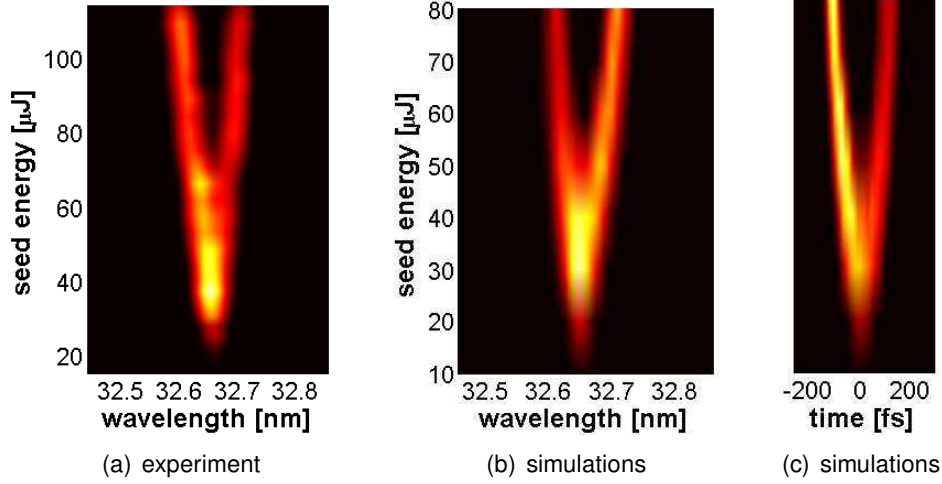
As it has been shown experimentally (see Fig. IV.9), the relative height of the peaks, that is different in the previous figure, can be easily controlled by changing the resonance conditions of the undulators. This is demonstrated also by simulations carried out with the 3D code Genesis (Fig. IV.15).

We now consider the conditions of the machine in which the results of double-peak production have been obtained (see Section IV.1.b).

IV.1.c.1   Case 1: realistic electron beam

A typical series of simulations carried out with the Perseo code leads to the spectral and temporal patterns shown in Fig. IV.16. The electron beam energy profile that has been considered is similar to the one reported in the bottom panel of Fig. III.9. The following parameters have been taken: $\chi_1 = 1\ Mev/ps$, $\chi_2 = 7\ Mev/ps^2$, emittance 1 $mm.mrad$, relative energy spread 0.01%, peak current $300\ A$. The radius of the seed has been considered as constant along the modulator (standard deviation of the transverse intensity distribution: $300\ \mu m$). The bandwidth and the duration of the seed have been experimentally characterized; they grow linearly as a function of the seed energy in the following ranges: $\sigma_\lambda = 0.35 - 0.45\ nm$ and $\sigma_t = 70 - 90\ fs$. If we consider the spectrum (left picture), the pattern is very similar to what has been obtained experimentally e.g., in Figs. IV.4 and IV.3. The splitting occurs for seed energies higher than $60\ \mu J$, corresponding to an intensity of $40\ GW/cm^2$. At seed energies higher than $100\ \mu J$, corresponding to an intensity of $60\ GW/cm^2$, the central modulation appears, both spectrally (left picture) and temporally (right picture).

The evolution of the FEL power as a function of the input seed signal (Fig. IV.17) is similar to what has been obtained experimentally. The FEL power first grows, reaching a peak before
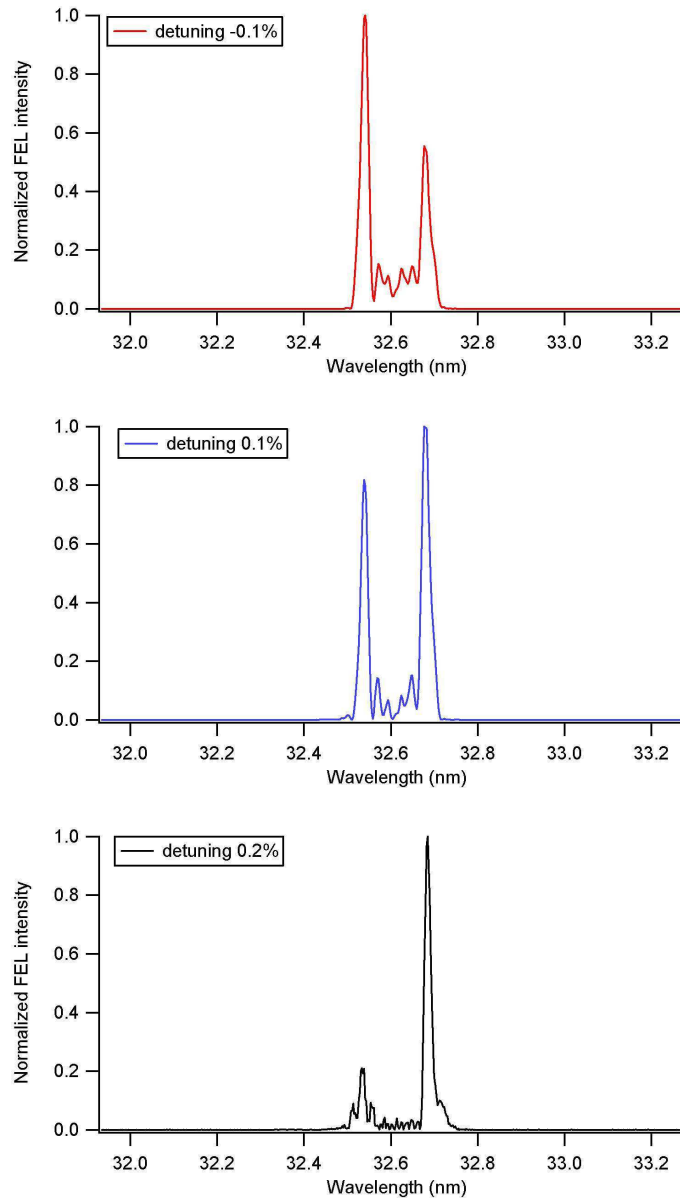
Figure IV.15: *Control of the relative height of the spectral peaks by changing the tuning condition of the undulators. Left: slight detuning towards shorter wavelengths (−0.1%); center: slight detuning towards longer wavelengths (+0.1%); right: strong detuning towards longer wavelengths (+0.2%).*

the splitting and then the overall power of the split pulses remains constant, even if lower than the overall power before splitting. In this respect, the result given by the simulation is slightly different with respect to what was obtained experimentally in Fig. IV.8, where the FEL signal was keeping on growing.

Let us look at the characteristics of the pulse before splitting (Fig. IV.18), which is well fitted by a gaussian: without surprise, while the signal of the FEL grows, both the duration and the bandwidth of the FEL emission increase, the evolution being exponential. In the temporal domain, this is explained by the fact that, when increasing the seed power, a larger part of the electron bunch receives the sufficient energy to get well bunched. Appropriate bunching
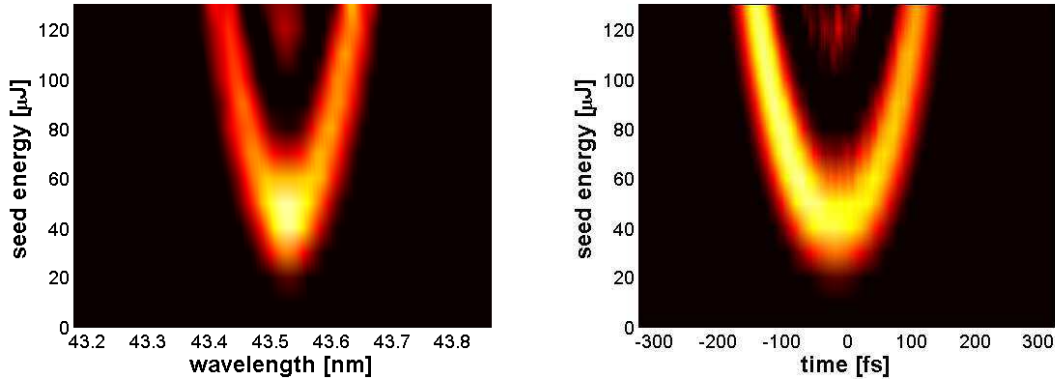
Figure IV.16: Output of Perseo simulations in the spectral (left) and time (right) domains.
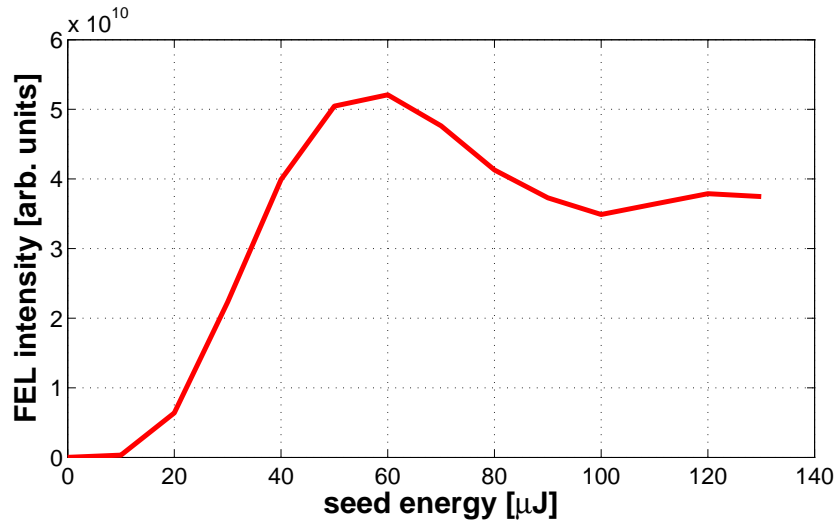
Figure IV.17: Evolution of the overall intensity of the FEL radiation, as a function of the seed energy.

conditions occur for a longer portion of the seed, which means also that a larger bandwidth is amplified since the seed is chirped: the "new" portions of the seed generating a sufficient bunching correspond to "new" wavelengths that are amplified. Consequently, as it is shown in the left panels of Fig. IV.18, the ratio FEL vs. seed duration and the ratio FEL vs. seed relative bandwidth are almost equal.

At saturation, Stupakov [127] predicts that the duration of the FEL pulse is equal to the one of the seed divided by $n^{1/3}$. According to it, we should obtain here that $H_t^{FEL} \approx 0.55 H_t^{seed}$. This is true for a seed energy $\sim 30~\mu J$, but at $\sim 50~\mu J$, the FEL duration almost reaches the one of the seed, since only the edges of the latter don't have enough intensity to induce the bunching of the electrons. However, as it is shown in Fig. IV.19, for a seed energy of $\sim 50~\mu J$, the temporal profile of the FEL pulse becomes slightly distorted, which corresponds to saturation. Hence, sufficently far from saturation, the Stupakov law is quite reliable, as it has been already checked in the previous chapter, where the simulations were done in the limit of clean spectral and temporal profiles, characterizing a situation of non-overbunching.
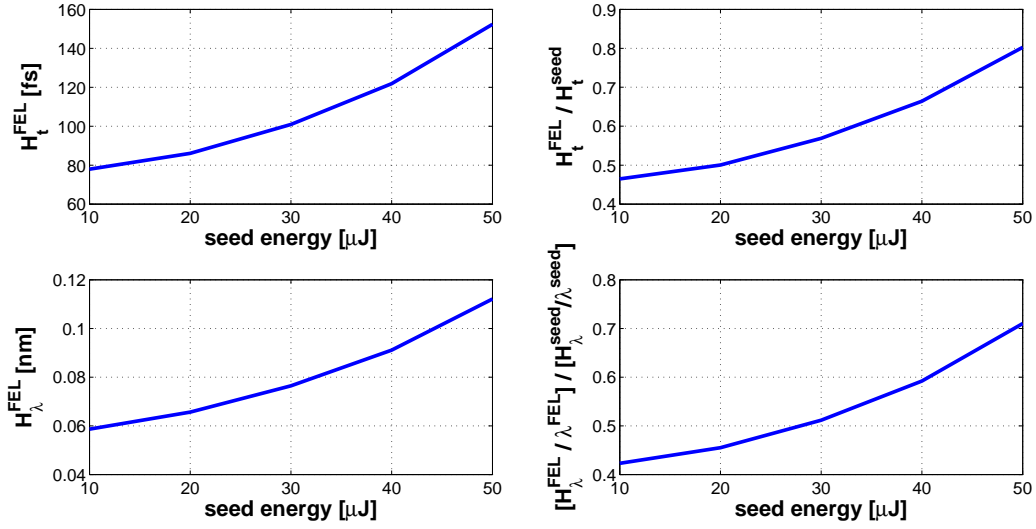
Figure IV.18: Temporal and spectral properties of the FEL emission before the regime of pulse splitting as a function the seed energy. Top left: FWHM duration of the FEL pulse. Bottom left: FWHM bandwidth of the FEL pulse. Top right: ratio of the FWHM duration of the FEL pulse vs. the one of the seed pulse. Bottome right: ratio of the relative bandwidth of the FEL pulse vs. the one of the seed pulse.
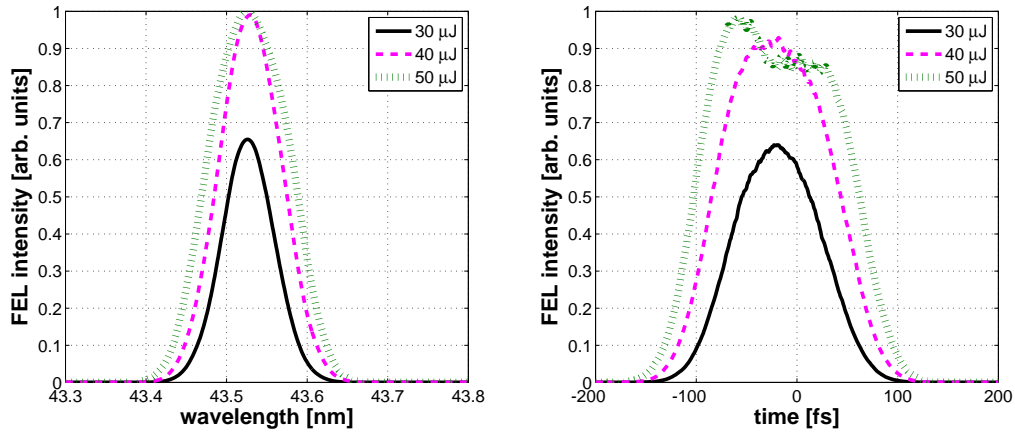
Figure IV.19: Spectral (left) and temporal (right) profiles of the FEL emission for an energy per pulse of the seed of 30 μJ (full line), 40 μJ (dashed line) and 50 μJ (dotted line).

From all this information about the bandwidth and the duration, it is possible to calculate the time-bandwidth product of the FEL pulse before splitting (Fig. IV.20). Since both the duration and bandwidth follow an exponential growth, the time-bandwidth product has the same behaviour as a function of the energy of the seed pulse. The time-bandwidth product of the latter increases also as a function of its energy since the spectrum is broadened at high intensities due to self-phase modulation. But this is not the major cause of the high time-bandwidth product of the FEL emission. Indeed, this cause is a minor one with respect to the fact that, as described before, the higher the seed energy, the longer the FEL duration and the broader the FEL spectrum: not only the FEL duration or the FEL bandwidth increase, but both! Moreover, as discussed in [128],

the higher the harmonic number, the higher the impact on the FEL emission. In other words, the time-bandwidth product is expected to be even more important at lower wavelengths.
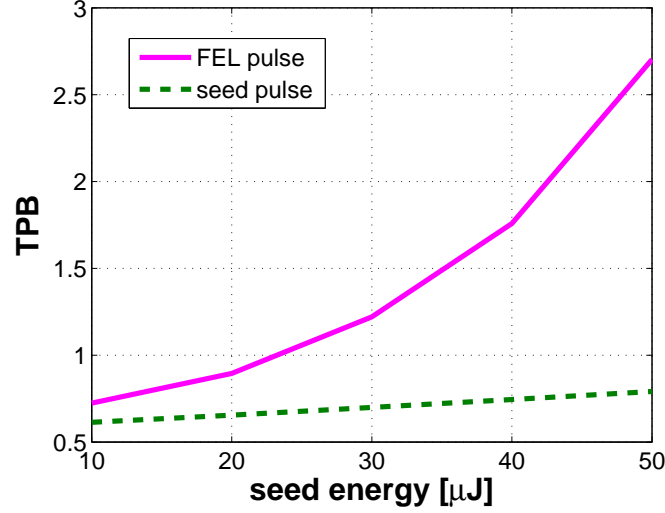
Figure IV.20: Time-bandwidth product of the FEL pulse before splitting (full line) and of the seed pulse (dashed line), as a function of the seed energy per pulse.

Let us now study the double peak emission, which is correlated to seed energies higher than $80\ \mu J$ (for a clear separation). Both temporally and spectrally, the peaks are well fitted by gaussians. Hence, the data analysis is made by taking advantage of these gaussian interpolations of the peaks. This makes things easier, since one can define the FWHM bandwidth/duration, the central wavelength of a peak, the temporal separation of the peaks, etc. Figure IV.21 shows the temporal separation of the two peaks as a function of the seed energy. The full line corresponds to the direct results of the simulations, while the dashed one to the estimation that can be made by means of Eq. IV.3 from the knowledge of the spectral separation between the peaks (i.e., the simulation results in the spectral domain). The agreement is good but not perfect. As it will be discussed later, this can be partly attributed to the presence of the electrons' chirp.

In Fig. IV.22, the spectral separation given by the simulations is associated to the temporal distance between the sub-pulses. This curve of $\Delta\lambda$ vs. Δt is a precious piece of information if someone wishes, for instance, to perform pump-probe experiments with the two split pulses and thus to know the time that separates them.

Fig. IV.23 shows the ratio between Δt and the FWHM duration of the seed as a function of the seed energy. This provides information on the positions at which occurs the lasing of each peak. For a seed energy of $100\ \mu J$, the lasing thus corresponds to positions where the electron bunch experiences half of the maximum seed peak power. At these positions, the bunching is optimum. The similar curve (right panel) is drawn for the ratio between the peaks separation and the seed relative bandwidth, and the evolution mimics the previous curve, which is normal since the chirp of the seed is linear.
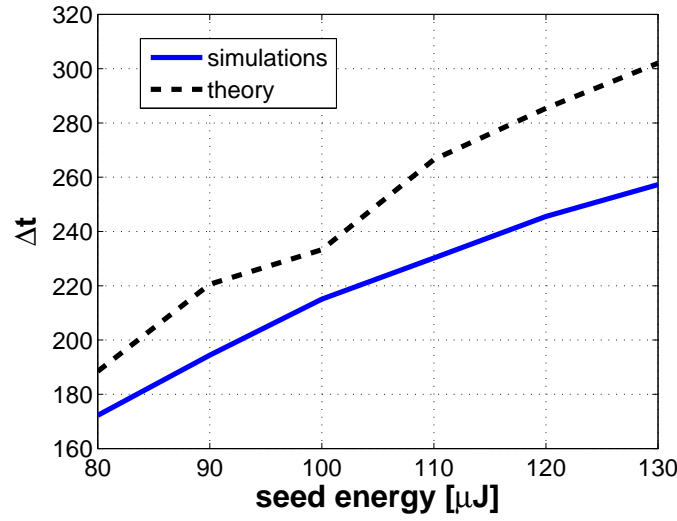
Figure IV.21: Evolution, as a function of the energy delivered by the seed, of the temporal distance between the split pulses, retrieved in the simulations (full line) and estimated by Eq. IV.3 (dashed line).
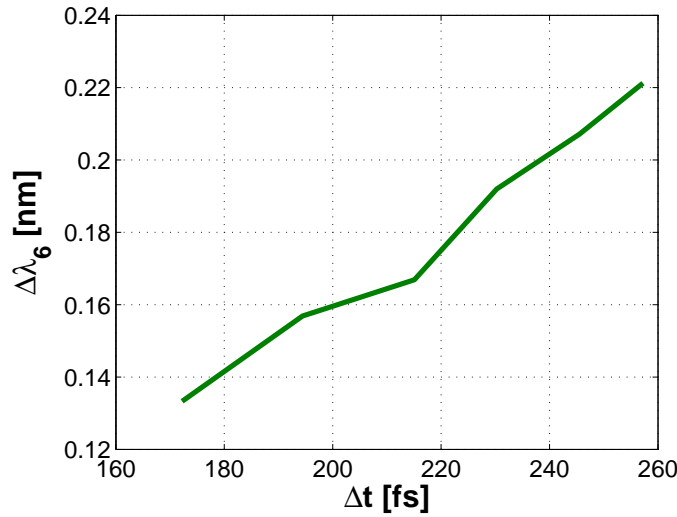
Figure IV.22: Correlation between the peak distance in the spectral and temporal domains, being function of the seed energy (see Fig. IV.21).

Now, if we look at the time-bandwidth product of the single peaks (Fig. IV.24), we see a very interesting thing: the time-bandwidth product decreases as a function of the strength of the splitting. For high seed energies, both peaks come very close to the Fourier limit, characterized by a time-bandwidth product of 0.441. In other words, starting from a relatively "poor" spectro-temporal quality of the FEL pulse in the "normal regime" (before splitting, see Fig. IV.20), one produces two sub-pulses that are almost Fourier-transform limited. This is due to the spectral and temporal narrowness of the split pulses, which thus barely see the phase curvature.

Finally, let us look at how the phase "propagates" along the FEL process. First, the FEL phase can be very well fitted by a parabola (ignoring values at low FEL signal, where the phase
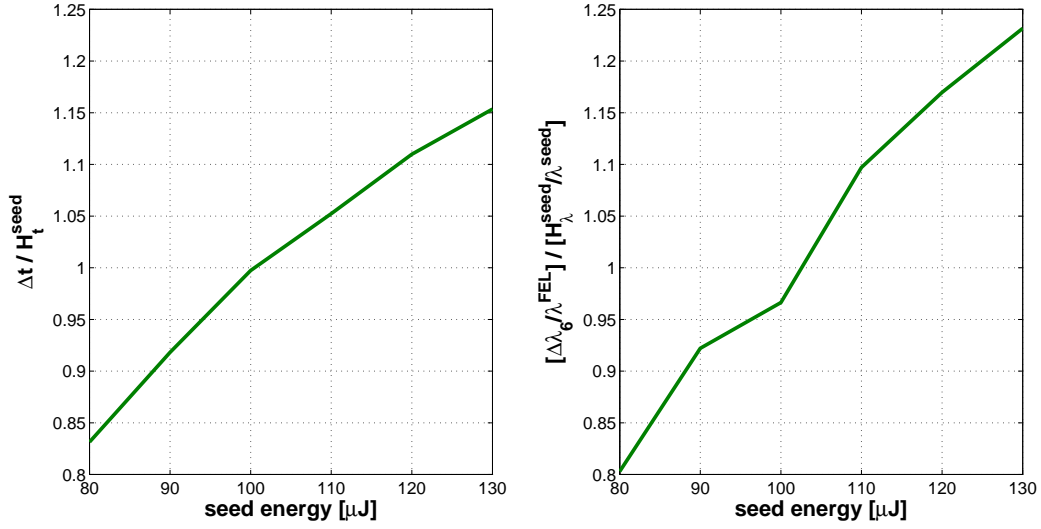
Figure IV.23: Left panel: evolution, as a function of the seed energy, of the ratio of the temporal distance between the sub-pulses vs. the FWHM duration of the seed. Right panel: evolution, as a function of the seed energy, of the ratio of the peaks spectral separation (relatively to the central wavelength of FEL emission) vs. the relative FWHM bandwidth of the seed.
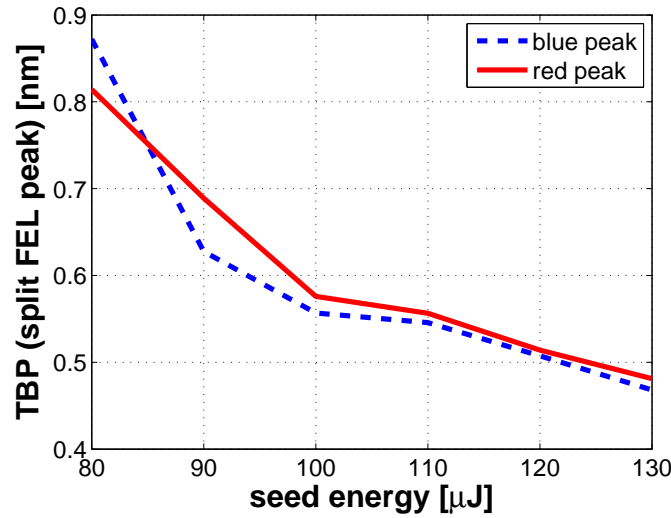
Figure IV.24: Time-bandwidth product of each of the two sub-pulses as a function of the energy delivered by the seed. The "blue peak" (dashed line) refers to the one at shorter wavelengths whereas the "red peak" refers to the one at longer wavelengths.

is meaningless) i.e., no high-order phase distortions appear in the FEL phase. The map of the temporal phase as a function of the seed energy is shown in the left panel of Fig. IV.25. In the right panel of the same Figure, we represented a phase that has a curvature equal to the harmonic order ($n = 6$) times the Γ_i parameter of the seed (Γ_i depends on the seed energy). The agreement between the left and the right pictures is quite good, especially for values of the seed energy corresponding to an unsplit FEL pulse (below $\sim 60 \ \mu J$). Therefore, $n\Gamma_i$ is a good approximation of the curvature of the temporal phase for relatively low values of the curvature
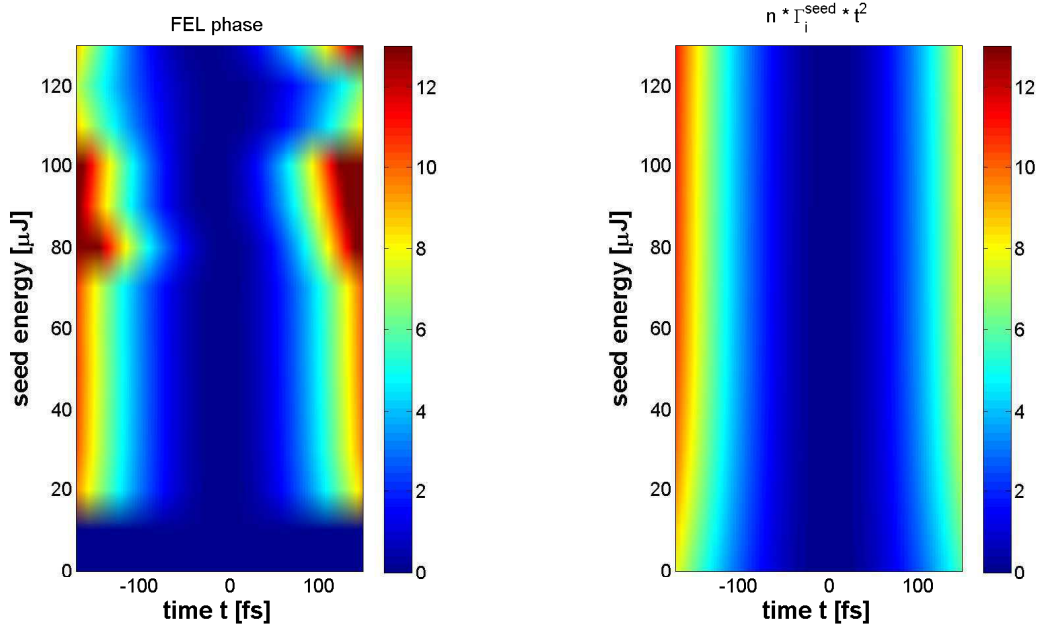
Figure IV.25: Left panel: map of the temporal phase, represented in false colors, as a function of the energy of the seed. Right panel: map of the quantity $n\Gamma_i t^2$ $(n = 6)$, represented in false colors, as a function of the energy of the seed.

of the electrons energy profile. We usually found an error smaller to 10 % between the true curvature of FEL phase and $n\Gamma_i$. Is this agreement improved when the electron bunch does not present an initial chirp? Let us see the next case.

IV.1.c.2   Case 2: flat electrons' energy profile

We saw in the previous chapter that the total phase of the FEL emission can be decomposed according to different contributions of the seed and of the electron beam. Hence, it is interesting to repeat the numerical study for a non-chirped electron beam. In this case, the chirp of the FEL emission depends only on the one of the seed and on the intrinsic chirp.

Here I will not show all the curves of the study as in the previous case, since it would be quite heavy. Indeed, as shown in Fig. IV.26, the splitting patterns are very similar to what is obtained in the case of a real electron beam (see Fig. IV.16): the double-peak formation is not affected by a slight inhomogeneity of the electron beam.

Let us focus only on the most interesting parameters. The first of them is the time-bandwidth product of the FEL emission before splitting. Figure IV.27 shows that, as expected, it grows as a function of the seed energy, but is lower than that a realistic electron beam (see Fig. IV.20), since in the latter case the chirp of the electrons bring an additional curvature to the FEL phase.

Now, we consider the double-peak regime. The function $\Delta\lambda_6$ vs. Δt (Fig. IV.28) is slightly different from the one obtained in the realistic case (Fig. IV.22). Indeed, in the latter case, the electrons quadratic chirp broadens the bandwidth so that the separation between the two peaks
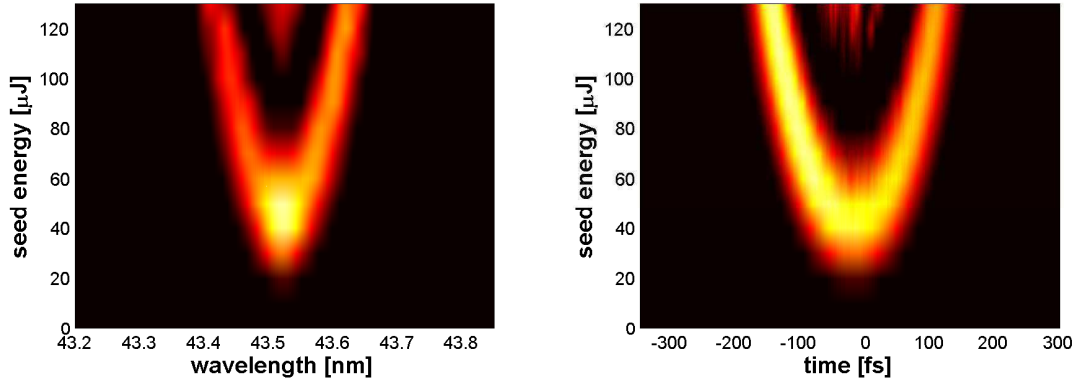
Figure IV.26: Output of Perseo simulations in the spectral (left) and time (right) domain for a flat electrons' energy profile.
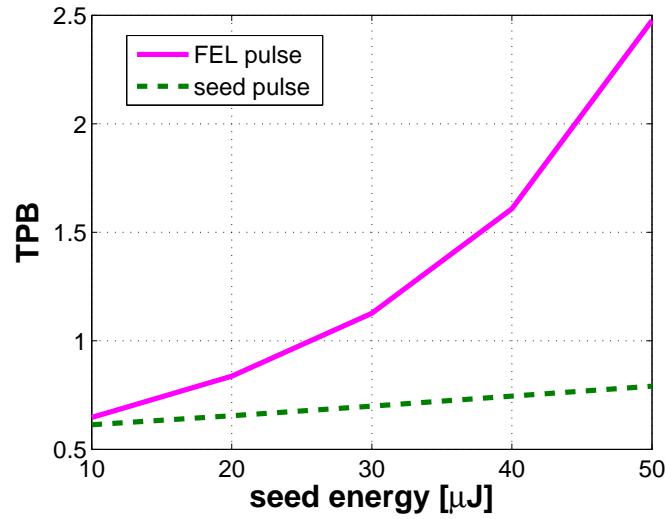
Figure IV.27: Time-bandwidth product of the FEL pulse before splitting (full line) and of the seed pulse (dashed line) as a function of the seed energy per pulse for a flat electrons' energy profile.

gets higher for a given temporal splitting (as will be discussed in Section IV.1.c.3). Controlling the chirp of the electrons offers the possibility to obtain, for instance, different longitudinal distances between the sub-pulses for a given spectral separation. This is a precious thing for potential pump-probe applications.

Figure IV.29 shows that the theoretical estimation of Δt is, in the case of an ideal electron beam, very close to the one measured in the simulations. As a matter of fact, in this case the relevance of Eq. IV.3 is not affected by the initial chirp of the electrons. The agreement is good especially at the beginning of the splitting i.e., before the central modulation appears. As in Fig. IV.21, there is still a discrepancy (even if less important) and the latter grows as the seed energy gets higher. A possible explanation is the following. The theoretical expression of Δt given in Eq. IV.2 relies on the fact that the seed phase is directly transmitted to the FEL phase and the other sources of chirp in the FEL emission are neglected. However, while increasing the
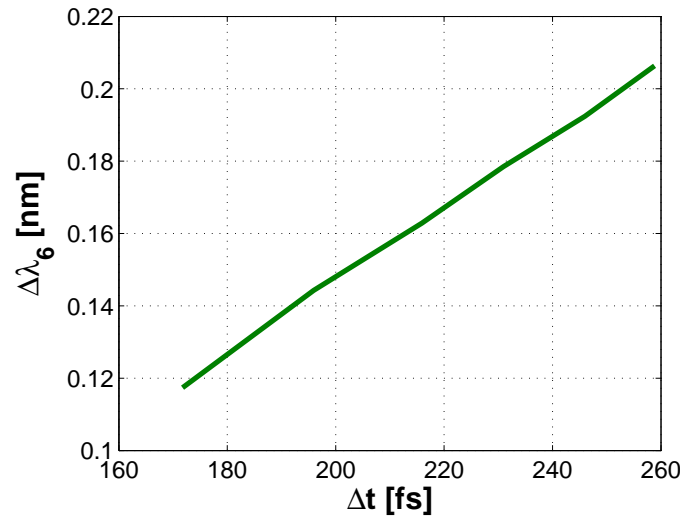
Figure IV.28: Correlation between the separation of the two peaks in the spectral domain and of the temporal distance of the two associated sub-pulses for a flat electrons' energy profile.

seed energy, there is a modification of the evolution of the modulation (in energy then spatial) of the electrons. The dispersion properties (see Eq. III.22) of the latter, that are the amplification medium, can thus be changed. In other words, for sufficiently high seed energies, the intrinsic chirp may be significantly modified and become non-negligible: this has a direct consequence on the relevance of the calculation of Δt.
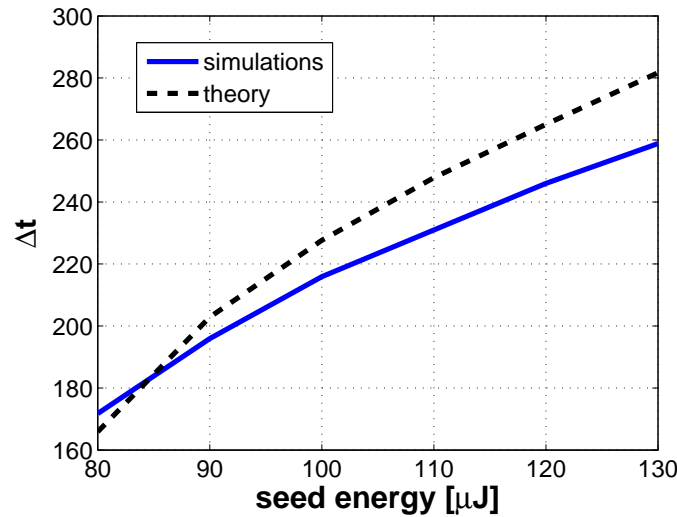
Figure IV.29: Evolution, as a function of the energy delivered by the seed, of the temporal distance between the split pulses retrieved in the simulations for a flat electrons' energy profile (full line) and estimated by Eq. IV.3 (dashed line).

The time-bandwidth product of the separate peaks is decreasing towards very low values. Figure IV.30 shows that it even goes under the Fourier-transform limit for highest seed energies...

In fact, at this point the assumption of two separate peaks is not true any more. For high seed
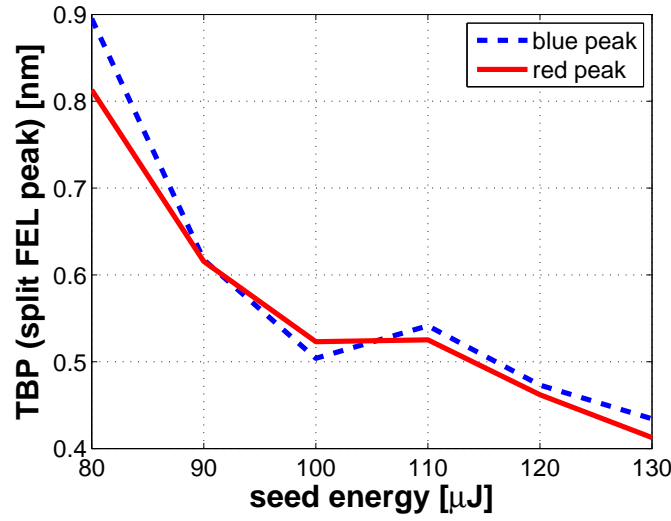
Figure IV.30: Time-bandwidth product of each of the two sub-pulses as a function of the energy delivered by the seed, for a flat electrons' energy profile. The "blue peak" (dashed line) refers to the one at shorter wavelengths whereas the "red peak" refers to the one at longer wavelengths.

energies, the central modulation of the FEL emission becomes non-negligible and wide, so that the electric field of the sub-pulses cannot be dissociated any more. This is shown in Fig. IV.31: for a clean double peak (left panel, seed energy of $90\ \mu J$), the peaks are clearly dissociated in time, whereas the central modulation becomes non-negligible for a higher saturation level (right panel, seed energy of $130\ \mu J$). This is the limit of the model which considers two independent peak/pulses. In any case, before this limit, the sub-pulses reach a very high level of temporal coherence: their time-bandwidth product is around 0.5 i.e., only $1.1 - 1.15$ times far from the Fourier-transform limit (this value is slightly higher for the case of the realistic electron beam due to the higher curvature of the FEL phase induced by the non-zero χ_2 coefficient).
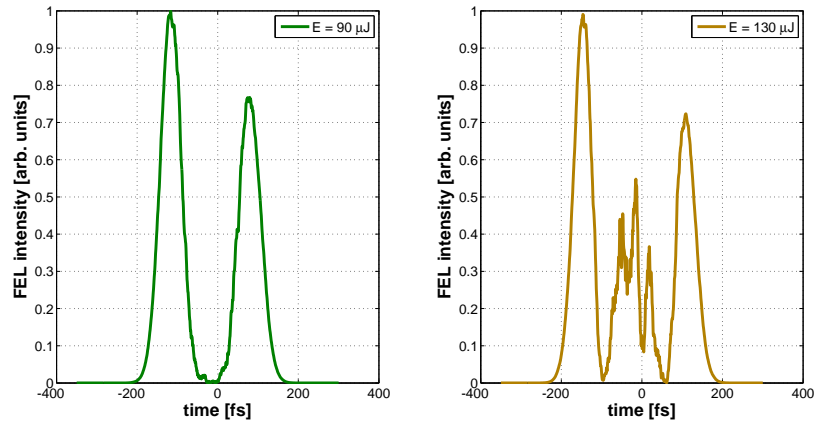
Figure IV.31: Temporal profile of the FEL emission given by simulations with a flat electrons' energy profile, for an energy per pulse of the seed of $90\ \mu J$ and of $130\ \mu J$.

Finally, let us look at the behaviour of the temporal phase. As it has been said, since the

electrons do not have any initial chirp, the FEL is not affected by this parameter. That is why, as shown in Fig. IV.32, the phase curvature can be very well fitted by $n\Gamma_i$. For a seed energy above $100\ \mu J$, the agreement is worsened, as in the case of the realistic electron beam (see Fig. IV.25). This situation corresponds to the presence of the central modulation in the spectral and temporal domains of the FEL emission. Below $10\ \mu J$ of seed energy, there is no FEL signal, hence the comparison is meaningless. We can thus say that, in the regimes of the FEL ranging from a slight amplification to a clean double-peak formation, the temporal FEL phase is equal to $n\Gamma_i t^2$.
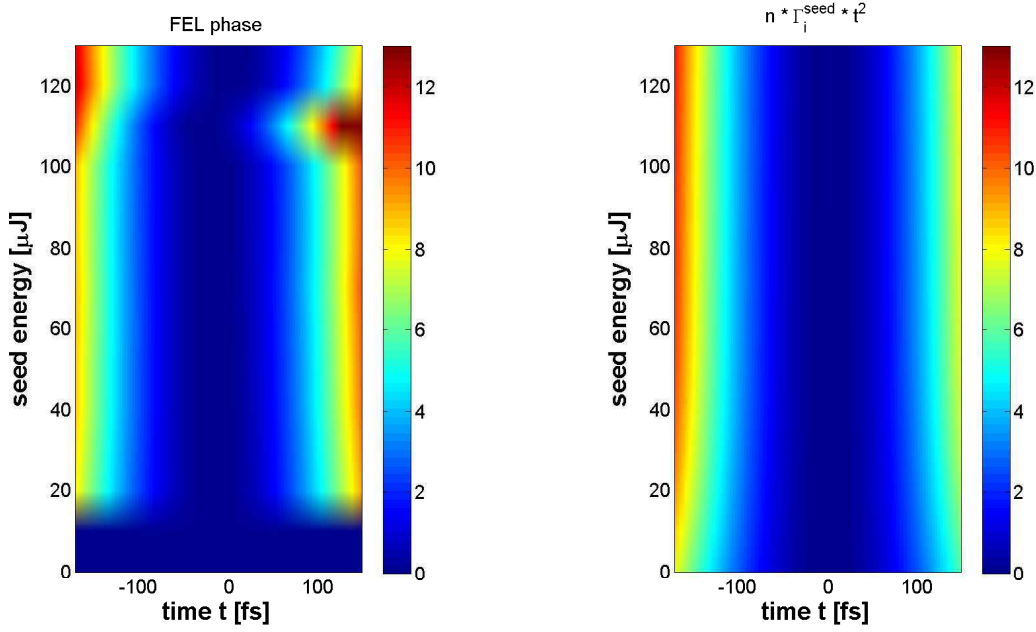
Figure IV.32: Left panel: map of the temporal phase, represented in false colors, as a function of the energy of the seed for a flat electrons energy profile. Right panel: map of the quantity $n\Gamma_i t^2$ ($n = 6$), represented in false colors, as a function of the energy of the seed.

IV.1.c.3   Note on the effect of electrons' quadratic energy chirp

Up to now, we only considered situations where the quadratic energy chirp of the electrons is small or absent, which corresponds to experimental situations at FERMI@Elettra. Let us see quickly what happens if this not the case. I carried out simulations with same parameters as before, without linear energy chirp and varying the quadratic one. In Fig. IV.33, we see that the value of χ_2 has almost no effect on the temporal shape of the FEL emission but that the overall bandwidth depends on it – without affecting the double peak formation – leading to a variation of the peaks separation. As a matter of fact, the quadratic energy chirp of the electrons acts on the spectrum in a similar way as the linear chirp of the seed, so that the electrons energy profile may add to or compensate the quadratic phase of the seed: if the effects of the electrons energy chirp and seed frequency chirp on the FEL phase can be of the same order of magnitude, this is

a very important point. However, the peculiarity of the electrons chirp is that it does not affect the temporal distance between the sub-pulses (the temporal shape of the FEL pulse being mainly dictated by the seed pulse), which would make a good option for varying the peaks spectral separation without affecting the temporal shape of the split pulses. On the other hand, spectral broadening and temporal lengthening are always associated in the FEL emission.
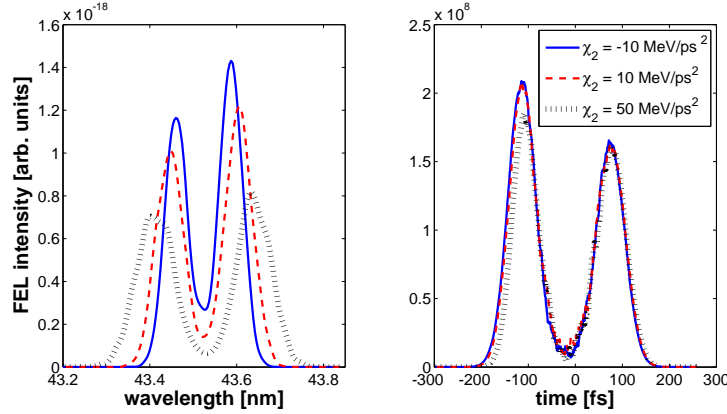
Figure IV.33: Comparison of the outputs of simulations carried out with the numerical code Perseo for different values of the quadratic chirp of the electrons (left: spectrum; right: temporal intensity), for the following parameters: seed bandiwdth $\sigma_\lambda = 0.47$ nm, duration $\sigma_t = 93$ fs, energy 70 μJ (with a standard deviation of the transverse intensity distribution of 500 μm) and central wavelength 261.1 nm; $R_{56} = 20$ μm; undulators tuned at the 6th harmonic of the seed (43.5 nm); electrons peak current 300 A, emittance 1 mm.mrad, relative energy spread 0.01% and linear chirp component $\chi_1 = 0$ Mev/ps^2. Full line: $\chi_2 = -10$ Mev/ps^2; dashed line: $\chi_2 = 10$ Mev/ps^2; dotted line: $\chi_2 = 50$ Mev/ps^2.

IV.2   Temporal shape determination

The work presented in this section is inspired by the need of retrieving experimentally the temporal shape of the FEL emission. At femtosecond time scales, and moreover in the sub-UV spectral region, obtaining the temporal information of light sources is a challenging task.

In the double peak production that has just been discussed, two close frequencies shifted in time are created: this is exactly what is needed for performing one of the most famous temporal diagnostics of femtosecond pulses, that is the SPIDER [101]. In the latter, the spectral phase is retrieved through the interference pattern of the two pulses, if the delay and the spectral separation between them are known. From the spectral phase and the spectrum, the temporal shape can be retrieved by a simple Fourier transform. We remind that an EUV SPIDER has already been successfully tested at CEA Saclay on a HHG source [129]. In our case, there are two issues: the two pulses that are involved must be identical and the wavelength shift between them must be very close ($\Delta\lambda \ll H_\lambda$). Even if the first problem can probably be handled experimentally, the second one would be more difficult to solve. Indeed, intrinsically, the two peaks have a "large" spectral difference due to fact that they stem from a strong chirp of the seed. Ideally, the

two single spectra should be almost completely superimposed so that a frequency modulation could occur inside this envelope: without this interference pattern on which the SPIDER relies, the spectral phase, and thus the temporal shape, cannot be retrieved. A solution would be to decrease the chirp of the FEL emission by acting on the chirp of the seed and/or the one of the electrons so as to bring closer the two peaks spectrally. However, the spectrum of each single peak could not be measured individually: therefore, how to know experimentally that the two peaks are identical, with similar width and height? Moreover, the number of periods of the beating depends on the spectral width and on the temporal distance between the sub-pulses. Experimentally, we tried to compensate the chirp of the seed by means of the compressor stage, but no beating has been observed in the spectrum: we could only assume that the pulse splitting was there, since the seed energy was strong enough to be in a regime of deep saturation and that the spectrum was distorted. But a finer control on the phase of each sub-pulse would be required, while here the phases of the two sub-pulses are strongly linked since they emanate from the same sources, that are seed and electrons chirps. For all these reasons, performing a SPIDER characterization of the FEL emission in the regime of double peak generation seems very difficult... but not impossible, and would merit to be studied theoretically and/or numerically.

SPIDER has already been performed on an FEL, for instance in [130] on a FEL operating at a wavelength of $266 \; nm$. But, to our knowledge, nothing has been done in the EUV spectral range, as a direct on-line and non-invasive diagnostic. A possibility is to seed the FEL with two successive pulses slightly shifted in wavelength, as discussed in [131]. If the electron bunch is homogeneous, it theoretically allows producing two EUV replicas, at wavelengths λ_n and $\lambda_n + \delta \lambda_n$, with a time separation that is easily controllable through a delay line on the seed stage. The double seeding has been successfully tested on FERMI@Elettra, as we demonstrated in [132]. The two seed pulses were produced by two separate lines of generation of the $260 - nm$ wavelength at the seed laser stage. An appropriate tilting of the nonlinear crystals in which occurs the third harmonic generation of the Ti:Sapphire source (whose spectrum is centered at $780 \; nm$) leads to a change of the phase-matching condition, thus enabling to slightly shift the central wavelength of the third harmonic of the Ti:Sapphire laser source. The aim of the experiment was to create two FEL frequencies that were significantly separated, hence it was not possible to study what happens when the two spectra are superimposed – but this should be done in the future. This experiment is a good possibility to perform EUV SPIDER on an FEL, even if this diagnostic would be invasive, but would also allow studying the far-field interference, and thus the preservation of temporal coherence along the bunch, of the two successive pulses.

In the previous study of double peak emission, we have remarked that the temporal and spectral patterns are very similar. This is not so surprising, since each sub-pulse corresponds to a spectral peak and therefore that the integrated signal of a given sub-pulse corresponds to the integrated signal of single peak in the frequency domain. But how far are these shapes similar, and why? The answer to this question has been found thanks to the contribution of

David Gauthier, who joined the team at Sincrotrone Trieste from CEA Saclay at the end of my thesis. His work allowed developing the study that is presented hereafter.

IV.2.a   Spectro-temporal equivalence

According to what has been seen up to now, the CHG FEL emission at FERMI@Elettra can be written as:

$$E(t) = a(t)e^{in\Gamma_i t^2},$$
(IV.4)

where $a(t)$ is the envelope representing the temporal shape (gaussian, slightly distorted, split in two sub-pulses, etc.) of the FEL emission. The $n\Gamma_i$ parameter of the quadratic phase term which is inherited from the chirp of the seed, the contribution of the electrons and the intrinsic FEL chirp being neglected. For simplicity, we do not take into account the fast oscillations at the central frequency of emission. The pulse spectrum is given by:

$$\tilde{I}(\omega) = |FT_\omega[a(t)e^{in\Gamma_i t^2}]|^2,$$
(IV.5)

where $FT_\omega[f(t)] = \int_{-\infty}^{+\infty} f(t)e^{-i\omega t}\,\mathrm{d}t$ is the direct Fourier transform of the function $f(t)$, from the temporal variable t to the frequency variable ω. One can make use of the same hypotheses employed by Fraunhofer for describing the far-field diffraction in paraxial approximation. Using the formalism of Fourier [76], we can write the previous relation as a convolution product:

$$\tilde{I}(\omega) = |\tilde{a}(\omega) * e^{-i\frac{\omega^2}{4n\Gamma_i}}|^2,$$
(IV.6)

where $\tilde{a}$ represents the Fourier transform of the envelope i.e., $FT_\omega[a(t)]$ and $e^{-i\frac{\omega^2}{4n\Gamma_i}}$ is the Fourier transform of the quadratic phase term $e^{in\Gamma_i t^2}$. An analogy can be drawn between the spectrum and the one-dimensional diffraction pattern originated from a "transversal field distribution". In the previous relation, the convolution with the exponential term plays a role similar to the longitudinal space propagation of a diffracted wave. In paraxial approximation, the propagation generates a linear dispersion of the spatial frequencies. In our case, this corresponds to the linear frequency dispersion in the pulse, caused by the quadratic phase term $n\Gamma_i t^2$ inherited from the seed. After the development of the convolution product, the spectrum can be written as an inverse Fourier transform FT^{-1} in the variable $\frac{\omega}{2n\Gamma_i}$:

$$\tilde{I}(\omega) = |FT^{-1}_{\frac{\omega}{2n\Gamma_i}}[\tilde{a}(\omega')e^{-i\frac{\omega'^2}{4n\Gamma_i}}]|^2,$$
(IV.7)

Let us focus on the exponential term $e^{-i\frac{\omega'^2}{4n\Gamma_i}}$. In far field diffraction, the Fraunhofer approximation assumes that this phase term varies slowly in the Fourier integration domain where the square

integral function $\tilde{a}(\omega)$ is different from zero. This condition is equivalent to:

$$\frac{STD[\tilde{a}(\omega)]^2}{4n\Gamma_i} \sim \frac{\sigma_\omega^2}{4n\Gamma_i} = N \ll 1. \tag{IV.8}$$

where $STD[\tilde{a}(\omega)]$ represents the standard deviation of the electric field envelope in the frequency domain. It is worth noting that the parameter N is analogous to the "Fresnel number" in diffraction. When the condition IV.8 is fulfilled, one can reasonably approximate the exponential term with unity. As a result, Fraunhofer diffraction pattern provides a direct representation of the Fourier transform of the initial field distribution. In our case, since $\tilde{a}(\omega)$ is the Fourier transform of the complex envelope $a(t)$, we finally get:

$$\tilde{I}(\omega) = |a(\frac{\omega}{2n\Gamma_i})|^2. \tag{IV.9}$$

We thus obtain the following noticeable result: under the condition IV.8, the spectrum of the linearly chirped FEL pulse provides a direct representation of its temporal shape, through the variable transformation $t = \frac{\omega}{2n\Gamma_i}$. It is also very important to stress that this result is applicable to any linearly chirped optical pulse verifying condition IV.8 (replacing $n\Gamma_i$ by the quadratic phase coefficient – e.g., Γ_i for the seed laser).

A schematic representation of the proposed "far-field" approach is given in Fig. IV.34. In the case of a non-chirped pulse (or with an arbitrary, non-quadratic, phase) the electric field envelope in the frequency domain is different from the one in the temporal domain. In the case of a linearly-chirped pulse, the electric field envelope in the frequency domain, $\tilde{a}(\omega)$, is the same as the one in the time domain (with the homotethic relation $t = \frac{\omega}{2n\Gamma_i}$).

IV.2.b Comparison with simulations

It it important to note that the result obtained hereabove is a very general one, even if here we will restrict to its application to the CHG FEL emission at FERMI@Elettra. In Section IV.1, we have shown that the inhomogeneity of the electron beam energy profile is sufficiently low, and for a linearly-chirped seed of temporal phase $\Gamma_i t^2$, the CHG emission is also linearly chirped and its temporal phase is well approximated by $n\Gamma_i t^2$, n being the harmonic order at which the radiators are tuned. We will thus here consider Eq. IV.4 with $n\Gamma = n\Gamma_i$. Moreover, according to Stupakov's law [127], the duration of a slightly saturated FEL emission is equal to the one of the seed times $n^{\frac{1}{3}}$. We checked the validity of this result for $n = 6$. Hence, the spectral width of the FEL emission is $\sigma_\omega^{FEL} \sim \frac{1}{n^{\frac{-1}{3}}\sigma_t^{seed}}$. We can thus rewrite Eq. IV.8 only in terms of the seed laser properties and the harmonic order:

$$\frac{(\sigma_\omega^{FEL})^2}{4n\Gamma_i} \sim \frac{1}{4n^{\frac{1}{3}}(\sigma_t^{seed})^2\Gamma_i} = N \ll 1. \tag{IV.10}$$
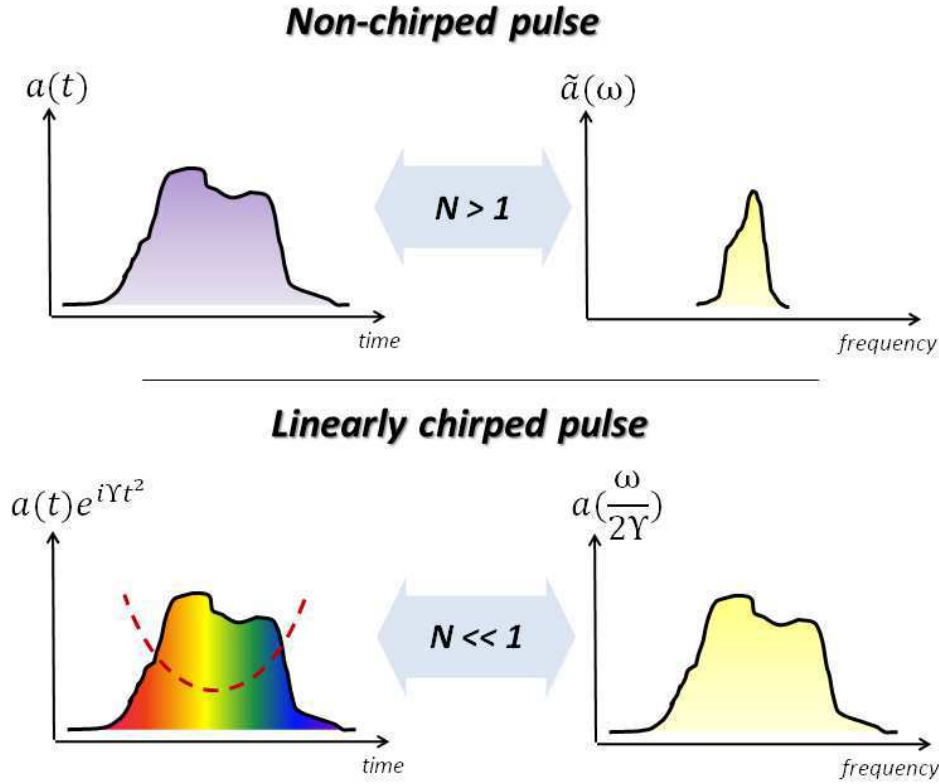
Figure IV.34: *Principle of the spectrum-time equivalence. Top panel: case of a non-chirped pulse (or not linearly chirped) with the temporal electric field envelope (left) and the spectral one (right). Bottom panel: case of a linearly chirped pulse (quadratic phase in dashed line) with the temporal electric field envelope (left) and spectral one (right), equivalent to the temporal one with the homothetic relation $t = \frac{\omega}{2n\Gamma_i}$.*

This relation offers a mean to determine the seed parameters to be used in order to ensure the validity of the proposed approach. In Eq. IV.10, the presence of $n^{\frac{1}{3}}$ is very important: it tells us that the condition of spectrum-time equivalence is more easily accessible for higher values of n. Indeed, as discussed in [128], the phase is more affected by the "incident" chirp of the seed at higher harmonic orders, thus condition IV.8 is facilitated at lower wavelengths.

In order to check our results, PERSEO simulations have been carried out at the harmonic order $n = 8$, with $\sigma_t^{seed} = 86.4\,fs$ (i.e., an FWHM duration if about $200\,fs$) and $\Gamma_i = 5.1 \cdot 10^{-5}\,fs^{-2}$ (obtained for an FWHM bandwidth of $0.9\,nm$). This gives, according to Eq. IV.10, $N = 0.16$. We can thus say that, in these conditions, we fulfill the condition of "far-field" approximation. As it can be seen in the top left panel of Fig. IV.35, corresponding to a normal regime of operation of the FEL (single pulse, slight saturation), our prediction is fully confirmed: the spectral (continuous) and temporal (dashed) profiles are very similar. In this figure, we represented the phase decomposed in the part $n\Gamma_i t^2$ inherited from the seed (dotted curve) and the remaining phase distortions (dash-dot line): the former dominates the latter. While a flat electron energy profile has been taken here, a curvature of $5\,MeV/ps^2$ (which is an experimentally reasonable value at FERMI@Elettra) has been considered for the result shown in the top right panel: the agreement remains excellent. As it has already been mentioned, for such small inhomogeneity

of the electrons energy profile, the effect on the FEL phase is negligible. In the bottom-left panel of the same figure, we considered the regime of pulse splitting. Remarkably, the method we propose is able to reproduce the simulated profile also in this case. Indeed, as shown e.g., in Fig. IV.32, the FEL phase can still be approximated by $n\Gamma_i t^2$ in this situation. Finally, the bottom-right panel shows the effect of the phase (and envelope) distortion induced by running the FEL in over-saturation (single but distorteb pulse). In this case, the quadratic phase term (dotted line) does not sufficiently dominate the other phase terms (dash-dot curve): this the reason why the theoretical approach partially fails in reproducing the simulated temporal profile.
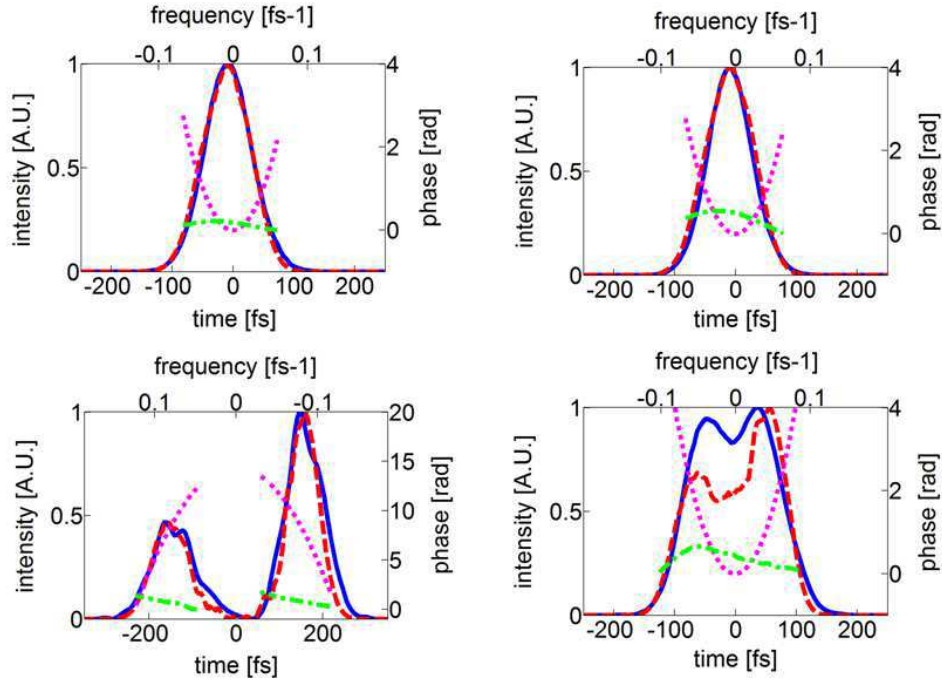
Figure IV.35: *Comparison between the temporal (continuous line) and spectral (dashed line) profiles obtained using the numerical code PERSEO: (top left) single pulse, slightly saturated regime with ideal electron beam; (top right) single pulse, slightly saturated regime with quadratic electron-beam energy profile (energy curvature: $5\ MeV/ps^2$); (bottom left) double-pulse regime; (bottom right) single pulse, over-saturated regime. In each panel, the temporal scale (bottom axis) is obtained from the spectral one (top axis), using the homothetic transformation given in Eq. IV.9. The phase is separated into the dotted curves representing the quadratic part $n\Gamma_i t^2$ (with $n=8$) and the dot-dashed curves correspond to the other phase terms.*

IV.2.c   Predictions for experimental results

Finally, we tested our approach by comparing theoretical results with measurements performed at FERMI@Elettra. The left panels of Fig. IV.36 display the temporal shape retrieved from the measured FEL spectrum, using Eq. IV.9 (with $n\Gamma_i = n\Gamma_i$). For the considered case, the FEL was operated at $32.5\ nm$ ($n=8$); the seed pulse had a measured FWHM duration of $200\ fs$ and a phase curvature $\Gamma_i = 5.1 \cdot 10^{-5}\ fs^{-2}$ (i.e., the same seed as we considered in the simulations hereabove, giving $N=0.16$). The measured value of the electron-beam energy

curvature was $5\,MeV/ps^2$. In the top left panel, we retrieve a pulse with quasi-Gaussian shape of $102\,fs$ duration (FWHM) and in the bottom-left one we have the retrieval of the temporal profile in the case of a double-peak spectrum. In order to corroborate our prediction, we do the reconstruction of the spectrum from this temporal retrieval by means of the following relation:

$$\tilde{I}_{rec}(\omega) = |FT_\omega[\sqrt{\tilde{I}(2n\Gamma_i t)}\exp^{in\Gamma_i t^2}]|, \tag{IV.11}$$

where $\tilde{I}(2n\Gamma_i t)$ is the measured spectrum evaluated at the homothetic coordinate $\omega = 2n\Gamma_i t$, and we compare it with the initial measured spectrum. The reconstructions are shown in the right panels of Fig. IV.36: the agreement is very satisfactory. The reconstructed spectrum provides a quantitative information about the validity of the proposed "far-field" approach, also in the situations in which a significant phase distortion and possible perturbations generated by any other noise source are present
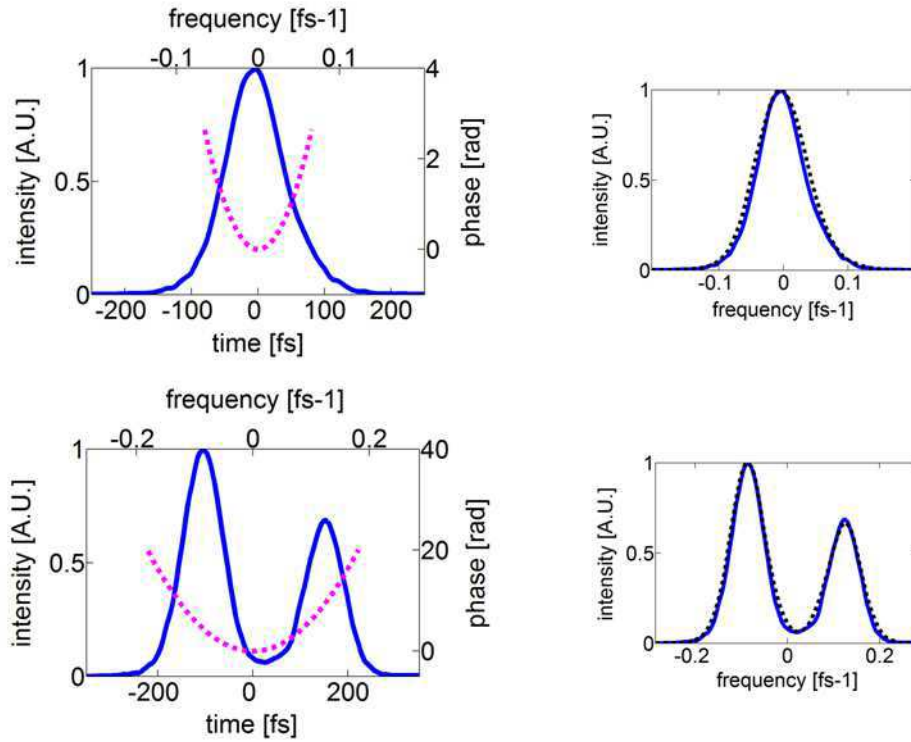
Figure IV.36: Top left panel: retrieved temporal shape (solid curve) from spectral measurement on FERMI@Elettra in the single-pulse regime. Bottom left panel: retrieved temporal shape (solid curve) from spectral measurement on FERMI@Elettra in the double-pulse regime. In both panels, the temporal scale (bottom axis) is obtained from the spectral one (top axis), using the homothetic transformation given in Eq. IV.9 and the dotted lines represent the quadratic phase term $n\Gamma_i t^2$. Right panels show the comparison between the measured spectra (solid line) and the reconstructed spectra (dotted line) from the left panels, calculated using Eq. IV.11.

IV.3   Summary

In this chapter, I presented a way to generate two close but distinct spectral peaks, to which are associated two femtosecond pulses separated by a few hundred of femtoseconds. The technique relies on the effect of the chirp carried by the seed laser on an FEL operating in deep saturation, which leads to the pulse splitting of the main FEL pulse into two sub-pulses. We realized the experiment on the FERMI@Elettra facility, generating, in the extreme-ultraviolet spectral region, two colours whose relative separation is $\frac{\Delta\lambda}{\lambda} \approx 0.01\%$. The spectral separation between the peaks can be managed by different parameters, that are the intensity of the seed, the strength of the dispersive section (as we demonstrated in [133]), the chirp of the seed and the chirp of the electrons.

An interesting point of this effect is that, starting from a single FEL pulse that is intrinsically relatively far from the Fourier-transform limit due to phase distortions of the seed and, in a smaller extent, of the electron bunch, especially at low harmonic orders, one may end up with two pulses very close to this limit i.e., exhibiting a spectro-temporal quality potentially appreciable for users' applications.

I provided a reliable estimation of the temporal distance between the two sub-pulses as a function of the chirp parameter of the seed Γ_i and the spectral separation between the peaks. From this we can draw the function in Fig. IV.37, which is a precious piece of information for the application to pump-probe experiments. It shows the different working points that would be accessible by varying Γ_i at fixed seed intensity and strength of the dispersive section.
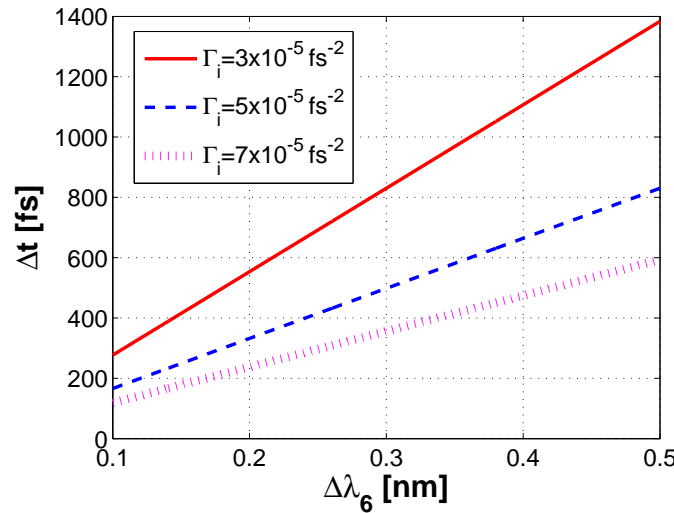
Figure IV.37: Estimation of the temporal distance between the two sub-pulses as a function of their measured spectral separation for a CHG emission at the 6th harmonic of the seed for different values of Γ_i.

Finally, I presented a study whose conclusion is that the temporal shape of any optical pulse with dominant linear chirp is identical to its spectrum, under the condition of Eq. IV.8. In our case,

this noticeable result provides a direct non-invasive diagnostic for the temporal reconstruction of seeded FEL, even in the regime of double pulse.

High-order harmonics generated by a tunable drive source

Contents

In the previous chapter, a solution for the generation of two-colour femtosecond pulses with controllable features has been presented. In some extent, one of its assets is the tunability of the wavelength (i.e., by the fact that there is a splitting that creates two new colours but also because these two wavelengths can be tuned, eventually independently). However, the two wavelengths remain very close from one another. In [134], we demonstrated the easy tunability of the FERMI@Elettra source: both coarse tunability, by changing the harmonic order on which the FEL is tuned, and fine tunability, by slight modification of the undulators' resonance for instance. Moreover, the presence of an optical parametric amplifier [135] as a seed laser, which can be used instead of the fixed-wavelength seed, is a huge advantadge. Hence, on FERMI@Elettra a full tunability over the whole EUV range is reached, which is very important for users' experiments. On HHG sources, the tunability is less evident but there are possibilities. A straightforward solution, that we study here, is to generate to rely on a widely tunable drive source.

V.1   Principle

The generation of fully tunable high-order harmonics has been demonstrated in [136] for harmonics around 150 nm. In this section, we extend this study to the whole ultraviolet spectral range, reported in our work published in [137]. The novelty of the results we obtained stems from
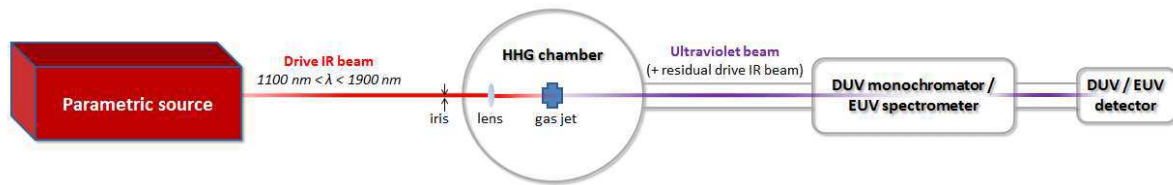
Figure V.1: *Layout of the experiment.*

the unique qualities of the source that we used to drive HHG. This driving source is characterized by a large wavelength tunability from 1100 to 1900 nm, a mJ-level pulse energy and short pulse duration of the order of 20 fs. In these conditions the generation of few-femtosecond harmonic radiation is ensured.

V.2   Experimental setup

The layout of the experiment is shown in Fig. V.1. The parametric source (Fig. V.2 [138]) is based on a Ti:Sapphire laser facility providing intense short pulses (tens of mJ energy; $60\ fs$ duration), centered at a wavelength of $790\ nm$, with a repetition rate of $10\ Hz$. A fraction of the beam is sent to a filament filled with krypton where self-phase modulation (see Section III.1.b) occurs, so as the spectrum is broadened. A set of chirped mirrors then allows compressing the pulse down to few femtosecond durations [85]. The output beam stems from difference frequency generation (DFG) [90] of spectrally broadened pulses. The generated pulses are amplified in a two-stage optical parametric amplifier (OPA1 and OPA2), each stage being pumped by a fraction of the Ti:Sapphire laser source spatially filtered by a modal filtering setup similar to the one described in Section II.2, leading to the production of $\approx 20-fs$ pulses with an energy up to $1.2\ mJ$, tunable from 1100 to $1900\ nm$. Tunability is achieved by rotating the crystals in the OPAs, thereby changing the phase-matching conditions.

The generation of the high-order harmonics of the near-IR driving pulses is achieved by focusing the laser beam with a lens of $15\ cm$ focal length on a jet of krypton gas (see Fig. V.1), which ensures a better harmonic conversion efficiency than lighter gases such as argon, at the price of a lower cutoff frequency. The gas is injected into the interaction chamber by an electromagnetic valve, mounted on a $x-y-z$ translation stage, operating at the same repetition rate as the laser. The jet has a diameter at nozzle of about $0.8\ mm$. An iris placed on the path of the driving beam adjusts the intensity at the focus, estimated to be at most $2 \cdot 10^{14}\ W/cm^2$. By changing the gas backing pressure (typically $2-5\ bars$), the gas pressure in the interaction region has been estimated to vary between 20 and $50\ mbars$. Such values, as well as the synchronization with the laser pulse, have been chosen to maximize the harmonic yield. The valve is placed downstream the laser beam waist until the position of maximum photon flux is reached. After the generation point, the harmonics co-propagate with the residual driving laser
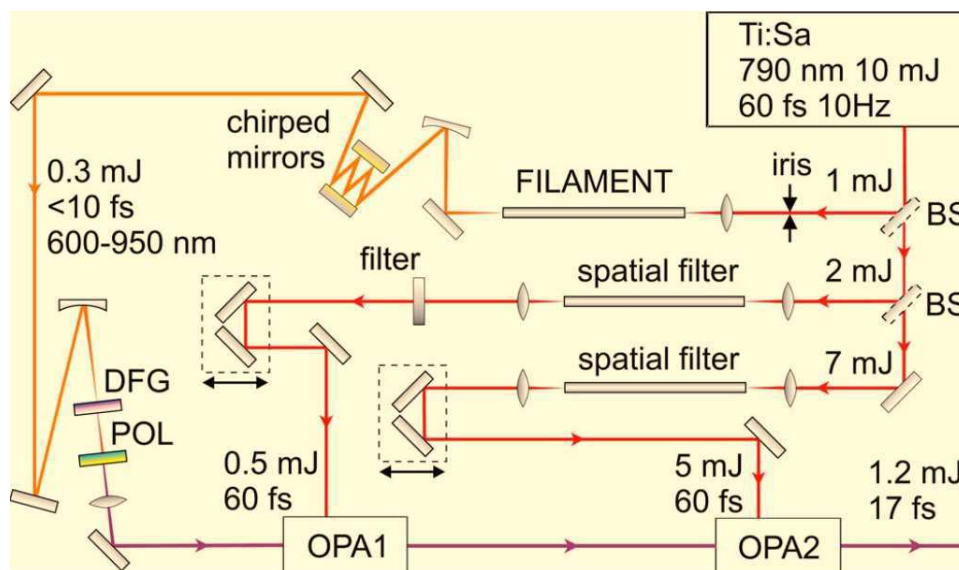
Figure V.2: *Driving laser source used for out HHG experiment: Ti:Sa, CPA Ti:sapphire laser; DFG, $200 - \mu m$-thick BBO crystal; POL, thin-film polarizer; BS, beam splitter. (taken from [138])*

through the instrument in use for the spectral analysis. The spectrum of the harmonic beam is acquired by two different detection systems: a scanning monochromator in the DUV and a spectrometer in the EUV, with suitable detectors. Detection systems in both DUV and EUV regions have been calibrated so as to allow measurement of the harmonic absolute photon flux.

To cover the deep-ultraviolet (DUV) and EUV spectral regions two different spectrometers have been used. Harmonic emission in the DUV was analyzed through a normal-incidence Czerny-Turner scanning monochromator (McPherson model 218) equipped with a $2400 - gr/mm$ $AlMgF_2$-coated grating. The monochromator selects a single harmonic or a spectral portion thereof. The photon flux at the exit slit of the monochromator is detected by a photomultiplier tube (Hamamatsu model R1414) with a tetraphenyl butadiene (TPB) phosphor photocathode to enhance the detection efficiency. Owing to the limited spectral range accessible to the grating, that has significant transmission for wavelengths above $\approx 130 \, nm$, only the harmonics ranging from the third to the eleventh order of the fundamental wavelength could be detected. The harmonic spectra at high resolution were obtained by scanning the grating, with a $300 - \mu m$ slit aperture, giving a bandwidth of $0.4 \, nm$.

The global response of the instrument (i.e., monochromator plus detector) has been absolutely calibrated using the facilities available at CNR-IFN and described in details in [139], in order to measure the DUV photon flux generated in the interaction region at the different harmonics. This was performed by tuning the monochromator to one of the harmonics and opening completely its slits. In such a way, the beam enters the monochromator without being clipped at the entrance slit and is diffracted by the grating. The harmonic of interest then exits the monochromator without being clipped at the output slit, and is detected by the photomultiplier. We verified that even with the slits completely open the different harmonics were clearly

separated at the output.

The signal in the EUV was analyzed through a grazing-incidence flat-field spectrometer equipped with a 1200-gr/mm gold-coated grating and tuned in the $80 - 35\ nm$ spectral region. The spectrum is acquired by a $40 - mm$-diameter microchannel plate intensifier with MgF_2 photocathode and phosphor screen optically coupled with a low-noise CCD camera. Also in this case, the global response of the instrument (i.e., grating and detector) has been absolutely calibrated, as described in detail in [140, 141]. Since the spectrometer works without an entrance slit, having the harmonics generation point as its input source, all the generated EUV photons enter the instrument and are diffracted onto the detector.

V.3   Results and discussions

V.3.a   Deep-ultraviolet region

Figure V.3 shows the spectral characterization from four sets of measurements, corresponding to four different wavelengths of the driving pulse: $1350, 1550, 1750$, and $1900\ nm$. One can see that, in our experimental conditions, the longer is the wavelength of the driving beam, the narrower is the bandwidth of the fundamental pulse and the one of its harmonics. It is important to stress that the stability of the beam provided by the parametric source ensures a very good reproducibility of the measurements.

Below 150 nm, the efficiency of the DUV monochromator is dramatically low. Thereby, the analysis of harmonic spectra has been done only down to 150 nm. Since the third harmonics of the considered driving IR wavelengths are generally located in the visible, i.e., out of the monochromator range, harmonic orders from fifth to ninth have been analyzed. As expected at these relatively low orders, the signal quickly decreases with increasing harmonic order. Indeed, the intensity of harmonics before the plateau region is related to the probability of multiphoton ionization of the gas atoms [142]. Like the driving beam, harmonics have a large bandwidth (a few tens of nanometers), intrinsic to an ultrashort pulse source.

The overlap of the harmonic spectra shows a full tunability of the source in the DUV spectral region (Fig. V.4). The range between 400 and 350 nm corresponds to either the fifth harmonic of a 1750–2000 nm fundamental beam or the third harmonic of a 1050–1200 nm fundamental beam. These wavelengths are the boundaries of the accessible spectral range of the used parametric source, so that in these regions the IR spectrum is less stable and moreover the beam energy is lower than in the 1350–1550 nm "peak region". Hence harmonics in the 400–350 nm region are also less intense. The third harmonic of a 1050–1200 nm fundamental beam can be generated with better conversion efficiency in the frame of classical nonlinear optics in crystals [143].

Figure V.5 clearly shows that when the driving wavelength ranges from 1350 to 1900 nm,
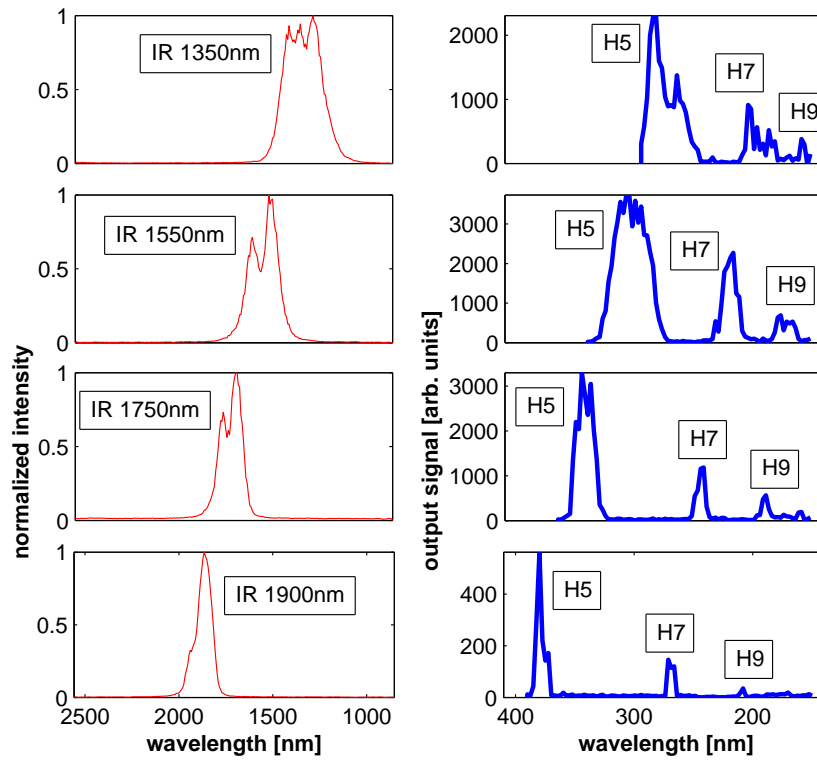
Figure V.3: IR spectra (left side) and corresponding harmonic spectra (right side) in the 400–150 nm spectral region. H5, H7 and H9 stand respectively for the fifth, seventh and ninth harmonics of the driving IR beam.
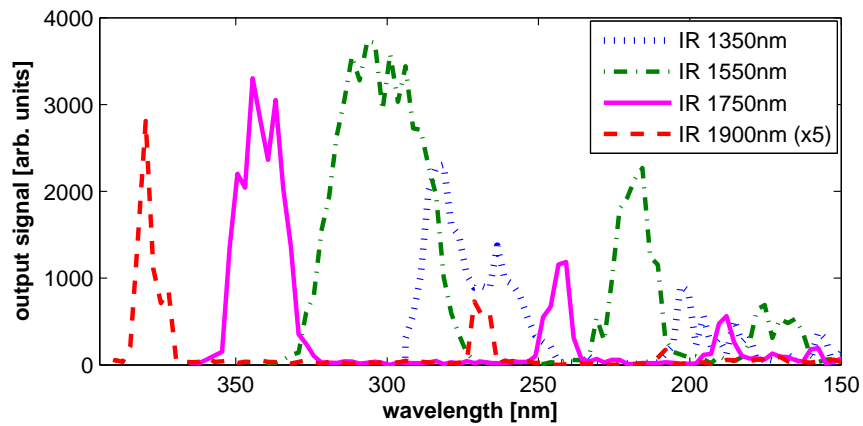
Figure V.4: Overlap of the harmonic spectra for four drive IR wavelengths (1350, 1550, 1750 and 1900 nm). The harmonic spectrum resulting from the drive wavelength of 1900 nm has been vertically magnified ($\times 5$).

Figure V.5: Tunability in the DUV. The lines represent the wavelength ranges that are covered by harmonic orders from fifth to evelenth, generated by drive wavelengths ranging from 1350 nm to 1900 nm.

Table V.1: Absolute number of photons provided in the DUV spectral range for four different drive wavelengths. Left column: central wavelength of the drive beam; center column: wavelengths corresponding to the peak signal of the indicated harmonics; right column: measured photons/shot for each harmonic.

drive IR [nm]	harmonic [nm (order)]	photons/shot
1160	414 (3rd)	2.0×10^8
	248 (5th)	6.1×10^7
	177 (7th)	3.6×10^7
1350	270 (5th)	4.2×10^7
	196 (7th)	1.8×10^7
	153 (9th)	1.3×10^7
1450	285 (5th)	6.1×10^7
	204 (7th)	1.6×10^7
	161 (9th)	8.2×10^6
1800	367 (5th)	1.3×10^7
	262 (7th)	7.0×10^6
	206 (9th)	3.4×10^6

as in these measurements, harmonic orders from fifth to eleventh completely cover the DUV spectral region. Furthermore, the third harmonic, not shown in Fig. V.5, also allows tunability in the visible region. Obviously this overlap and thereby the tunability in the ultraviolet range improve at shorter wavelengths, where narrower IR tunability is thus sufficient.

The photon flux of the harmonics has been measured by fully opening the slits of the monochromator in order to get all the signal on the photomultiplier. The results are summarized in Table V.1. Around 10^7 photons per shot are generated in the DUV spectral region, corresponding to a beam energy of the order of 10 pJ. One sees that the higher the driving wavelength, the smaller the harmonic photon flux. Regarding the ninth harmonic of the driving laser for 1350, 1450 and 1800 nm drive wavelengths (λ_{IR}), the wavelength scaling of the harmonic conversion efficiency is estimated to be about λ_{IR}^{-6}. Even if the exact scaling at con-

stant peak intensity cannot be provided here (as it would require a dedicated experiment), we underline that such an estimate is in agreement with recent theoretical studies which show that the harmonic efficiency in the plateau region scales as λ_{IR}^{-6}, not as λ_{IR}^{-3} as previously believed [144]. Moreover, in [145], the conversion efficiency of further plateau harmonics (from 78 to 39 nm) has recently been measured to be proportional to $\lambda_{IR}^{-6 \pm 1.1}$ in krypton. Although increasing the driving wavelength allows to extend the harmonic plateau [146], there is a penalty in terms of harmonic efficiency. As already explained in Chapter I, the lowering of harmonic efficiency at longer driving wavelength can be well understood in the frame of the semi-classical model since it corresponds to a longer time spent by the electrons into the continuum before recombination and thus, a higher probability to be lost and not to be involved in the harmonic emission.

V.3.b   Extreme-ultraviolet region

The same procedure has been followed for the measurements performed in the EUV region, using the detection system described before. Harmonic spectra are reported in Fig. V.6 for three different driving wavelengths (1350, 1450, 1550 nm) and their overlap in the 45–35 nm spectral range is shown in Fig. V.7. Figure V.8 shows that by varying the driving wavelength from 1350 nm to 1550 nm one attains the full tunability in the EUV, through relatively high-order harmonics. An interesting point is that one specific ultraviolet wavelength can be obtained from multiple drive wavelengths through different harmonic orders.

The shapes of DUV (Fig. V.3) and EUV (Fig. V.6) harmonics are noticeably different. In the first case, the use of a scanning monochromator involves unsmooth spectra due to shot-to-shot fluctuations of the IR energy and the harmonic generation process. Besides, the resolution of the EUV detection system is about 1.6 times smaller than that in the DUV. One main point to consider is that the generation of harmonics obeys to different mechanisms in these spectral regions. In the perturbative framework, the spectrum of the nth harmonic field can be represented as a nth-order autoconvolution of the spectrum of the fundamental field. Thus complex spectral structures in the fundamental spectrum can be inherited by the low harmonics such as, in Fig. V.3, the fifth harmonic of a 1350-nm central drive wavelength. This is not seen in higher harmonics (Fig. V.6), since the generation mechanism is there attributed to the inteference among EUV emissions corresponding to different electron quantum trajectories.

The absolute number of photons in the EUV is reported in Table V.2 for harmonic orders 21, 29 and 35 of 1350, 1450 and 1550 nm driving wavelengths. Such a photon flux corresponds to an energy per harmonic per shot about two orders of magnitude smaller than in the DUV. The different nature of the harmonic generation process and of phase matching conditions for low and high harmonics can also explain the difference of photon flux between the DUV and EUV spectral regions.
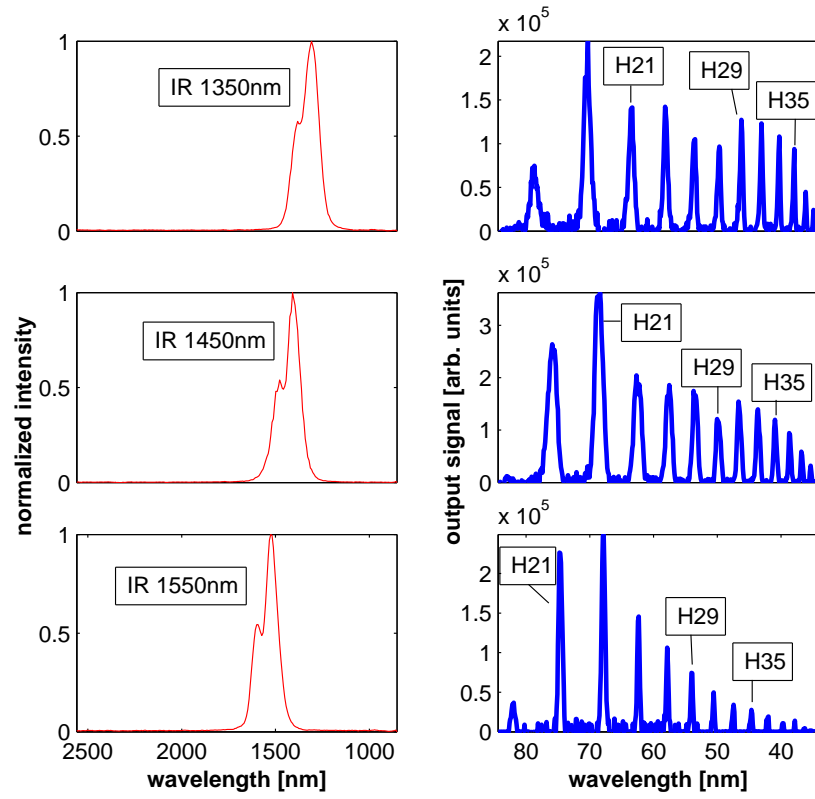
Figure V.6: *IR spectra (left side) and corresponding harmonic spectra (right side) in the 85–30 nm spectral region. H21, H29 and H35 stand respectively for the $21^{st}, 29^{th}, 35^{th}$ harmonic order of the drive IR beam.*
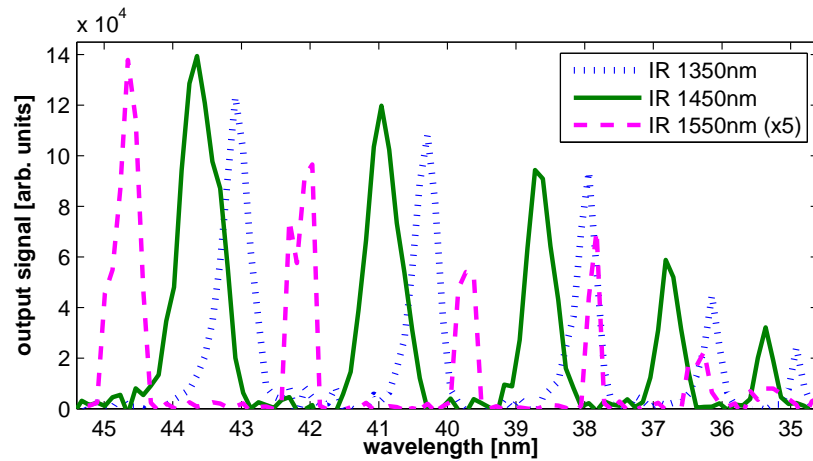
Figure V.7: *Overlap of the harmonic spectra in the range 45–35 nm for three drive IR wavelengths (1350, 1450 and 1550 nm). The harmonic spectrum resulting from the drive wavelength of 1550 nm has been vertically magnified (×5).*
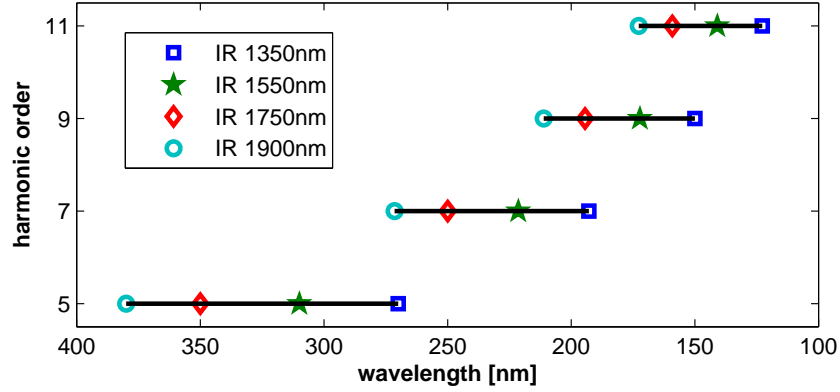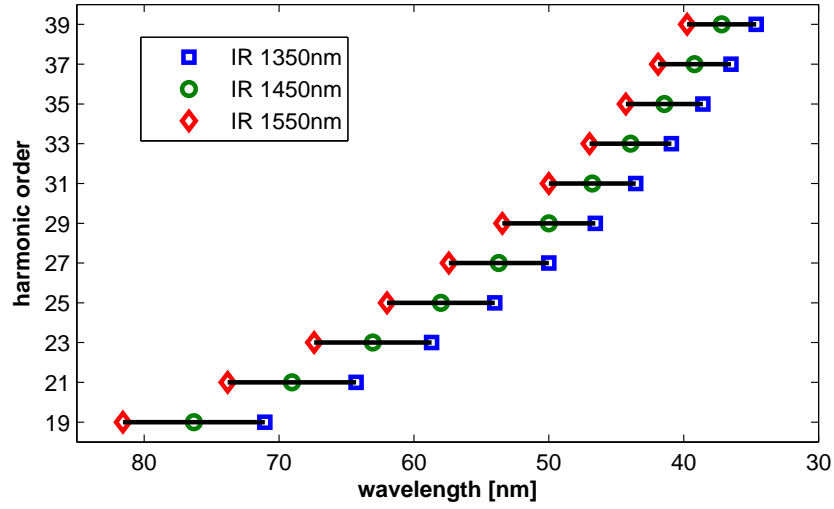
Figure V.8: Tunability in the EUV. The lines represent the wavelength ranges that are covered by harmonic orders from number nineteen to thirty-nine, generated by drive wavelengths ranging from 1350 nm to 1550 nm.

Table V.2: Absolute number of photons provided in the EUV spectral range for three different drive wavelengths. Left column: central wavelength of the drive beam; center column: wavelengths of harmonic orders 21, 29 and 35; right column: measured photons/shot for each harmonic.

drive IR [nm]	harmonics [nm]	photons/shot
1350	63	1.3×10^4
	46	5.8×10^3
	38	2.8×10^3
1450	69	4.4×10^4
	50	9.9×10^3
	41	4.7×10^3
1550	75	1.4×10^4
	54	3.1×10^3
	45	6.5×10^2

Different strategies can be pursued to overcome this low photon flux. As a first possibility, one could design a more powerful parametric source [147]. A complementary strategy is the improvement of the HHG process in terms of tunability and conversion efficiency. In this respect, a promising technique that could be investigated is mixing the fundamental wavelength of the parametric source with either its second harmonic or with a standard powerful Ti:Sa laser source, as demonstrated in [148] or similarly in [149]. Moreover, as shown in [150], using the simultaneous irradiation of an extreme-ultraviolet pulse, the dependence of the harmonic yield from the wavelength of the driving beam can be significantly reduced.

V.4   Summary

The full tunability of a femtosecond photon beam produced through HHG driven by a parametric source has been demonstrated in the whole ultraviolet spectral range. This source opens the way to novel scientific experiments. The main drawback comes from the relatively low harmonic conversion efficiency, resulting from a drive wavelength longer than in classic HHG setups. Increasing the harmonic photon flux would extend the range of possible scientific experiments.

Conclusion and prospects

Free-Electron Lasers and High-order Harmonic Generation sources compete together in the attractive challenge that is to extend the possibilities of scientific applications towards the X-rays. In this extent, we studied some of required qualities of such facilities.

In this manuscript, I first presented the good results of spatial coherence of the light provided at FERMI@Elettra. A fundamental aspect to be understood is: how the seeding could improve the transverse quality of the FEL emission? For answering to this question, it will be possible to perform, on FERMI@Elettra, measurements of spatial coherence also in SASE mode, which would enable doing a fair comparison on the same facility, at the same wavelength i.e., in the same machine conditions. In addition to this, the propagation of the spatial phase should be studied, via systematic wavefront measurements on the seed laser and on the FEL emission, changing the properties of the seed. Furthermore, many questions remain open concerning the effects of the transverse characteristics of the electron beam. Wavefront measurements have already been done on SASE sources [151, 152], and can also be compared with results obtained at FERMI@Elettra. However, the wavefront sensor is often use as a tool for optimizing the beam focusing for experiments, and thus used after specific mirrors. In parallel, we studied the optimization of the spatial quality of an infrared beam used for driving HHG. A noticeable enhancement has been measured. Now, it would be of great interest to see if the properties of coherence and wavefront quality are also transmitted via HHG, and how it could depend on the generation configuration. For the moment, wavefront characterizations on FEL sources give contradictory results [153, 154].

This spatial study has been followed by a work relying on the chirp properties in a seeded FEL. A first application is the production of two separate pulses with different wavelengths, which could be used as a self-standing source for two-colour pump-probe experiments, without requiring an external laser. The production of two colours can be put in parallel with the Young's experiment that we implemented for coherence measurements: the two sub-pulses interfere temporally, and the temporal quadratic phase of the FEL emission corresponds in the Young's experiment to the spatial dispersion that is induced during propagation. Both studies are therefore similar and the interference fringes that are observed in the Young's experiment are the analogy of the beating structure that is observed temporally with a two-colour spectrum. The spectrum corresponds to the Fourier transform of the temporal intensity and the far-field diffraction pattern of coherence measurements is the spatial Fourier transform of the two point sources that are the slits. As we mentioned in Chapter I, FERMI@Elettra is now made of a second stage allowing to generate lower wavelengths. Preliminary results let think that the amplification, in the second stage, of two FEL peaks produced in the first stage is successful. Beyond that, the behaviour of the two-colour FEL in high-gain regime, and the transverse properties of the

emission will have to be studied. Even if it is quite novel, the two-colour emission of an FEL is not completely new. We can cite the case of [155, 156], which was however in the mid-infrared region and where the two peaks were produced simultaneously, which resulted in a strong temporal modulation due to the frequency beating. More recently, a potential soft X-rays two-colour source has been discussed in [157], however without wavelength tunability and temporal control.

A second application of the presence of quadratic phase in the FEL emission is the direct retrieval of the temporal shape of the pulses [158]. Here again, we can rely on a spatio-temporal analogy: the Fraunhofer diffraction corresponds to the "far-field" approximation that we found in the case of a linearly-chirped optical pulse, which allows to retrieve its temporal shape similarly to the fact that we obtain a typical and easy-to-study diffraction pattern if we are in far-field spatially. The quadratic term of the FEL phase induces a temporal dispersion of the pulse spectral component. The instantaneous frequency at a given time is the result of the interference of multiple spectral components. The number of spectral components contributing to it is large for small temporal dispersion (i.e., small chirp) and decreases for increasing temporal dispersion (i.e., large chirp). For sufficiently large chirps, one can approximately associate a single spectral component to each temporal position in the pulse. When this happens, the temporal form of the pulse becomes similar to its spectral shape.

A very interesting prospect concerning the presence of quadratic temporal phase in the FEL radiation, and the possibility to manage it easily before the emission by means of the seed laser chirp, is its chirped-pulse amplification [64]. This hot topic has been discussed for a long time [159, 160, 161] but its implementation on FERMI@Elettra would be an important step for the production of even more intense, but also of shorter and Fourier-transform limited pulses. No specific stretcher would be required prior to the undulators since the chirp stems mainly from the seed, but also from the electrons. The chirp of the latter and its quantification, and its combination with the one of the seed, is also part of the upcoming spectro-temporal studies on seeded FEL's.

The tunability of the wavelength of the EUV radiation, an important asset for experiment, is possible either in FEL's or in HHG facilities. However, a lack of standard HHG sources is the impossibility to generate radiation whose polarization is tunable. On the other hand, as we demonstrated in [162], FEL's are capable to provide elliptical to circular polarization without any effort. The possibility to generate circularly polarized high-order harmonics is thus a big challenge that will have to be taken up. Finally, especially in FEL sources where efforts have been mostly focused on spatial and spectral studies, further temporal characterizations (intensity shape, longitudinal coherence) are required.

As a final word, it is important to stress that FEL and HHG sources are not only two tools that are in competition for providing the best EUV light. First, they are complementary since it has been demonstrated in [163] that HHG can be used for injecting seeded FEL's, allowing to reach even shorter wavelength while providing high photon fluxes with coherent radiation. They can

also be used together in pump-probe experiments. Beyond that, they are two great supports for electromagnetism and atomic studies, be there experimental, numerical or theoretical, and for the understanding of physical processes.

Bibliography

[1] A. Zewail, "Laser femtochemistry", Science **242**, 1645 – 1653 (1988).

[2] S. Monticone et al., "Complex Nature of the UV and Visible Fluorescence of Colloidal ZnO Nanoparticles", J. Phys. Chem. B **102**, 16 (1998).

[3] P. Dumon et al., "Picosecond Dynamics of Cation-Macrocycle Interactions in the Excited State of an Intrinsic Fluorescence Probe: The Calcium Complex of 4-(N-Monoaza-15-crown-5)-4'-phenylstilbene", J. Phys. Chem. **98**, 41 (1994).

[4] W. Uhmann et al., "Time-Resolved FT-IR Absorption Spectroscopy Using a Step-Scan Interferometer", Applied Spectroscopy **45**, 3 (1991).

[5] J. N. Moore, P. A. Hansen and R. M. Hochstrasser, "Iron-carbonyl bond geometries of carboxymyoglobin and carboxyhemoglobin in solution determined by picosecond time-resolved infrared spectroscopy", Chem. Phys. Lett. **138**, 110 (1987).

[6] A. Zumbusch, G. R. Holtom and X. S. Xie, "Three-Dimensional Vibrational Imaging by Coherent Anti-Stokes Raman Scattering", Phys. Rev. Lett. **82**, 4142–4145 (1999).

[7] Philip J. Reid, Steven D. Wickham and Richard A. Mathies, "Picosecond UV resonance Raman spectroscopy of the photochemical hydrogen migration in 1,3,5-cycloheptatriene", J. Phys. Chem. **96**, 14 (1992).

[8] Marcos Dantus, Mark J. Rosker, and Ahmed H. Zewail, "Femtosecond real-time probing of reactions. II. The dissociation reaction of ICN", J. Chem. Phys. **89**, 6128 (1988).

[9] J. Oberlé, G. Jonusauskas, E. Abraham, C. Rullière, "Enhancement and sub-picosecond dynamics of optical non-linearities of excited-states: trans-stilbene in solution", Chem. Phys. Lett. **241**, 281 (1995).

[10] J. Oberlé, G. Jonusauskas, E. Abraham, C. Rullière, "Third-order optical non-linearities of excited states in diphenyl-polyene derivatives: a sub-picosecond study", Optics Communications **124**, 616 (1996).

[11] S. Woutersen, U. Emmerichs and H. J. Bakker, "Femtosecond mid-IR pump-probe spectroscopy of liquid water: Evidence for a two-component structure", Science **278**, 5338 (1997).

[12] H. N. Chapman et al., "Femtosecond diffractive imaging with a soft-X-ray free-electron laser", Nature Physics **2**, 839 – 843 (2006).

[13] J. M. J. Madey, "Stimulated emission of bremsstrahlung in a periodic magnetic field", J. App. Phys. **42**, 1906 – 1913 (1971).

[14] P. Schmüser, M. Dohlus and J. Rossbach, *Ultraviolet and soft X-ray free-electron lasers* (Springer Verlag, 2008).

[15] M. Ferray, A. L'Huillier, X. F. Li, L. A. Lompre, G. Mainfray and C. Manus, "Multiple-harmonic conversion of $1064\ nm$ radiation in rare gases", JOSA B **21**, 3 (1988).

[16] R. Trebino, *Frequency-Resolved Optical Gating: The Measurement of Ultrashort laser Pulses* (Kluwer Publishers, Boston, 2002).

[17] J. C. Diels and W. Rudolph, "Ultrashort laser pulse phenomena", *Academic press* (2006).

[18] J. W. Goodman, *Statistical Optics* (Wiley Classics Library, 2000).

[19] I. Boscolo, V. Stagno, "The converter and the transverse optical klystron", Il Nuovo Cimento B **58**, 267 (1980).

[20] D. Attwood, *Soft x-rays and extreme ultraviolet radiation: principles and applications* (Cambridge University Press, 2000).

[21] F. Curbis, PhD thesis (Università degli studi di Trieste, 2008).

[22] L. Giannessi, "Overview of Perseo, a system for simulating FEL dynamics in Mathcad", in Proceedings of the Free-Electron Laser Conference 2006, MOPPH026.

[23] S. Reiche, "GENESIS 1.3: a fully 3D time-dependent FEL simulation code", Nucl. Instr. Meth. A **429**, 243–248 (1999).

[24] W. M. Fawley, "A user manual for GINGER and its post-processor XPLOTGIN", Report LBNL-49625 (2001).

[25] S. G. Biedron, H. P. Freund and S. V. Milton, "3D FEL code for the simulation of a high-gain harmonic generation experiment", in Optoelectronics' 99 - Integrated Optoelectronic Devices, 96–108 (1999).

[26] R. Bonifacio, L. Di Salvo Souza, P. Pierini and N. Piovella, "The superradiant regime of a FEL: analytical and numerical results", Nucl. Instr. Meth. A **296**, 358 (1990).

[27] L. H. Yu, "Generation of intense uv radiation by subharmonically seeded single-pass free-electron lasers", Phys. Rev. A **44**, 5178 (1991).

[28] M. Sands, "The Physics of Electron Storage Rings: an Introduction", prepared for the U.S. atomic energy commission under contract NO. AT(04-3)-515 (1970).

[29] C. Svetina, A. Abrami, I. Cudin, C. Fava, S. Gerusina, R. Gobessi, L. Rumiz, G. Sostero, M. Zangrando and D. Cocco, "Characterization of the FERMI@Elettra's on-line photon energy spectrometer", Proc. SPIE **8139**, 81390J (2011).

[30] M. Zangrando, A. Abrami, D. Cocco, C. Fava, S. Gerusina, R. Gobessi, N. Mahne, E. Mazzucco, L. Raimondi, L. Rumiz, C. Svetina and F. Parmigiani, "The photon beam transport and diagnostics system at FERMI@Elettra, the Italian seeded FEL source: commissioning experience and most recent results", Proc. SPIE **8504**, 850404 (2012).

[31] K. Wille, *The physics of particle accelerators: an introduction* (Clarendon Press, 1996).

[32] A. Amir, Y. Greenzweig, "Three-dimensional free electron laser gain and evolution of optical modes", Nucl. Instr. Meth. A **250**, 404 (1986).

[33] I. Ben-Zvi, K. M. Yang, L. H. Yu, "The fresh-bunch technique in FELS", Nucl. Instr. Meth. A **318**, 726 (1992).

[34] E. Allaria, D. Castronovo, P. Cinquegrana, P. Craievich, M. B. Danailov, A. Demidovitch, G. D'Auria, M. Dal Forno, G. De Ninno, S. Di Mitri, B. Diviacco, W. M. Fawley, M. Ferianis, E. Ferrari, L. Froehlich, G. Gaio, L. Giannessi, R. Ivanov, N. Mahne, B. Mahieu, I. Nikolov, F. Parmigiani, G. Penco, L. Raimondi, C. Serpico, P. Sigalotti, C. Scafuri, S. Spampinati, C. Spezzani, M. Svandrlik, C. Svetina, M. Trovò, M. Veronese, D. Zangrando, M. Zangrando, "Two-stage seeded soft-X-ray free-electron laser", Nature Photon. **7**, 913—918 (2013).

[35] T. Brabec, *Strong Field Laser Physics* (Springer Verlag, 2008).

[36] P. Salières, A. L'Huillier, P. Antoine, and M. Lewenstein, "Study of the spatial and temporal coherence of high-order harmonics," Adv. At. Mol. Opt. Phys. **41**, 83–142 (1999).

[37] P. A. Franken, A. E. Hill, C. W. Peters and G. Weinreich , "Generation of optical harmonics", Phys. Rev. Lett. **7**, 118–119 (1961).

[38] G. H. C. New and J. F. Ward, "Optical third harmonic generation in gases", Phys. Rev. Lett. **19**, 556–559 (1967).

[39] P. B. Corkum, "Plasma Perspective on Strong-Field Multiphoton Ionization", Phys. Rev. Lett. **71**, 1994 (1993).

[40] Jeffrey L. Krause, Kenneth J. Schafer, and Kenneth C. Kulander , "High-order harmonic generation from atoms and ions in the high intensity regime", Phys. Rev. Lett. **68**, 3535–3538 (1992).

[41] Y. Mairesse, A. de Bohan, L. J. Frasinski, H. Merdji, L. C. Dinu, P. Monchicourt, P. Bréger, M. Kovacev, R. Taïeb, B. Carré, H. G. Müller, P. Agostini and P. Salières, "Attosecond Synchronization of High-Harmonic Soft X-rays", Science **302**, 1540–1543 (2003).

[42] Philippe Balcou, Pascal Salières, Anne L'Huillier and Maciej Lewenstein, "Generalized phase-matching conditions for high harmonics: The role of field-gradient forces", Phys. Rev. A **55**, 3204–3210 (1997).

[43] Pascal Salières, Anne L'Huillier, and Maciej Lewenstein, "Coherence Control of High-Order Harmonics", Phys. Rev. Lett. **74**, 3779–3779 (1995).

[44] E. Constant, D. Garzella, P. Bréger, E. Mével, Ch. Dorrer, C. Le Blanc, F. Salin, and P. Agostini, "Optimizing high harmonic generation in absorbing gases: Model and experiment", Phys. Rev. Lett. **82**, 1668–1671 (1999).

[45] Andy Rundquist, Charles G. Durfee, Zenghu Chang, Catherine Herne, Sterling Backus, Margaret M. Murnane, Henry C. Kapteyn, "Phase-Matched Generation of Coherent Soft X-rays", Science **280**, 1412–1415 (1998).

[46] J.H. Eberly, Q. Su and J. Javanainen, "Nonlinear Light Scattering Accompanying Multiphoton Ionization", Phys. Rev. Lett. **62**, 881 (1989).

[47] K. Kulander, K. Schafer and J. Krause, *Super Intense Laser-Atom Physics* (Plenum Press 1993).

[48] M. Lewenstein, Ph. Balcou, M.Y. Ivanov, A. L'Huillier and P.B. Corkum, "Theory of high-harmonic generation by low-frequency laser fields", Phys. Rev. A **49**, 2117 (1994).

[49] W. Becker, S. Long and J.K. McIver, "Modeling harmonic generation by a zero-range potential", Phys. Rev. A **50**, 1540 (1994).

[50] J. F. Hergott, M. Kovacev, H. Merdji, C. Hubert, Y. Mairesse, E. Jean, P. Breger, P. Agostini, B. Carré and P. Salières, "Extreme-ultraviolet high-order harmonic pulses in the microjoule range," Phys. Rev. A **66**, 021801 (2002).

[51] A. Singer, I. A. Vartanyants, M. Kuhlmann, S. Duesterer, R. Treusch and J. Feldhaus, "Transverse-Coherence Properties of the Free-Electron-Laser FLASH at DESY", Phys. Rev. A **101**, 254801 (2008).

[52] I. A. Vartanyants et al., "Coherence properties of individual femtosecond pulses of an X-ray Free-Electron Laser", Phys. Rev. Lett. **107**, 144801 (2011).

[53] J. C. H. Spence, U. Weierstall and M. Howells, "Coherence and sampling requirements for diffractive imaging", Ultramicroscopy **101**, 149 – 152 (2004).

[54] R. A. Bartels, A. Paul, M. M. Murnane, H. C. Kapteyn, S. Backus, Y. Liu and D. T. Attwood, "Absolute determination of the wavelength and spectrum of an extreme-ultraviolet beam by a Young's double-slit measurement", Opt. Lett. **27**, 9 (2002).

[55] R. A. Bartels et al., "Generation of Spatially Coherent Light at Extreme Ultraviolet Wavelengths", Science **297**, 376 (2002).

[56] I. A. Vartanyants and A. Singer, "Coherence properties of hard x-ray synchrotron sources and x-ray free-electron lasers", New J. Phys. **12**, 035004 (2010).

[57] E. Wolf and E. Collett, "Partially coherent sources which produce the same far-field intensity distribution as a laser", Opt. Commun. **25**, 3 (1978).

[58] E. Wolf, "New theory of partial coherence in the space-frequency domain. Part I: spectra and cross-spectra of steady-state sources", JOSA **72**, 3 (1982).

[59] F. Gori, "Mode propagation of the field generated by Collett-Wolf Schell-Model source", Opt. Commun. **46**, 3 (1983).

[60] G. Gbur and E. Wolf, "The Rayleigh range of Gaussian Schell-model beams", J. Mod. Opt **48**, 11 (2001).

[61] L. Mandel and E. Wolf, *Optical Coherence and Quantum Optics* (Cambridge University Press, 1995).

[62] X. Ge et al., "Impact of wave front and coherence optimization in coherent diffractive imaging", accepted for publication b Optics Express.

[63] A. Maréchal, Revue d'Optique **26**, 257 (1947).

[64] D.Strickland and G. Mourou, "Compression of amplified chirped optical pulses", Opt. Comm. **56**, 219 (1985).

[65] E. Takahashi, Y. Nabekawa, M. Nurhuda, and K. Midorikawa, "Generation of high-energy high-order harmonics by use of a long interaction medium," J. Opt. Soc. Am. B **20**, 158-165 (2003).

[66] W. Boutu, T. Auguste, J. P. Caumes, H. Merdji and B. Carré, "Scaling of the generation of high-order harmonics in large gas media with focal length", Phys. Rev. A **84**, 053819 (2011).

[67] A. Ravasio, D. Gauthier, F. R. N. C. Maia, M. Billon, J-P. Caumes, D. Garzella, M. Géléoc, O. Gobert, J-F. Hergott, A-M. Pena, H. Perez, B. Carré, E. Bourhis, J. Gierak, A. Madouri, D. Mailly, B. Schiedt, M. Fajardo, J. Gautier, P. Zeitoun, P. H. Bucksbaum, J. Hajdu and H. Merdji, "Single-Shot Diffractive Imaging with a Table-Top Femtosecond Soft X-Ray Laser-Harmonics," Phys. Rev. Lett. **103**, 028104 (2009).

[68] D. Gauthier, M. Guizar-Sicairos, X. Ge, W. Boutu, B. Carré, J. R. Fienup, and H. Merdji, "Single-shot Femtosecond X-Ray Holography Using Extended References," Phys. Rev. Lett. **105**, 093901 (2010).

[69] M. Nisoli et al., "High-Brightness High-Order Harmonic Generation by Truncated Bessel Beams in the sub-10-fs Regim ", Phys. Rev. Lett. **88**, 033902 (2002).

[70] P. Villoresi et al., "Optimization of high-order harmonic generation by adaptive control of a sub-10 fs pulse wave front ", Opt. Lett. **29**, 207 (2004).

[71] W. Boutu et al., "High-order-harmonic generation in gas with a flat-top laser beam ", Phys. Rev. A **84**, 063406 (2011).

[72] V. Ramanathan, J. Lee, S. Xu, X. Wang, and D. H. Reitze, "Analysis of Thermal Aberrations in a High Average Power Single-Stage Ti:Sapphire Regenerative Chirped Pulse Amplifier" in Frontiers in Optics, OSA Technical Digest (CD) (Optical Society of America, 2006), paper FTuS4.

[73] G. P. Agrawal, *Nonlinear Fiber Optics* (Academic Press, New York, 2006).

[74] R. Paschotta, "Beam quality deterioration of lasers caused by intracavity beam distortions," Opt. Express **14**, 6069-6074 (2006).

[75] H. Kogelnik and T. Li, "Laser Beams and Resonators," Appl. Opt. **5**, 1550-1567 (1966).

[76] J. W. Goodman, *Introduction to Fourier optics* (Roberts & Company Publishers, 2005).

[77] E. Hecht, *Optics* (Addison Wesley, 2001).

[78] P. M. Celliers, K. G. Estabrook, R. J. Wallace, J. E. Murray, L. B. Da Silva, B. J. MacGowan, B. M. Van Wonterghem, and K. R. Manes, "Spatial Filter Pinhole for High-Energy Pulsed Lasers," Appl. Opt. **37**, 2371-2378 (1998).

[79] S. Sinha, K. Dasgupta, S. Sasikumar, and S. Kundu, "Saturable-absorber-based spatial filtering of high-power laser beams," Appl. Opt. **45**, 4947-4956 (2006).

[80] R. K. Tyson, "Using the deformable mirror as a spatial filter: application to circular beams," Appl. Opt. **21**, 787-793 (1982).

[81] H. Yan-Lan, Z. Hao-Bin, T. Ji-Chun, D. Dao-Yi, Z. Guang-Wei, W. X. Dong, W. Xiao, "Two-dimensional non-spatial filtering based on holographic Bragg gratings," Chinese Phys. B **19** 074215 (2010).

[82] S. Szatmári, Z. Bakonyi and P. Simon, "Active spatial filtering of laser beams," Optics Comm. **134**, 199 (1997).

[83] G. Doumy, F. Quéré, O. Gobert, M. Perdrix, P. Martin, P. Audebert, J.-C. Gauthier, J.-P. Geindre, and T. Wittman, "Complete characterization of a plasma mirror for the production of high-contrast ultraintense laser pulses," Phys. Rev. E **69**, 026402-1 (2004).

[84] A. Jullien, O. Albert, F. Burgy, G. Hamoniaux, J.-P. Rousseau, J.-P. Chambaret, F. Augé-Rochereau, G. Chériaux, J. Etchepare, N. Minkovski, and S. M. Saltiel, "10^{-10} temporal contrast for femtosecond ultraintense lasers by cross-polarized wave generation," Opt. Lett. **30**, 920 (2005).

[85] M. Nisoli, S. De Silvestri, and O. Svelto,"Generation of high energy 10 fs pulses by a new pulse compression technique," Appl. Phys. Lett. **68**, 2793 (1996).

[86] A. Ksendzov, T. Lewi, O. P. Lay, S. R. Martin, R. O. Gappinger, P. R. Lawson, R. D. Peters, S. Shalem, A. Tsun, and A. Katzir, "Modal filtering for midinfrared nulling interferometry using single mode silver halide fibers," Appl. Opt. **47**, 5728-5735 (2008).

[87] H.-C. Bandulet, D. Comtois, A. D. Shiner, C. Trallero-Herrero, N. Kajumba, T. Ozaki, P. B. Corkum, D. M. Villeneuve, J.-C. Kieffer and F. Légaré, "High harmonic generation with a spatially filtered optical parametric amplifier," J. Phys. B: At. Mol. Opt. Phys. **41**, 245602 (2008).

[88] G. Cheriaux, P. Rousseau, F. Salin, J. P. Chambaret, Barry Walker and L. F. Dimauro, "Aberration-free stretcher design for ultrashort-pulse amplification", Opt. Lett. **21**, 414 – 416 (1996).

[89] Patrick Georges, Frederick Estable, François Salin, Jean Philippe Poizat, Philippe Grangier and Alain Brun, "High-efficiency multipass Ti:sapphire amplifiers for a continuous-wave single-mode laser", Opt. Lett. **16**, 144 – 146 (1991).

[90] B. E. A. Saleh and M. C. Teich, *Fundamentals of Photonics* (Wiley, 2007).

[91] M. W. Sasnett, "Propagation of multimode laser beams - the M^2 factor," in Physics and Technology of Laser Resonators, D. R. Hall and P. E. Jackson, Hilger (1989).

[92] ISO 11146-1:2005.

[93] A. E. Siegman, "How to (Maybe) Measure Laser Beam Quality," in DPSS (Diode Pumped Solid State) Lasers: Applications and Issues, M. Dowley, ed., Vol. 17 of OSA Trends in Optics and Photonics (Optical Society of America, 1998), paper MQ1.

[94] J. A. Stratton, "Electromagnetic theory," McGraw–Hill Book Co., New-York and London (1941).

[95] E. Snitzer, "Cylindrical Dielectric Waveguide Modes," J. Opt. Soc. Am. **51**, 491-498 (1961).

[96] E. Marcatili and R. Schmeltzer, "Hollow metallic and dielectric waveguides for long distance optical transmission and lasers," Bell Syst. Tech. J. **43**, 1783–1809 (1964).

[97] J. J. Degnan, "Waveguide laser mode patterns in the near and far field", Appl. Opt. **12**, 1026 (1973).

[98] E. G. Neumann, *Single Mode Fibers: Fundamentals* (Springer-Verlag Berlin and Heidelberg GmbH and Co. K, 1988).

[99] H. Norman and W. Horst, *Laser Resonators and Beam Propagation: Fundamentals, Advanced Concepts and Applications* (Springer, 2005).

[100] B. Lü, B. Zhang and B. Cai, "Propagation and diffraction of apertured higher-order Gaussian beams", J. Mod. Optic. **40**, 1731 – 1743 (1993).

[101] C. Iaconis and I. A. Walmsley, "Spectral Phase Interferometry for Direct Electric-Field Reconstruction of Ultrashort Optical Pulses," Opt. Lett. **23**, 792–794 (1998).

[102] S. Kazamias, F. Weihe, D. Douillet, C. Valentin, T. Planchon, S. Sebban, G. Grillon, F. Augé, D. Hulin and Ph. Balcou, "High order harmonic generation optimization with an apertured laser beam", The European Physical Journal D **21**, 335 – 359 (2002).

[103] B. Mahieu, D. Gauthier, M. Perdrix, X. Ge, W. Boutu, F. Lepetit, F. Wang, B. Carré, T. Auguste, H. Merdji, D. Garzella, O. Gobert, "Spatial quality improvement of high-energy Ti:Sapphire laser beam by Modal Filtering", in preparation.

[104] A. I. Gonzalez and Y. Mejia, "Nonredundant array of apertures to measure the spatial coherence in two dimensions with only one interferogram", J. Opt. Soc. Am. A **28**, 6 (2011).

[105] M. D. Alaimo, M. A. C. Potenza, M. Manfredda, G. Geloni, M. Sztucki, T. Narayanan and M. Giglio, "Probing the transverse coherence of an undulator x-ray beam using brownian particles", Phys. Rev. Lett. **103**, 19 (2009).

[106] M. B. Danailov, A. Demidovich, R. Ivanov, I. Nikolov, P. Sigalotti, P.Cinquegrana, "Desing and first experience with the FERMI seed laser", in Proceedings of the Free-Electron Laser Conference 2011, TUOC4.

[107] M. Danailov and P. Sigalotti, "STATUS OF THE FERMI LASER SYNCHRONIZATION WORK AT ELETTRA", Presentation at the 2nd Timing and Synchronization Workshop, Trieste (2009).

[108] M. Ferianis, F. Kaertner, F. O. Ilday, J. W. Kim, J. Chen, A. Winter, J. Staples, R. Willcox, "Generation and distribution of stable timing signals to synchronize RF and lasers at the FERMI@Elettra FEL facility", in Proceedings of the 27th Free-Electron Laser Conference (2005).

[109] M. Ferianis, Andrea Borga, Andrea Bucconi, Leon Pavlovic, Mauro Predonzani, Fabio Rossi, "ALL-OPTICAL FEMTOSECOND TIMING SYSTEM FOR THE FERMI@ELETTRA FEL ", in Proceedings of the Free-Electron Laser Conference 2011, FROAI2.

[110] M. Ferianis, "STATE OF THE ART IN HIGH-STABILITY TIMING, PHASE REFERENCE DISTRI-BUTION AND SYNCHRONIZATION SYSTEMS ", in Proceedings of PAC09 in Vancouver (Canada), WE3GRI02.

[111] FERMI@Elettra Conceptual Design Report.

[112] T. P. Wangler, "RF linear accelerators", *Wiley-VCH* (2008).

[113] P. Emma, "X-Band RF Harmonic Compensation for Linear Bunch Compression in the LCLS", LCLS-N-01-1 (2001).

[114] J. B. Murphy, S. Krinsky and R. L. Gluckstern, "Longitudinal wakefield for synchrotron radiation", in Proceedings of the 1995 Particle Accelerator Conference **5**, 2980–2982 (1995).

[115] P. Craievich, S. Di Mitri, M. Ferianis, M. Veronese, M. Petronio and D. Alesini, "A transverse RF deflecting cavity for the FERMI@ Elettra project", in Proceedings of the 8th DIPAC (2011).

[116] S. Di Mitri et al., "Design and simulation challenges for FERMI@ elettra", Nucl. Inst. and Meth. A **608**, 19–27 (2009).

[117] A. A. Lutman, G. Penco, P. Craievich and J. Wu, "Impact of an initial energy chirp and an initial energy curvature on a seeded free electron laser: free electron laser properties", Journal of Physics A **42**, 085405 (2009).

[118] M. Xie, "Exact and variational solutions of 3D eigenmodes in high gain FELs", Nucl. Instr. Meth. A **445**, 59 (2000).

[119] J. Wu, J. B. Murphy, P. J. Emma, X. Wang, T. Watanabe and X. Zhong, "Interplay of the chirps and chirped pulse compression in a high-gain seeded free-electron laser", JOSA B **24**, 484–495 (2007).

[120] G. Dattoli, E. Sabia, P. L. Ottaviani, S. Pagnutti and V. Petrillo, "Longitudinal dynamics of high gain free electron laser amplifiers", PRST-AB **16**, 030704 (2013).

[121] T. Shaftan and L. H. Yu, "High-gain harmonic generation free-electron laser with variable wave-length", Phys. Rev. E **71**, 046501 (2005).

[122] E. Allaria, "FEL commissioning at FERMI@Elettra", talk at Free-Electron Laser Conference 2011, WEOBI1.

[123] G. De Ninno, E. Allaria, M. Coreno, F. Curbis, M. B. Danailov, E. Karantzoulis, A. Locatelli, T. O. Menteş, M. A. Nino, C. Spezzani, and M. Trovò, "Generation of Ultrashort Coherent Vacuum-Ultraviolet Pulses Using Electron Storage Rings: A New Bright Light Source for Experiments", Phys. Rev. Lett. **101**, 053902 (2008).

[124] E. Allaria, R. Appio, L. Badano, W.A. Barletta, S. Bassanese, S.G. Biedron, A. Borga, E. Busetto, D. Castronovo, P. Cinquegrana, S. Cleva, D. Cocco, M. Cornacchia, P. Craievich, I. Cudin, G. D'Auria, M. Dal Forno, M.B. Danailov, R. De Monte, G. De Ninno, P. Delgiusto, A. Demidovich, S. Di Mitri, B. Diviacco, A. Fabris, R. Fabris, W. Fawley, M. Ferianis, E. Ferrari, S. Ferry, L. Froehlich, P. Furlan, G. Gaio, F. Gelmetti, L. Giannessi, M. Giannini, R. Gobessi, R. Ivanov, E. Karantzoulis, M. Lonza, A. Lutman, B. Mahieu, M. Milloch, S.V. Milton, M. Musardo, I. Nikolov, S. Noe, F. Parmigiani, G. Penco, M. Petronio, L. Pivetta, M. Predonzani, F. Rossi, L. Rumiz, A. Salom, C. Scafuri, C. Serpico, P. Sigalotti, S. Spampinati, C. Spezzani, M. Svandrlik, C. Svetina, S. Tazzari, M. Trovo, R. Umer, A. Vascotto, M. Veronese, R. Visintini, M. Zaccaria, D. Zangrando and M. Zangrando, "Highly coherent and stable pulses from the FERMI seeded free-electron laser in the extreme ultraviolet", Nat. Photonics **6**, 699–704 (2012).

[125] M. Labat, N. Joly, S. Bielawski, C. Szwaj, C. Bruni, and M. E. Couprie, "Pulse Splitting in Short Wavelength Seeded Free Electron Lasers", Phys. Rev. Lett. **103**, 264801 (2009).

[126] B. Mahieu, E. Allaria, D. Castronovo, M. B. Danailov, A. Demidovich, G. De Ninno, S. Di Mitri, W. M. Fawley, E. Ferrari, L. Fröhlich, D. Gauthier, L. Giannessi, N. Mahne, G. Penco, L. Raimondi, S. Spampinati, C. Spezzani, C. Svetina, M . Trovò and M . Zangrando, "Two-colour generation in a chirped seeded Free-Electron Laser: a close look", Opt. Exp. **21**, 22728–22741 (2013).

[127] G. Stupakov, "Effect of finite pulse length and laser frequency chirp on HGHG and EEHG seeding", SLAC Report No. SLAC-PUB-14639 (2011).

[128] D. Ratner, A. Fry, G. Stupakov and W. White, "Laser phase errors in seeded free electron lasers", PRST-AB **15**, 030702 (2012).

[129] Y. Mairesse, O. Gobert, P. Bréger, H. Merdji, P. Meynadier, P. Monchicourt, M. Perdrix, P. Salières and B. Carré, "High Harmonic XUV Spectral Phase Interferometry for Direct Electric-Field Reconstruction", Phys. Rev. Lett. **94**, 173903 (2005).

[130] Z. Wu, H. Loos, Y. Shen, B. Sheehy, E. D. Johnson, S. Krinsky, J. B. Murphy, J. Rose, T. Shaftan, X.-J. Wang and L. H. Yu, "SPECTRAL PHASE MODULATION AND CHIRPED PULSE AMPLIFICATION IN HIGH GAIN HARMONIC GENERATION", Proceedings of the 2004 FEL conference.

[131] H. P. Freund and P. G. O'Shea, "Two-Color Operation in High-Gain Free-Electron Lasers", Phys. Rev. Lett **84**, 13 (2000).

[132] E. Allaria, F. Bencivenga, R. Borghes, F. Capotondi, D. Castronovo, P. Charalambous, P. Cinquegrana, M. B. Danailov, G. De Ninno, A. Demidovich, S. Di Mitri, B. Diviacco, D. Fausti, W. M. Fawley, E. Ferrari, L. Fröhlich, D. Gauthier, A. Gessini, L. Giannessi, R. Ivanov, M. Kiskinova, G. Kurdi, B. Mahieu, N. Mahne, I. Nikolov, C. Masciovecchio, E. Pedersoli, G. Penco, L. Raimondi, C. Serpico, P. Sigalotti, S. Spampinati, C. Spezzani, C. Svetina, M. Trovò and M. Zangrando, "Two-colour pump–probe experiments with a twin-pulse-seed extreme ultraviolet free-electron laser", Nature Comm. **4**, 2476 (2013).

[133] G. De Ninno, B. Mahieu, E. Allaria, L. Giannessi and S. Spampinati, "Chirped Seeded Free-Electron Lasers: Self Standing Light Sources for Two-Color Pump-Probe Experiments", Phys. Rev. Lett. **110**, 064801 (2013).

[134] E. Allaria et al., "Tunability experiments at the FERMI@Elettra free-electron laser", New J. Phys. **14**, 113009 (2012).

[135] G. Cerullo and S. De Silvestri, "Ultrafast optical parametric amplifiers", Rev. Sci. Instrum. **74**, 1 (2003).

[136] M. Bellini, "Generation of widely tunable harmonic pulses in the UV and VUV from a NIR optical parametric amplifier", Appl. Phys. B **70**, 773 (2000).

[137] B. Mahieu, S. Coraggia, C. Callegari, M. Coreno, G. De Ninno, M. Devetta, F. Frassetto, D. Garzella, M. Negro, C. Spezzani, C. Vozzi, S. Stagira, L. Poletto, "Full tunability of laser femtosecond high-order harmonics in the ultraviolet spectral range", Appl. Phys. B **108**, 43–49 (2012).

[138] C. Vozzi et al., "Millijoule-level phase-stabilized few-optical-cycle infrared parametric source", Opt. Lett. **32**, 2957 (2007).

[139] L. Poletto, A. Boscolo, and G. Tondello, "Characterization of a charge-coupled-device detector in the 1100-0.14-nm (1-eV to 9-keV) spectral region", Appl. Opt. **38**, 29 (1999).

[140] L. Poletto, G. Tondello, and P. Villoresi, "High-order laser harmonics detection in the EUV and soft x-ray spectral regions", Rev. Sci. Instr. **72**, 2868 (2001).

[141] L. Poletto, S. Bonora, M. Pascolini, and P. Villoresi, "Instrumentation for analysis and utilization of extreme-ultraviolet and soft x-ray high-order harmonics", Rev. Sci. Instr. **75**, 4413 (2004).

[142] X. Tong and S. Chu, "Multiphoton ionization and high-order harmonic generation of He, Ne, and Ar atoms in intense pulsed laser fields: Self-interaction-free time-dependent density-functional theoretical approach", Phys. Rev. A **64**, 013417 (2001).

[143] R. Craxton, "High efficiency frequency tripling schemes for high-power Nd: glass lasers", J. of Quant. Elec. **17**, 9 (1981).

[144] J. Tate et al., "Scaling of wave-packet dynamics in an intense midinfrared field", Phys. Rev. Lett. **98**, 013901 (2007).

[145] A. D. Shiner et al., "Wavelength scaling of high harmonic generation efficiency", Phys. Rev. Lett. **103**, 073902 (2009).

[146] T. Popmintchev et al., "Extended phase matching of high harmonics driven by mid-infrared light", Opt. Lett. **33**, 18 (2008).

[147] E. J. Takahashi et al., "10 mJ class femtosecond optical parametric amplifier for generating soft x-ray harmonics", Appl. Phys. Lett. **93**, 041111 (2008).

[148] F. Calegari et al., "Efficient continuum generation exceeding 200 eV by intense ultrashort two-color driver", Opt. Lett. **34**, 3125 (2009).

[149] P. Lan et al., "Optimization of infrared two-color multicycle field synthesis for intense-isolated-attosecond-pulse generation", Phys. Rev. A **82**, 053413 (2010).

[150] K. Ishikawa et al., "Wavelength dependence of high-order harmonic generation with independently controlled ionization and ponderomotive energy", Phys. Rev. A **80**, 011807 (2009).

[151] B. Flöter et al., "Beam parameters of FLASH beamline BL1 from Hartmann wavefront measurements ", Nucl. Instr. and Meth. A **635**, 108–112 (2011).

[152] R. Bachelard et al., "Wavefront Analysis of Nonlinear Self-Amplified Spontaneous-Emission Free-Electron Laser Harmonics in the Single-Shot Regime", Phys. Rev. Lett. **106**, 234801 (2011).

[153] J. Gautier et al., "Optimization of the wave front of high order harmonics", Eur. Phys. J. D **48**, 459 – 463 (2008).

[154] J. Lohbreier et al., "Maximizing the brilliance of high-order harmonics in a gas jet", New J. Phys. **11**, 023016 (2009).

[155] R. Prazeres, F. Glotin, C. Insa, D. A. Jaroszynski and J.M. Ortega, "Two-colour operation of a Free-Electron Laser and applications in the mid-infrared", Eur. Phys. J. D 3 **3**, 87-93 (1998).

[156] D. A. Jaroszynski, R. Prazeres, F. Glotin and J.M. Ortega, "Two-colour operation of the free-electron laser using a step-tapered undulator", Nucl. Instr. and Meth. **358**, 1 (1995).

[157] N. Rohringer et al., "Atomic inner-shell X-ray laser at 1.46 nanometres pumped by an X-ray free-electron laser", Nature **481**, 488 (2012).

[158] D. Gauthier, B. Mahieu and G. De Ninno, "Spectro-temporal analysis for pulse shape determination: application to the seeded free electron laser", Phys. Rev. A **88**, 033849 (2013).

[159] L. H. Yu, E. Johnson, D. Li and D. Umstadter, "Femtosecond free-electron laser by chirped pulse amplification", Phys. Rev. E **49**, 4480 (1994).

[160] F. Frassetto, L. Giannessi and L. Poletto, "Compression of XUV FEL pulses in the few-femtosecond regime", Nucl. Instr. and Meth. A **593**, 14–16 (2008).

[161] C. Feng, L. Shen, M. Zhang, D. Wang, D. Zhao and D. Xiang, "Chirped-pulse amplification in a seeded free-electron laser for generating high-power ultra-short radiation", Nucl. Instr. and Meth. A (2013).

[162] C. Spezzani, E. Allaria, M. Coreno, B. Diviacco, E. Ferrari, G. Geloni, E. Karantzoulis, B. Mahieu, M. Vento and G. De Ninno, "Coherent Light with Tunable Polarization from Single-Pass Free-Electron Lasers ", Phys. Rev. Lett. **107**, 084801 (2011).

[163] G. Lambert et al., "Injection of harmonics generated in gas in a free-electron laser providing intense and coherent extreme ultraviolet light", Nature Phys. **4**, 296 (2008).

Spectro-temporal properties of a linearly-chirped Gaussian pulse

The electric field in the temporal domain can be written, in the longitudinal dimension, as the product of its amplitude E_0, a first exponential representing the Gaussian envelope and a second one for the oscillations of the field:

$$E(t) = E_0 e^{-\Gamma_r t^2} e^{-i\Phi(t)} \tag{A.1}$$

We consider a linearly-chirped pulse. If the slope of the frequency dependence is $2\Gamma_i$, we can write it as:

$$\omega(t) = \omega_0 + 2\Gamma_i t \tag{A.2}$$

The information about the oscillations is contained in $\Phi(t)$: the instantaneous frequency is given by $\omega(t) = \frac{d\Phi(t)}{dt}$ and thus, by integration, we get:

$$\Phi(t) = \omega_0 t + \Gamma_i t^2 + \varphi_0 \tag{A.3}$$

By order, we get the linear term corresponding to the "fast" oscillations at the mean frequency ω_0, the quadratic phase that is a slowly varing frequency and a constant phase. If we neglect the latter, that has no effect on $\omega(t)$, the temporal electric field can be represented by:

$$E(t) = E_0 e^{-\Gamma t^2 - i\omega_0 t} \tag{A.4}$$

with $\Gamma = \Gamma_r + i\Gamma_i$. The temporal intensity is given by:

$$
\begin{aligned}
I(t) &= E(t) \cdot E^*(t) \\
&= \left(E_0 e^{-\Gamma t^2 - i\omega_0 t} \right) \cdot \left(E_0 e^{-\Gamma^* t^2 + i\omega_0 t} \right) \\
&= E_0^2 e^{-2\Gamma_r t^2}
\end{aligned}
\tag{A.5}
$$

Since the intensity profile is also Gaussian, we identify $\Gamma_r = \frac{1}{4\sigma_t^2}$ where σ_t is thus the standard deviation of the temporal intensity profile (not of the electric field envelope). The positions at

which the intensity reaches the half of its maximum correspond to:

$$e^{-2\Gamma_r t^2} = \frac{1}{2}$$

$$-2\Gamma_r t^2 = \ln(\frac{1}{2}) = \ln(1) - \ln(2) = -ln(2)$$

$$t = \pm\sqrt{\frac{\ln 2}{2\Gamma_r}} \tag{A.6}$$

Therefore, the full-width at half maximum of the temporal intensity profile is:

$$H_t = 2\sqrt{\frac{\ln 2}{2\Gamma_r}} = \sqrt{\frac{2\ln 2}{\Gamma_r}} = 2\sigma_t\sqrt{2\ln 2} \tag{A.7}$$

The electric field in the spectral domain is given by the Fourier transform of Eq. A.4:

$$\tilde{E}(\omega) = \frac{1}{\sqrt{2\pi}}\int_{-\infty}^{+\infty} E(t)e^{i\omega t}\,\mathrm{d}t$$

$$= \frac{1}{\sqrt{2\pi}}E_0\int_{-\infty}^{+\infty} e^{-\Gamma t^2 - i\omega_0 t}e^{i\omega t}\,\mathrm{d}t$$

$$= \frac{1}{\sqrt{2\pi}}E_0\int_{-\infty}^{+\infty} e^{-\left[\Gamma t^2 - i(\omega-\omega_0)t\right]}\,\mathrm{d}t \tag{A.8}$$

The trick to solve this integral is to do a "completion of the square" of the argument of the exponential, $\left[\Gamma t^2 - i(\omega - \omega_0)t\right]$. This argument can be written in the form $(at + b)^2 - b^2 = a^2t^2 + 2abt$. By identification, we get $a = \sqrt{\Gamma}$ and $b = -\frac{i(\omega-\omega_0)}{2\sqrt{\Gamma}}$, and thus can rewrite the integral:

$$\tilde{E}(\omega) = \frac{1}{\sqrt{2\pi}}E_0 e^{b^2}\int_{-\infty}^{+\infty} e^{-(at+b)^2}\,\mathrm{d}t \tag{A.9}$$

We operate a variable change: $u = at + b$ and $\frac{du}{dt} = a$. We now get:

$$\tilde{E}(\omega) = \frac{1}{a\sqrt{2\pi}}E_0 e^{b^2}\int_{-\infty}^{+\infty} e^{-u^2}\,\mathrm{d}u \tag{A.10}$$

We get a well-known Gauss integral which is solved easily. First, the integral can be seen as a square root:

$$\int_{-\infty}^{+\infty} e^{-u^2}\,\mathrm{d}u = \sqrt{\int_{-\infty}^{+\infty} e^{-x^2}\,\mathrm{d}x\int_{-\infty}^{+\infty} e^{-x^2}\,\mathrm{d}x} = \sqrt{\int_{-\infty}^{+\infty} e^{-x^2}\,\mathrm{d}x\int_{-\infty}^{+\infty} e^{-y^2}\,\mathrm{d}y}$$

$$= \sqrt{\int_{-\infty}^{+\infty}\int_{-\infty}^{+\infty} e^{-(x^2+y^2)}\,\mathrm{d}x\,\mathrm{d}y} \tag{A.11}$$

We change the latter expression to polar coordinates:

$$\int_{-\infty}^{+\infty} e^{-u^2}\,du = \sqrt{\int_0^{2\pi}\int_{-\infty}^{+\infty} e^{-r^2} r\,dr\,d\theta} = \sqrt{2\pi \frac{e^{-r^2}}{-2}\bigg|_0^{+\infty}} = \sqrt{\pi} \tag{A.12}$$

Hence, we finally obtain:

$$\tilde{E}(\omega) = \frac{1}{\sqrt{2\Gamma}} E_0 e^{-\frac{(\omega-\omega_0)^2}{4\Gamma}} \tag{A.13}$$

We can develop the above equation in order to separate the envelope and the phase terms. It gives:

$$\tilde{E}(\omega) = \frac{1}{\sqrt{2\Gamma}} E_0 e^{-\frac{\Gamma_r}{4|\Gamma|^2}(\omega-\omega_0)^2} e^{i\frac{\Gamma_i}{4|\Gamma|^2}(\omega-\omega_0)^2} \tag{A.14}$$

In the spectral domain, the electric field thus has also a Gaussian envelope: nothing surprising, the Fourier transform of a Gaussian is a Gaussian. The spectrum is given by:

$$\begin{aligned}
\tilde{I}(\omega) &= \tilde{E}(\omega) \cdot \tilde{E}^*(\omega) \\
&= \left(\frac{1}{\sqrt{2\Gamma}} E_0 e^{-\frac{\Gamma_r}{4|\Gamma|^2}(\omega-\omega_0)^2} e^{i\frac{\Gamma_i}{4|\Gamma|^2}(\omega-\omega_0)^2} \right) \cdot \left(\frac{1}{\sqrt{2\Gamma^*}} E_0 e^{-\frac{\Gamma_r}{4|\Gamma|^2}(\omega-\omega_0)^2} e^{-i\frac{\Gamma_i}{4|\Gamma|^2}(\omega-\omega_0)^2} \right) \\
&= \frac{1}{2\sqrt{|\Gamma|}} E_0^2 e^{-\frac{\Gamma_r}{2|\Gamma|^2}(\omega-\omega_0)^2} \tag{A.15}
\end{aligned}$$

Considering σ_ω as the standard deviation of this Gaussian intensity profile i.e., $\frac{1}{2\sigma_\omega^2} = \frac{\Gamma_r}{2(\Gamma_r^2+\Gamma_i^2)}$, we obtain $\Gamma_i = \pm\frac{1}{4\sigma_t^2}\sqrt{4\sigma_t^2\sigma_\omega^2 - 1}$. And finally, the FWHM of the spectrum is:

$$H_\omega = 2\sqrt{2\ln 2\,\Gamma_r\left[1 + \left(\frac{\Gamma_i}{\Gamma_r}\right)^2\right]} = 2\sigma_\omega\sqrt{2\ln 2} \tag{A.16}$$

Let us look at the time-bandwidth product:

$$\begin{aligned}
H_t \cdot H_\omega &= \sqrt{\frac{2\ln 2}{\Gamma_r}} \cdot 2\sqrt{2\ln 2\,\Gamma_r\left[1 + \left(\frac{\Gamma_i}{\Gamma_r}\right)^2\right]} \\
&= 4\ln 2\sqrt{1 + \left(\frac{\Gamma_i}{\Gamma_r}\right)^2} \\
&\geqslant 4\ln 2 \tag{A.17}
\end{aligned}$$

If we consider the frequency $\nu = \frac{\omega}{2\pi}$, we have $H_t \cdot H_\nu \geqslant \frac{4\ln 2}{2\pi} \approx 0.441$, which is the well-known value of the Fourier limit for a Gaussian pulse. For a given spectrum, the amount of chirp (here, only linear, characterized by Γ_i) drives the lengthening of the pulse duration.

It is more common to work with wavelengths, so it is useful to rewrite the time-bandwidth

product as a function of λ. Since $\frac{\Delta \nu}{\nu} = \frac{\Delta \lambda}{\lambda}$, we get that $\Delta \nu = \frac{\nu \Delta \lambda}{\lambda} = \frac{c \Delta \lambda}{\lambda^2}$ and thus:

$$H_t \cdot H_\lambda \geqslant \frac{4\lambda^2 \ln 2}{2\pi c} \qquad \text{(A.18)}$$

Hermite polynomials

In Section II.1.d, the Hermite polynomials $H_n(x)$ are used for describing the functions composing the cross-spectral density of a Gauss-Schell Model beam. However, in the literature one can find different definitions for the Hermite polynomials. The one that is used in this thesis is the following:

$$
\begin{aligned}
H_0(x) &= 1 \\
H_1(x) &= 2x \\
H_p(x) &= 2xH_{p-1}(x) + 2(p-1)H_{p-2}(x),
\end{aligned}
\tag{B.1}
$$

with $p \geqslant 2$.

Articles

1. "Coherent Light with Tunable Polarization from Single-Pass Free-Electron Lasers", published in *Physical Review Letters* (2011).

2. "Full tunability of laser femtosecond high-order harmonics in the ultraviolet spectral range", published in *Applied Physics B* (2012).

3. "Tunability experiments at the FERMI@Elettra free-electron laser", published in *New Journal of Physics* (2012).

4. "Highly coherent and stable pulses from the FERMI seeded free-electron laser in the extreme ultraviolet", published in *Nature Photonics* (2012).

5. "Chirped Seeded Free-Electron Lasers: Self Standing Light Sources for Two-Color Pump-Probe Experiments", published in *Physical Review Letters* (2013).

6. "Two-colour generation in a chirped seeded Free-Electron Laser: a close look", published in *Optics Express* (2013).

7. "Spectro-temporal analysis for pulse shape determination: application to the seeded free electron laser", published in *Physical Review A* (2013).

8. "Two-color pump-probe experiment with twin-pulse-seed XUV free electron laser", published in *Nature Communications* (2013).

9. "Two-stage seeded soft-X-ray free-electron laser", published in *Nature Photonics* (2013).

10. "Spatial quality improvement of high-energy Ti:Sapphire laser beam by Modal Filtering", in preparation